Examining the Caloric Curve in Ar+Sc and Kr+Nb systems

By

Richard John Shomin II

A DISSERTATION

Submitted to
Michigan State University
in partial fulfillment of the requirements
for the Degree of

DOCTOR OF PHILOSOPHY

Department of Physics and Astronomy

2003

ABSTRACT

Examining the Caloric Curve in Ar+Sc and Kr+Nb systems

By

Richard John Shomin II

Excited state populations and isotope temperatures have been measured as a function of the energy of the outgoing particle for central Kr+Nb and Ar+Sc collisions at E/A=100 MeV. Temperatures are extracted from these measurements that increase significantly with energy of the outgoing particle. These results indicate the presence of important cooling mechanisms that operate on the time scale of the collective expansion of the system. They raise questions about the widespread interpretation of multi-fragmentation data in terms of equilibrium statistical models and indicate the necessity of using models that take such cooling mechanisms directly into account.

In memory of my father

Richard John Shomin I

June 20, 1933 - February 7, 2003

–

and to my wife Pearl and my family

This dissertation was typeset in LaTeX 2_ε

and printed on 25%/20# White Rag Paper - cotton content

-

-

-

Zero'th Law or Axiom of Thermodynamics

Associated with any simple system there is a function θ of the variables defining the state such that θ must have the same value for all substances in thermal equilibrium with one another. As a result some values of the physical parameters of each substance cannot be arbitrary. θ is known as the emperical temperature and is not unique since any arbitrary single-valued function $\phi(\theta)$ will serve equally as an emperical temperature. Once a particular function ϕ is chosen for any one substance the emperical temperature is determined for all substances.

slight change of ref [126]

CONTENTS

LIST OF TABLES

LIST OF FIGURES

Chapter 1

Introduction

1.0.1 Background and Motivation

In general, little can be experimentally learned about nuclei without subjecting them to collisions. Gentle grazing collisions between nuclei can succeed in exciting them to their low lying quantum states. More central collisions at low energies can succeed in merging them together to form excited compound nuclei. Like less excited nuclei formed in grazing collisions or nuclei in their ground states, these compound nuclei are droplets of a "Fermi liquid" formed of nucleons, i.e. neutrons and protons[8].

This dissertation is primarily concerned with what happens to these hot Fermi liquid drops when one increases the incident energy. Experiments show that in central collisions of equal mass nuclei at incident energies of E/A=35 MeV or more, nuclear systems undergo a multifragment disintegration. This means that the final state of such collisions consists of nucleons, light clusters and intermediate mass fragments with $3 \leq Z \leq 30$. Models, which assume that statistical equilibrium is achieved during the collision, predict such final multi-fragment final states are the consequence of the nuclear system entering a mixed phase consisting of Fermi liquid drops i.e. fragments, and a gas of nucleons and light clusters [14, 11, 12, 13, 95, 37].

The nucleon-nucleon interaction is attractive at small distances but repulsive at even smaller distances, a characteristic that it shares with the van der Waals interaction. Like macrocopic fluids where the van der Waals equation of state applies, nuclear matter undergoes a first liquid-gas phase transition from a Fermi liquid [8] into a nucleonic gas. The phase diagram is expected to display critical point predicted to occur at about a temperatures of the order of 10-15 MeV [26, 25]. The experimentally observed multifragmentation phenomena, discussed above, are assumed to be a consequence of this underlying bulk phase transition.

One key issue concerns how nuclear systems formed in collisions evolve to multifragmentation. A commonly proposed scenario for this evolution was described in an early paper by Lopez and Siemens [67]. In this scenario, a hot and compressed composite system is formed after the collision of two nuclei. After initial compression, the system expands nearly isentropically (i.e. at nearly constant entropy) until the compressibility of nuclear matter becomes negative. At this point the system is mechanically unstable, density fluctuations grow exponentially with time, the system breaks up and fragmentation occurs. This scenario is supported by more modern transport theory calculations. [85, 23]

The central assumption for many experimental and theoretical studies is that this multi-fragmentation final state is produced at thermal equilibrium [78, 31, 22, 29, 30] The primary support for this comes from the comparison of experimental fragment multiplicities and charge distributions to equilibrium fragmentation model predictions [29, 30]. Even these predictions, however, have difficulty reproducing the data by assuming complete fusion of projectile and target, followed by multi-fragment decay [125, 5, 7]. Instead, one must assume that a significant fraction of the nucleons and the energy is carried away by pre-equilibrium emission prior to multi-fragmentation [125, 98, 6].

Given a scenario of initial contact of projectile and target, followed by preequilibrium emission, expansion and equilibration, analysis have been performed within the equilibrium framework. Such analysis, include the extraction of "critical exponents" from analyses of fragment charge distributions [31], signals of negative heat capacity [22, 28] and extraction of the nuclear caloric curve T(E*) [91, 80, 104, 81]. Fig. 1.1 shows temperatures extracted from Au+Au collisions at E/A=600 MeV by the Aladin group [91]. The horizontal axis is an experimental measure of the thermal excitation energy derived by assuming experimental multiplicities and energy spectra are thermal over a limited angular and rapidity domain and making some corrections for unobserved particles. The vertical axis are temperatures of multifragmentating system obtained by using an isotopic thermometer first proposed by Albergo [3].

$$T_{ISO} = \frac{\Delta B}{\ln(a\Delta Y)} \tag{1.1}$$

where

$$\Delta Y = \frac{Y(A_1, Z_1)/Y(A_1+1, Z_1)}{Y(A_2, Z_2)/Y(A_2+1, Z_2)}, \tag{1.2}$$

$$\Delta B = B(A_1, Z_1) - B(A_1+1, Z_1) - B(A_2, Z_2) + B(A_2+1, Z_2) \tag{1.3}$$

and

$$a = \frac{(2J_{Z2,A2}+1)\,(2J_{Z1,A1+1}+1)}{(2J_{Z1,A1}+1)\,(2J_{Z2,A2+1}+1)} \left[\frac{A_2\,(A_1+1)}{A_1\,(A_2+1)}\right]^{3/2}. \tag{1.4}$$

Here $Y(A, Z)$ is the yield of a given fragment with mass A and charge Z; $B(A, Z)$ is the binding energy of this fragment; and $J_{Z,A}$ is the ground state spin of a nucleus with charge Z and mass A. In the data shown in Fig. 1.1, Z_1, Z_2, A_1 and $A_2 = 2, 3, 3$ and 6, respectively, i.e. the relevant isotopes are $^{3,4}He$ and $^{6,7}Li$ and this thermometer is sometimes called the "HeLi" thermometer. The sensitivity to temperature of the HeLi thermometer is derived from the large difference between the binding energies

of the two helium isotope, which minimizes the influence of the secondary decay of heavier nuclei, also emitted during the collision, which decay by emitting the detected Helium and Lithium isotopes, enhancing their yields.

Three regions were identified in Fig. 1.1 by the authors of ref. [91]. There is a region at $\langle E_0\rangle/\langle A_0\rangle < 3$ MeV, where the isotopic temperature increases rapidly. This trend is reproduced by the curve $T_{HeLi} = \sqrt{10\langle E_0\rangle/\langle A_0\rangle}$; the dependence on $\langle E_0\rangle/\langle A_0\rangle$ is consistent with the Fermi gas level density expression for the temperature of an excited nucleus of excitation energy $\langle E_0\rangle$ and mass (nucleon number) $\langle A_0\rangle$. At higher excitation energies, there is a plateau region of nearly constant temperature reminiscent of that for a system undergoing a first order phase transition at constant pressure. At even higher excitation energy, the temperature increases linearly as might be expected for an ideal gas. However, it should be noted that the trends of the data demarcating these regions are not as clear as the lines suggest.

Eq.1.1 can be derived from the simple Grand Canonical Ensemble expression for the primary fragment yield for ith fragment in its kth state before secondary decay:

$$Y_{i,k}(N,Z,T) = V\frac{A_i^{3/2}}{\lambda_T^3}(2J_{i,k}+1)\exp\frac{N\mu_n + Z\mu_p + B_{i,k}(N,Z)}{T_i}\,, \qquad (1.5)$$

where μ_p and μ_n are the proton and neutron chemical potentials, B_{ik} and J_{ik} are the binding energy and spin of the fragment in the k^{th} state, and V is the free (unoccupied) volume of the system. The insertion of the ground state yields predicted by Eq. 1.5 into Eq. 1.1 results in the cancellation of the chemical potential terms; the spin and mass number terms contribute to the factor a in Eq. 1.4. The derivation of Eq. 1.1 from the Grand Canonical Ensemble is the most transparent way to obtain these results, but the dependence on temperature predicted by Eq. 1.4 is also observed in microcanonical ensemble calculations [11, 12, 13, 14, 104] and models where the fragments are emitted from the surface of a cooling and expanding thermal source [61]. In all of these cases, however, calculations of the yields of secondary fragments

after sequential decay require some accounting for feeding from the particle decay of highly excited heavier nuclei which decay to the measured fragments [14, 104, 140].

Some questions were immediately raised about the interpretation suggested by these curves. These questions become obvious when one considers the projectile fragmentation mechanism that produces the fragments and the helium and lithium isotopes used to construct the temperatures in Fig. 1.1. At 600 MeV, experimental studies show that one is in the domain of limiting fragmentation [98]. The different values for $\langle E_0 \rangle / \langle A_0 \rangle$ correspond to different impact parameters where the impact parameter and the projectile remnant, from which multi-fragmentation is occurring, decreases monotonically with $\langle E_0 \rangle / \langle A_0 \rangle$. Taking this dependence into account, this trend of rising T_{HeLi} at $\langle E_0 \rangle / \langle A_0 \rangle \geq 10 MeV$ was alternatively interpreted as indicative of a system size dependence of the caloric curve [80]. This proposed system size dependence reflects ideas stemming from calculations of the maximum or limiting temperatures of heavy reaction residues produced in heavy ion collisions , which predicts more highly charged residues produced at larger impact parameters to be more unstable with respect to expansion leading to lower values of the limiting temperature [64]. To disentangle these differing interpretations, it is useful to hold the system size constant while varying the excitation energy.

After this dissertation was initiated, the Aladin group attempted to do this by measuring the caloric curve for central Au+Au collisions as a function of the incident energy[100]. Fig. 1.2 shows measured values for the HeLi thermometer (solid squares) as well as temperatures extracted from ratios of the populations of excited states of ^4He, ^5Li, and ^8Be fragments. According to the grand canonical expression of Eq. 1.4, the ratio of the yields for two states of the same emitted fragment is given by

$$\frac{Y_{i,1}(N,Z,T)}{Y_{i,2}(N,Z,T)} = \frac{2J_{i,1}+1}{2J_{i,2}+1} \cdot e^{-(E_1^* - E_2^*)/T,} \tag{1.6}$$

which can be inverted to obtain the temperature T. Clearly, temperatures from the

HeLi thermometer increase more rapidly than those from the three excited state thermometers. This led to speculations that the excited state thermometers were somehow incorrect because they did not follow the energy dependence of the HeLi thermometer [100].

Since this measurement, many other caloric curve measurements have been undertaken. Some authors have found significant discrepancies between different temperatures obtained by different isotopic thermometers [113]. In principle, all thermometric measurements of a system at equilibrium should yield the same temperature. Some of these differences were reconciled by taking the influence of secondary decay of heavier isotopes into account [50, 140, 113] and by proposing a system size dependence of the caloric curve as discussed above [80] . In fact, temperatures extracted from excited state and isotopic thermometers, measured for central Au+Au collisions at E/A=35 MeV and corrected for secondary decay by Huang et al. [50] , are in total agreement with each other and yield "freeze-out" temperature, before secondary decay, of approximately 4.5 MeV.

The present dissertation was undertaken to further explore the dependence of the various thermometric measurements on the size of the system. Isotopic and excited state thermometer measurements were made for central Kr+Nb and Ar+Sc collisions as a function of incident energy. When combined with the Au+Au measurements of refs. [100, 50] this provides three systems in which "caloric curve" measurements have been obtained at fixed system size.

A second goal is to determine the extent to which global equilibrium can be applied to multi-fragmentation processes. Considering the wide-spread application of equilibrium concepts, it is somewhat surprising that the validity of this underlying assumption is not more rigorously tested. At low energies, where comparatively long-lived metastable excited compound nuclei are formed in central collisions, it is

well known that the evaporative emission from the surfaces of such nuclei is well described by a non-equilibrium rate equation. At much higher energies, E/A=200 MeV, there is not enough time in central collisions for equilibration to occur. Indeed, if equilibrium is a valid approximation to multi-fragmentation reactions, it would be the unique instance where equilibrium applies. Thus, the extent to which global or local equilibrium is a valid approximation is of primary importance.

One way to probe the validity of global equilibrium is search directly for evidence of radiative (evaporative) cooling. Such tests have been performed at lower energies [137] where isotopic temperatures, extracted from very energetic particles, were compared to those extracted from particles emitted with energies near the Coulomb barrier. Statistical surface emission models [35, 139] generally predict that the most energetic particles originate from the earliest times when the system is at the highest temperature. Thus, clear indications for the importance of non-equilibrium cooling mechanisms can be obtained by comparing temperatures for more energetic and less energetic particles. In addition, tests of the validity of the local equilibrium assumed in statistical surface emission models can be performed by examining whether the relative yields of energetic particles are consistent with a thermal picture. Such tests of global equilibrium and local equilibrium are performed in this dissertation.

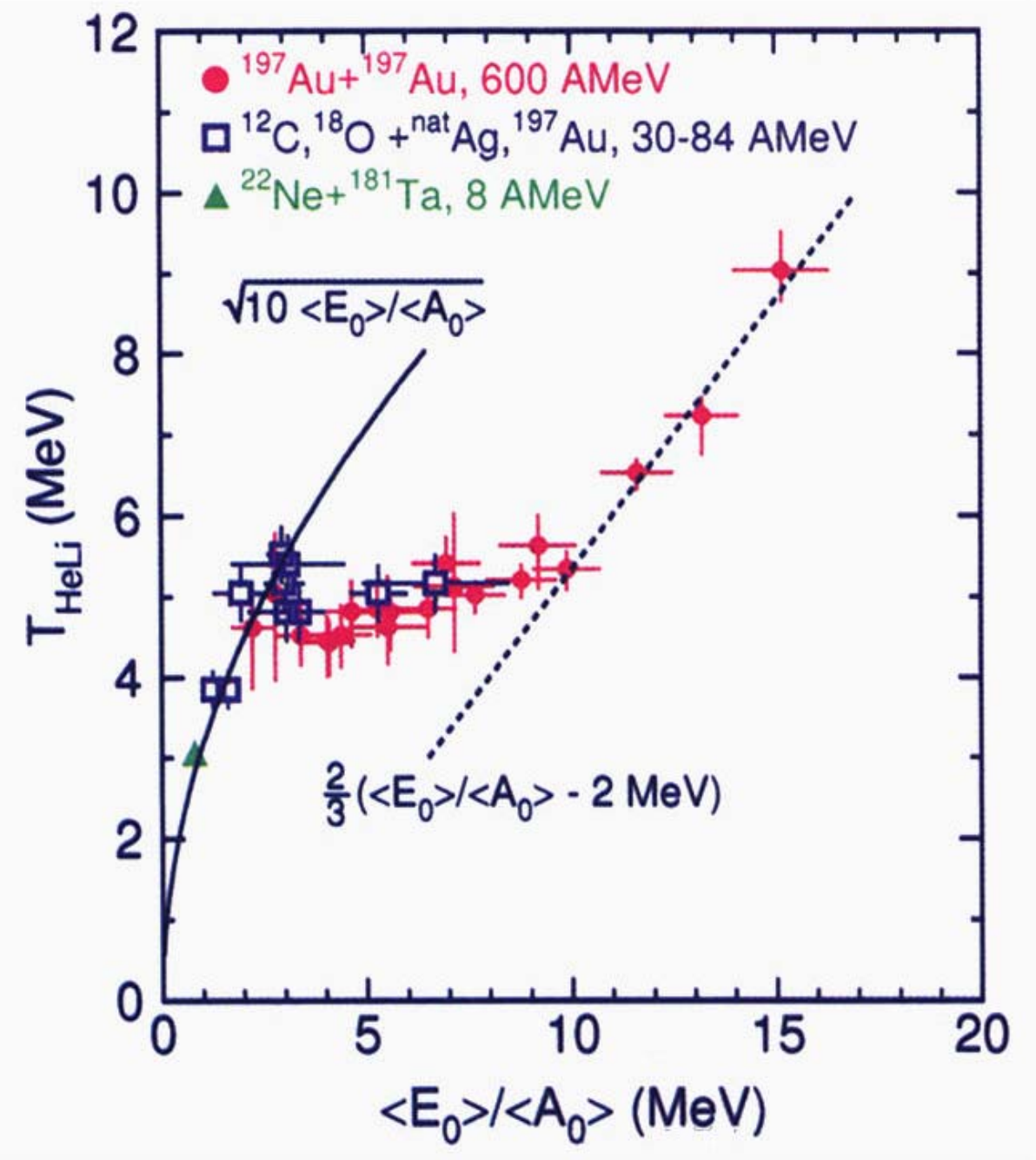

Figure 1.1: Nuclear caloric curve of Pochodzalla et al 1995 [91].

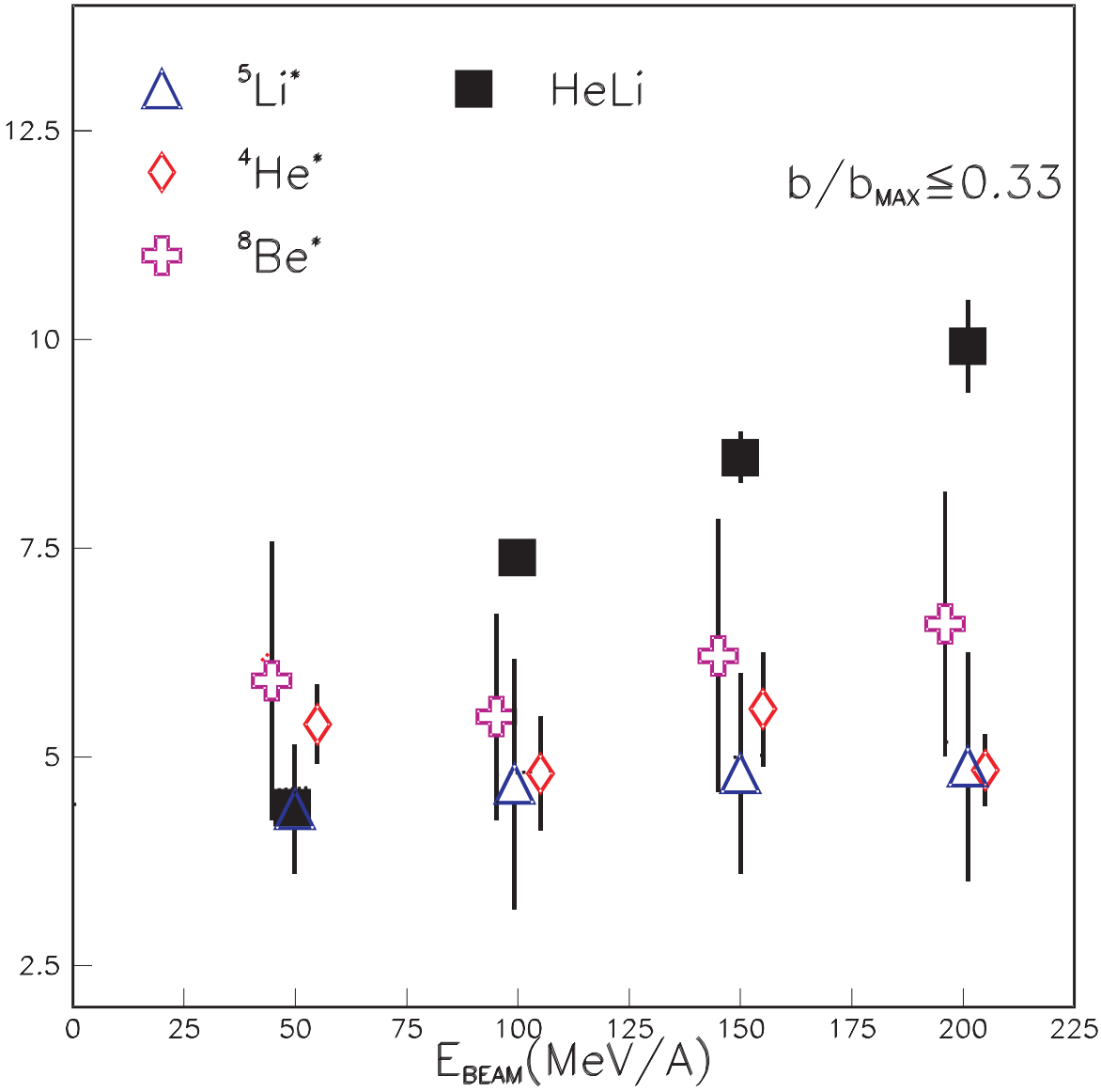

Figure 1.2: Temperature extractions of Serfling et. al. [100]. The system was $^{197}Au + ^{197}Au$ for beam energies from E/A=50 to 200 MeV.

1.0.2 Thesis Organization

Chapter two describes the setup for the experiment, which involved both the 4π array and the Catania hodoscope. Chapter three describes the calibration of the data and its reduction to physical quantities such as the type, energy and angle of each emitted particle. Chapter four describes single particle observables such as the single particle spectra, multiplicities and quantities, such as the isotopic temperatures, that can be derived from single particle data that have been gated on central collisions. Some simple comparisons to statistical models are performed here that indicate a failure of global equilibrium but offer support for local equilibrium concepts. Chapter five describes the two particle coincidence data and their reduction to obtain excited state populations. Here, additional information about the importance of non-equibrium cooling phenomena are obtained. Chapter six summarizes the findings of this thesis.

Chapter 2

The Experiment

This thesis experiment involved two major devices: (1) the Catania 96 element hodoscope and (2) the NSCL 4π detector. The former is a moderate resolution array that was used to measure isotopic yields for Z$\leq$4. The latter covered much of the solid angle not reserved for the Catania array and was used to select the range of impact parameters measured in the collision. In addition, four silicon (IMF) telescopes were employed to extend the measurements of isotopic yields to heavier Intermediate Mass Fragments (IMF's) with Z=5-8. In the following, the experimental run plan, the mechanical layout and electronic readout of the array are described.

2.1 Mechanical Layout

Figure 2.1 shows a photograph of the experimental setup. In white, one can see various elements of the NSCL 4π detector. At the center, there is the highly segmented forward array of the NSCL 4π detector, a cluster of 45 phoswich detectors centered about the beam axis downstream from the target. The larger white detectors are various hexagonal and pentagonal detector modules of the 4π detector that cover larger scattering angles. During the experiment, two hexagonal modules were removed

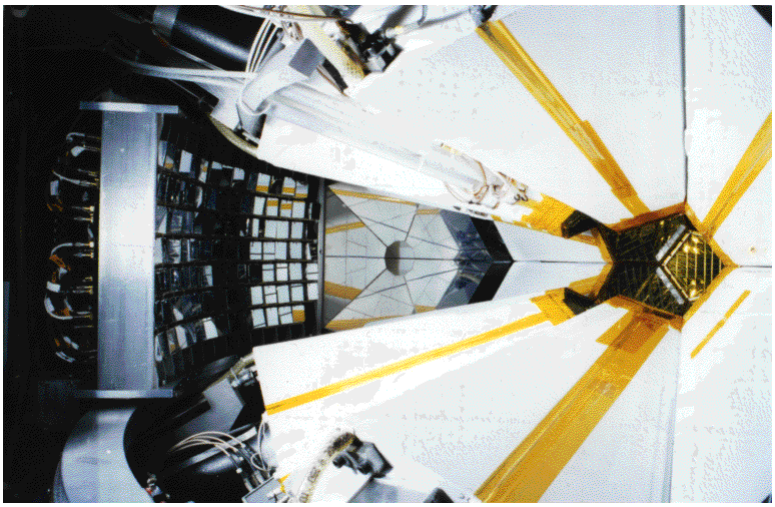

Figure 2.1: Experimental setup. The beam enters from the right through the hole in the center of the photo of the forward array detector. The Catania array is at the left of the photo. *Images in this dissertation are presented in color.*

to allow the Catania hodoscope to view the target.

On the left side of the Figure 2.1, there is the silver colored Catania hodoscope in its aluminum frame. The view of the hodoscope is from the side; however, one can see the front faces of the silicon detectors for many of the 96 telescopes of the Catania hodoscope. The hodoscope was mounted on a rail which allowed the angle of the central detector of the hodoscope to vary over the angular range $40.3^o < \theta < 67.0^o$. This angle was varied throughout the experiment to optimize the coverage by the hodoscope for particles emitted at 90 degrees in the center of mass.

Figure 2.2 shows a schematic drawing of the layout of the experiment. It is an overhead view that emphasizes the relative placement of the Catania hodoscope and IMF telescopes. The IMF telescopes were also placed at angles where modules of the NSCL 4π detector were removed, but were positioned so as to avoid blocking the passage of particles from the target to the Catania hodoscope. Rough locations of the back surfaces of the NSCL 4π detector modules are shown in outline. Figure 2.3 shows a more detailed three-dimensional view of the 4π detector . The 4π modules are inserted into this hexagonal and pentagonal chamber and occupy most of the

inner volume as one can see in Fig 2.1

2.2 The NSCL 4π detector

The experiment used the NSCL 4π array as a central collision filter. Impact parameters were selected by the multiplicity of identified charged particles. When complete the 4π array detected particles from angles from the beam axis of 7^o-157^o using 215 plastic $\triangle$E-E phoswich detectors. This array uses a soccer ball (truncated icosahedron) geometry of 32 faces (12 pentagons, 20 hexagons). During the experiment two hexagonal 4π modules were removed to install the higher resolution Catania 96 detector hodoscope. The pentagonal sector at zero degrees was covered by 45 phoswich detector elements of the High-rate array plus a 16 element Maryland Forward Array The relative placement of these arrays is schematically shown in figures 2.4 and 2.5. The Maryland Forward array was not used in this experiment and removed.

The hexagonal modules of the NSCL 4π array covered a solid angle of 65.96 msr. Each hexagonal module was subdivided into identical 6 triangular plastic phoswich detectors. The pentagonal modules of the 4π detector covered a solid angle of 49.92 msr. Each pentagonal module was subdivided into 5 identical triangular plastic phoswich detectors. Table 2.1, gives the polar and azimuthal angles of these hexagonal and pentagonal modules in a rest frame aligned with the beam direction or polar axis and the x axis with the horizontal plane (beam right). The experiment primarily used the phoswich detectors of the 4π array . Each phoswich detector consisted of a thin fast plastic followed by a thick slow plastic, which was coupled to a phototube. In the electronics described below the light from the fast and slow scintillator are digitized. Using the dependence of the energy loss of the fast plastic for the charge and mass of the ion it is possible to determine the particle and the isotope as well if the elements are hydrogen or helium. The various particle types will make different contours on a

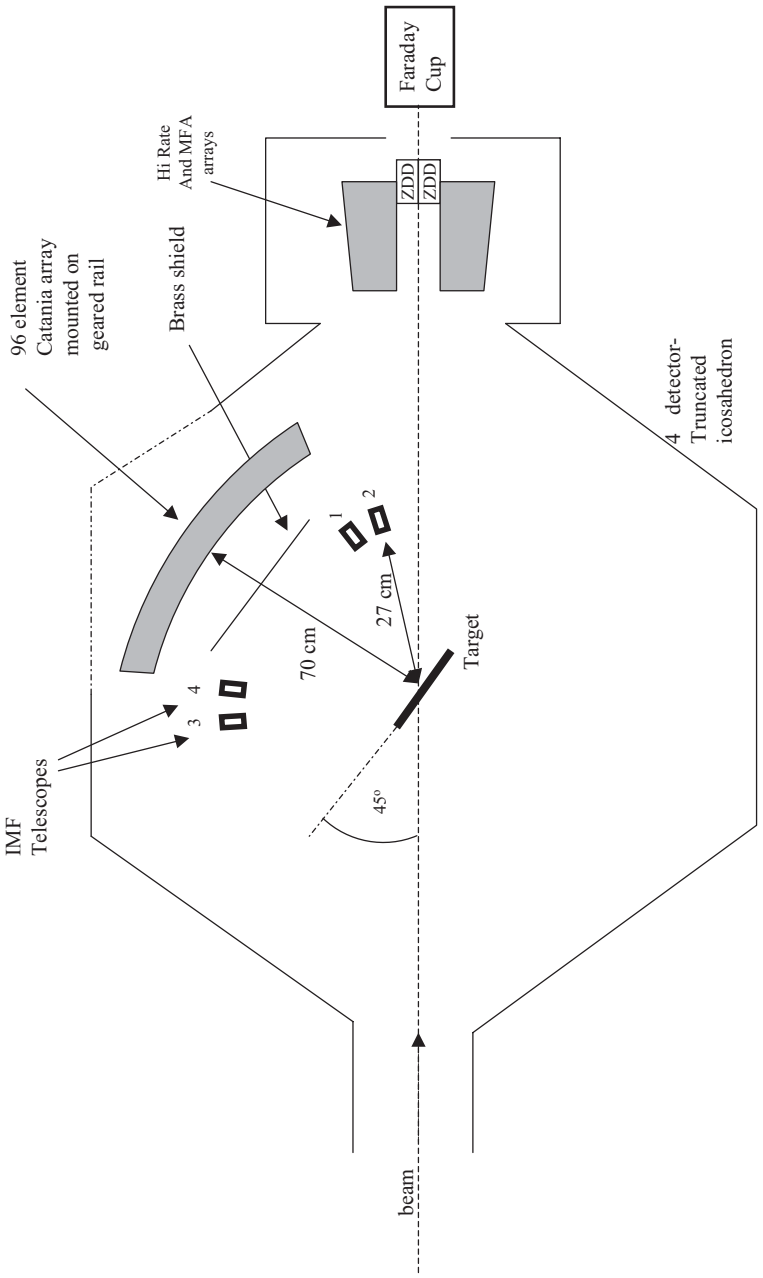

Figure 2.2: Experimental geometry. Detail drawings of the Hi Rate and MFA Arrays are given in the following figures.

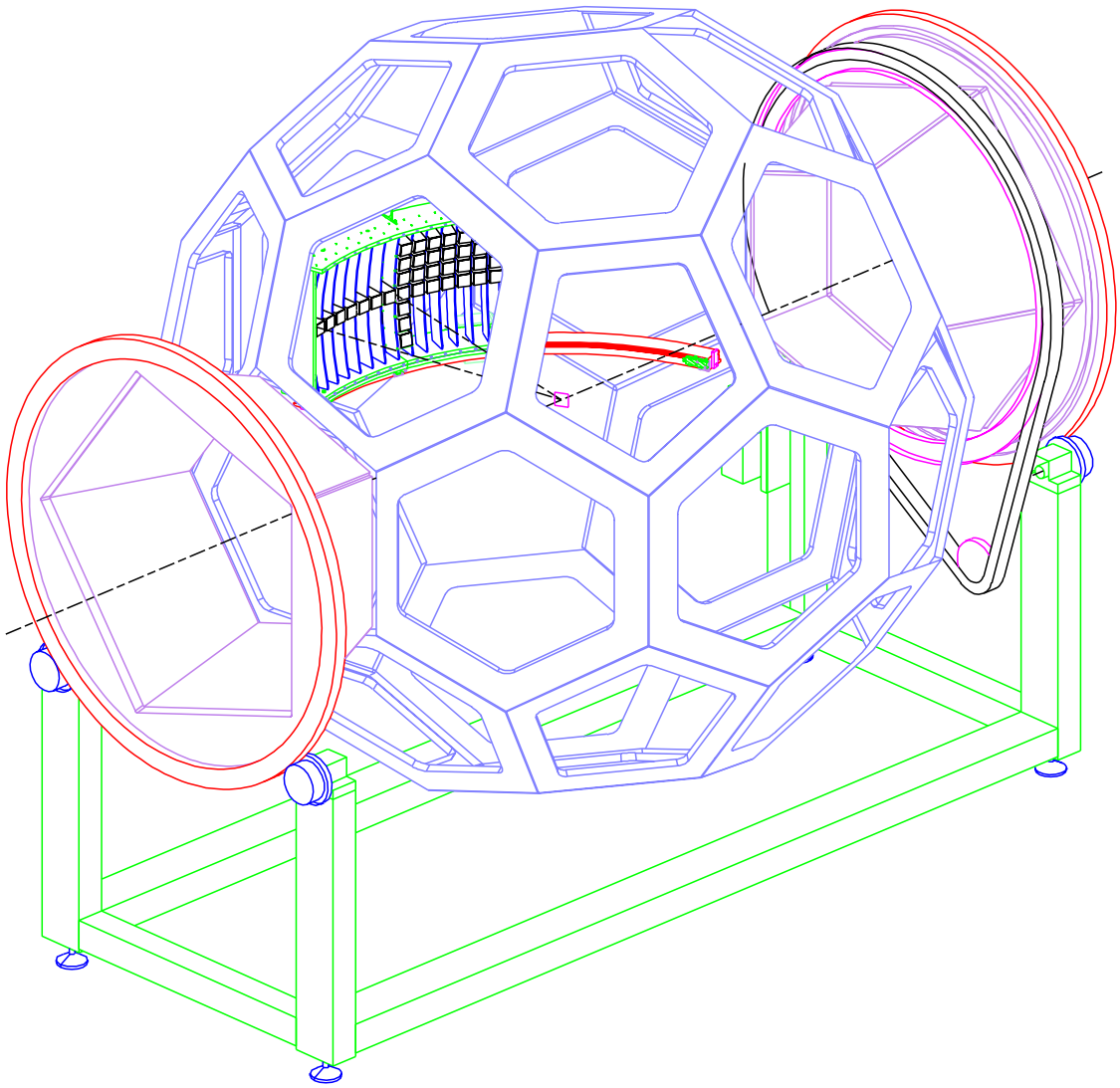

Figure 2.3: 4π frame showing position of hodoscope. Drawing by Craig Snow.

plot of the signals from the fast scintillator versus the signal amplitude in the slow scintillator.

The different time constants of the fast and slow plastic of the phoswich in the NSCL 4π detector modules allow one to distinguish the signals from each scintillator. In particular, the energy deposited in the fast plastic results in light emission with 1 ns rise time and a 20 ns fall time from the fast plastic with an intensity that is roughly proportional to the energy deposited in the fast plastic. Conversely, the energy deposited in the slow plastic results in light emission with a 20 ns rise time and a 180 ns fall time with an intensity that is roughly proportional to the energy deposited in the slow plastic. The photomultiplier converts the superposition of these two light pulses into an electronic pulse.

Figure 2.6 shows an electronics diagram for the processing of signals from the NSCL 4π detector. After the phototube, the signal from each phoswich scintillator is split into three signals by an analogue splitter. One of the these signals is sent to the input of a Phillips leading edge discriminator and the other two are delayed by 100 ns and sent into Fast Encoding and Readout Adc's (FERA's). One of these Fera's is gated by a logic signal of 50 ns length so as to integrate the signal from the fast plastic [119]. The output of this FERA is roughly proportional to the energy loss in the fast plastic. The other FERA is gated by a logic signal of 100 ns[119] length, which is delayed by 10-20 ns so as to integrate the signal from the slow plastic [119]. The output of this FERA is roughly proportional to the energy loss in the slow plastic.

Each Phillips discriminator handles 16 of the NSCL 4π phoswich scintillators. It generators a linear output which is proportional to the number of signals it receives that are "hit", i.e. over the common threshold. All of these linear signals from each of the NSCL 4π Phillips discriminators are combined in a passive linear adder which generates a linear output with an amplitude that is proportional to the total number

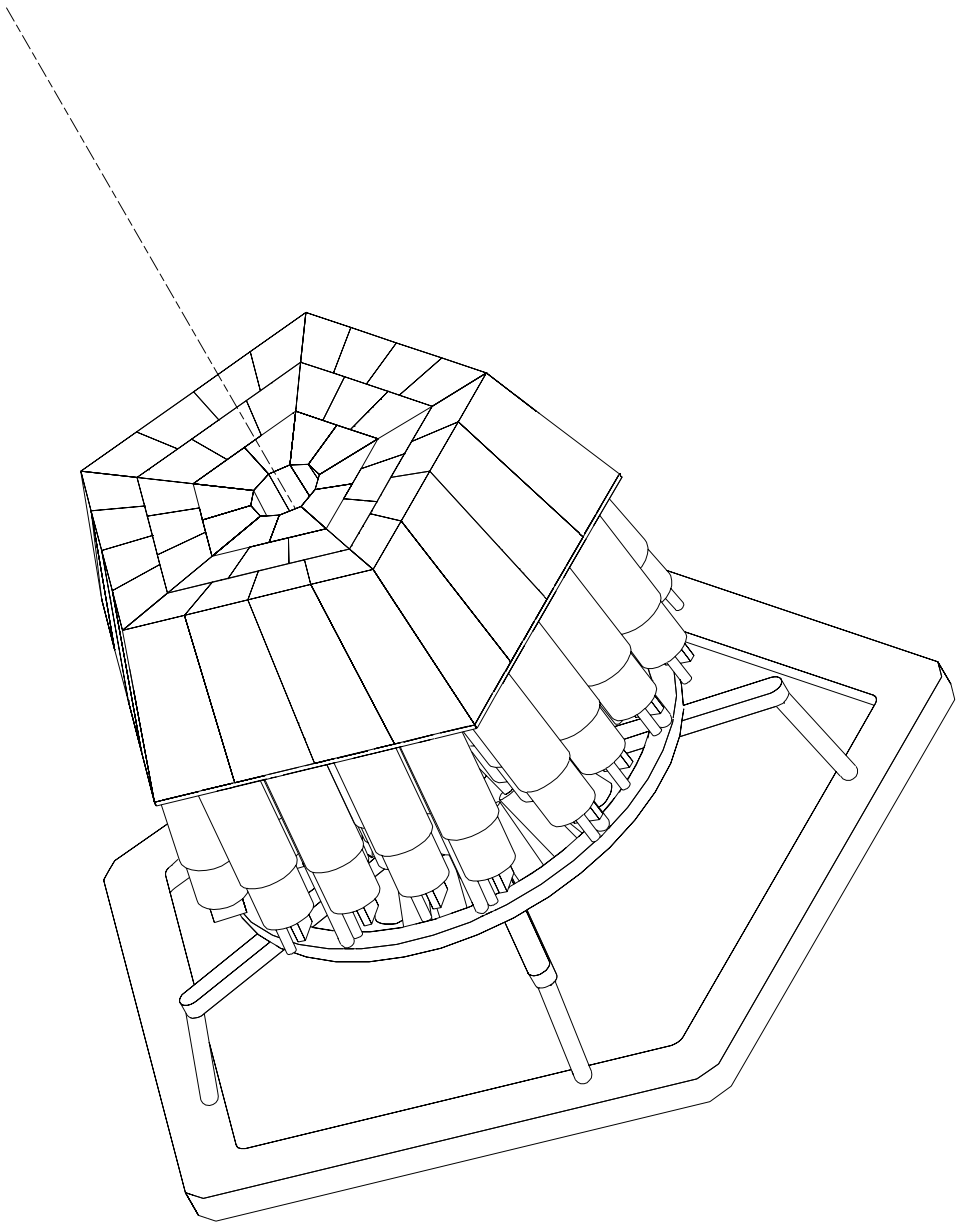

Figure 2.4: 4π High rate array with exit beam shown. The angle of the detectors closest to the beam axis is about 5.4 degrees. Source: NSCL 4π Group.

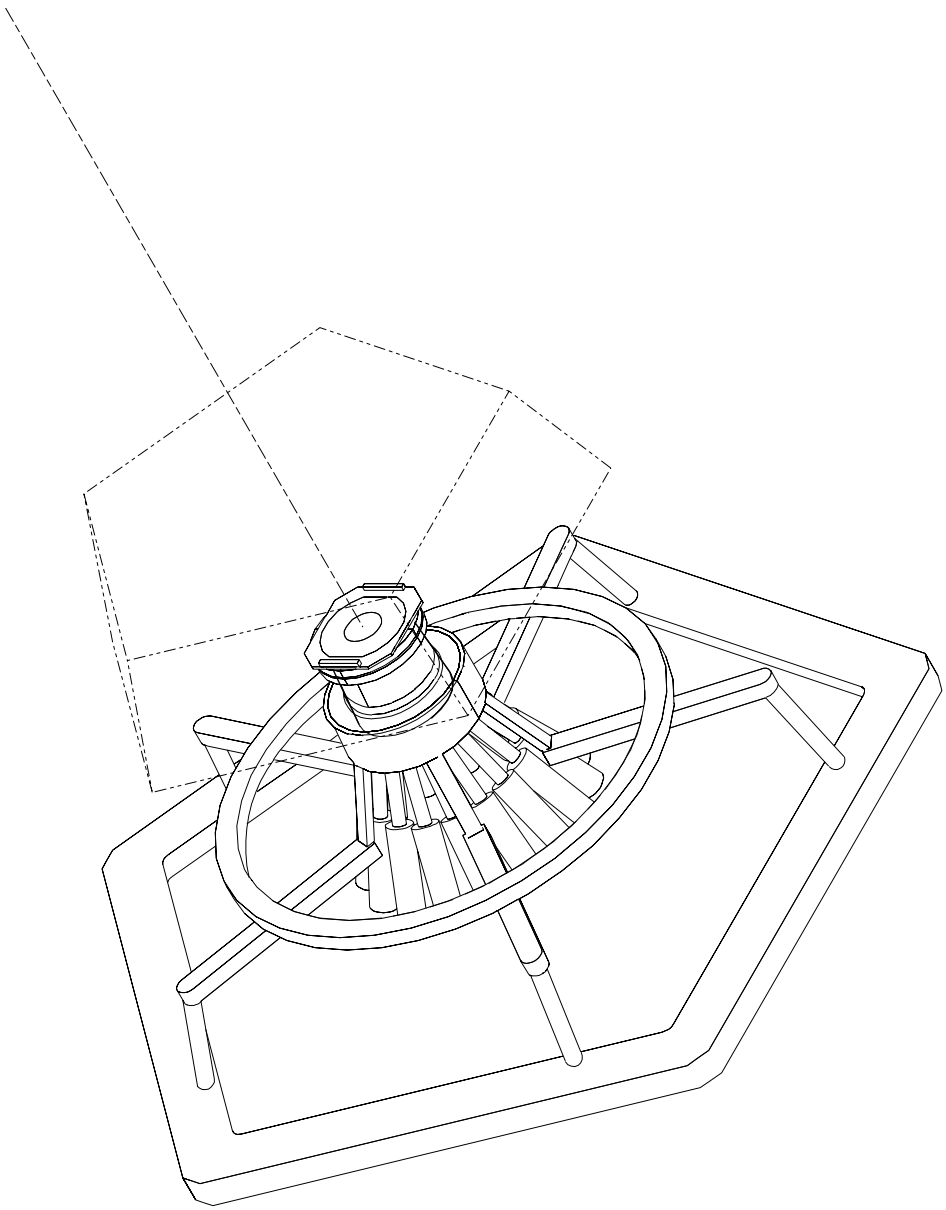

Figure 2.5: 4π Maryland Forward Array attached underneath the High Rate Array. Was not used during the experiment. Source: NSCL 4π Group.

#	A_θ	A_ϕ	B_θ	B_ϕ	C_θ	C_ϕ	D_θ	D_ϕ	E_θ	E_ϕ	F_θ	F_ϕ
1	23.1	342.0	32.3	5.6	46.0	356.3	51.7	342.0	46.0	324.7	32.3	318.4
2	23.1	270.0	32.3	293.6	46.0	287.3	51.7	270.0	46.0	252.7	32.3	246.4
3	23.1	198.0	32.3	221.6	46.0	215.3	51.7	198.0	46.0	180.7	32.3	174.4
4	23.1	126.0	32.3	149.6	46.0	143.3	51.7	126.0	46.0	108.7	32.3	102.4
5	23.1	54.0	32.3	77.6	46.0	71.3	51.7	54.0	46.0	36.7	32.3	30.4
6	54.7	298.0	54.7	314.0	67.3	317.5	74.6	306.0	67.3	294.5	-	-
7	54.7	226.0	54.7	242.0	67.3	245.5	74.6	234.0	67.3	222.5	-	-
8	54.7	154.0	54.7	170.0	67.3	173.5	74.6	162.0	67.3	150.5	-	-
9	54.7	82.0	54.7	98.0	67.3	101.5	74.6	90.0	67.3	78.5	-	-
10	54.7	10.0	54.7	26.0	67.3	29.5	74.6	18.0	67.3	6.5	-	-
11	64.9	342.0	72.4	355.0	86.5	354.5	93.5	342.0	86.5	329.6	72.4	329.0
12	64.9	270.0	72.4	283.0	86.5	282.4	93.5	270.0	86.5	257.6	72.4	257.0
13	64.9	198.0	72.4	211.0	86.5	210.4	93.5	198.0	86.5	185.6	72.4	185.0
14	64.9	126.0	72.4	139.0	86.5	138.4	93.5	126.0	86.5	113.6	72.4	113.0
15	64.9	54.0	72.4	67.0	86.5	66.4	93.5	54.0	86.5	41.6	72.4	41.0
16	86.5	306.0	93.5	318.4	107.6	319.0	115.1	306.0	107.6	293.0	93.5	293.6
17	86.5	234.0	93.5	246.4	107.6	247.0	115.1	234.0	107.6	221.0	93.5	221.6
18	86.5	162.0	93.5	174.4	107.6	175.0	115.1	162.0	107.6	149.0	93.5	149.6
19	86.5	90.0	93.5	102.4	107.6	103.0	115.1	90.0	107.6	77.0	93.5	77.6
20	86.5	18.0	93.5	30.4	107.6	31.0	115.1	18.0	107.6	5.0	93.5	5.6
21	105.4	342.0	112.7	353.5	125.3	350.0	125.3	334.0	112.7	330.5	-	-
22	105.4	270.0	112.7	281.5	125.3	278.0	125.3	262.0	112.7	258.5	-	-
23	105.4	198.0	112.7	209.5	125.3	206.0	125.3	190.0	112.7	186.5	-	-
24	105.4	126.0	112.7	137.5	125.3	134.0	125.3	118.0	112.7	114.5	-	-
25	105.4	54.0	112.7	65.5	125.3	62.0	125.3	46.0	112.7	42.5	-	-
26	128.3	306.0	134.0	323.3	147.7	329.0	156.9	306.0	147.7	282.4	134.0	288.7
27	128.3	234.0	134.0	251.3	147.7	257.6	156.9	234.0	147.7	210.4	134.0	216.7
28	128.3	162.0	134.0	179.3	147.7	185.6	156.9	162.0	147.7	138.4	134.0	144.7
29	128.3	90.0	134.0	107.3	147.7	113.6	156.9	90.0	147.7	66.4	134.0	72.7
30	128.3	18.0	134.0	35.3	147.7	41.6	156.9	18.0	147.7	354.4	134.0	0.7

Table 2.1: Mean polar angles for Ball Phoswiches in degrees. The lettering A,B,... is the azimuthal ordering of each pentagon or hexagon. The first column is the Module(#) number. Source: NSCL 4π Manual

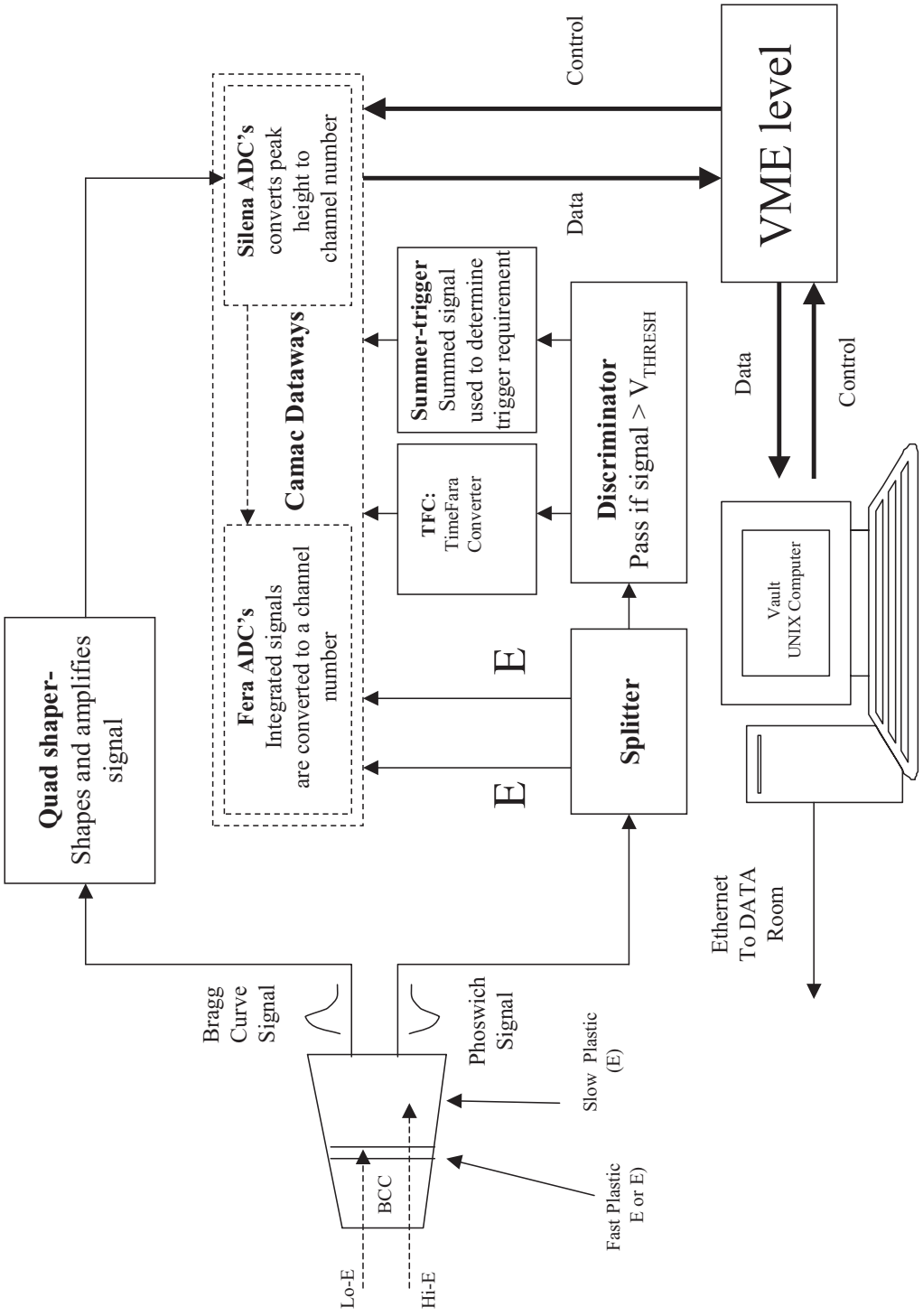

Figure 2.6: 4π Array electronics. reproduced from Dan Magestro's Thesis and NSCL 4π Users manual. In this experiment, the Bragg curve gas counters was evacuated and were not used. In this mode most energetic particles generate phoswich signals, which were processed by the electronics as described in the text .

of NSCL 4π phoswich detectors that are hit anywhere in the NSCL 4π array. This linear output is sent to a discriminator; the threshold of this discriminator selected the minimum desired multiplicity of events and the output of this discriminator is the trigger for the 4π detector. Finally, the Fera ADC's integrated the signals and converted the charge of the signal within the gate signal to a channel number.

The various channel numbers for the detected particles are written to tape by a computer in the vault. The vault computer is controlled via the ethernet from the data room. The vault computer also controls the threshold levels for the various discriminators.

2.3 Catania Hodoscope

The Catania hodoscope consisted of 96 identical telescopes. Figure 2.7 shows a schematic drawing of a telescope. Figure 2.9 shows a 3D view of the Catania hodoscope frame with about three quarters of the detectors missing. Each telescope consists of a 300 μm thick silicon detector ΔE followed by a 6 cm thick CsI(Tl) detector that is read out by a photodiode. The silicon detectors have active areas of 31x31 mm^2 and the CsI(Tl) detectors are tapered and large enough to detect all particles that penetrate the silicons when the hodoscope is placed a distance of 70 cm from the target. The silicon ΔE's are sufficiently planar so as to resolve isotopes up to Z=4. Details of the isotopic resolution are discussed in the next chapter. A shield constructed of 20 mg/cm^2 brass shim stock was used to prevent electrons produced by interactions of the beam with the target from reaching the detectors.

The telescopes of the Catania hodoscope were mounted at a distance of 70 cm from the target in a rectangular array consisting of 14 vertical columns of 7 telescopes. Each telescope subtended a solid angle of 1.83 msr. The angular separation between adjacent telescopes was 0.76 degrees in both vertical and horizontal directions. The

horizontal (polar) angle of the center of the array was varied during the experiment. The actual angles are given in table 2.2 along with the corresponding beams and targets for each specific measurement.

Operationally, the main practical differences between a photodiode readout of light generated by an ion traversing a CsI(Tl) and a direct readout of ionization generated in a silicon detector is that the CsI(Tl) has a slower time constant and the CsI(Tl) signal is roughly 20X smaller per unit energy loss. In practice, very similar electronics can be used and therefore were used for the readout of both silicon and CsI(Tl) detectors. Figure 2.8 shows an electronics diagram which describes the silicon or CsI(Tl) detectors of the Catania Hodoscope or the Silicon detectors of the IMF(SiLi) telescopes. The linear output of the Pre-amps has a signal that rises to a peak quickly in about 100 ns then falls slowly in 40 μs. This signal is split in the shaper and filtered to produce a fast and slow signal. The fast signal has a rise time of about 100 ns and a fall time of about 500 ns . The slow signal rises to a peak in about 2 μs and falls to zero in about 5-8 μs. The fast signal goes to the discriminator and the slow signal goes to a Phillips peak sensing ADC. The output of the discriminator is a standard negative Nim signal. The outputs of both discriminators are OR'd . One output of the OR goes to a stop input of a time to Fera converter(TFC) then to a Fera ADC where a channel number is determined that is proportional to the time of arrival relative to the event trigger, and another output goes to a large OR with signals from all of the telescopes . For each event, there will be an output signal from the OR which has a leading edge defined by the first detector that detects a particle in the event. This output signal is sent to the octal constant fraction(OCF). This OCF is indicated on both the dead-time logic diagram and on the logic diagram for the Catania and IMF telescopes. The output of the OCF is the pre-master signal.

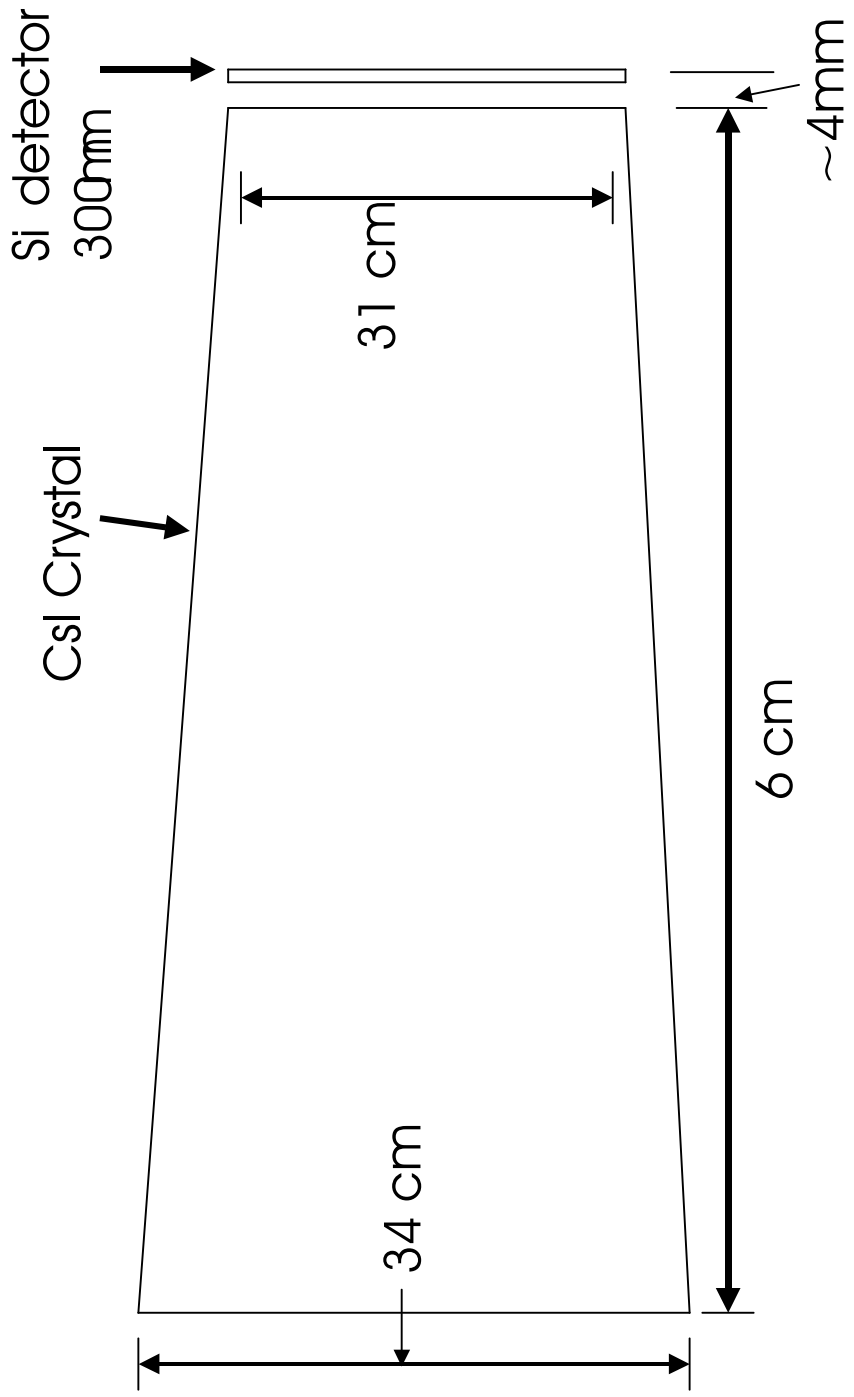

Figure 2.7: Side view of the Catania telescope geometry. The front and rear surfaces are square.

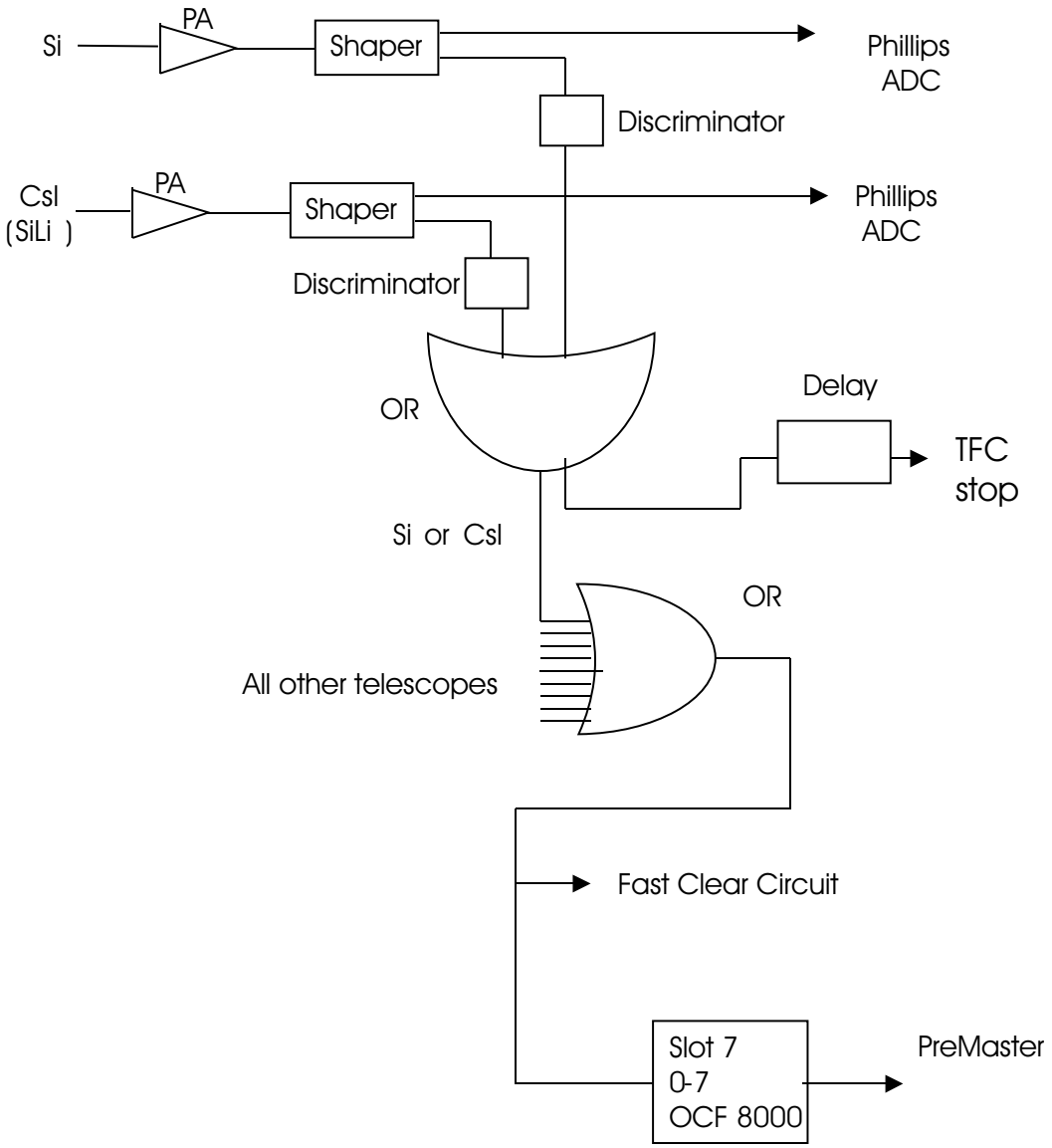

Figure 2.8: Logic diagram. Applicable for both Catania or IMF telescopes.

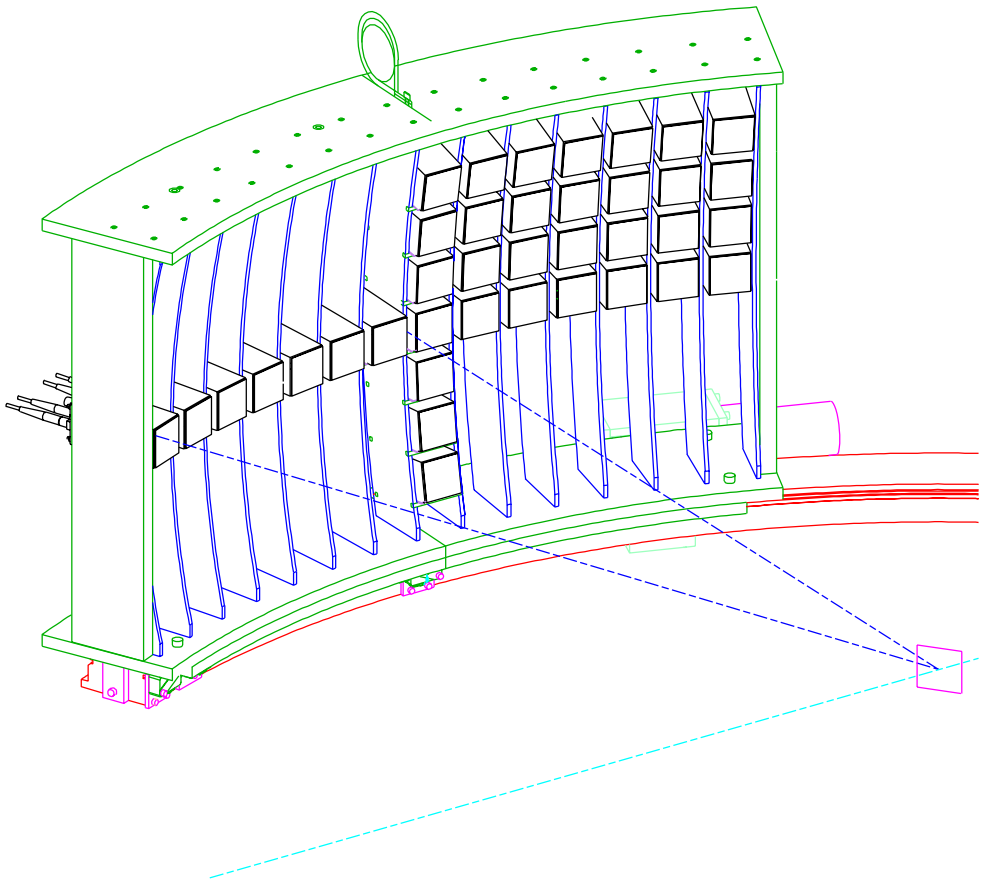

Figure 2.9: Catania Hodoscope frame. Drawing by Craig Snow.

2.4 IMF Telescopes

Four silicon telescopes were used to measure heavier fragments with $4 \leq Z \leq 9$. Each telescope consisted of a 75 μm thick silicon ΔE, and a 5 mm thick Si(Li) E detector. The silicon ΔE's are sufficiently uniform as to resolve isotopes up to Z=10. Details of the isotopic resolution are discussed in the next chapter. These telescopes were placed at a distance of 27 cm from the target and subtended solid angles of 2.21 msr. The polar angles of the telescopes were 27, 36, 75, 84 degrees; Essentially the same electronics was used to process the signals from the IMF telescopes as for the telescopes of the Catania hodoscope. A description of the electronics, is given in the preceding section of this chapter.

2.5 Experimental trigger

The premaster signals on the bottom of Figure 2.8 appears again in the top left corner of Figure 2.10 as inputs to the dead time logic diagram of the experiment . The 4π signal usually arrives first at the OCF because the plastic scintillator signals of the 4π detectors are considerably faster at generating a signal than the signals from the Catania Hodoscope or IMF telescopes. The premaster signal is converted to a master signal if the data acquisition system is not already busy with a previous event. One output of the master signal goes to the input of the 4π Master Logic FanIn/FanOut. Another part goes to the ADC gate circuitry on the upper right part of the diagram that opens the IMF or Catania ADC's to take the data. If the computer is busy, however, the FaraFaucet will generate a busy signal to the dead time OR and this will veto the master signal. On the bottom of the diagram we have the fast clear cicuits. Because the 4π detector is intrinsically much faster than the other detectors we had to start the data acquisition to read the 4π data even before we knew whether

there is data from Catania or IMF telescopes. The purpose of this fast clear circuit logic signals is to clear the 4π ADC's and TDC's if there are no Catania hodoscope or IMF telescope signals. The fast clear circuit also provides a signal to the dead-time OR gate to block new data until the clearing process is complete.

2.6 Experimental measurements

The objective of measuring the caloric curve in central collisions required measurements as a function of incident energy up to the maximum feasible energy of the cyclotron. As the beam intensity generally decreases with incident energy, the target thickness was varied to try to keep the overall counting rate of the experiment more constant. By this means, we kept the experiment counting rate at the maximum value limited by the acquisition system at all but the highest energy.

Table 2.2 lists the beams, targets, trigger conditions and hodoscope angles for the various runs. For the main Ar+Sc and Kr+Nb data taking runs, the plan involved measuring coincidence data with the hodoscope and IMF trigger in place and also data with 4π running by itself (4π singles). These latter measurements provide an unbiased multiplicity distribution that can be used to relate the impact parameter to the charged particle multiplicity. Unfortunately, the 4π singles measurements were not accurately performed at 120 MeV/A. At the other incident energies, these measurements were performed successfully.

Looking at the table one can see that experimental runs were peformed using ^{86}Kr beams at energies of 35, 70, 100, and 120 MeV/A using a variety of target thicknesses. Experimental runs were also performed using ^{36}Ar beams, at energies of 50, 100, and 150 MeV/A on a ^{45}Sc target of 3mg/cm^2 areal density. For both experimental runs the targets were mounted at an angle at 45^o from the beam axis. As the angle of the center of the detector array was situated at about 40^o the detected particles were

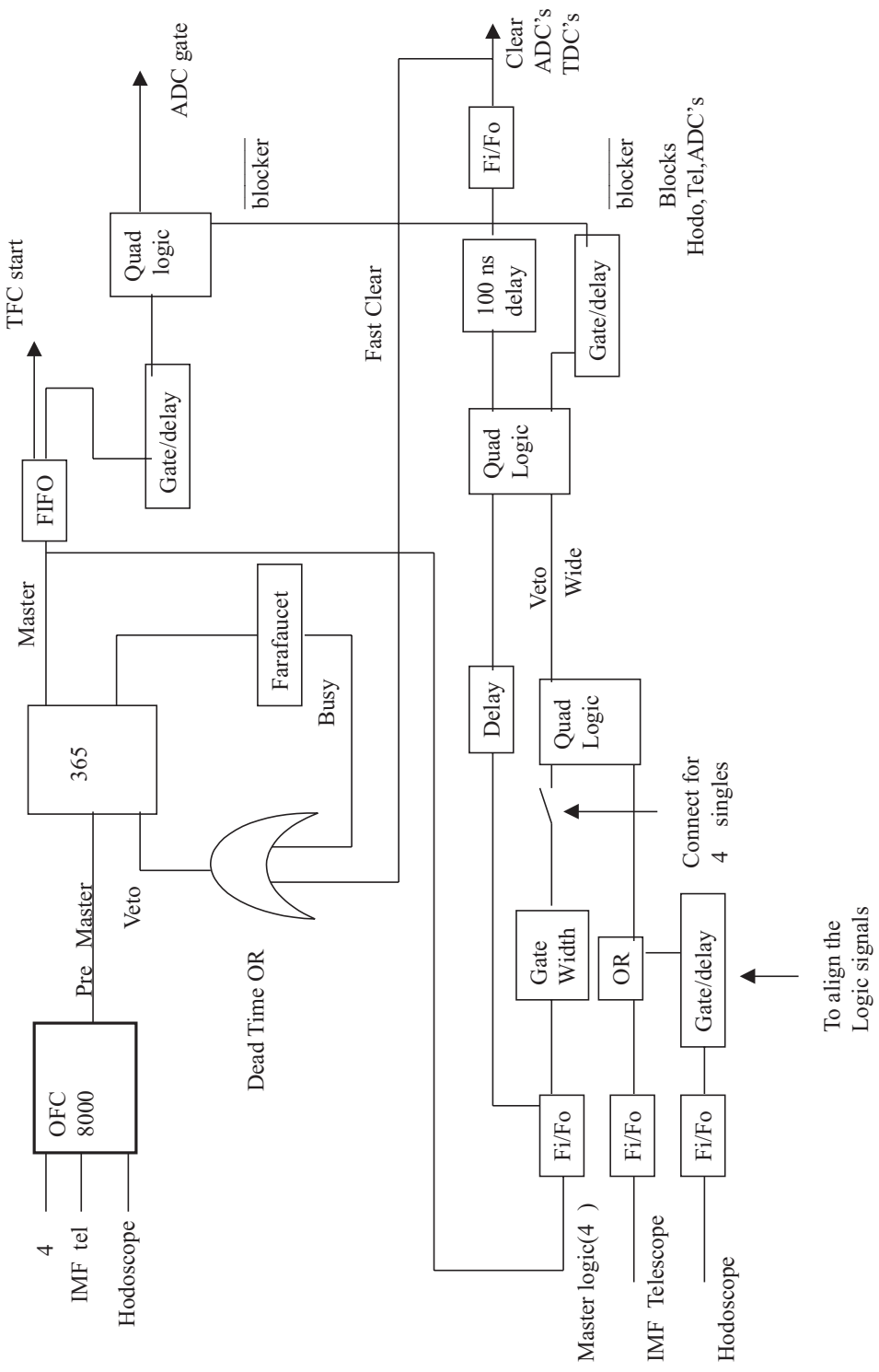

Figure 2.10: Dead time logic.

Beam	E/A (MeV)	Target	Hodoscope angle (degrees)
^{86}Kr	120	Niobium 40mg/cm^2	40.1
^{86}Kr	100	Niobium 20mg/cm^2	42.6
^{86}Kr	70	Niobium 20mg/cm^2	48.6
^{86}Kr	35	Niobium 20mg/cm^2	55.9
^{86}Kr	35	Niobium 6mg/cm^2	55.9
^{36}Ar	150	Scandium 3mg/cm^2	40.6
^{36}Ar	100	Scandium 3mg/cm^2	42.6
^{36}Ar	50	Scandium 3mg/cm^2	29.3
^{86}Kr	35	Plastic(CH_2)	Home(40.6)
^{86}Kr	35	Plastic(CH_2)	44.8
^{86}Kr	35	Plastic(CH_2)	49.8
^{86}Kr	35	Plastic(CH_2)	54.7
^{86}Kr	35	Plastic(CH_2)	59.6
^{86}Kr	35	Plastic(CH_2)	64.6
^{86}Kr	35	Plastic(CH_2)	(Limit Switch(68.3)
^{4}He	22	Plastic(CH_2)	Home(40.6)
^{4}He	21.79	Plastic(CH_2)	50.70
^{4}He	21.79	Plastic(CH_2)	60.64
^{4}He	40	Plastic(CH_2)	Home(40.6)
$\alpha(^{212}Bi)$ (^{228}Th parent)	6.09/4	Si calibration	N/A
$\alpha(^{212}Po)$ (^{228}Th parent)	8.78/4	Si calibration	N/A

Table 2.2: Angles measured from beam axis to array center. The difference between the first detector and the center of the array is 18.6^o

emitted at 90^o distributed about the normal to the center of the target. Table 2.2 shows the beam type, the beam energy, the target type and the angle of detector #1 of the Catania hodoscope for each measurement in the experiment.

In addition to the main experimental Ar+Sc and Kr+Nb runs, there were calibration runs during which hydrogen and helium isotopes of precise energies were measured in inverse kinematics for reactions on a hydrogen (polyethylene) target. Calibrations were also performed with alpha sources. The calibration data from these measurements are discussed in the next chapter.

Chapter 3

Calibration and data processing

In this chapter we explain how the raw data for the Catania hodoscope that exists in the form of data words from the ADC's and TDC's, are converted into energies, charges and masses of specific particles. We also explain how information about the impact parameter for the collisions was extracted from the data for the 4π array. The extractions of temperatures and isoscaling properties from these calibrated data are described in chapters 4 and 5.

3.1 Data reduction plan

Figure 3.1 gives an overview of the plan for converting the raw data, which moves as integer data from the ADC's and TDC's in the data acquisition setup, into the final results. In the first pass through the analysis, the uncalibrated data on tape is sorted and manipulated to give calibrated data on disk. This stage involves reducing the 4π data to obtain the charged particle multiplicity and identifying the particles in the hodoscope and determining their energies. These principal tasks are described in subsequent sections of this chapter.

Below this first pass on the diagram, the analysis splits into two pathways. One

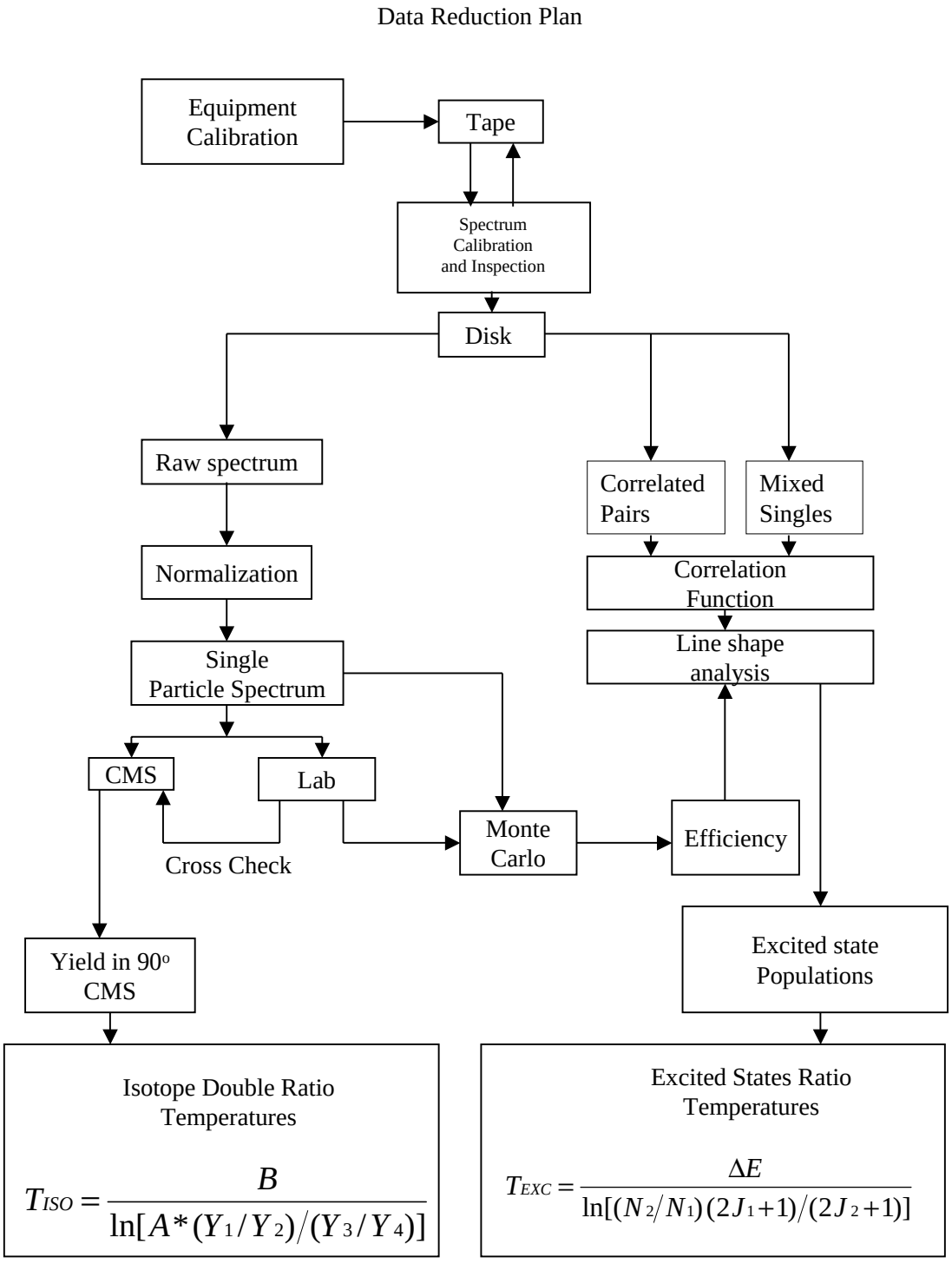

Figure 3.1: Data reduction plan.

involves constructing differential multiplicity spectra, which are needed for the isoscaling and isotopic temperature analyses discussed in the subsequent section. The other pathway is used to construct the coincidence and mixed-singles analyses that are essential for the correlation function and excited state temperature analyses discussed in Chapter 5. Cross-links between these analyses pathways, indicated in the diagram, are important for the construction of correlation functions. These will be discussed further in Chapter 5.

3.2 Impact parameter selection

As a function of impact parameter, many observables for the colliding system change rapidly. To the degree that the change in a specific observable depends strongly and monotonicaly on the impact parameter, the impact parameter can be determined from that observable. Examples of suitable observables that have been so used include the observed total charged particle multiplicity N_c, the midrapidity charge [89], the transverse energy [89] and the total charge of beam velocity fragments [91]. In this dissertation, we deduced the impact parameter for total charged particle multiplicity N_c. At incident velocities that exceed the fermi velocity $v_f = \sqrt{(\frac{2E}{m_N})} \approx 0.3c$. N_c largely reflects emission from a "participant" region formed by the merging of approximately equal numbers of nucleons from projectile and target where these two incident nuclei overlap. Both the size of the participant region and the charged particle multiplicity decrease monotonically with impact parameter b ; the remainder of the nucleons are carried away from the collision in projectile- and target-like residues that emit few charged particles.

Figure 3.2 shows the distributions for the total multiplicity of charged particles detected in the 4π detector for Kr+Nb collisions. These data were taken in minimum bias runs where the ball multiplicity trigger discriminator was set at voltages

corresponding to the acceptance of events with $N_C \geq 1$. Figure 3.3 shows the corresponding distributions for Ar+Sc collisions. Unfortunately, the minimum bias data for Kr+Nb collisions at E/A=120 MeV were not usable and are therefore not shown.

If one assumes the charged particle multiplicity decreases monotonically with impact parameter, one can use these multiplicity distributions to obtain a relationship between N_c and the "reduced" impact parameter $\hat{b} = b/b_{MAX}$, where b_{MAX} is the maximum value of b corresponding to the lowest multiplicities included in the trigger. This relationship is:

$$\hat{b} = \left(\frac{b}{b_{MAX}}\right) = \sqrt{\int_{N_C}^{\infty} P(N_C) dN_C}\,, \tag{3.1}$$

where:

$$P(N_C) = \frac{Events(N_C)}{\int_{N_C=1}^{\infty} Events(N_C) dN_C}\,, \tag{3.2}$$

Figures 3.2, and 3.3 show the relationship between $\hat{b}$ and N_C given by 3.1 for the Kr+Nb and Ar+Sc collisions, respectively. The relationship for Kr+Nb collisions at E/A=120 MeV, where minimum bias data was unavailable, was extrapolated from the Kr+Nb data at E/A=100 MeV by rescaling the P(N_C) of E/A=100 to the E/A=120 MeV P(N_C).

Careful examination of Figures 3.2 and 3.3 reveals that the majority of events occur at large impact parameters characterized by low charged particle multiplicity. In order to acquire data at small impact parameter more efficiently, the bulk of the data were taken with a hardware threshold on the ball multiplicity trigger discriminator set at voltages corresponding to a higher minimum multiplicity $N_{C,min}$. Table 3.1 shows the values for $N_{C,min}$ for the 4π ball multiplicity trigger setting during the main data taking runs. Even higher thresholds corresponding to higher $N_{C,min}$ and consequently smaller $\hat{b}$ were set later in software during the analyses. The main analyses in this

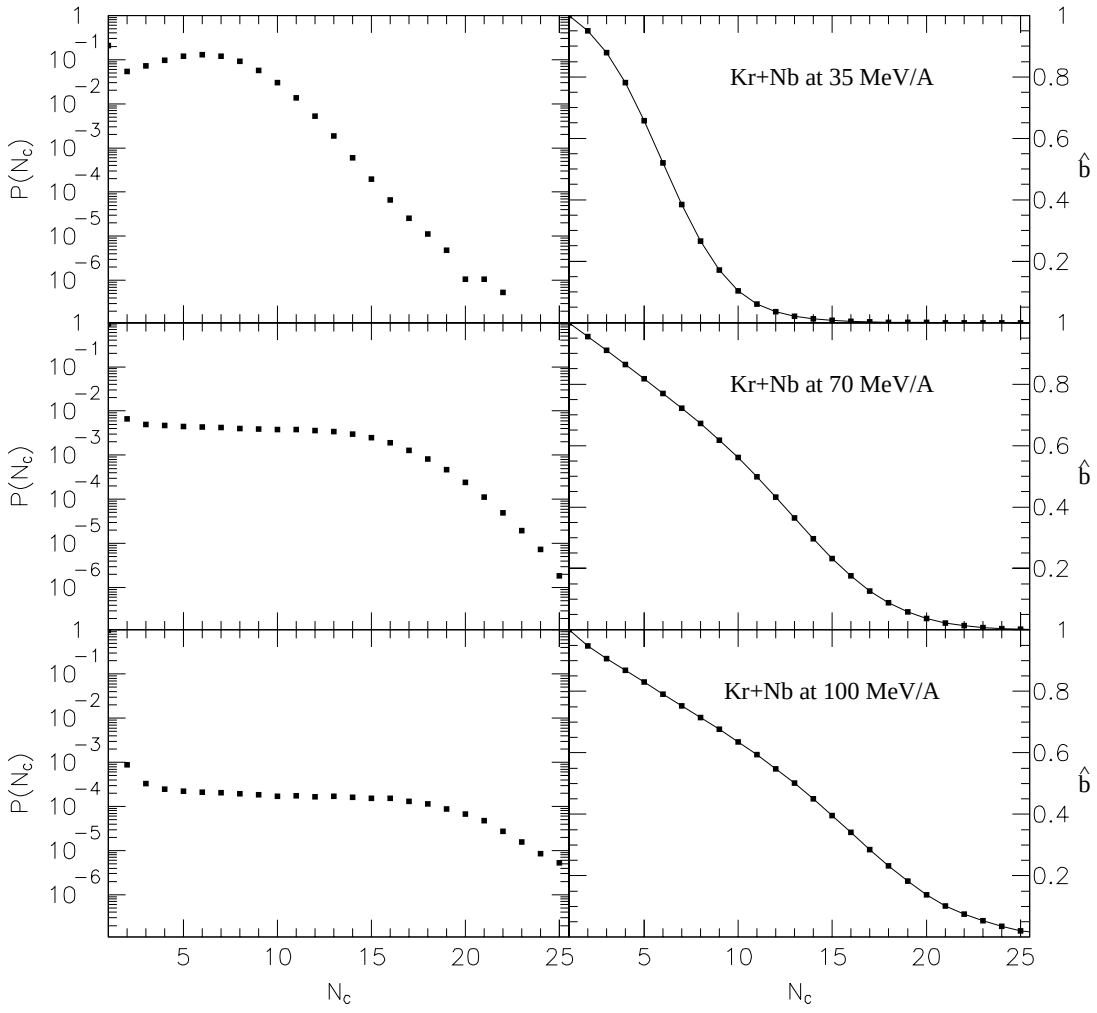

Figure 3.2: $P(N_C)$ (left panels) and Reduced impact parameter (right panels) vs charged particle multiplicity for Kr+Nb at 35,70,100 respectively .

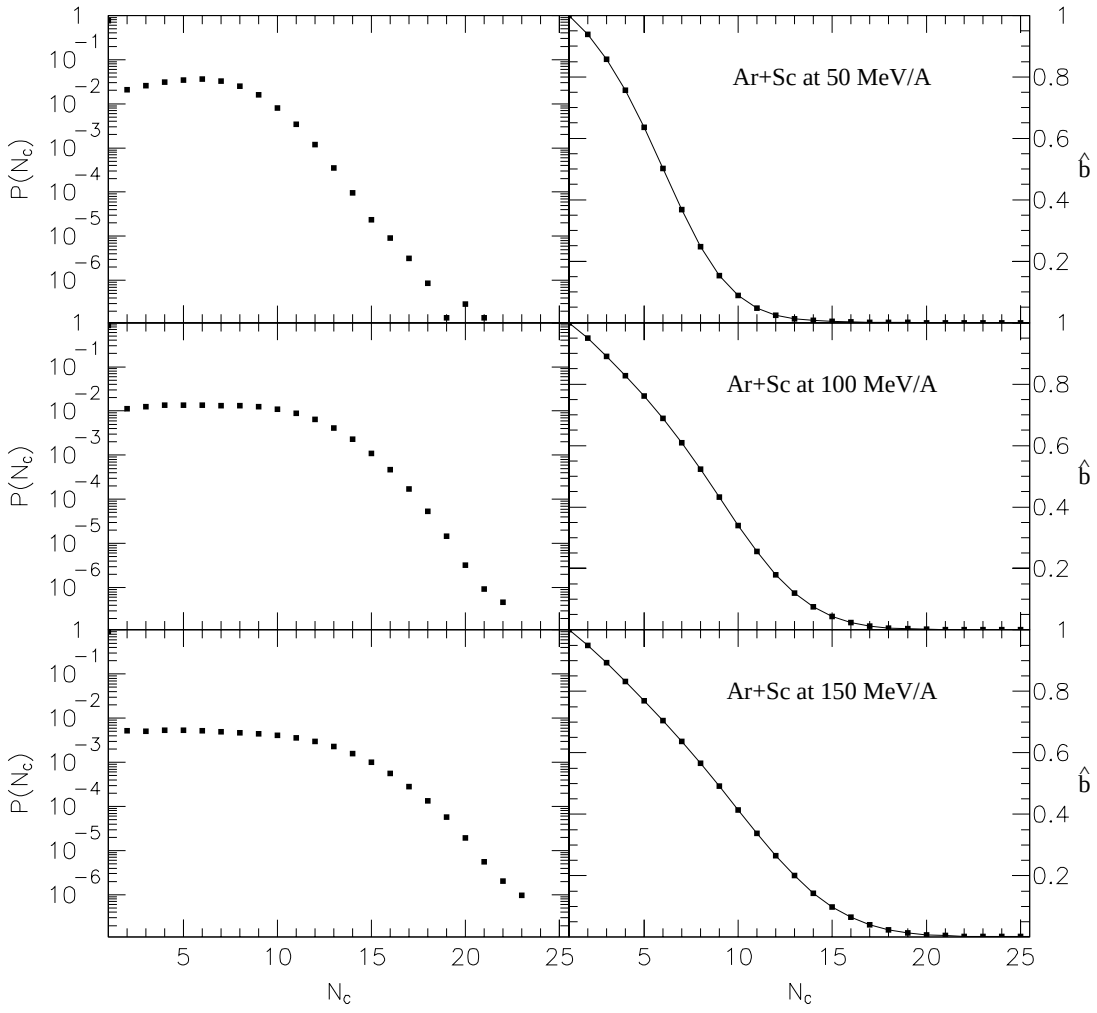

Figure 3.3: $P(N_C)$ (left panels) and Reduced impact parameter (right panels) vs charged particle multiplicity for Ar+Sc at 50,100,150 respectively .

Beam and target	Beam E/A (MeV)	Multiplicity Trigger Thresholds
^{86}Kr on ^{93}Nb	35	2,5
^{86}Kr on ^{93}Nb	70	5
^{86}Kr on ^{93}Nb	100	4
^{86}Kr on ^{93}Nb	120	4
^{36}Ar on ^{45}Sc	50	3
^{36}Ar on ^{45}Sc	100	5
^{36}Ar on ^{45}Sc	150	5

Table 3.1: System type and Ball trigger settings.

dissertation were performed with software cuts corresponding to $\hat{b} \leq 0.45$ and $\hat{b} \leq 0.21$. We note that these minimum settings practically eliminate false triggers on cosmic rays. Even at minimum bias settings, cosmic ray triggers contributed at the level of one percent or less due to the large counting rate difference between the collision and cosmic ray counting rates.

3.3 Particle Identification

Both the silicon - CsI(Tl) telescopes of the Catania Hodoscope and the Silicon - Si(Li) heavy ion telescopes used the mass and charge dependence of electronic energy loss to distinguish the masses and charges of the various particles. This energy loss ΔE, described by the Bethe-Bloch formula, is given approximately by

$$\Delta E = const \cdot Z^2 \cdot A/E \cdot f(v) \tag{3.3}$$

where Z, A and E are the proton number, mass number and energy of the charged particle, and $f(v)$ is a slow (logarithmic) function of the velocity of the particle. It results in characteristically hyperbolic relationships between the energy loss in the first (silicon) ΔE detector and second (Si(Li) or CsI(Tl)) stopping detectors in the stack. These correlations are shown and discussed below for both the IMF and Hodoscope

telescopes.

3.3.1 IMF telescope PID

Figure 3.4 shows the correlation between the energy loss in the silicon ΔE detector and energy deposited in the Si(Li) stopping detector. Between the two red solid curves in the figure, one can see scatter plot contours with higher counts that correspond to the energy loss relationships expected for the various lithium isotopes ^{6}Li, ^{7}Li, ^{8}Li, and ^{9}Li. These red solid curves, drawn using standard energy loss predictions, can be used to define an experimental PID observable that assumes different values for each isotopes.

For example, to obtain the PID for the lithium isotopes, one uses the upper PID_B and lower PID_A solid curves to interpolate a PID value as follows:

$$PID_P = \frac{X_P - X_A}{X_B - X_A}\left(PID_B - PID_A\right) + PID_A. \tag{3.4}$$

This provides a single observable PID_P that assumes a constant value for all particles of a given isotope, regardless of their energies. After similar interpolations are performed for all of the particles, one obtains the results shown in Fig. 3.5 where the PID values are plotted as a function of the energy of the detected particle. The different isotopes are clearly separated, enabling two dimensional gates to be set about each of the relevant isotopes. Fig. 3.6 shows the typical resolution between the different isotopes, obtained when this two dimensional spectrum is projected on the y-axis. Clearly, the resolution on this one dimensional spectrum is quite good. Nevertheless, the use of two dimensional gates, such as the one drawn in Fig. 3.5 about the ^{10}B data, provides a cleaner distinction between neighboring isotopes.

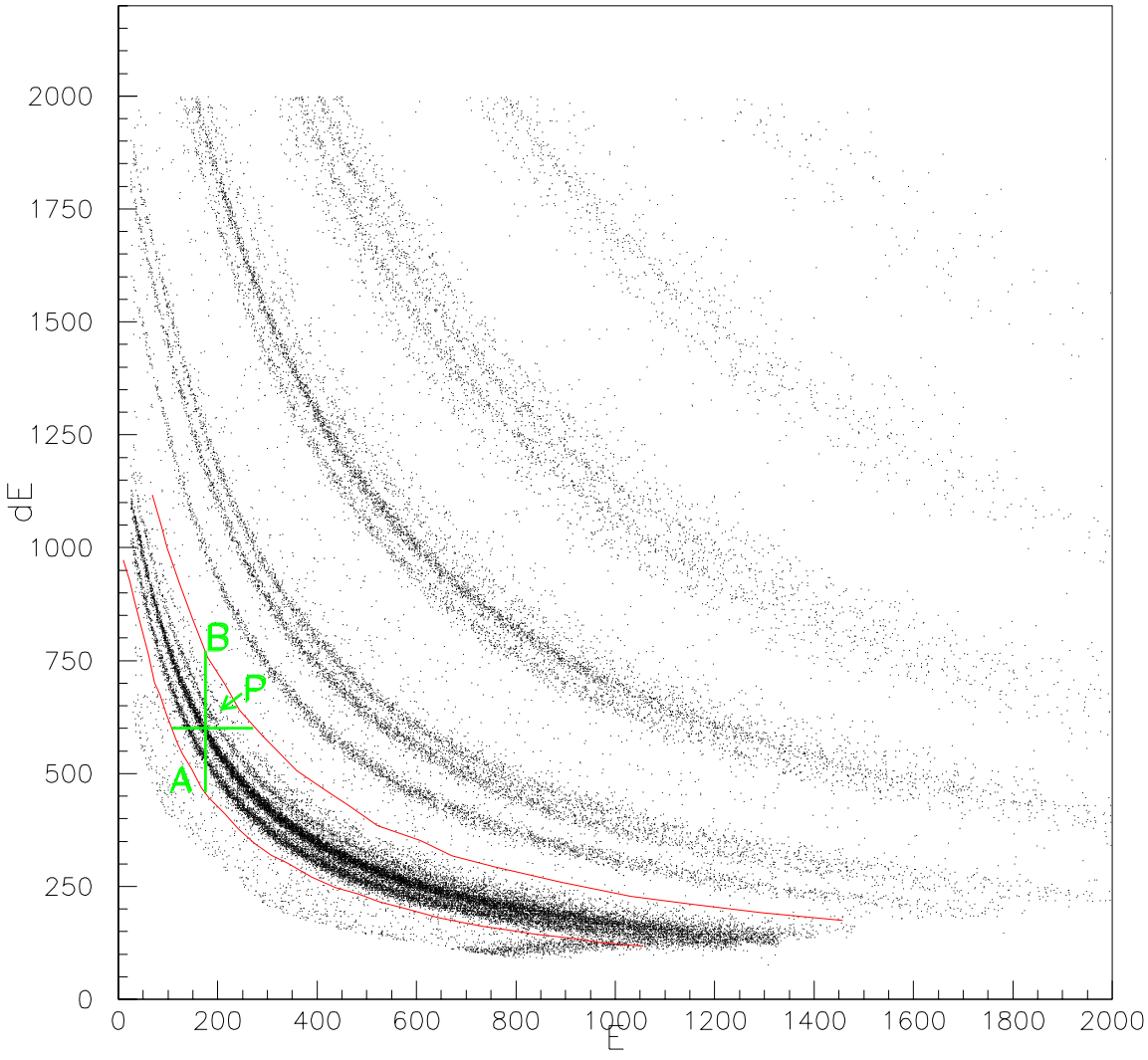

Figure 3.4: IMF telescope dE vs E spectrum for Kr+Nb at 120 MeV/A. Here a point is being interpolated in the ^{7}Li band between the red marked PID curves above and below the Lithium region of the spectrum.

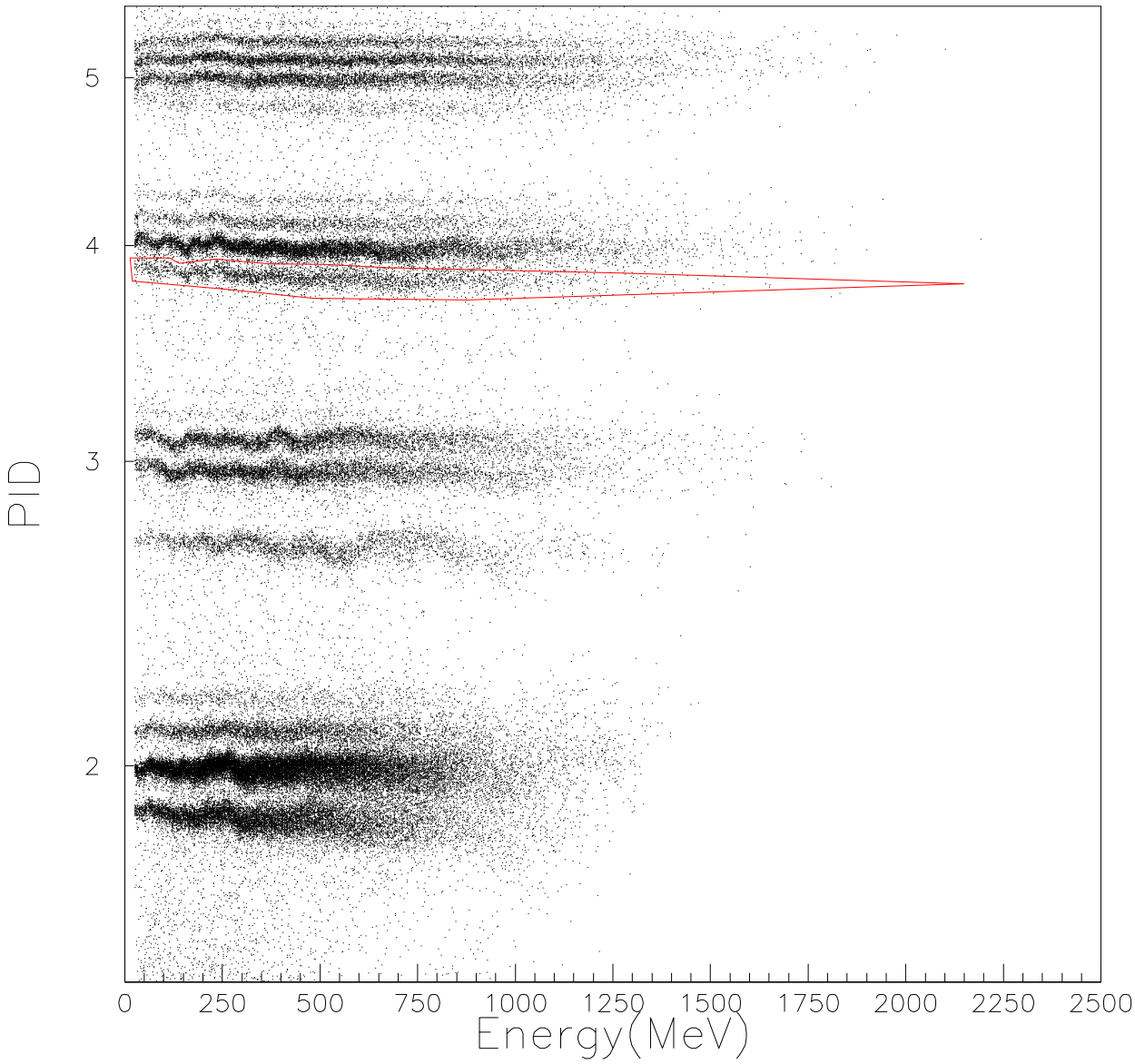

Figure 3.5: A graphical cut to extract the yield of ^{10}B for Kr+Nb colisions at $(E)_{beam}$=35 A/U

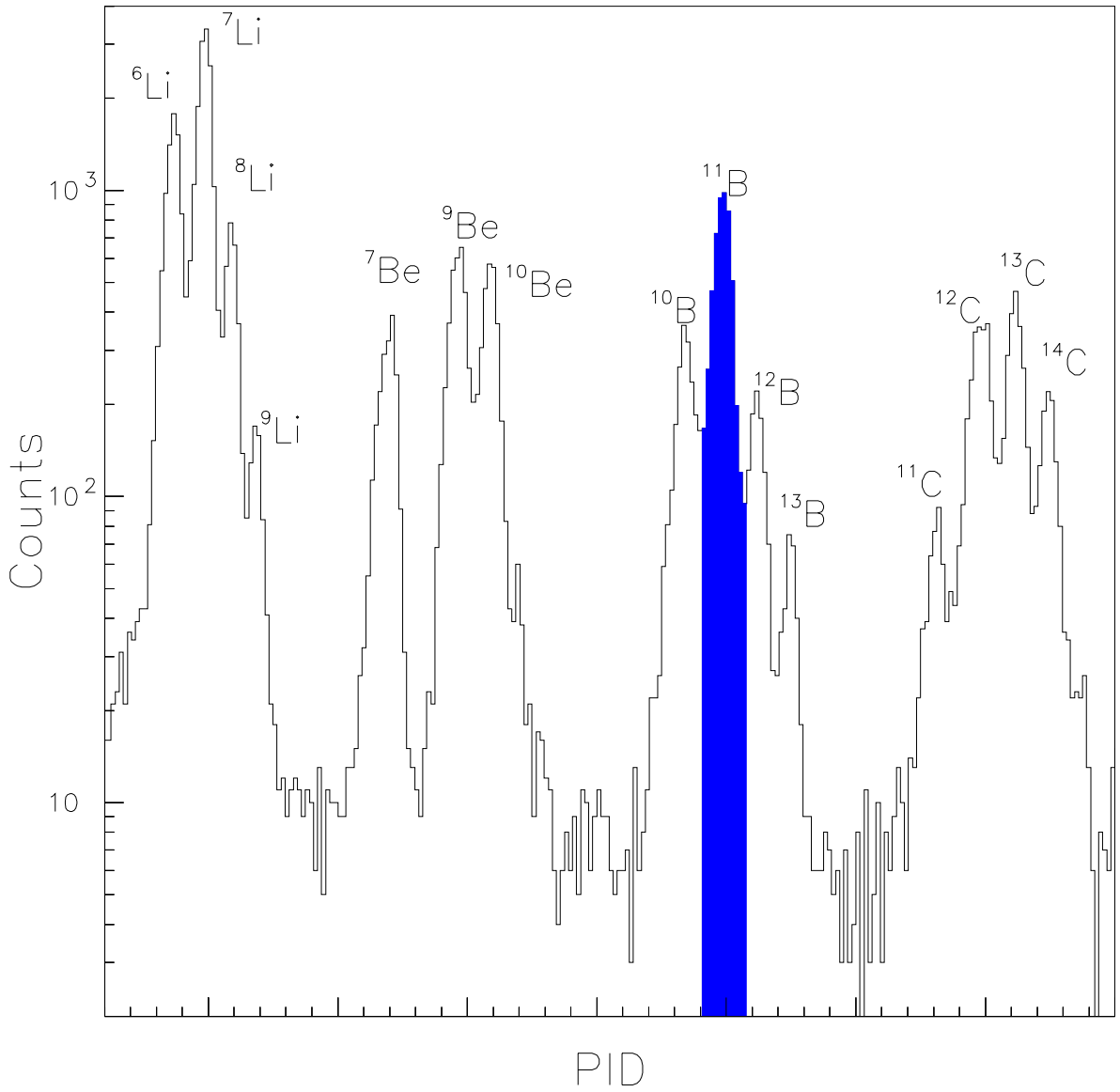

Figure 3.6: IMF pid spectrum for Kr+Nb histogram plot $(E)_{beam}$ = 35 A/U, The yield is obtained by integrating a peak between minima. The yield of ^{11}B is being extracted here.

3.3.2 Catania Hodoscope PID

PID observables were constructed for telescopes in the Catania Hodoscope similar to those constructed for the heavy ion telescopes. The PID gates on each isotope were defined by quartic curves that were fit so as to follow the valleys of minimum counts between neighboring isotopes. Gates for twelve isotopes, p,d,t,^{3}He,^{4}He,^{6}He,^{6}Li,^{7}Li,^{8}Li, ^{7}Be,^{9}Be,^{10}Be, were so obtained. An example of the PID gates are shown in figure 3.7.

3.4 Calibrations

The output signals of the silicon and Si(Li) detectors of the heavy ion telescopes and of the Catania hodoscope are uncalibrated. To enable conversion of these signals to energy values, calibrations with pulsers, alpha sources and beam particles were performed. These calibrations are described in this section.

3.4.1 Silicon calibrations

In silicon detectors, an electron-hole pair is created for every 3.6 eV of deposited energy. This charge is swept to collecting electrodes at opposite ends of each detector; the total collected charge is linearly related to the deposited energy. In general, the amplifiers and ADC's for the silicon detectors are highly linear. Nevertheless, the output values from each ADC must be corrected for any non-linearity and a calibration constant relating pulse height to energy for each ADC must be determined. The first step in the calibration procedure was to correct for non-linearities using a BNC pulser that has stringent linearity specifications. This pulser injects charge at the input of the detector preamp that is approximately linearly related to the DIAL setting on the pulser. In order to correct for the possibility of any small non-linearities,

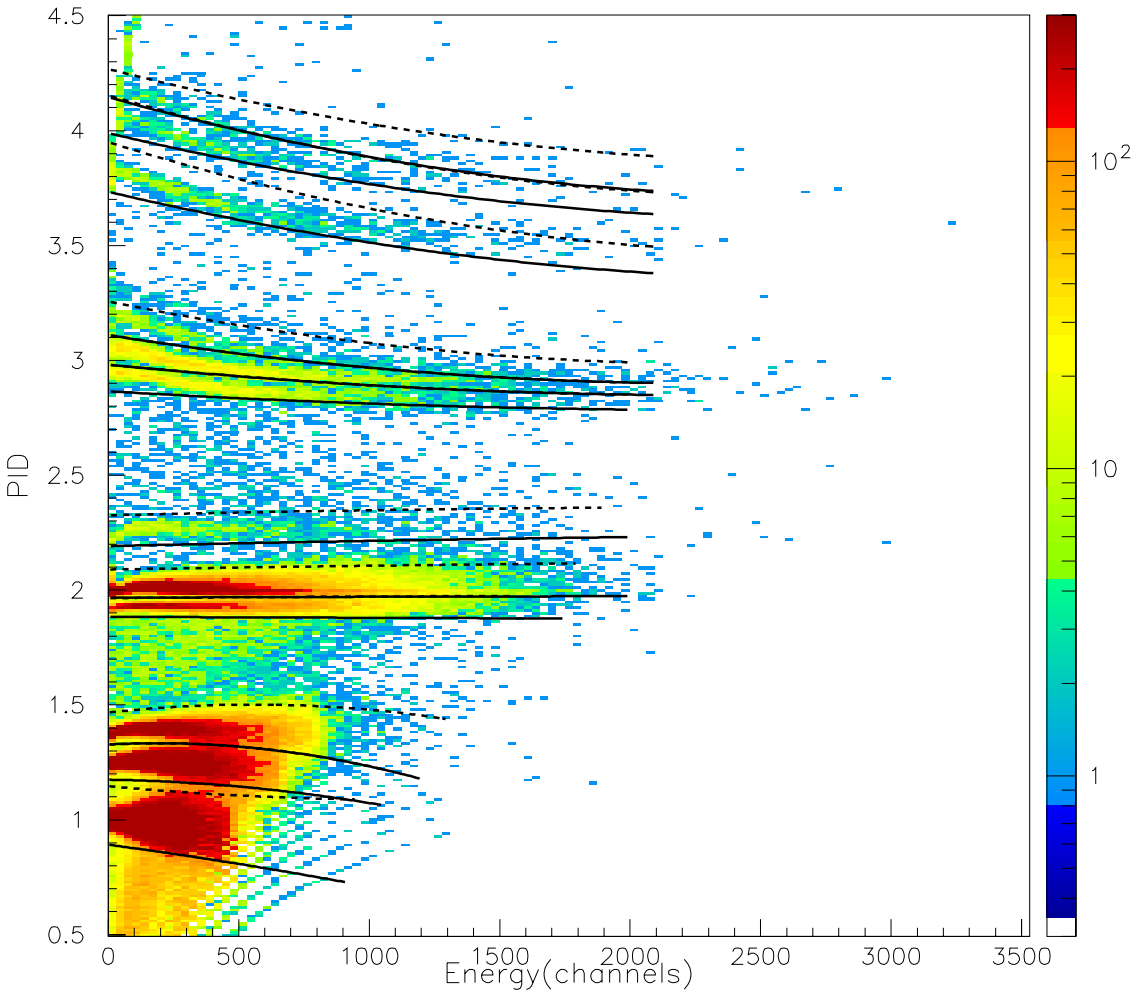

Figure 3.7: Catania PID gates for detector 27 The data are for Kr+Nb at 120 Mev/A. Solid curves are lower gates. Dotted curves are upper gates. In some cases solid and dashed curves coincide for neighboring isotopes. PID error is estimated from this plot.

a non-linear fit to well spaced pulser calibration points of the form

DIAL = (a1 + a2*ch)(1-a3*ch*exp(-a4*ch))*a5

converts the ADC channel number "ch" to a linear variable that is precisely equal to the DIAL setting on the pulser. The final energy calibration is then accomplished by measuring the pulse heights corresponding to 8.78 MeV alphas from the decay of a ^{212}Po daughter using a ^{228}Th source. This introduces another calibration constant a6 that adjusts the linearized ADC value to give the correct energy E.:

E = a6*(a1 + a2*ch)(1-a3*ch*exp(-a4*ch))*a5).

In the case of the Catania hodoscope telescopes, the calibrated silicon energies could then be used with particles of known energy that punch through the silicon detectors. and stop in the CsI(Tl) detectors. In order to determine the thicknesses of the relevant silicon detectors, this operation was performed with the recoil beams that were used to calibrate the CsI(Tl) detectors. The resulting thicknesses are listed in table3.2.

3.4.2 CsI calibration

Calibration reactions [39],[65] were performed by elastically scattering protons from a plastic target using ^{86}Kr beams at E/A = 35 MeV/U and ^{4}He beams at energies of E/A = 22.0, 21.79, and 40.0 MeV. The helium beams also provided calibrations for d, t, ^{3}He and ^{4}He particles using an assortment of reactions listed in Table 3.3. These calibrations were performed with the brass foil removed, which allowed one to measure lower energy protons emitted at backward angles near 90^{o} without having to make large corrections for the energy loss in the foil. The ADC values for the CsI(Tl) detectors were corrected for the offset using a calibrated pulser. Then a linear fit was performed using the peak values for the recoil protons in the CsI(Tl) spectrum and the known energies for the p, d, t, ^{3}He and ^{4}He, corrected for energy loss in the target, the silicon ΔE detector and in the Mylar foil covering the CsI(Tl) crystal.

Det.	μm	Det.	μm	Det.	μm	Det.	μm	Det.	μm	Det.	μm	Det.	μm	Det.	μm
1	317	13	309	25	304	37	299	49	307	61	311	73	310	85	312
2	311	14	304	26	311	38	307	50	305	62	307	74	308	86	312
3	304	15	301	27	303	39	301	51	302	63	301	75	309	87	303
4	310	16	304	28	309	40	310	52	304	64	301	76	309	88	309
5	319	17	304	29	300	41	310	53	299	65	309	77	308	89	310
6	302	18	303	30	309	42	301	54	298	66	307	78	311	90	308
7	301	19	304	31	301	43	302	55	300	67	305	79	312	91	313
8	308	20	304	32	309	44	306	56	307	68	310	80	306	92	310
9	310	21	308	33	302	45	315	57	305	69	310	81	302	93	303
10	300	22	311	34	307	46	316	58	310	70	302	82	303	94	304
11	316	23	302	35	308	47	310	59	305	71	311	83	303	95	312
12	304	24	306	36	308	48	304	60	304	72	309	84	303	96	304

Table 3.2: Measured Catania Silicon detector thicknesses.The uncertaintly is about ± 4 μm

Reaction	States and energies
p(^{4}He,p)^{4}He	0.0 MeV
^{12}C(^{4}He,d)^{14}N*	8.96 Mev
^{12}C(^{4}He,t)^{13}N*	0.0,3.51,6.89 Mev
^{12}C(^{4}He,^{3}He)^{13}C*	0.0,3.86 MeV
^{12}C(^{4}He,^{4}He)^{12}C*	0.0,4.44MeV
p(^{86}Kr,^{86}Kr)p	Knockout(elastic)

Table 3.3: Calibration Reactions used in the experiment.

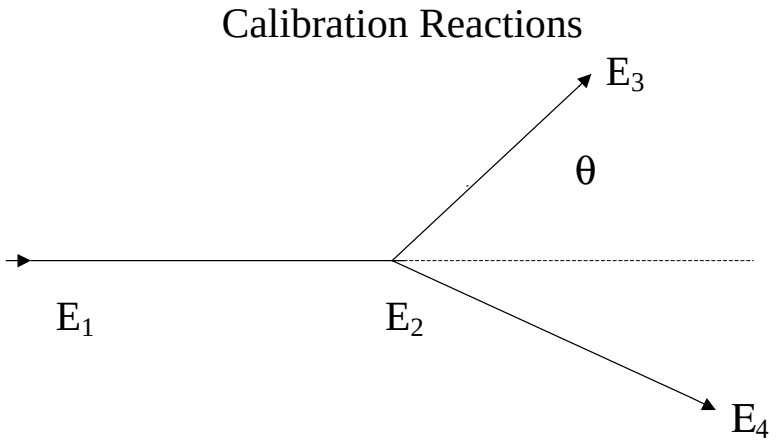

Figure 3.8: Relativistic Kinematics.

Subsequent analyses of the data taken during the regular runs required additional corrections to the energy for the energy losses in the Scandium and Niobium targets and energy losses in the 25 μm brass sheet that was employed to stop delta electrons from the target.

The calibration was achieved by comparing the pulser corrected ADC channel numbers to the energies of the detected particles given by the two body kinematics. The kinematic equation for calculating the total energy for a particle(including rest energy) emitted by the two body reaction indicated in the above figure 3.8 is:

$$E_3 = \frac{fE_{tot} + [f^2E_{tot}^2 - [E_{tot}^2 - p_1^2c^2cos^2\theta][f^2 + 4p_1^2c^2m_3^2c^4]]^{1/2}}{2(E_{tot}^2 - 2p_1^2c^2cos^2\theta)}$$

where $f = m_1^2c^4 + m_2^2c^4 + m_3^2c^4 - m_4^2c^4 + 2E_1m_2c^2$ and $E_{tot} = E_1 + m_2c^2$. Since our measurement of the kinetic energy $T_{3,correct}$ is made after the particles lose energy in the target etc,$T_3 = E_3 - m_3c^2$ The energy the Cesium Iodide crystal registers is

$T_{3,corr} = E_3 - m_3^2c - \Delta E_{target} - \Delta E_{brass} - \Delta E_{Si}$

Here $T_{3,corr}$ is the kinetic energy deposited in the Cesium iodide crystal, ΔE_{target} is the energy loss in the target, ΔE_{brass} is the energy loss in the brass absorber, and ΔE_{Si} is the energy loss in the silicon detector. We compared $T_{3,corr}$ to the measured channel in order to obtain the calibration constants for the CsI. Later, all the calibrated contributions to the energy coming from that deposited in the CsI , $T_{3,corr}$ the silicon ΔE, the brass absorber Δ_{brass} and the target Δ_{target} are added together for each detected particle in order to obtain the total kinetic energy of the particle as it is emitted in the reaction.

Chapter 4

Single Particle Observables

In this chapter we focus upon the analyses of single particle observables. These include the differential multiplicities of emitted particles, and quantities derived from them such as the isoscaling parameters and isotopic temperatures. We also provide some comparisons between these experimental observables and the predictions of statistical models. These comparisons provide one test of whether thermal equilibrium approaches like the Statistical Multifragmentation Model (SMM) can be used to understand the caloric curve.

4.1 Moving source Models

4.1.1 Model Description

At incident velocities greater than the Fermi velocity of the nucleons contained in the projectile and target, particle emission occurs over timescales commensurate with that of the collision. This rapid emission occurs primarily from "participant" region where nucleons from the projectile and target strongly overlap, where matter first becomes compressed and then expands in response to the pressure within the compressed region. Slower emission occurs from projectile and target "spectator" remnants that

miss colliding directly with the other nucleus but become excited during the collision nonetheless. It is reasonably accurate at $E/A > 100$ MeV and below such energies, to view the emission of Intermediate Mass Fragments $IMF(20 > Z > 2)$ and Light Charged Particles $LCP(Z < 3)$ as originating from three sources after collision as given schematically in figure 4.1. There is a central source commonly termed the participant source. In addition, there is a much slower source and a much faster source from the decay of the target and projectile spectator remnants, respectively [88, 16, 122, 41].

In this simplified picture, illustrated in Fig. 4.1, the participant region is composed of target nucleons, whose trajectories intersect the projectile and of projectile nucleons, whose trajectories intersect the target. All the other target and projectile nucleons comprise the target and projectile spectators, respectively. Naturally, the relative sizes of projectile and target spectators reflect the mass asymmetry of the entrance channel. They have the same masses for symmetric collsions between identical protectiles and targets. The target spectator mass will exceed that of the projectile spectator when the target mass is larger than that of the projectile, etc. Very often, the emission patterns of these three sources are assumed to be isotropic in their center of mass frames. However, this is an idealization because the rapid emission from the participant source, envisioned by this picture, may preclude the complete mixing of the projectile and target nucleons in the participant and the resulting participant emission may appear as if it were from a continuum of sources, a concept proposed first in the original "firestreak" model. [41] Such a continuum of sources is closer to the predictions of dynamical calculations such as those obtained by the Boltzmann-Uehling-Uhlenbeck (BUU) equation. [9]

Energy spectra for hydrogen and helium isotopes emitted in Kr+Nb reactions at $\hat{b} \leq 0.45$ and E/A = 35, 70 100 and 120 MeV are shown in Figs. 4.2 and 4.3. At

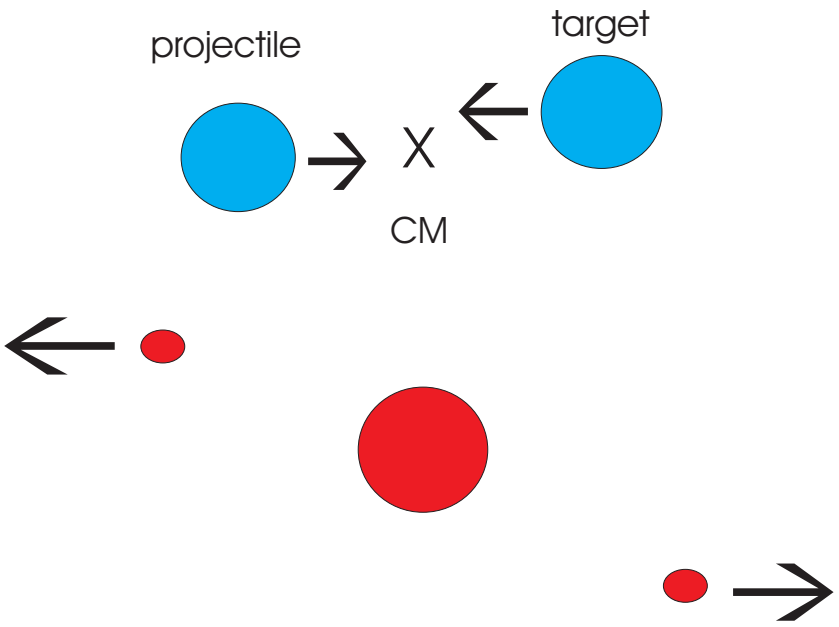

Figure 4.1: In the participant-spectator model, it is assumed that the emission pattern from the collision can be approximated as originating a participant source formed by the overlap of the projectile and target nuclei during the collision and from projectile and target spectator sources that contain nucleons whose trajectories avoid the overlap region.

most angles, the spectra display maxima at low energies and decrease smoothly with energy. The variation of the cross section with scattering angle and energy is large; care is needed in the analysis of such spectra into order to get accurate differential or total multiplicities for the various particle species. In this dissertation, we first try a simple decomposition of the emission pattern into participant and projectile and target spectator sources in order to accurately parameterize the emission over the angular domain explored by the Catania hodoscope. We modify the form of this decomposition as needed to improve the description of the data. The hodoscope was centered about angles that correspond to $\theta_{CM} \approx 90^o$ in the rest frame for the collision of a nucleon from the projectile with one from the target. Since this corresponds closely to nucleons emitted to $\theta_{CM} = 90^o$ from the participant source, accurate fitting of the participant source is more important than describing the spectator sources which emit mainly to unmeasured scattering angles.

4.1.2 Single Particle spectra fitting

In the following we start our description of the emission from participant, target and projectile spectator sources with the expression of Ref. [52, 53], which was used in that work to describe the spectra of fragments with $2 \leq Z \leq 8$ produced in Au+Au collisions at E/A=100 MeV. We have used different forms for the fitting expression, which differ in the way that the effects of collective radial expansion of the participant source and for sideward deflection of the two spectator sources are handled. When these effects are included, we use the following expression:

$d^2\langle M \rangle / d\Omega dE =$

$$\frac{d^2\langle M_1 \rangle}{dE d\Omega}\left(\boldsymbol{p}_1\right) + \int_0^{2\pi} \frac{d\phi_R}{2\pi} \sum_{i=2}^{3} \frac{d^2\langle M_i \rangle}{dE d\Omega}\left(\boldsymbol{p}_i, \boldsymbol{v}_i\left(\phi_R\right), V_i\right) \ , \tag{4.1}$$

where E denotes the kinetic energy and $\boldsymbol{p}_i$ the momentum of the emitted particle; $\boldsymbol{v}_i$ denotes the velocity and V_i, the effective Coulomb barrier of the i-th source; and Φ_R denotes the azimuthal angle of the reaction plane [53]. Here, $\frac{d^2\langle M_i\rangle}{dEd\Omega}(\boldsymbol{p}_i, 0, V_i)$ is defined in the rest frame of the source $\boldsymbol{v}_i = 0$ by a Relativistic Boltzmann distribution[62, 86]:

$$P_i(E)dE = \frac{4\pi}{< M_i >}\frac{d^2 < M_i >}{dEd\Omega}dE = \frac{1}{< M_i >}\frac{d < M_i >}{dE}dE =$$

$$\Theta(E - V_i)\frac{(E + mc^2 - V_i)\sqrt{((E + mc^2 - V_i)^2 - m^2c^4)}}{2(\frac{T}{mc^2})^2K_1(\frac{mc^2}{T}) + (\frac{T}{mc^2})K_0(\frac{mc^2}{T})}\frac{e^{-\frac{E+mc^2-V_i}{T_i}}dE}{m^3c^6}\ , \qquad (4.2)$$

and $\frac{d^2<M_i>}{dEd\Omega}(\boldsymbol{p}_i, \boldsymbol{v}_i(\phi_R))$ is obtained from Eq. 4.2 by Lorentz transformation.

In Eq. 4.2, T_i is the temperature of the Maxwellian source and $\Theta(E - V_i)$ is the unit step function and E is the kinetic energy of the particle. The sum in eq 4.1 is over the target and projectile spectator sources, M_i is the particle multiplicity, V_i is the kinetic energy gained by Coulomb repulsion and E_i is kinetic energy. K_0 and K_1 are MacDonald functions. Note that this equation reduces to the standard classical Maxwell-Boltzmann Distribution for $E_i = 0$ and $V_i = 0$ and small T.

In some of the fits, the form of the participant source $\frac{d^2\langle M_1\rangle}{dEd\Omega}(\boldsymbol{p}_1)$ was chosen in order to model a collective radial flow. For this, a self similar radial expansion $\overrightarrow{v}(\overrightarrow{r}) = c\beta_{exp}\overrightarrow{r}/R_s$ of the spherical participant source (i=1 in Eq. 4.1) was assumed which attains its maximum velocity $c\beta_{exp}$ at the surface $r = R_s$. The velocities of individual particles were assumed to be thermally distributed about the local radial expansion velocity with temperature T_1. Coulomb expansion after breakup was modelled in the limit of large β_{exp}; particles with charge Z_f , emitted from a source with charge Z_s , gained a kinetic energy of $\Delta E_{Coul}(r) = Z_f(Z_s - Z_f)e^2r^2/R_s^3$, without changing their direction. In the c.m. frame one obtains[52]:

$$\frac{d^2\langle M_1\rangle}{dEd\Omega} = \frac{3}{4\pi R_S^3}\int_0^{R_S} r^2dr\int d\Omega_r\int dE'\frac{d^2P'}{dE'd\Omega}(\boldsymbol{p}, \boldsymbol{v}(\boldsymbol{r}), 0)\delta(E' - E + \Delta E_{Coul}(r))\ , \quad (4.3)$$

where the direction of the particle's momentum is assumed to be unchanged. The total spectrum is obtained by inserting Eq. 4.3 into Eq. 4.1 as the participant source.

In other fits, the collective expansion of the participant source was neglected, the form of the participant source $\frac{d^2\langle M_1\rangle}{dEd\Omega}(\boldsymbol{p}_1)$ in its rest frame was given by Eq. 4.2. Regardless of the choice of fitting function, the source spectra must be transformed from the rest frame of the source to the LAB frame, using the formula:

$d^2\langle\ M_i\ \rangle/d\Omega dE_{lab} = (p_{lab}/p_{so,i})$*$\mathrm{d}^2\langle M_i\rangle$ / $\mathrm{d}\Omega\ dE_{so}$,

where E_{so} and $p_{so,i}$ are the energy and momentum of the particle in the source frame.

In general, Eq. 4.1 has up to 13 free parameters for a three source system, Three multiplicity parameters M_i , three temperatures T_i , three Coulomb parameters Z_i , one expansion parameter β_{exp} for the participant, a maximum Coulomb energy for emission from the surface of the participant, one parallel β_Z and one perpendicular β_X velocity component for the spectators relative to the participant. For symmetric collisions, one can assume certain symmetries in the fitting parameters for the two spectator sources, i.e. $\langle M\rangle_2 = \langle M\rangle_3$, $Z_2 = Z_3$ and $T_2 = T_3$. Even though Kr+Nb and Ar+Sc are not precisely symmetric systems, we invoke this constraint because the experimental data are over an angular domain that avoids much of the spectator sources and is therefore insufficient to constrain the projectile and target spectator sources independently. Later, the influence of the remaining asymmetry in the emission pattern was addressed by including a multiplicative anisotropy on the overall emission pattern.

Fits to the spectra for hydrogen and helium isotopes using Eq. 4.1, with M_i, T_i and Z_i as fit parameters and non-zero values for the collective expansion velocity β_{exp} are shown by the solid lines in Figs. 4.2 and 4.3. The parameters for these fits are given in Table 4.1. In general, the temperature and source velocity fit parameters for the various particles differ significantly at each incident energy. Corresponding

fits without collective expansion for ^3He and ^4He are shown in Figs. 4.5 and 4.6 of the next section and the parameters for these fits are given in Table 4.2. The fits with and without collective expansion are comparable. Because the collective part of the energy of the detected fragment $E_{coll} \approx 1/2 M_{frag} v_{coll}^2$ is proportional to the fragment mass, clear sensitivity to the β_{exp} may only expected for heavier fragments with $A \geq 12$ [53]. In any case, the source parameters for the various particles are not consistant with three defined unique sources. This may indicate either that the sources are not well defined by analysis, or that the three source analysis neglects important effects in the emission or both. Certainly, the angular domain of the data is not sufficient to show the parameters of the spectator accurately enough. The lack of coverage in the experiment at the more forward angles precludes the extraction of the parameters describing the projectile source. Loss of coverage at forward angles also removes lower parts of the center of mass spectra for the participant source and makes it difficult to extract the collective radial velocity from the mean values of the kinetic energy in the center of mass. The lack of coverage in the backward angles makes it difficult to determine the parameters of the target spectator source.

In general, the parameters of the fit procedure are not determined uniquely by the present analysis. The values for the parameters are model dependent and less directly connected to the actually measurements than one would like. This is not a seriuos problem for the experiment because the main goal is to determine the excited state population of emitted particle fragments. This is easily achieved with this experimental setup. We therefore use the fits only to assist us in interpolating the data so as to obtain accurate values for the cross section at angles near $\theta_{CM} \approx 90^o$, and to enable simulation the detection efficiency for the measurements of excited state populations as discussed in chapter 5. For this purpose, the values for the parameters are immaterial; the only relevant issue is whether the fits accurately describe the

data.

Particle	Beam	β_{cm}	β_{exp}(mid)	βx(sp)	βz(sp)	T_{sp}	T_{mid}	Multiplicity	Multiplicity	V_{sp}	V_{mid}	$\frac{Y_{mid}}{Y_{tot}}$
-	AMeV	-	-	-	-	MeV	MeV	$< M >_{sp}$	$< M >_{mid}$	MeV	MeV	%
d	70	0.1831	0.11	0.0934	0.1617	3.94	17	0.5729	3.4300	1.65	6.24	99
t	70	0.1831	0.11	0.0862	0.1688	10.69	14.27	0.8870	2.2460	1.61	6.24	99
^{3}He	70	0.1831	0.11	0.1107	0.1620	6.87	22.39	0.1867	0.8401	2.68	11.70	99
^{4}He	70	0.1831	0.11	0.0000	0.1638	14.75	9.42	3.8800	3.9150	2.99	12.30	95
d	100	0.2173	0.14	0.0571	0.1988	9.04	21.98	0.8904	4.5140	1.65	6.24	99
t	100	0.2173	0.14	0.0937	0.1978	14.17	16.46	1.4790	2.9090	1.61	6.24	98
^{3}He	100	0.2173	0.14	0.0982	0.1910	9.47	27.01	0.2205	1.2070	2.68	13.89	99
^{4}He	100	0.2173	0.14	0.0000	0.1052	19.77	17.95	2.6120	1.5780	2.99	12.61	52
d	120	0.2369	0.17	0.0982	0.2130	11.67	23.02	1.6550	6.3400	1.65	6.24	98
t	120	0.2369	0.17	0.0837	0.2190	17.68	14.07	2.1040	4.0403	1.61	6.24	97
^{3}He	120	0.2369	0.17	0.0940	0.2095	11.26	26.09	0.3419	1.7440	3.00	12.80	99
^{4}He	120	0.2369	0.17	0.0003	0.1275	21.65	17.52	2.8930	2.6360	2.76	12.40	59

Table 4.1: LCP Single particle fit parameters for Kr+Nb using the 3 source, central radial expansion model.

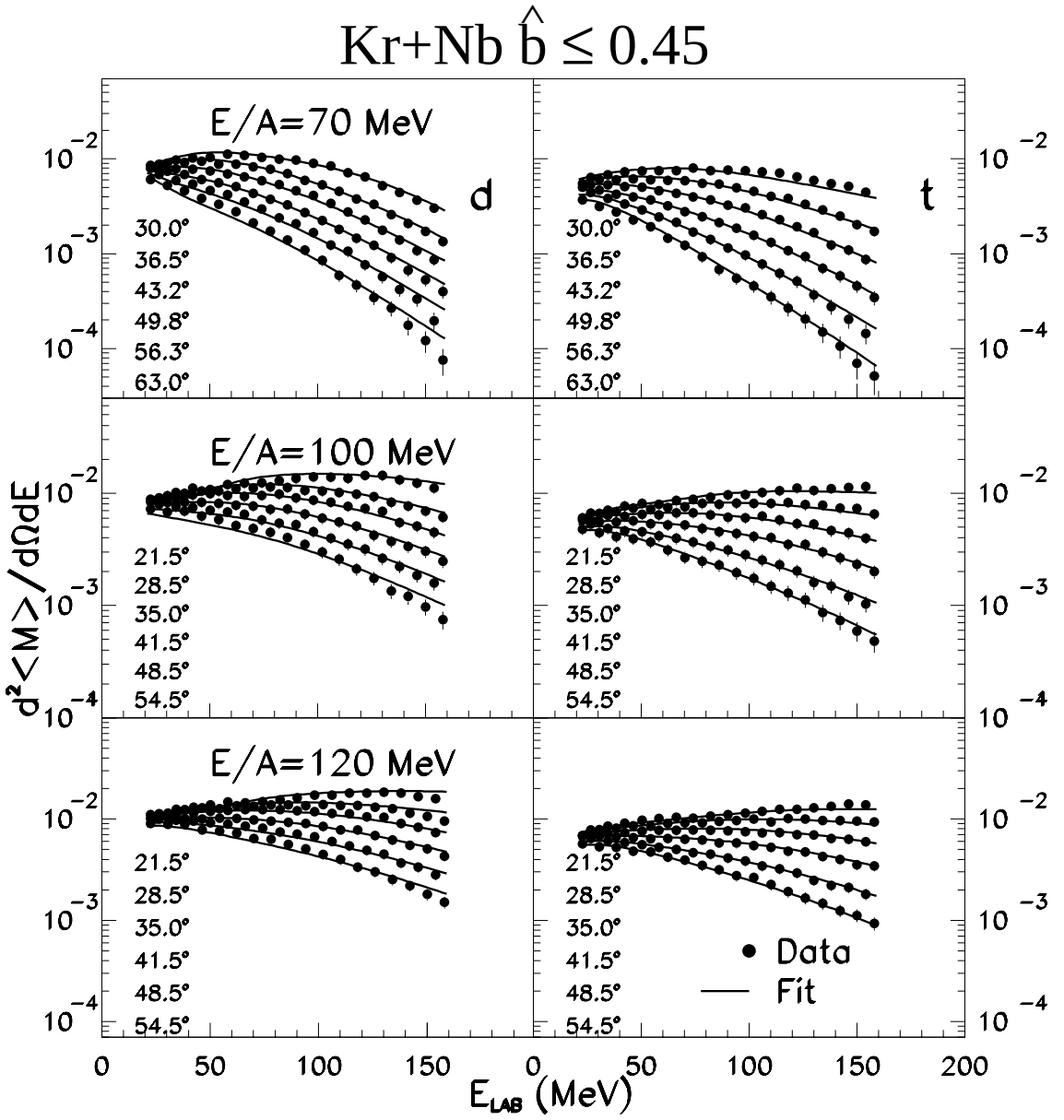

Figure 4.2: d,t fits using the 3 source fit with a radially expanding isotropic participant source.

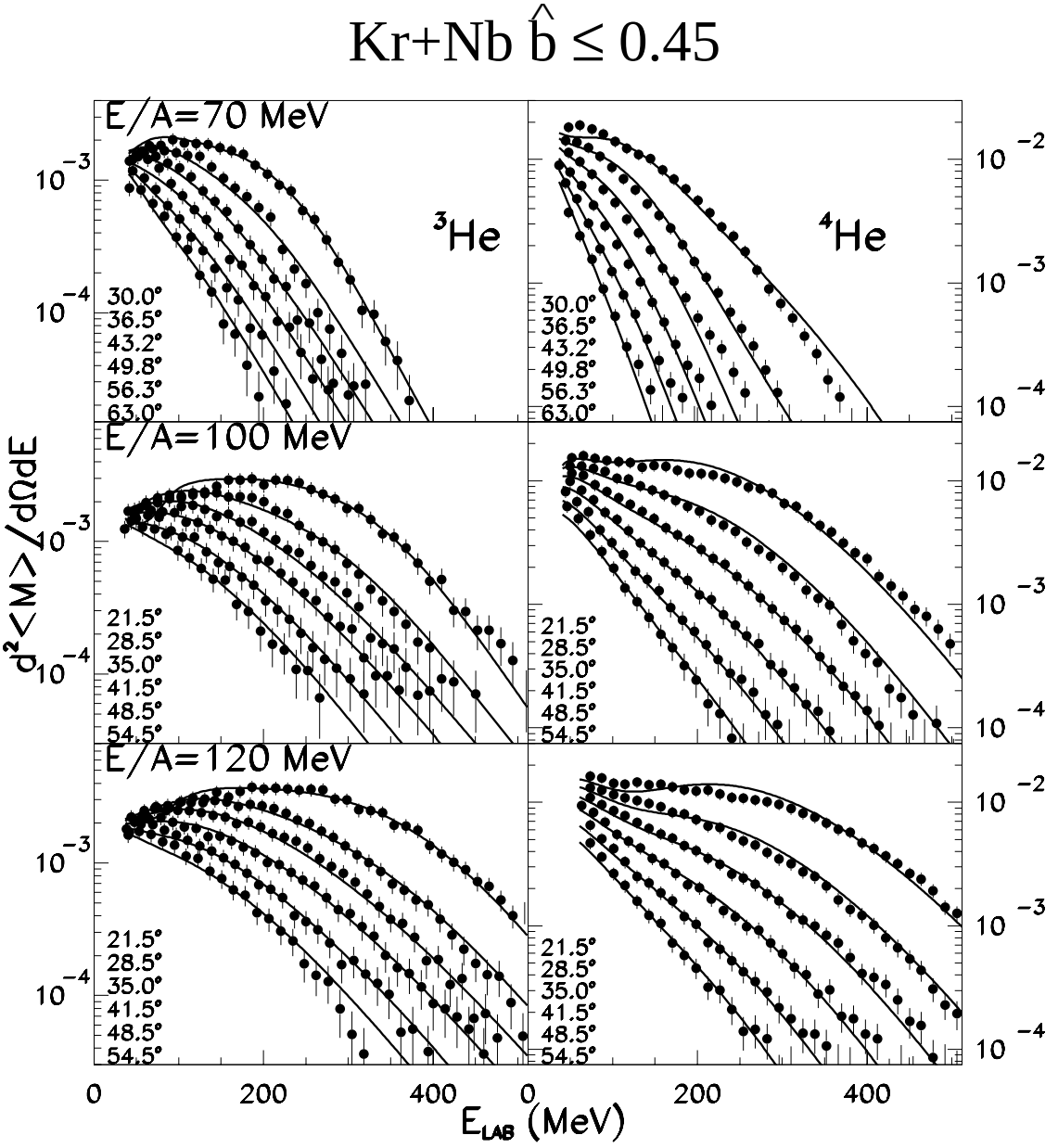

Figure 4.3: ^3He,^4He fits using the 3 source fit with a radially expanding isotropic participant source.

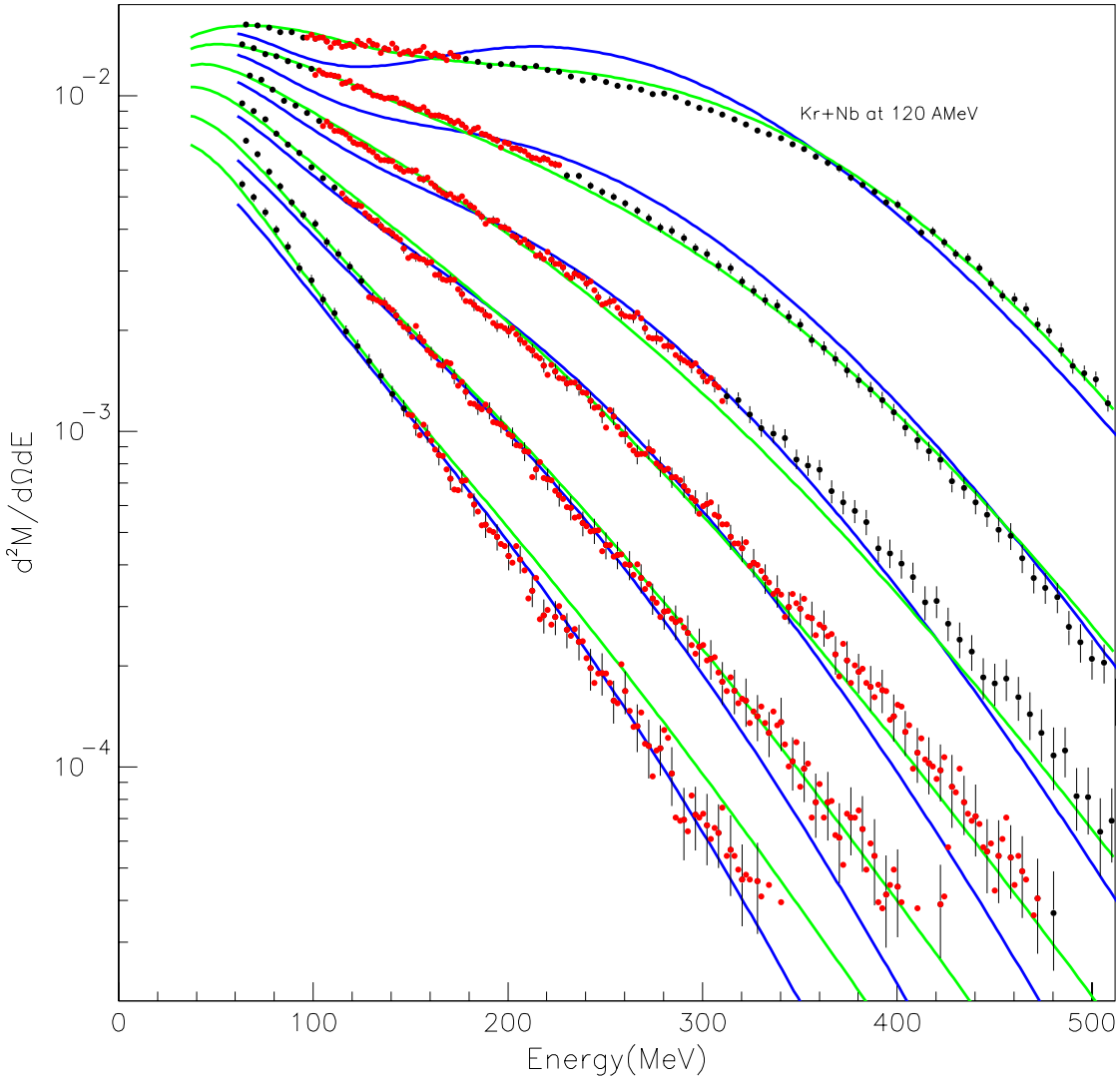

Figure 4.4: ^4He fit for Kr+Nb at 120 AMeV of figure 4.3, the green curve fit is the fit that includes the asymmetric parameterization of equation 4.4, the data highlighting at $70^o \leq \theta_{CM} \leq 110^o$.

4.2 Improved fits and extraction of the single particle observables

4.2.1 Introduction of source anisotropies

Most of the fits to the hydrogen and helium isotope spectra in Figs. 4.2 - 4.3 are sufficient to allow extraction of the cross section at angles near $\theta_{CM} \approx 90^o$ to within an estimate accuracy of 15 percent. Fits to the spectra for α particles at E/A = 120 do not fit the data at the important angles and energies (indicated as the red points in Figure 4.4) that correspond to $70^o \leq \theta_{CM} \leq 110^o$. This problem becomes more severe when fitting the spectra for even heavier particles.

4.2.2 Asymmetric source parameterization

In order to obtain a better representation of the data, we have explored alternative fitting functions. It appears that these difficulties can basically be surmounted by making the predicted emission pattern more asymmetric than Eq. 4.2 predicts. The resulting formula is inelegant, but does succeed in representing the data well, enabling the desired extraction of the cross section at angles near $\theta_{CM} \approx 90^o$. The inclusion of asymmetric terms in the source fits were needed by problems we observed with the isotropy of the energy spectra in the C.M. system. A Fourier cosine series was included as a multiplicative factor to correct for this. This shaping may reflect the small asymmetry in the entrance channel or that the dynamical emission process is poorly approximated by a set of isotropically emitting sources. With this modification, the source function in the CM frame becomes:

$$d^2\langle M\rangle \;/\; d\Omega \mathrm{dE} =$$

$$\left[\frac{d^2\langle M_1\rangle}{dEd\Omega}\left(\boldsymbol{p}_1, 0, V_1\right) + \int_0^{2\pi}\frac{d\phi_R}{2\pi}\sum_{i=2}^{3}\frac{d^2\langle M_i\rangle}{dEd\Omega}\left(\boldsymbol{p}_i, \boldsymbol{v}_i\left(\phi_R\right), V_i\right)\right]\cdot\left[1+\sum_{k=1}^{N_{terms}} a_k cos(k*\Theta_{CM})\right] \;, \tag{4.4}$$

where the sum in the left factor is one participant and 2 spectators. The a_k coefficients in the right factor are fit parameters in the cosine series, which is summed over the number of terms (N_{terms}) that can be constrained adequately by the data.

Symmetry was invoked to reduce the number of fit parameters. In particular, we required the target and projectile source to be reflections of each other across the C.M., i.e. $(M_{tar}, T_{tar}, V_{tar}) = (M_{pro}, T_{pro}, V_{pro})$. For these spectators we add two more parameters for spectator velocity vectors $\beta\perp$ and $\beta\|$ relative to the beam axis. With the parameters $(Z_{mid}, A_{mid}, T_{mid})$ for the participant source we have $8+N_{terms}$ parameters in total. With this many parameters the physical meaning of each parameter is not very clear; however, we believe the lack of clarity is outweighed by the improved quality of the fits we use below to interpolate the yields accurately and thereby calculate physical quantities with greater confidence. We find that two fourier terms (n=3,5) are sufficient to obtain good fits. To the spectrum only a small anisotropy is needed reflecting the small entrance channel asymmetry. Comparing fits to the ^4He spectra in Figure. 4.4 we see that the improved fit with only two odd terms at most (green lines) while not perfect, fits the large cross section data in the important region at $\theta_{CM} \approx 90^o$. This turns out to be true for all of the isotopes in Figures 4.5 - 4.12. The fit parameters are listed in table 4.2 .

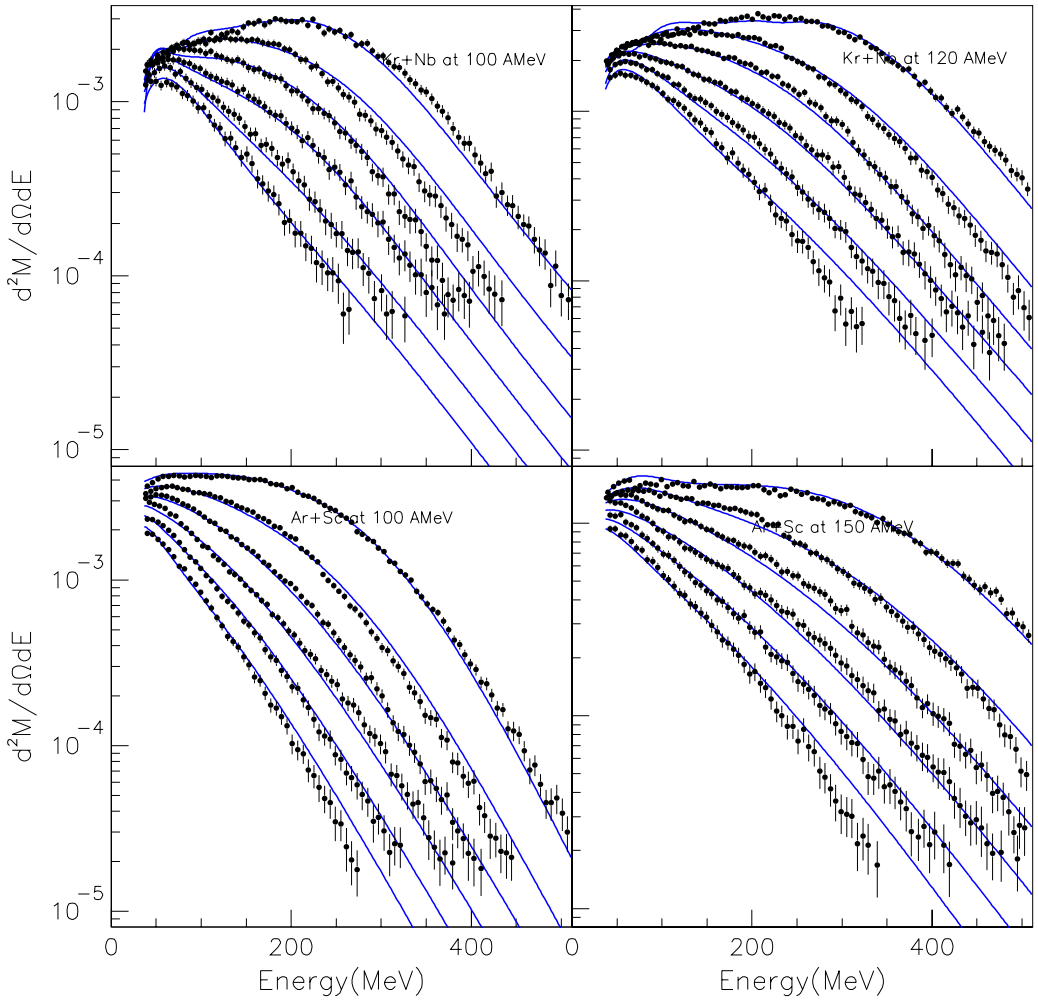

Figure 4.5: Plot of $\frac{d^2M}{dEd\Omega}$ versus Energy. A Fourier perturbed 3 source fit of ^{3}He for ^{86}Kr+^{93}Nb at 100,120 MeV/A and ^{36}Ar+^{45}Sc at 100,150 MeV/A respectively.

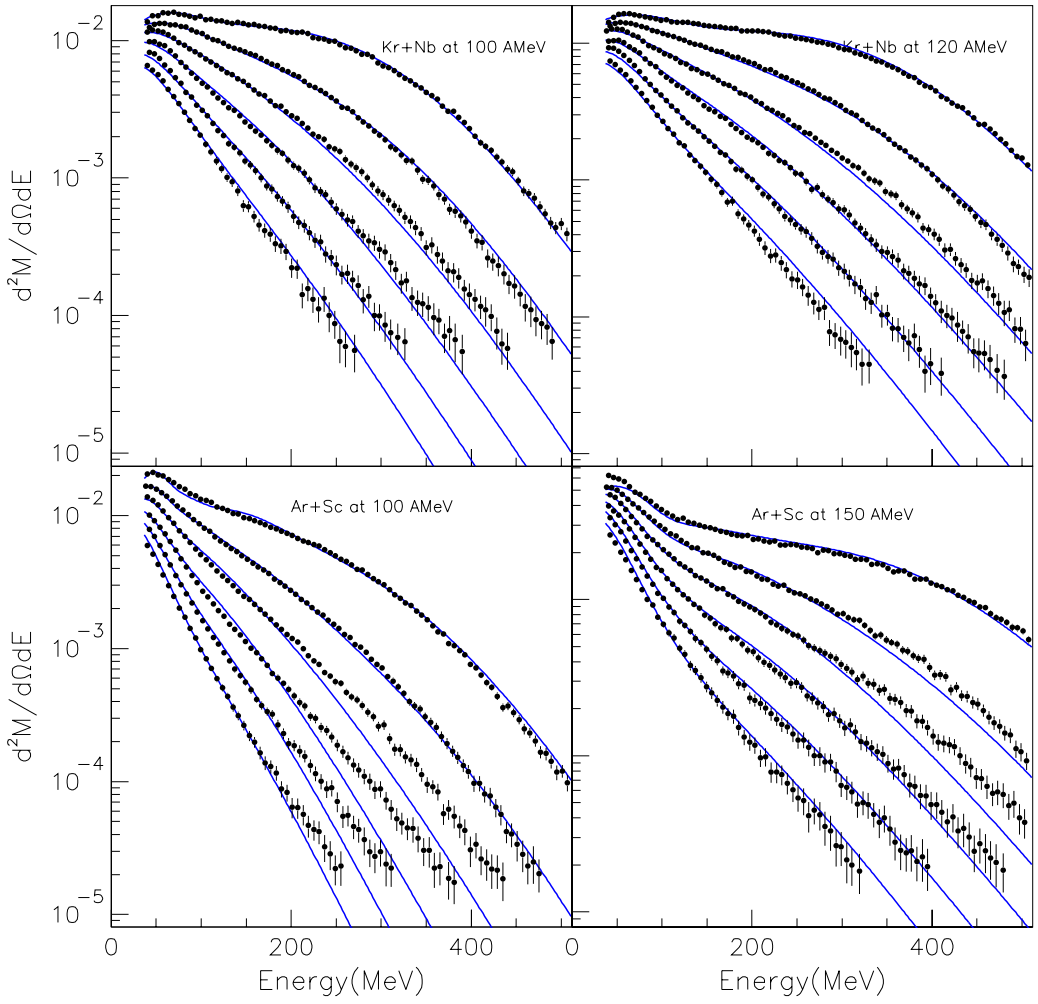

Figure 4.6: Plot of $\frac{d^2M}{dEd\Omega}$ versus Energy. A Fourier perturbed 3 source fit of ^{4}He for ^{86}Kr+^{93}Nb at 100,120 MeV/A and ^{36}Ar+^{45}Sc at 100,150 MeV/A respectively.

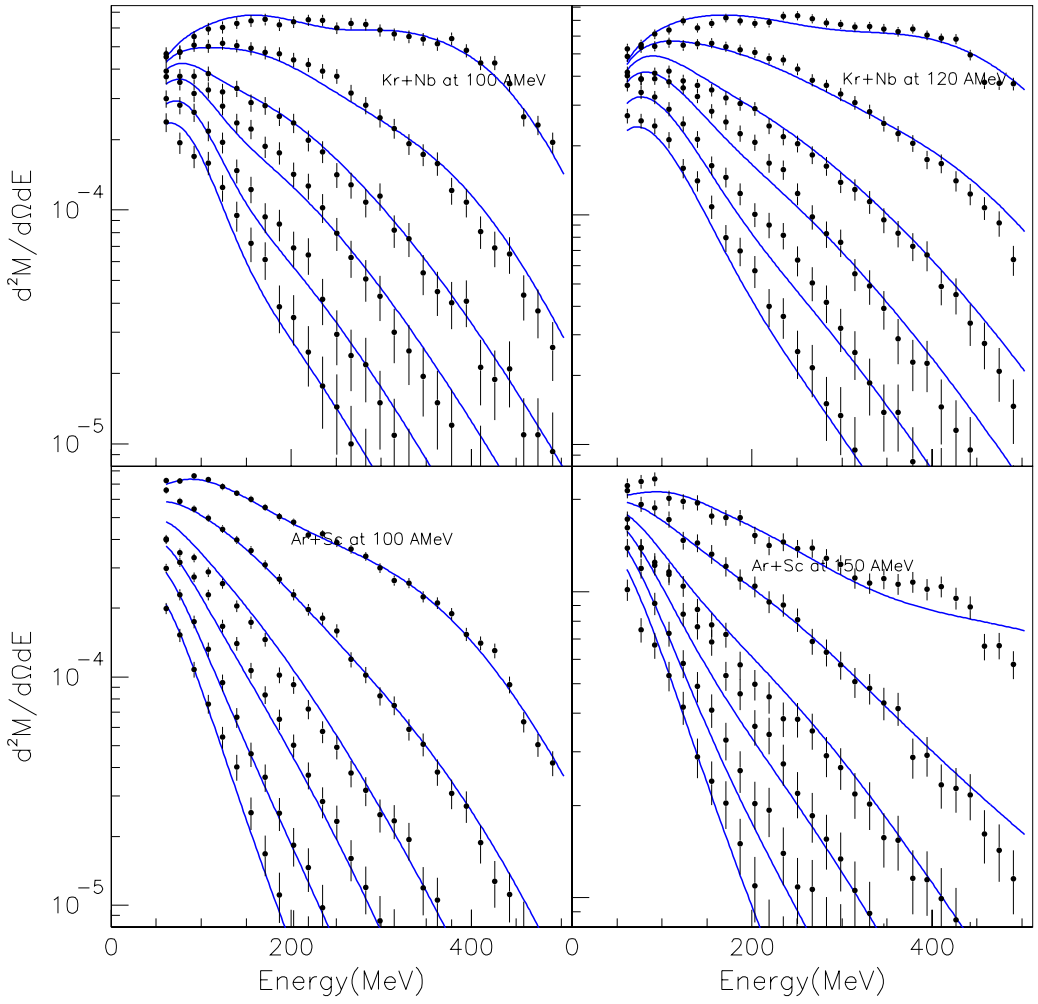

Figure 4.7: Plot of $\frac{d^2M}{dEd\Omega}$ versus Energy. A Fourier perturbed 3 source fit of ^{6}Li for ^{86}Kr+^{93}Nb at 100,120 MeV/A and ^{36}Ar+^{45}Sc at 100,150 MeV/A respectively.

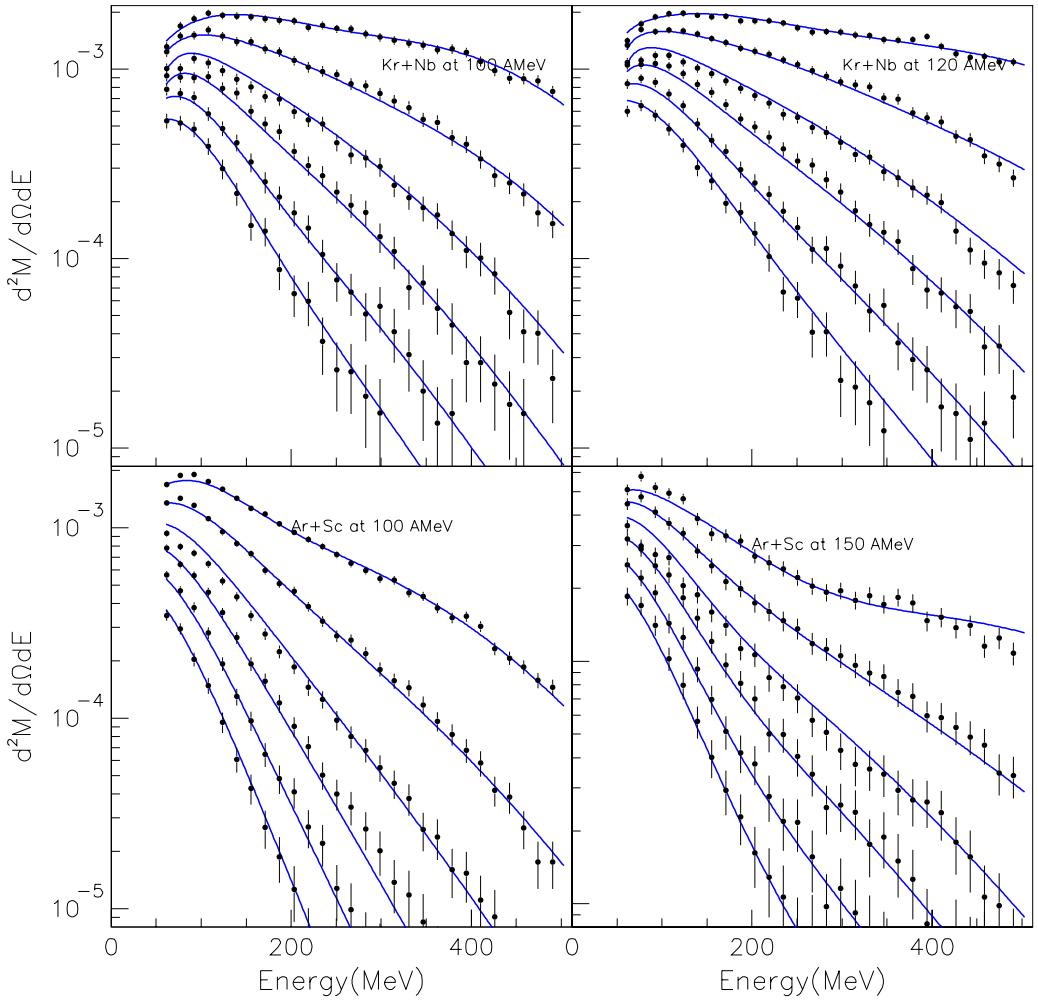

Figure 4.8: Plot of $\frac{d^2M}{dEd\Omega}$ versus Energy. A Fourier perturbed 3 source fit of ^{7}Li for ^{86}Kr+^{93}Nb at 100,120 MeV/A and ^{36}Ar+^{45}Sc at 100,150 MeV/A respectively.

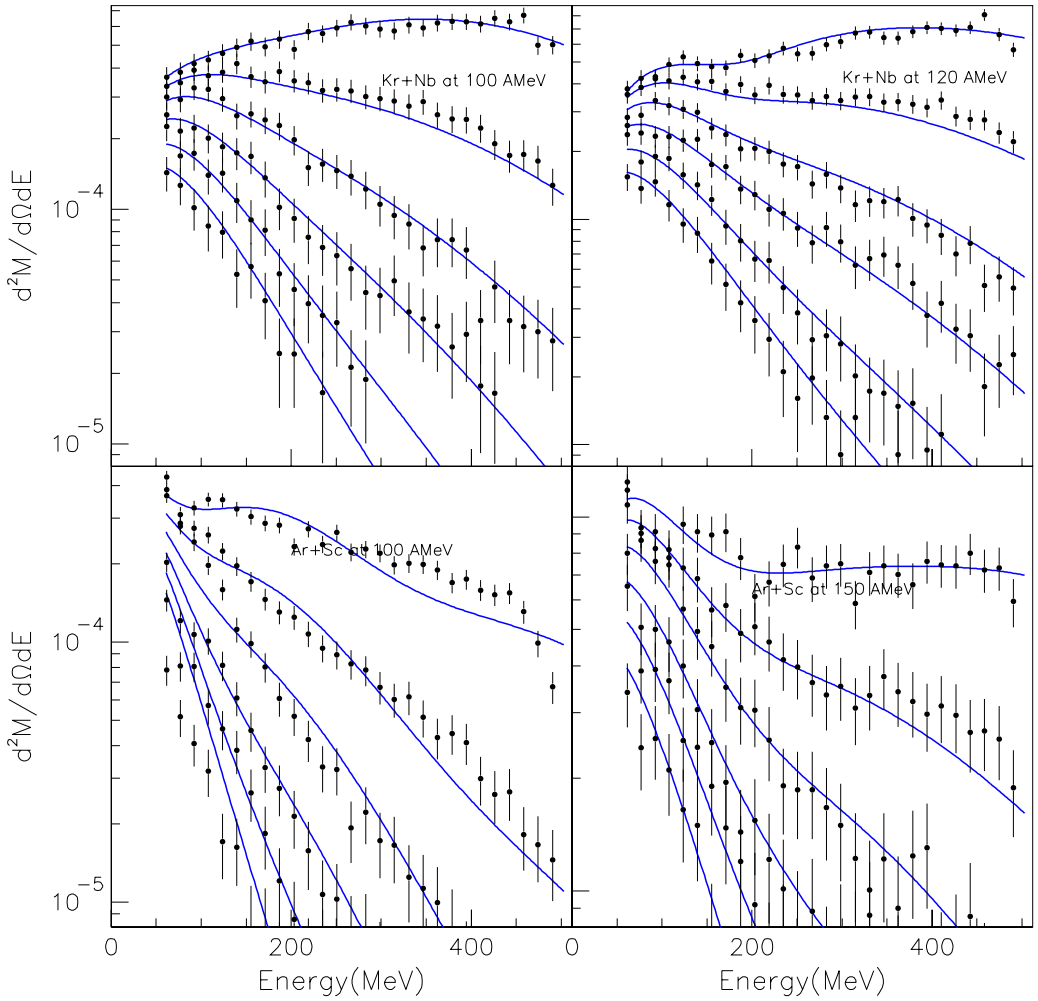

Figure 4.9: Plot of $\frac{d^2M}{dEd\Omega}$ versus Energy. A Fourier perturbed 3 source fit of ^{8}Li for ^{86}Kr+^{93}Nb at 100,120 MeV/A and ^{36}Ar+^{45}Sc at 100,150 MeV/A respectively.

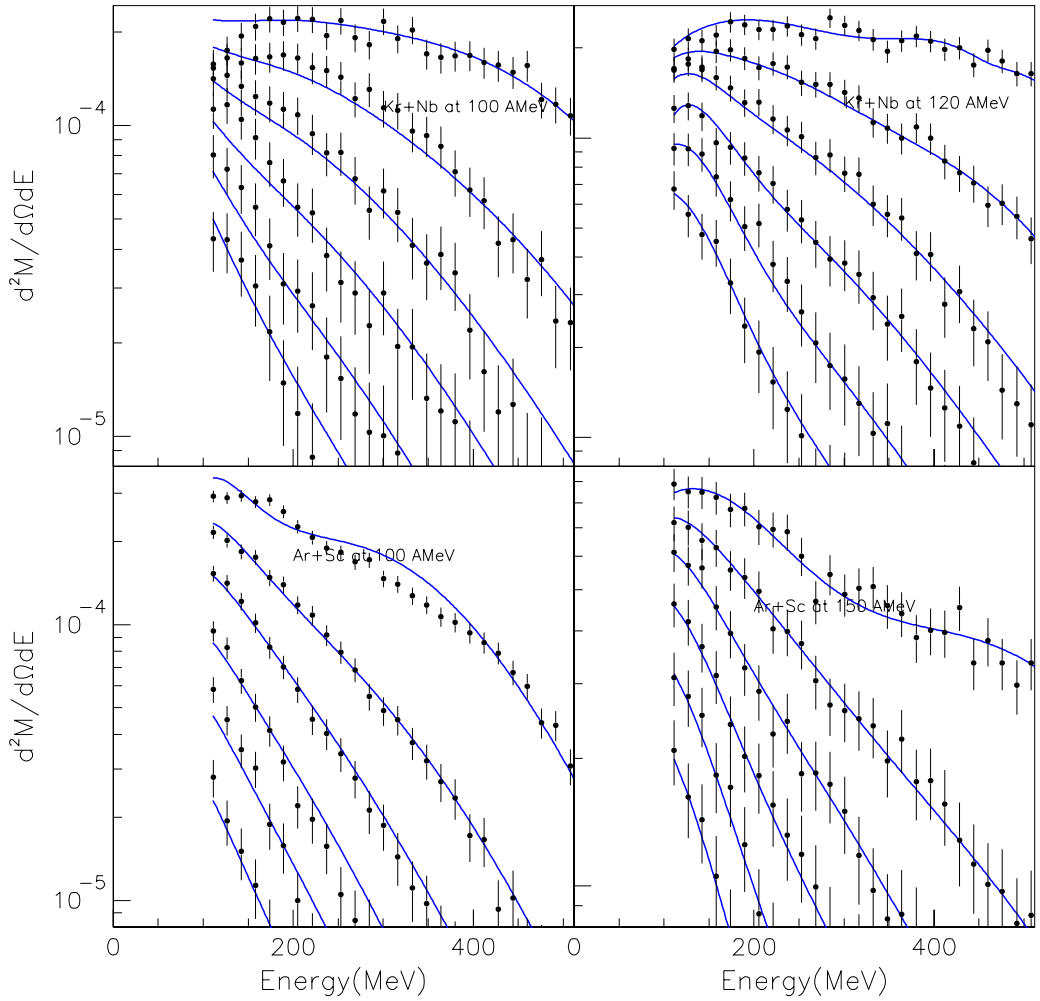

Figure 4.10: Plot of $\frac{d^2M}{dEd\Omega}$ versus Energy. A Fourier perturbed 3 source fit of ^{7}Be for ^{86}Kr+^{93}Nb at 100,120 MeV/A and ^{36}Ar+^{45}Sc at 100,150 MeV/A respectively.

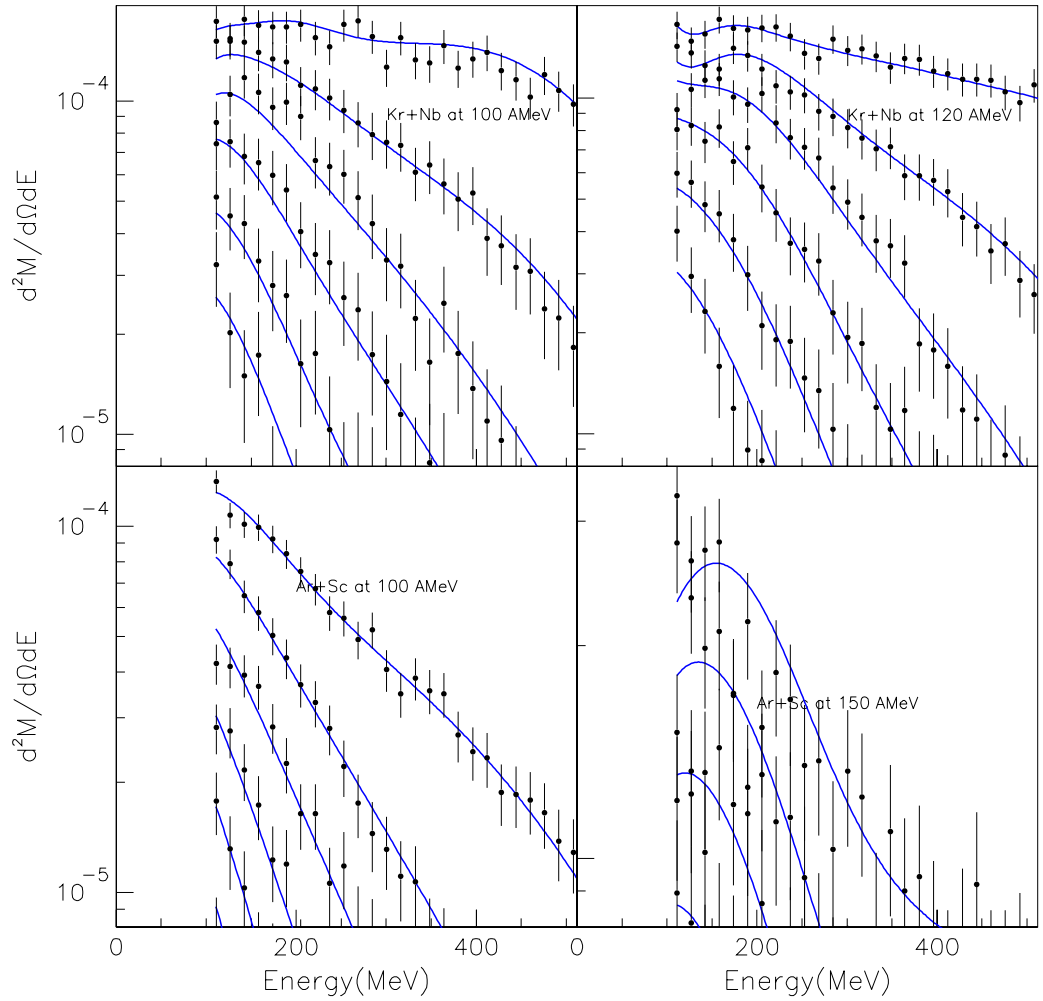

Figure 4.11: Plot of $\frac{d^2M}{dEd\Omega}$ versus Energy. A Fourier perturbed 3 source fit of ^{9}Be for ^{86}Kr+^{93}Nb at 100,120 MeV/A and ^{36}Ar+^{45}Sc at 100,150 MeV/A respectively.

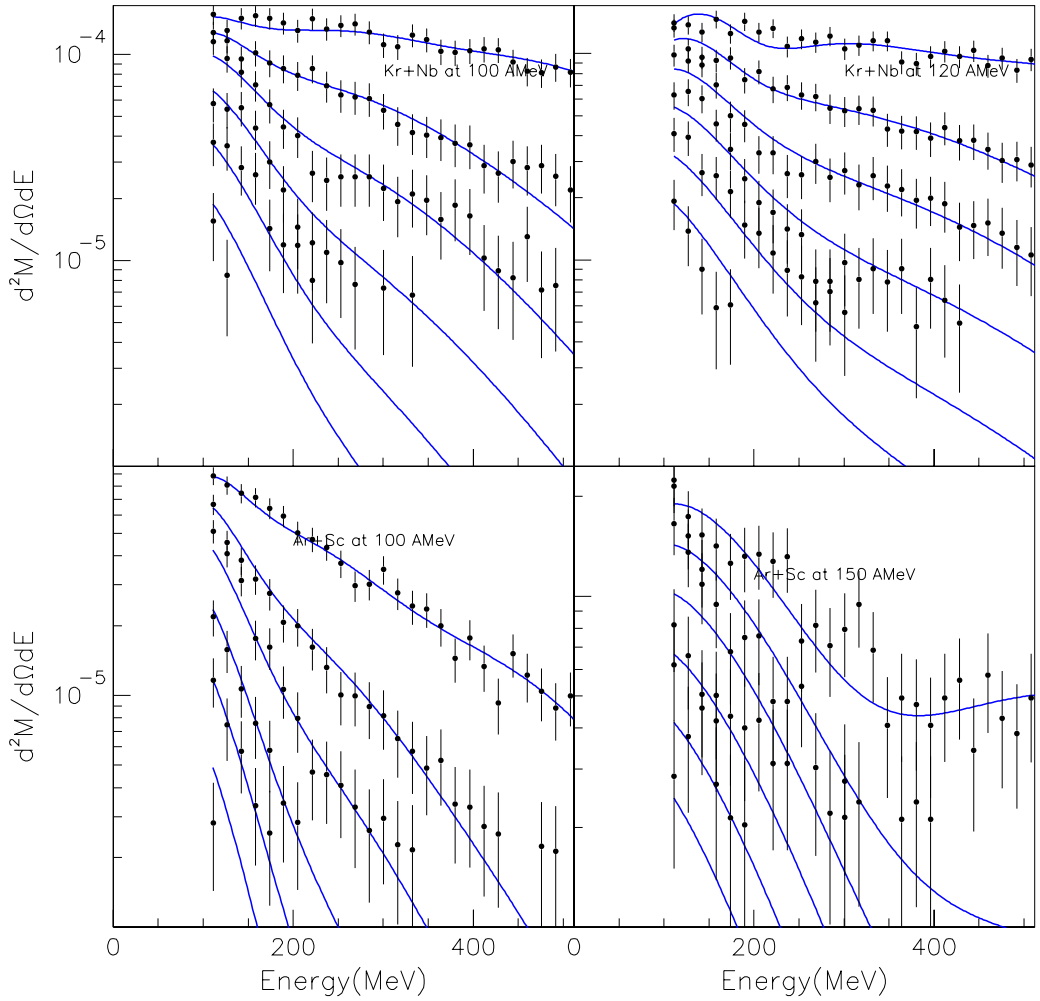

Figure 4.12: Plot of $\frac{d^2M}{dEd\Omega}$ versus Energy. A Fourier perturbed 3 source fit of ^{10}Be for ^{86}Kr+^{93}Nb at 100,120 MeV/A and ^{36}Ar+^{45}Sc at 100,150 MeV/A respectively.

Particle	System	b_{exp}(mid)	βx(sp)	βz(sp)	T_{sp}	T_{mid}	Multiplicity	Multiplicity	a_3	a_5
-	Type AMeV	-	-	-	MeV	MeV	$< M >_{sp}$	$< M >_{mid}$	-	-
^{4}He	Kr+Nb120	0.0	0.0558	0.1524	15.5217	33.7894	5.2100	1.2892	0.1187	0
^{6}Li	Kr+Nb120	0.0	0.1036	0.1274	11.5098	25.6009	1.2230	0.7078	0.03407	0
^{7}Be	Kr+Nb120	0.0	0.1137	0.1138	9.14990	47.6620	0.2793	0.2830	0.05701	0
^{4}He	Ar+Sc150	0.0	0.0000	0.1838	18.9360	37.2592	2.6070	0.2995	0.2483	0.1142
^{6}Li	Ar+Sc150	0.0	0.0000	0.1977	30.2280	37.0899	1.5546	0.1452	0.2156	0.05947
^{7}Be	Ar+Sc150	0.0	0.0748	0.1308	16.7382	40.9932	0.2482	0.0630	0.2250	0.00

Table 4.2: Single particle fit parameters using the 3 source, without central radial expansion and fourier perturbation.The asymmetric cosine coefficients a_3,a_5 are given in the table.

Because of its large number of terms, it is difficult to assess what changes in the the emission pattern Eq. 4.4 introduces that makes it better represent the data than did Eqs. 4.1 and 4.2. One way to represent this is to examine the predicted emission patterns as functions of the transverse momentum $p_\perp = \sqrt{p_x^2 + p_y^2}$ and the rapidity parallel to the beam. Figs. 4.19 and 4.20 show $d^2\langle M\rangle/pdEd\Omega$ fits for ^4He for the three source fit using Eq. 4.2 for Fig. 4.20 and the three source fit using Eq. 4.5 for Fig.4.19. In these figures, the colored region indicates the calculated yield within the experimental acceptance bounded by the solid lines and the dashed lines indicate the angular domain $70^0 \leq \theta_{CM} \leq 110^o$ over which the data were averaged to obtain the final results for data at $\theta_{CM} \approx 90^o$. Basically, these improvements in the fits resulted in a slight backward peaked anisotropy in the emission pattern reflecting the fact that the ^{93}Nb target has a charge Z that is 6 larger than that of the ^{86}Kr projectile. Figs. 4.13 through 4.18 show a similar trend for the Ar+Sc system for the beam energy of 150AMeV and for ^6Li, ^7Be and ^4He respectively.

Using these fits, accurate interpolations of the energy spectra of isotopes emitted into the angular interval $70^0 \leq \theta_{CM} \leq 110^o$ were obtained. We cross checked this approach by comparing the integration of the fitting function over this angular domain to the the average of the experimental data $\langle \frac{d^2M}{dE_{CM}\,d\Omega_{CM}} \rangle$ where

$$\langle \frac{d^2M}{dE_{CM}d\Omega_{CM}} \rangle = \frac{1}{N}\sum_1^N \frac{d^2M}{dE_{lab}d\Omega_{lab}} \frac{dE_{lab}d\Omega_{lab}}{dE_{CM}d\Omega_{CM}} \,,$$

Here the sum runs over the measured laboratory angles and energies that correspond to the given center of mass energy and over the center of mass angular interval $70^0 \leq \theta_{CM} \leq 110^o$. While the above expression has the advantage of being directly based on experiment, it can potentially lead to errors because the placement of detectors in the lab may not provide a sufficiently uniform coverage of the laboratory center of mass angular domain. Averaging the fit function over $70^0 \leq \theta_{CM} \leq 110^o$ avoids this problem.

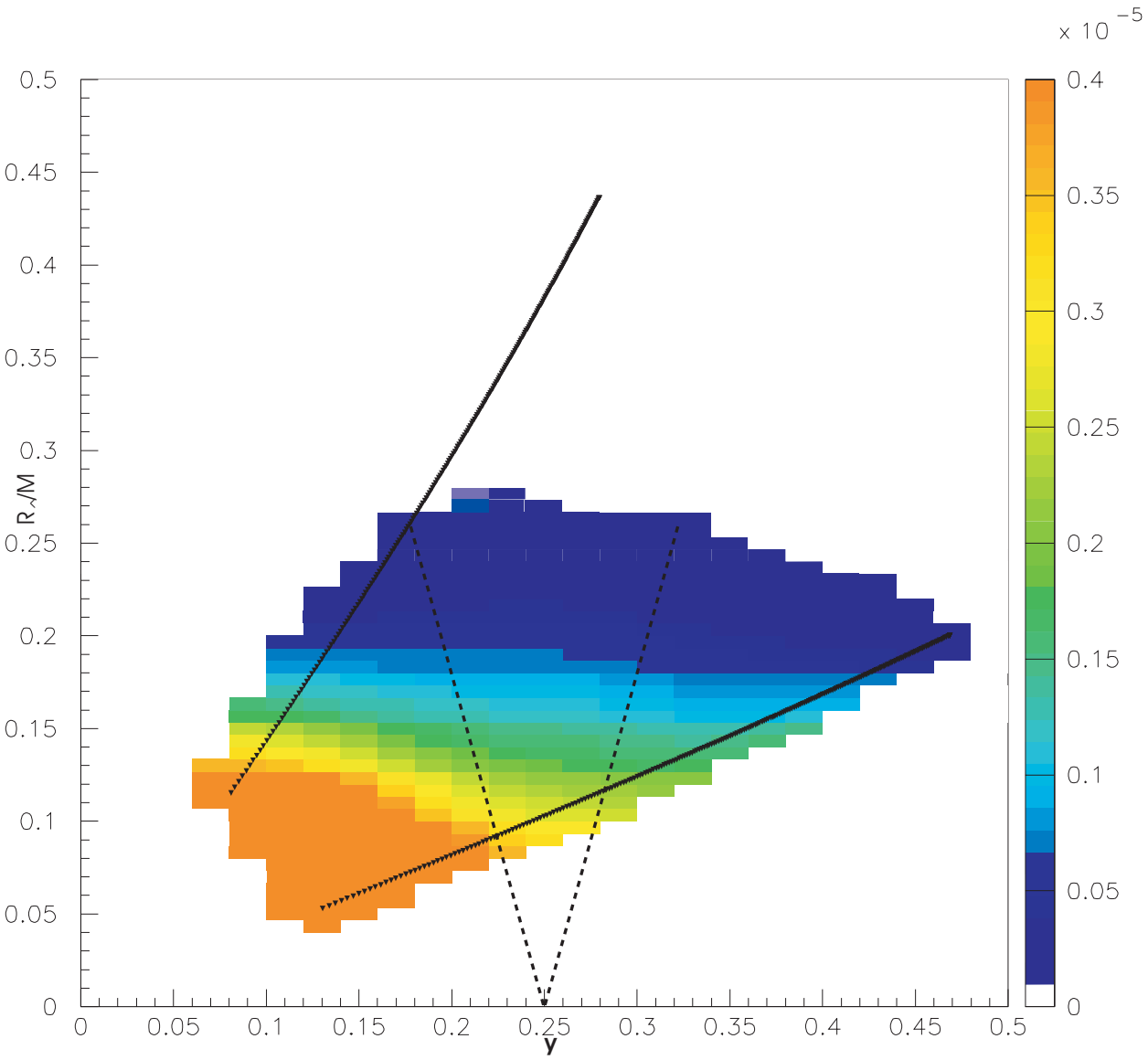

Figure 4.13: Rapidity plot of Catania acceptance region of 3 source with expanding central midsource with Fourier perturbation for ^{4}He for Ar+Sc at 150MeV. The solid lines delineate the experimental acceptance.The dashed lines correspond to the gate $70^0 \leq \theta_{CM} \leq 110^o$

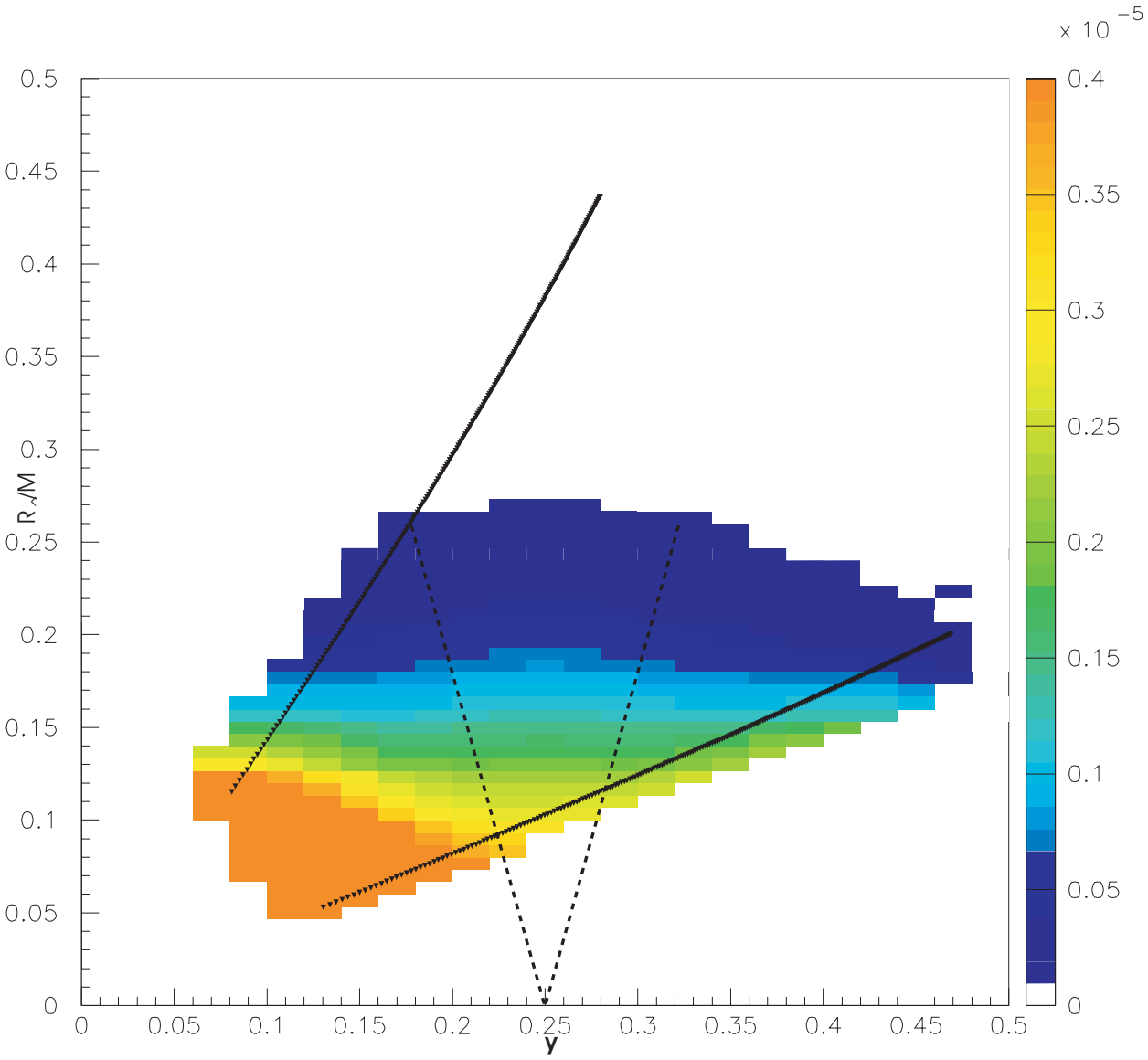

Figure 4.14: Rapidity plot of Catania acceptance region of 3 source with standard expanding central source for ^{4}He for Ar+Sc at 150MeV. The solid lines delineate the experimental acceptance.The dashed lines correspond to the gate $70^0 \leq \theta_{CM} \leq 110^o$

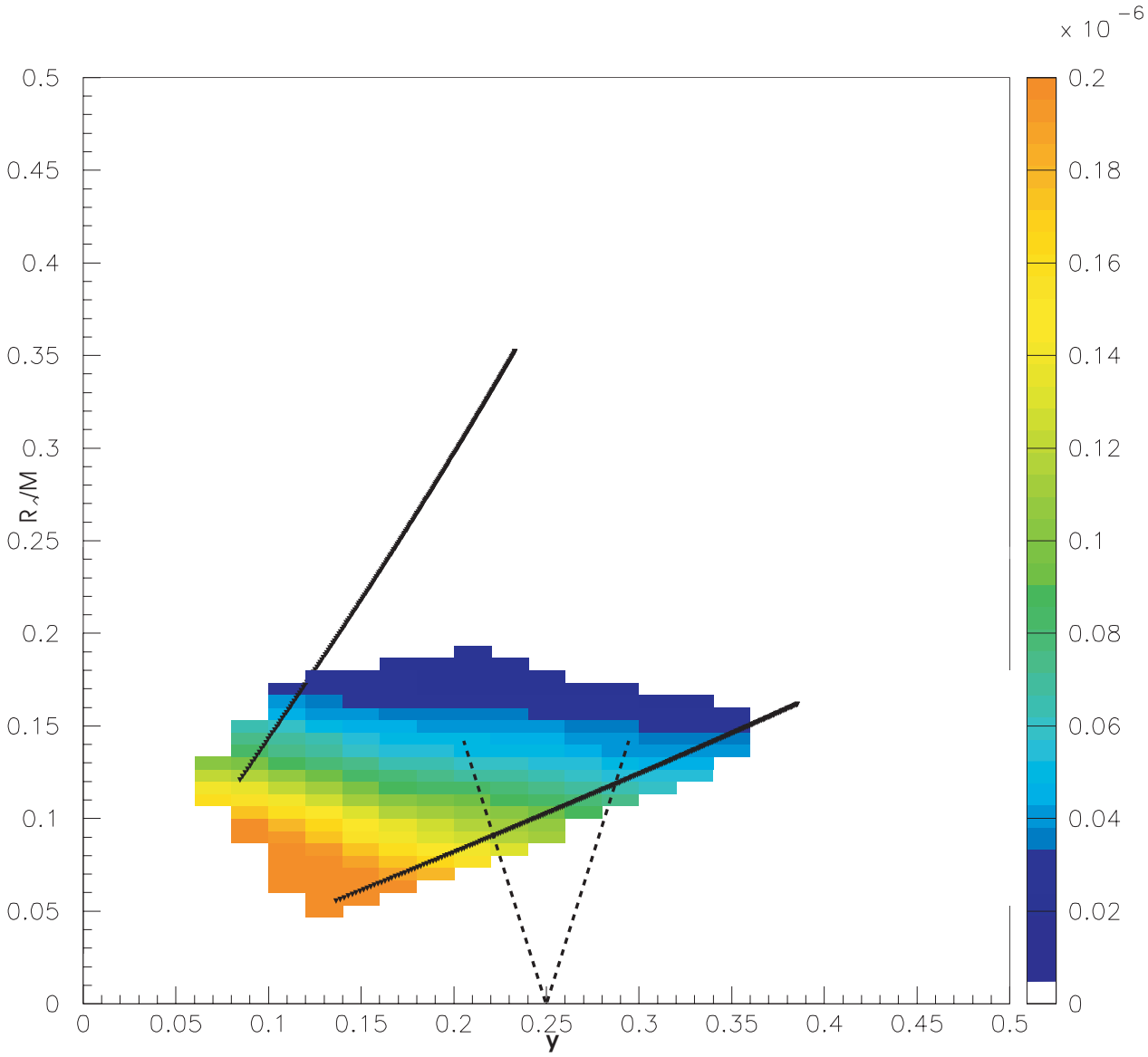

Figure 4.15: Rapidity plot of Catania acceptance region of 3 source with expanding central source with Fourier perturbation for ^{6}Li for Ar+Sc at 150MeV. The solid lines delineate the experimental acceptance.The dashed lines correspond to the gate $70^0 \leq \theta_{CM} \leq 110^o$

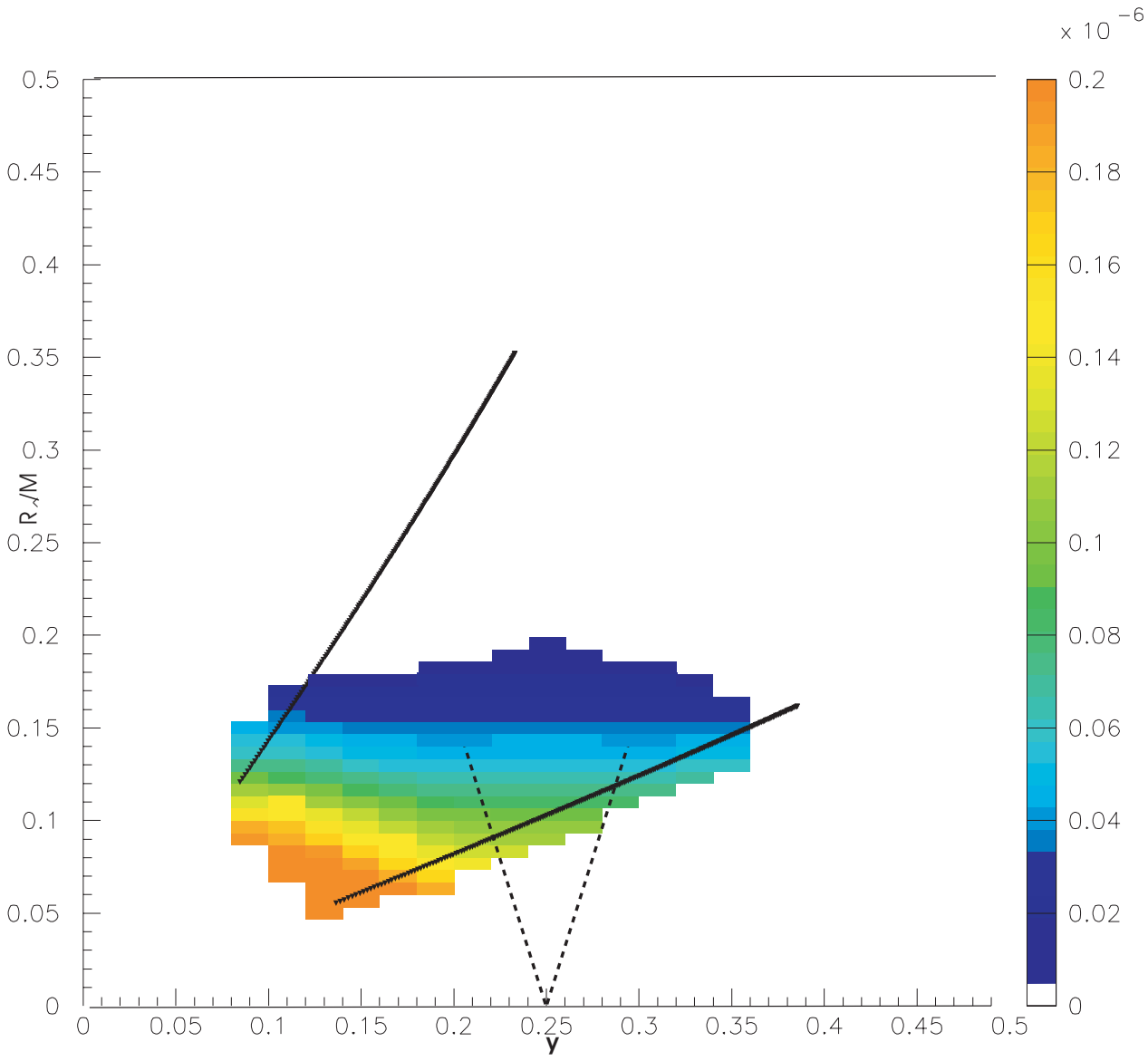

Figure 4.16: Rapidity plot of Catania acceptance region of 3 source with standard expanding central source for ^{6}Li for Ar+Sc at 150MeV. The solid lines delineate the experimental acceptance.The dashed lines correspond to the gate $70^0 \leq \theta_{CM} \leq 110^o$

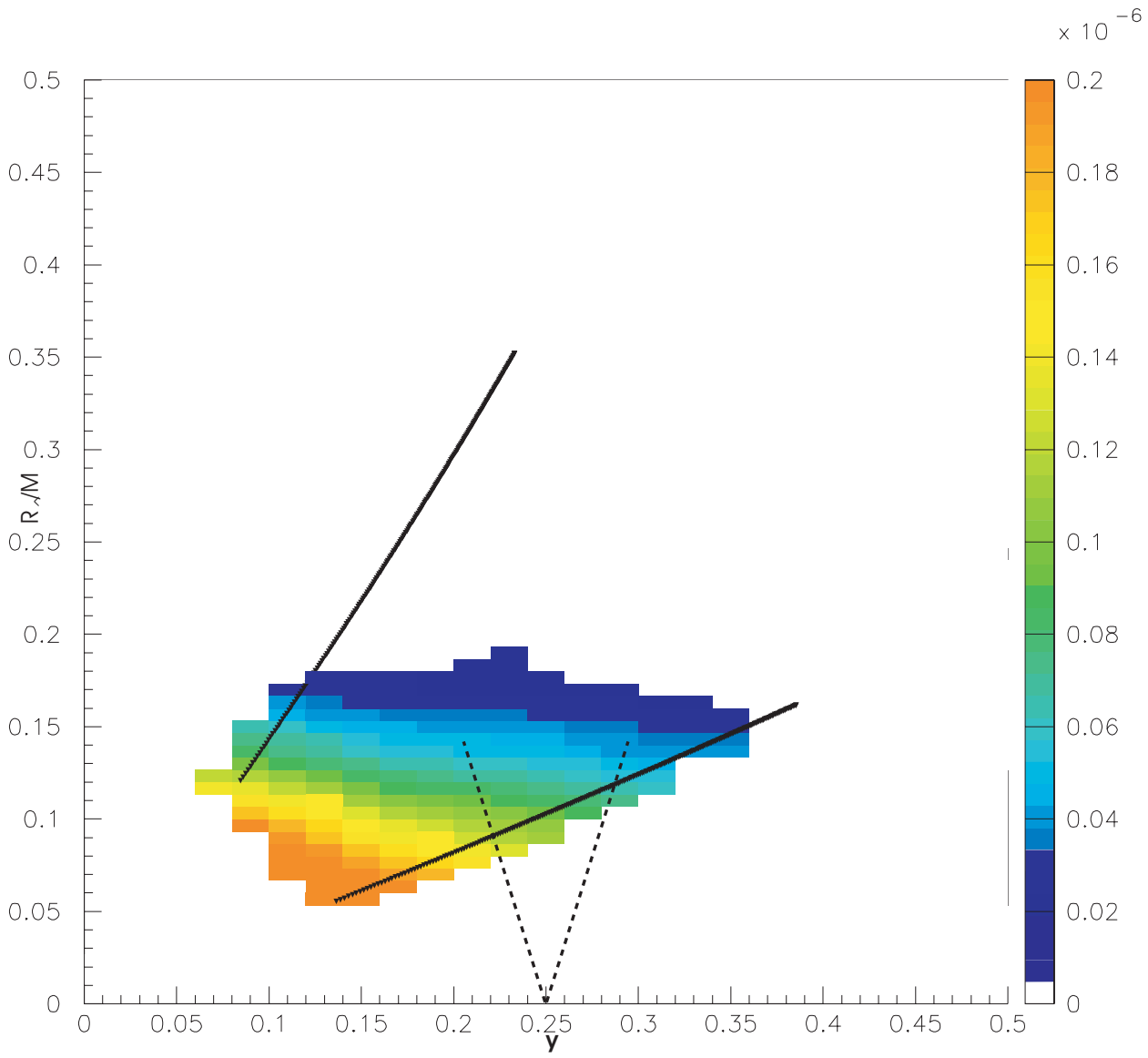

Figure 4.17: Rapidity plot of Catania acceptance region of 3 source with expanding central source with Fourier perturbation for ^{7}Be for Ar+Sc at 150MeV. The solid lines delineate the experimental acceptance.The dashed lines correspond to the gate $70^0 \leq \theta_{CM} \leq 110^o$

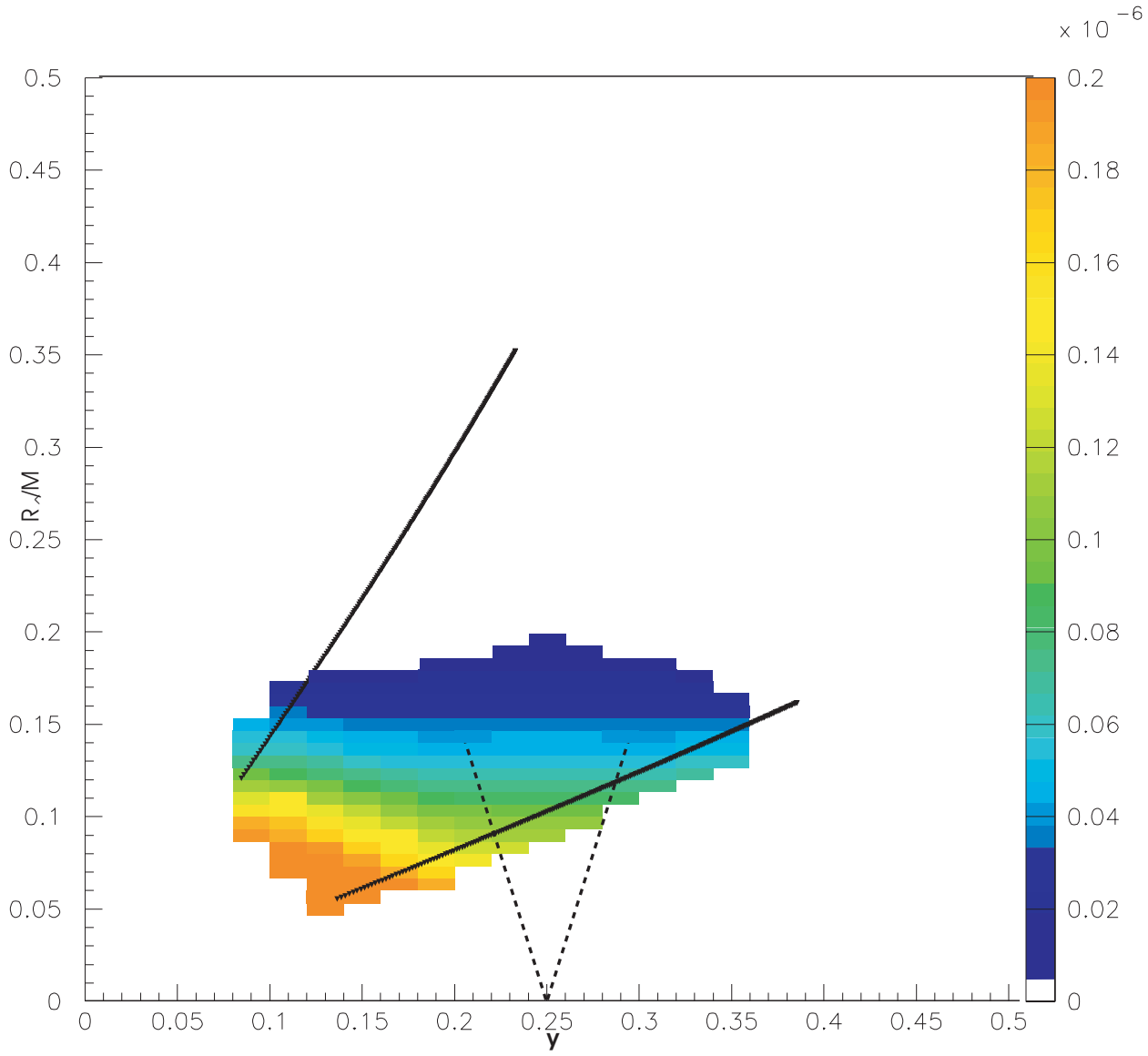

Figure 4.18: Rapidity plot of Catania acceptance region of 3 source with standard expanding central source for ^{7}Be for Ar+Sc at 150MeV. The solid lines delineate the experimental acceptance.The dashed lines correspond to the gate $70^{0} \leq \theta_{CM} \leq 110^{o}$

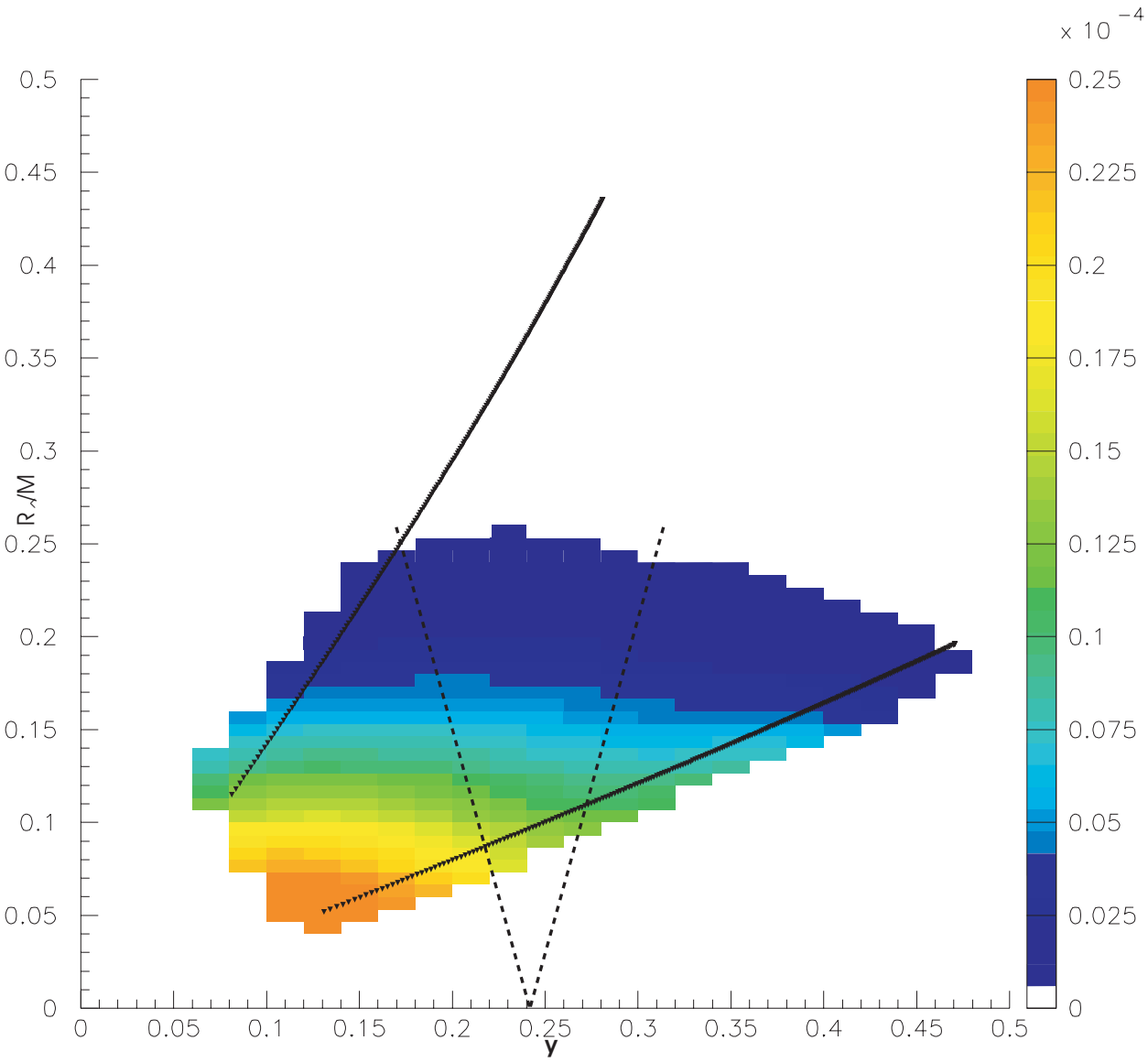

Figure 4.19: Rapidity plot of Catania acceptance region of 3 source with expanding central source with Fourier perturbation for ^{4}He for Kr+Nb at 120MeV. The solid lines delineate the experimental acceptance.The dashed lines correspond to the gate $70^0 \leq \theta_{CM} \leq 110^o$

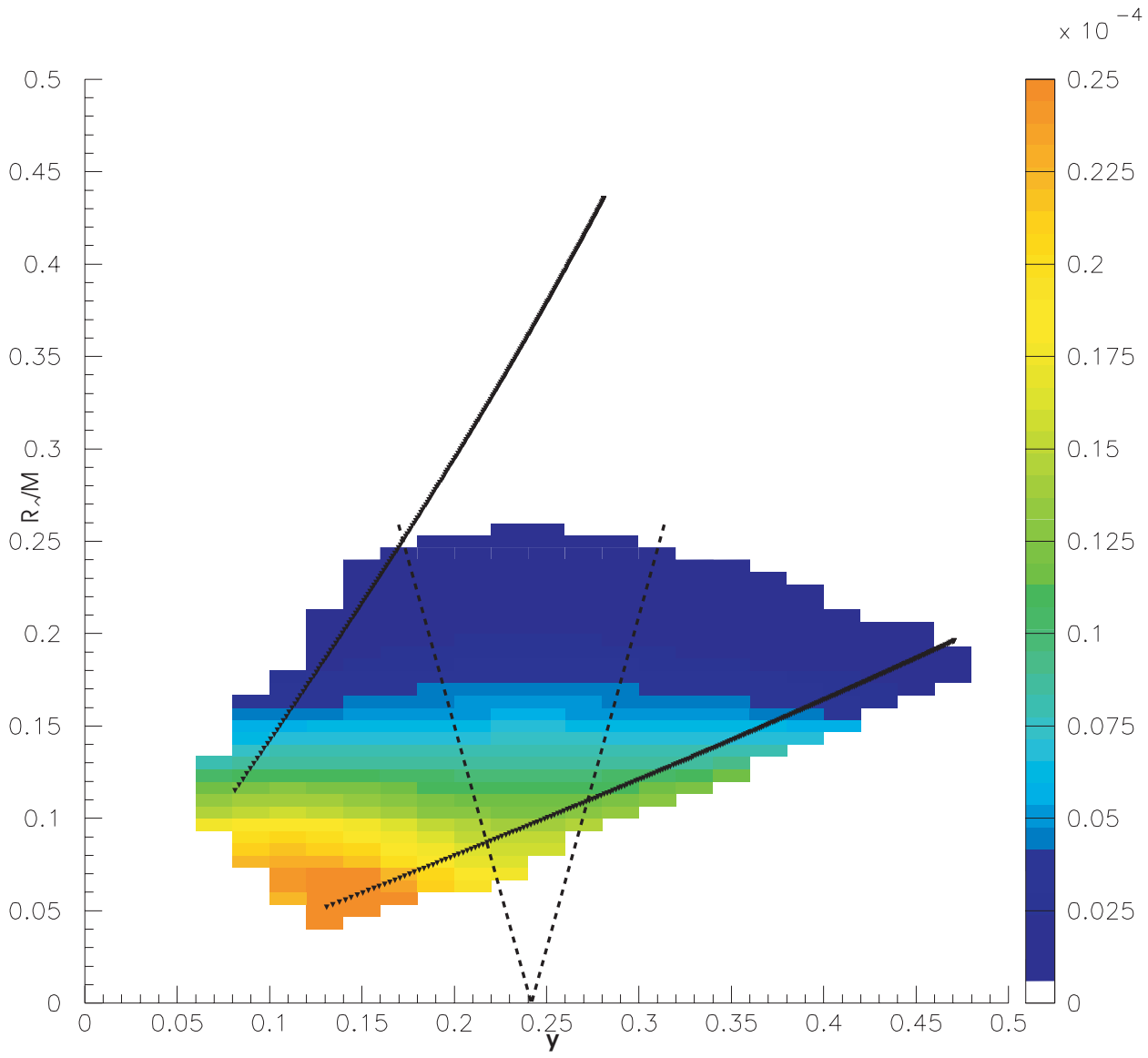

Figure 4.20: Rapidity plot of Catania acceptance region of 3 source with standard expanding central source for ^{4}He for Kr+Nb at 120MeV. The solid lines delineate the experimental acceptance.The dashed lines correspond to the gate $70^0 \leq \theta_{CM} \leq 110^o$

Figure 4.21 shows a comparison between the average of the experimental data (points) and the average of the fitting function (curve)for ^4He. This curve is plotted in red for $E/A > 5$ MeV and in green for $E/A < 5$ MeV. Above $E/A = 5MeV$, where the two procedures can be directly compared, they agree within the statistics of the averaged data. We conclude that the integration of the fit is at least as accurate as the average of the experimental data and therefore use it to extract the average experimental differential multiplicities over $70^0 \leq \theta_{CM} \leq 110^o$. Both are limited by the statistical accuracy of the data and by the accuracy $\pm 5\%$ of the experimental particle identification gates. We estimate these uncertainties and combine them to obtain the uncertainties in the differential multiplicities we provide below. We note that the experimental acceptance of the device covers $E_{CM}/A > 5MeV$, but that the yields at lower CM energies have significant systematic uncertainty. In the following, we will apply an energy threshold $E_{CM}/A > 5$ MeV to many of the quantities we extract from the experimental data.

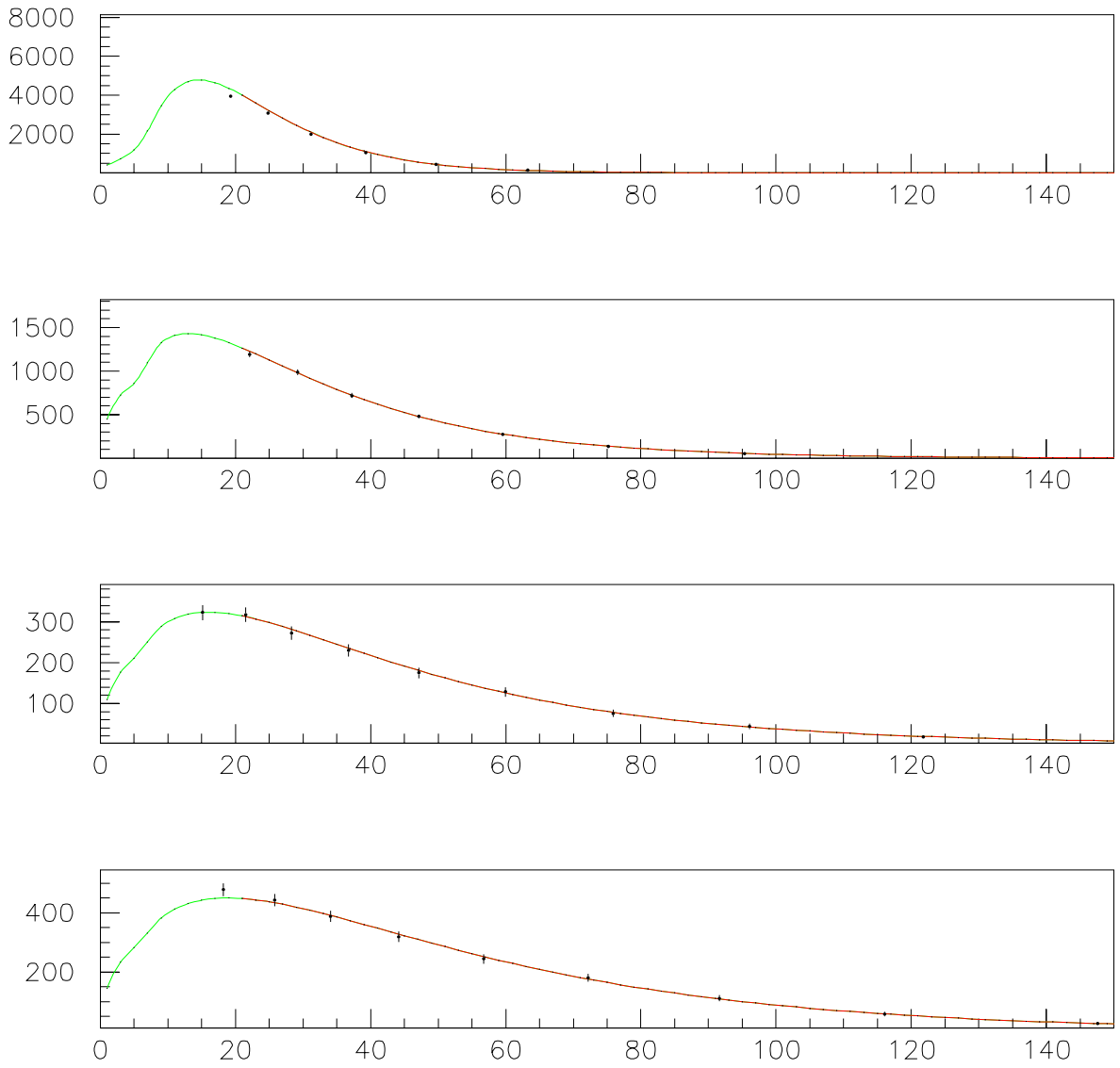

Figure 4.21: CM spectra of counts versus energy for Kr+Nb, $(E)_{beam}$=35-120 A/U. using asymmetric parameterization source model, the yield is obtained integrating from 5A(MeV) to ∞ .

4.3 Isotopic Temperatures and Isoscaling Parameterizations

4.3.1 Extraction of Isotopic Temperatures

Transforming the fits of the energy spectra to the center of mass and integrating over energy for an angular cut of $70^0 \leq \theta_{CM} \leq 110^o$, we can obtain integrated multiplicities for the participant source. Dividing by the solid angle corresponding to this angular cut, we obtain the average differential multiplicities $\langle |dM(\theta_{CM} \approx 90^o)/d\Omega|_{CM} \rangle$.

From these differential multiplicities, one can form double isotopic ratios and extract isotopic temperatures as discussed in Section 3.1. First, we utilize multiplicities obtiained by integrating over energies of $E_{CM}/A \geq 5MeV$ where the experimental information is more complete. We have tried to extrapolate these values for $E_{CM} = 0$, but have concluded that such extrapolation introduces unacceptable contributions to the uncertainties of the integrated yields due to uncertainties in extrapolating the yields from the projectile and target spectators and there are also effects of cooling on the energy spectrum to energies below the experimental thresholds.

The isotopic yields of fragments depends directly on their binding energies and, for equilibrated systems, upon the temperature and isotopic composition of the fragmenting system. Within equilibrium models of nuclear multifragmentation, temperatures can be obtained via Eq. 4.5 [3, 49] from the ratios of yields neighboring isotopes prior to secondary decay :

$$\frac{Y(A_1, Z_1)/Y(A_1 + 1, Z_1)}{Y(A_2, Z_2)/Y(A_2 + 1, Z_2)} = \frac{1}{a} \exp(B/T_{iso}) \tag{4.5}$$

where $Y(A_i,Z_i)$ is the yield for the isotope with mass A_i and charge Z_i , a is a statistical factor determined by spin values and kinematic factors , $B = E_B(A_1,Z_1)$- $E_B(A_1+1,Z_1)$- $E_B(A_2,Z_2)+E_B(A_2+1,Z_2)$, and $E_B(A_i+1,Z_i)$ is the binding energy of

the i th nucleus. Temperatures may be obtained from the yields by inverting Eq. 4.5.

Feeding of the measured yields from the secondary decay of heavier particle unbound nuclei alters these ratios and consequently, the extracted temperature values. The influence of feeding can be reduced by focusing upon ratios with a very large binding energy difference B. In practical terms, this requires the incorporation into the double ratio of a single ratio involving either $^{3}He/^{4}He$, $^{11}C/^{12}C$ or $^{15}O/^{16}O$ as these are the only ratios involving neighboring light isotopes that have binding energy differences significantly greater than 10 MeV.

While insufficient carbon and oxygen isotopes penetrate the silicon ΔE counters of the Catania array to allow analyses, we are able to analyze double isotopic ratios involving the $^{3}He/^{4}He$ ratio over a large acceptance using the Catania array. In Figs. 4.22 and 4.24, we show values for the isotopic temperature obtained for central Kr+Nb and Ar+Sc collisions from the $pd/^{3,4}He$, $dt/^{3,4}He$, $^{6,7}Li/^{3,4}He$, $^{7,8}Li/^{3,4}He$, and $^{9,10}Be/^{3,4}He$ isotopic ratios using Eq. 4.5 with the values for a and B given in table 4.3 corresponding to the spin degeneracy factors and binding energies appropriate to the fragments in their ground states. All of these ratios increase with incident energy consistent with a monotonic increase in excitation energy per nucleon.

At the incident energy of 100A MeV where both systems have measurements, the isotope ratio temperatures obtained in the Ar+Sc are consistently higher than the temperatures obtained in the Kr+Nb system even though the uncertainties are large. We note that a dependence of isotopic temperatures on the system size has been reported previously [80].

There is a big difference between the temperatures obtained for the various double ratios via Eq. 4.5 as shown in figures 4.22 and 4.23. Such differences have been attributed to the secondary decay of heavier particle unstable fragments. Such decays enhance the yields of nuclei that are included in the relevant double ratio. Such decays

modify the relationship between the double ratio and the temperature away from that given in Eq. ref 4.5. In ref [111] it was proposed that one can model the correction for secondary decay by assuming that it can be described by Eq. 4.5 but with a different value for a. Because we do not have a good model independent description for the hot primary fragments, we adopt this approach instead of theoretically calculating the secondary decay directly as done by ref. [140, 104, 50]. Specifically, this approach stipulates that the temperature T_{em} can be obtained from the T_{iso} value provided by Eq. 4.5:

$$\frac{1}{T_{em}} = \frac{1}{T_{iso}} - \frac{ln\kappa}{B}\,, \tag{4.6}$$

where κ is an empirical correction factor. Figs. 4.23 and 4.25 show values for T_{em} obtained from the values for T_{iso} shown in Figures 4.22 and 4.24 using the empirical correction factors in Table 4.3 [117]. The resulting values for T_{em} still display an increase with incident energy, but the variations between the corrected temperatures T_{em} for different isotope ratios are much smaller than for T_{iso}. The slope of energy dependence of the corrected temperatures, T_{em}, is larger for the Ar+Sc system Figure 4.25 than for the Kr+Nb system Figure 4.23. From the heavy ion telescopes, some analyses would be performed involving the $^{11}C/^{12}C$ ratio. The $^{15}O/^{16}O$ ratio would not be analyzed as the statistics were insufficient. Results obtained from the $^{11,12}C/^{6,7}Li$ double isotope ratio are indicated in Figures 4.23,4.25 by the square points. Interestingly, these latter points do not increase as strongly with incident energy as do the temperature values obtained from the $pd/^{3,4}He$, $dt/^{3,4}He$, $^{6,7}Li/^{3,4}He$, $^{7,8}Li/^{3,4}He$, and $^{9,10}Be/^{3,4}He$ double isotope ratios. These latter ratios fundamentally derive their sensitivity to temperature from the large binding energy difference between ^{3}He and ^{4}He. If the carbon and helium isotopes extracted from the same region at the same time, the system is not in equilibrium or there are significant problems with the method of isotopic thermometry. On the other hand, helium and

carbon isotopes originate from different regions or they are emitted at different times, one would expect that they would emit at different temperatures. This latter possibility appears likely. In the following two sections, we first examine whether the light particle yields are consistent with them being emitted along with the heavier fragments from a globally equilibrated system. Then we examine whether the yields themselves are consistent with emission from subsystems in local thermal equilibrium, an assumption upon which the validity of isotopic thermometry strongly depends.

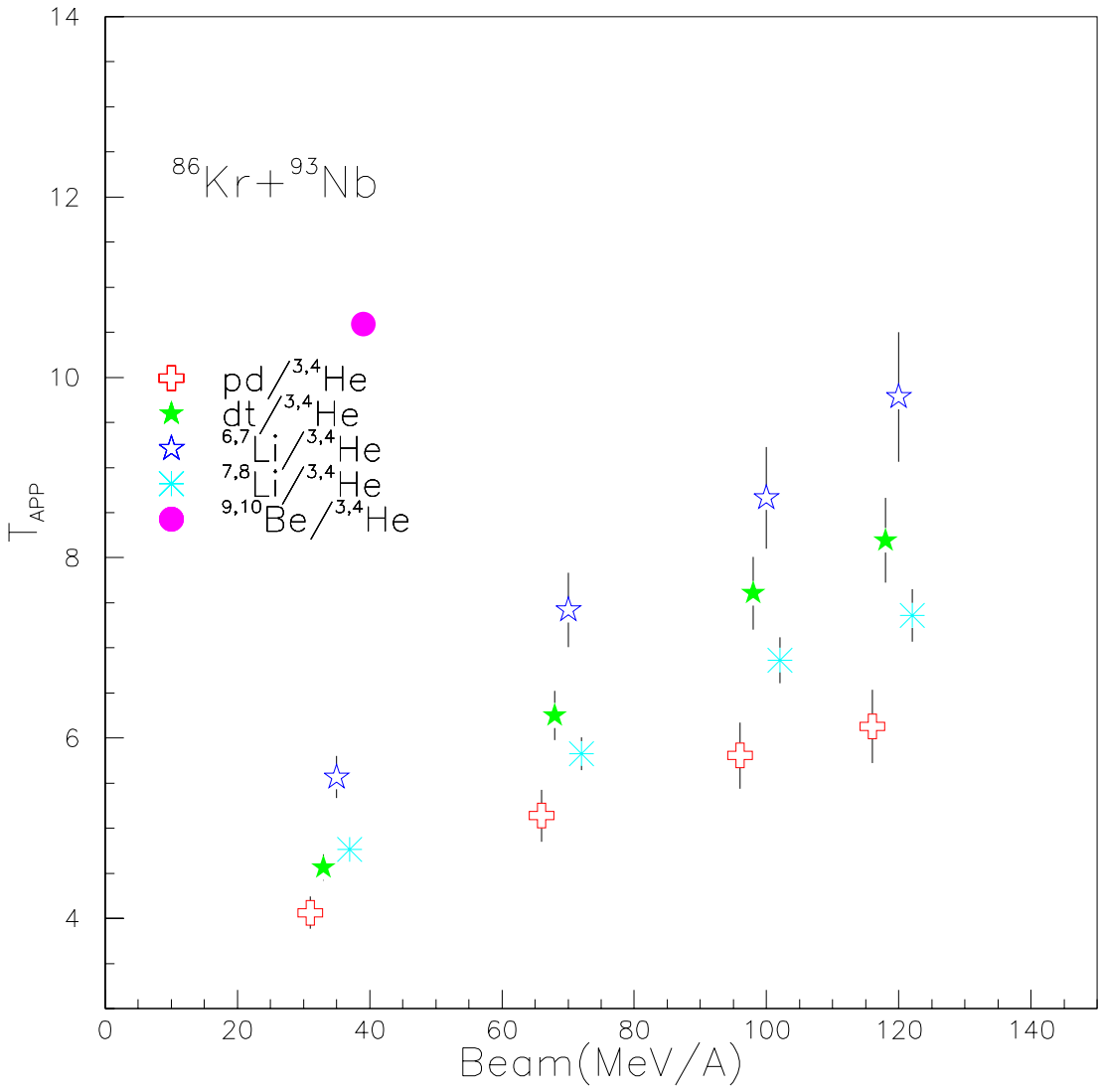

Figure 4.22: Apparent isotope temperatures for Kr+Nb $(E)_{beam}$ 35-120 A/U, obtained by inverting eq 4.7 with the extracted yields from 5A(MeV) to ∞ as input. Error bars include PID error on neighboring isotopes.

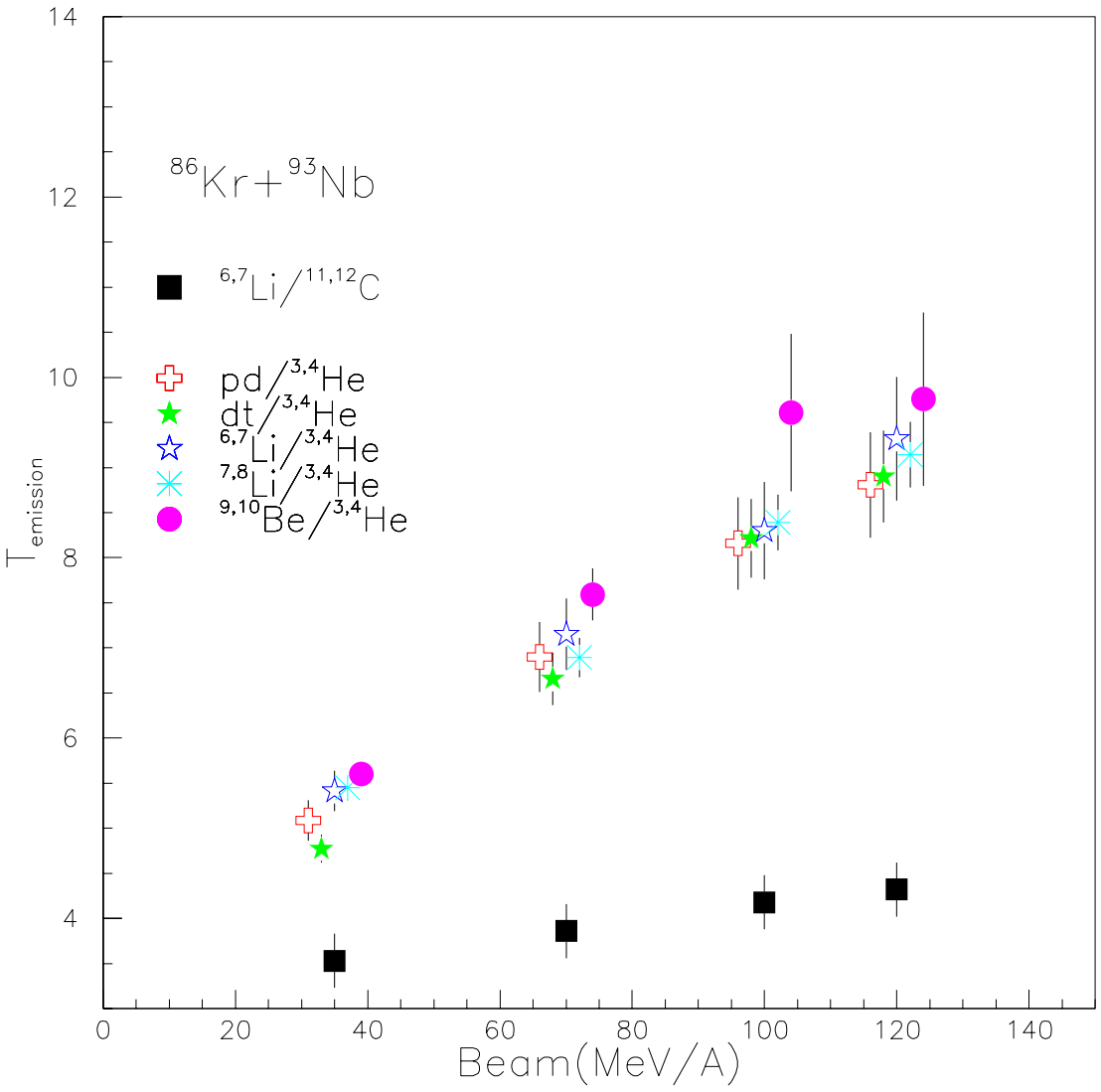

Figure 4.23: Emission temperatures for Kr+Nb $(E)_{beam}$ 35-120 A/U. using the asymmetric parameterization source model and yield extracted from 5A(MeV) to ∞ Error bars include PID error on neighboring isotopes.

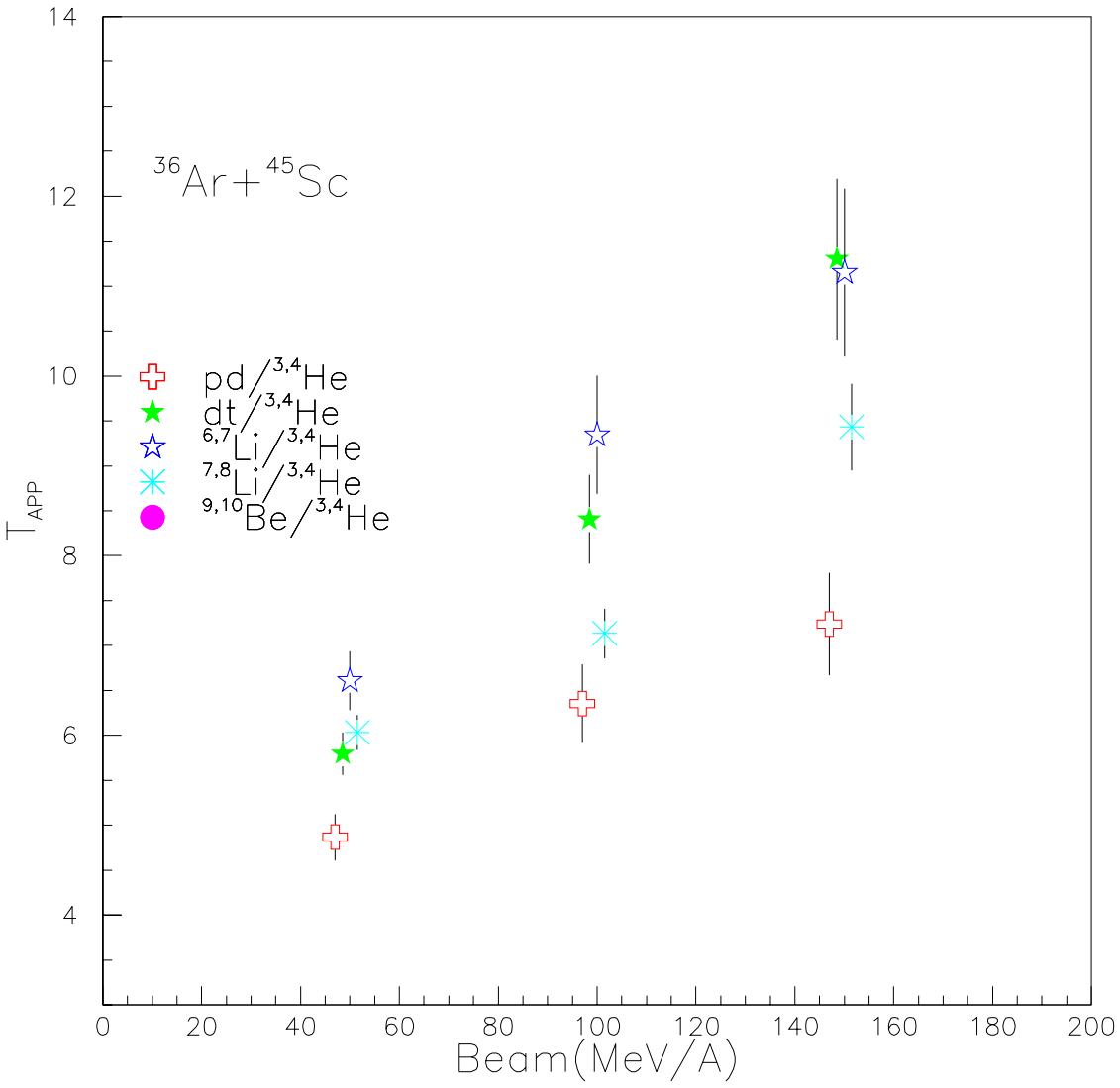

Figure 4.24: Apparent isotope temperatures for Ar+Sc $(E)_{beam}$ 50-150 A/U, obtained by inverting eq 4.7 with the extracted yields from 5A(MeV) to ∞ as input. Error bars include PID error on neighboring isotopes.

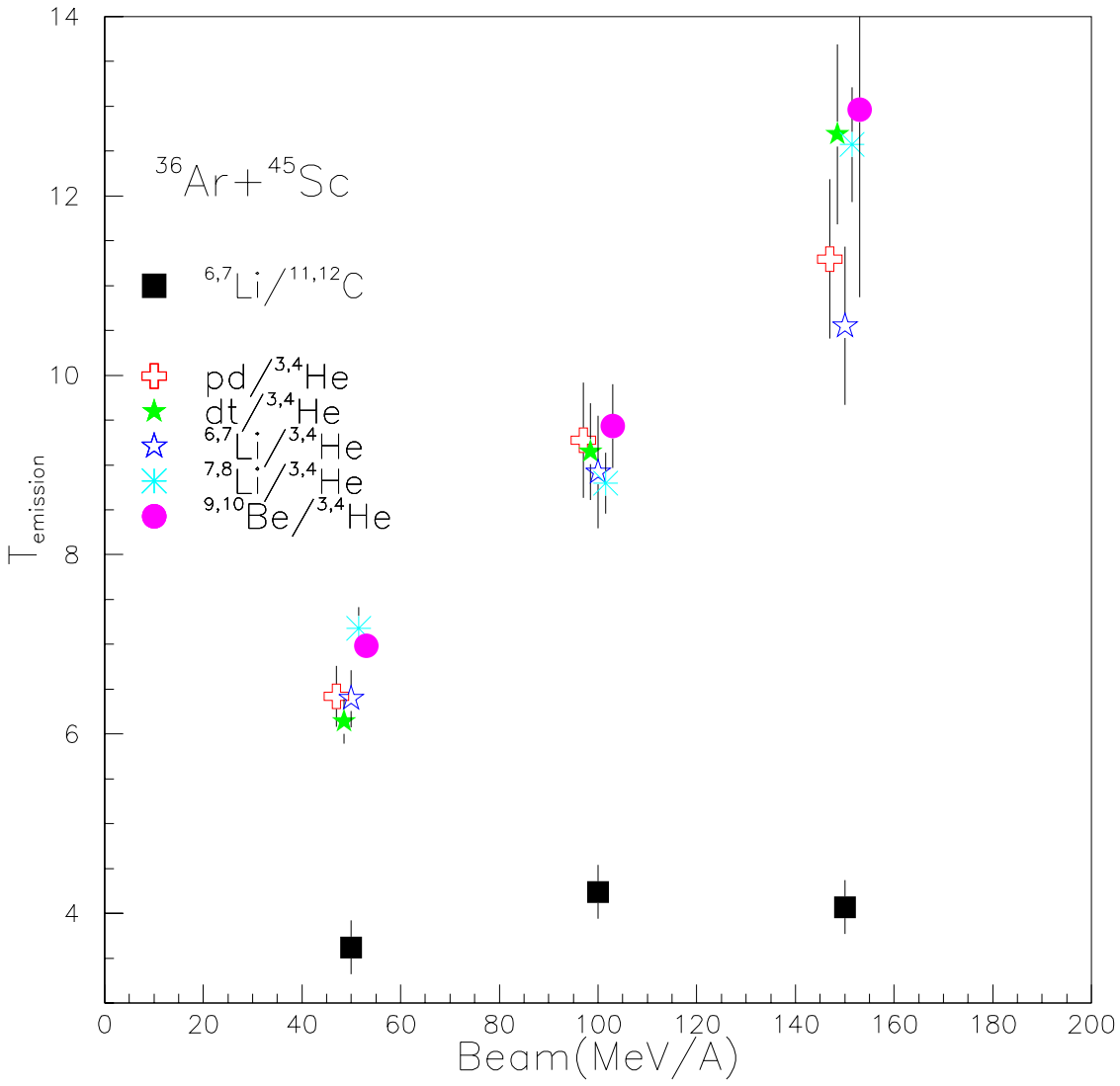

Figure 4.25: Emission temperatures for Ar+Sc $(E)_{beam}$ 50-150 A/U. using the asymmetric parameterization source model and yield extracted from 5A(MeV) to ∞ Error bars include PID error on neighboring isotopes.

4.3.2 Comparisons with Equilibrium Multifragmentation Models

Two assumptions underly the caloric curve analyses of ref [91] First one assumes that the emitting system is equilibrated at the time that the intermediate mass fragments are emitted. Second, one assumes that the various yields entering the Albergo thermometer expression Eq. 4.5 are emitted at the same time, from the same region and described by the same temperature as describes the fragment observables.

Concerning the relevance of a equilibrium description of fragmentation process, we note that comparisons of the Statistical Multifragmentation Model (SMM) calculations to experimental data have widely been performed. This model assumes that equilibrium is achieved and predicts that multifragmentation occurs as the result of a low density phase transition in nuclear matter from a fermionic liquid to a gas. Good agreement between SMM calculations and the measured Intermediate Mass Fragment (IMF) charge distributions, multiplicities and energy spectra can be obtained for SMM source parameters that are carefully chosen [97, 30, 113]. On the other hand, comparisons with data reveal that, the optimal choices for the mass, charge and excitation energy of the equilibrated source become progressively less than the mass, charge and available excitation energy of the total system as the incident energy is increased [135, 50, 3]. This suggests that progressively more nucleons are emitted by preequilibrium mechanisms prior to the freezeout stage described by SMM. Similar problems have been also observed for peripheral collisions [30, 97]. These prior studies suggest that one cannot describe the emission of all particles in a common bulk multifragmentation approach.

When one applies equilibrium approaches to the fragmentation process, it is generally assumed that the missing mass, charge and excitation energy is carried away primarily by emitted preequilibrium light particles and not by the IMF's [30, 97, 113,

135, 3]. Such assumptions allow comparisons of IMF observables to SMM calculations but such comparisons become especially suspect when they rely heavily upon the light particle observables as well. Temperature measurements that rely heavily upon ratios of the yields of Helium isotopes may suffer from this problem [3, 140, 75]. Quantitative analyses of such data must account for the influence of preequilbrium light particle emission as well as for other time dependent radiative and expansive cooling mechanisms [43, 91, 98, 142].

In the following, we investigate whether light cluster production in Kr + Nb central collisions at 70, 100 and 120 AMeV is consistent with an equilibrium picture that assumes simultaneous emission of light clusters and heavy fragments. Previous measurements with this system have revealed that fragment multiplicities are larger in central collisions, where they increase with incident energy [114]. Fragmentation occurs over a short time scale [115, 99]; with many features well described by "instantaneous" bulk multifragmentation models [114, 21]. Nontheless, rapid sequential decay processes cannot be definitively ruled out provided that such processes occur within a time scale of the order 70 fm/c [115, 99]. For such short time scales, however, the distinction between sequential and "instantaneous" bulk multifragmentation becomes somewhat semantic. While many features of the multifragment final state are well described by equilibrium at a single freezeout density and temperature, we have shown in the previous subsection that the temperatures extracted from the relative isotopic abundances of helium and lithium isotopes greatly exceed those extracted from the relative isotopic abundances of somewhat heavier ^{12}C isotopes [75].

Here, we reexamine this discrepancy and make detailed comparisons with statistical and dynamical calculations in order to assess whether light particle and IMF emission in energetic central nucleus-nucleus collisions can be self consistently described within a single freezeout picture. We concentrate on light clusters emitted

to center of mass angles of $70^o \leq \theta_{CM} \leq 110^o$ from the "participant" region, and compare these data to statistical models.

The data points in Fig. 4.26 correspond to the observed values for at $\theta_{CM} = 90^o$ for d, t, ^{3}He and ^{4}He particles and two gates on the impact parameter. Consistent with the trends deduced from inclusive data [40], the extracted d, t and ^3He multiplicities increase with beam energy over this energy range while multiplicity of ^4He decreases slightly. This difference in the trends for d, t and ^3He relative to that for ^4He can be better displayed by the ratios of the yields for d, t and ^3He divided by that for ^4He. This is shown in Figure 4.27.

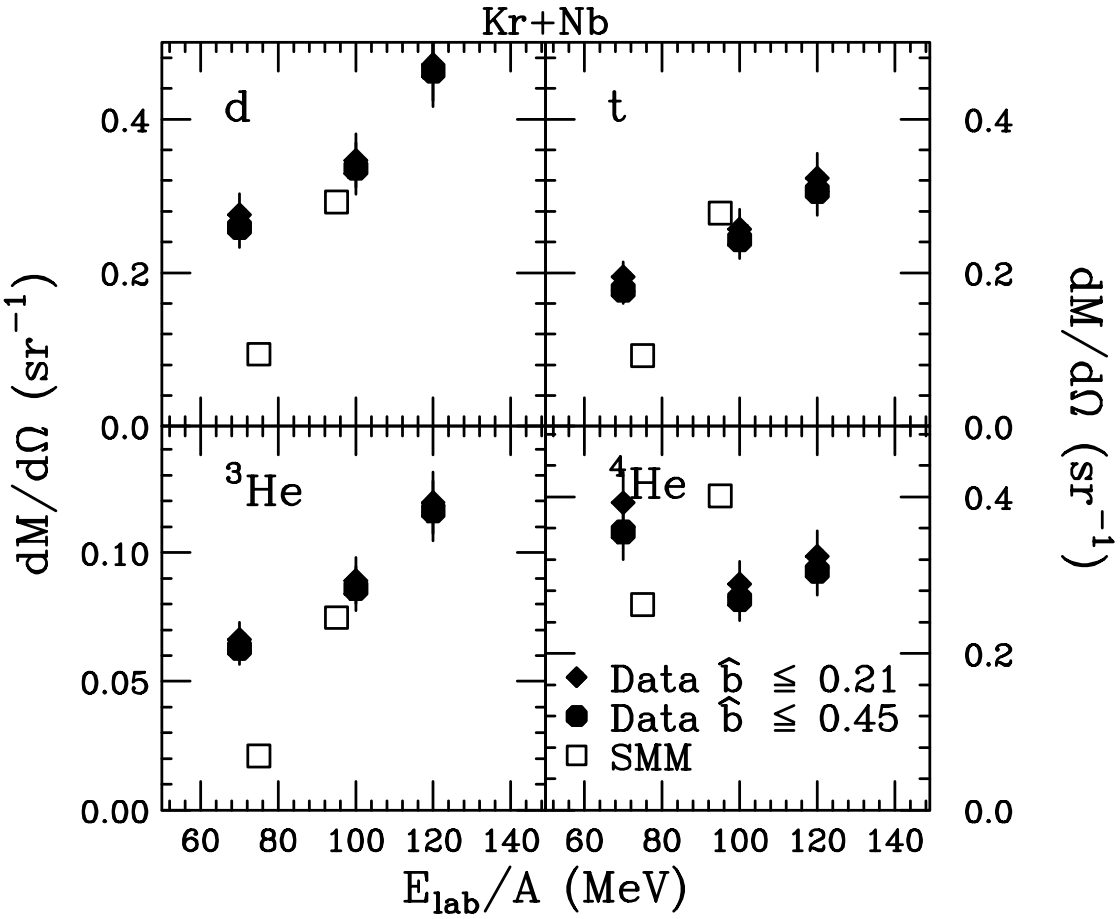

Figure 4.26: LCP Multiplicity vs Beam Energy. .

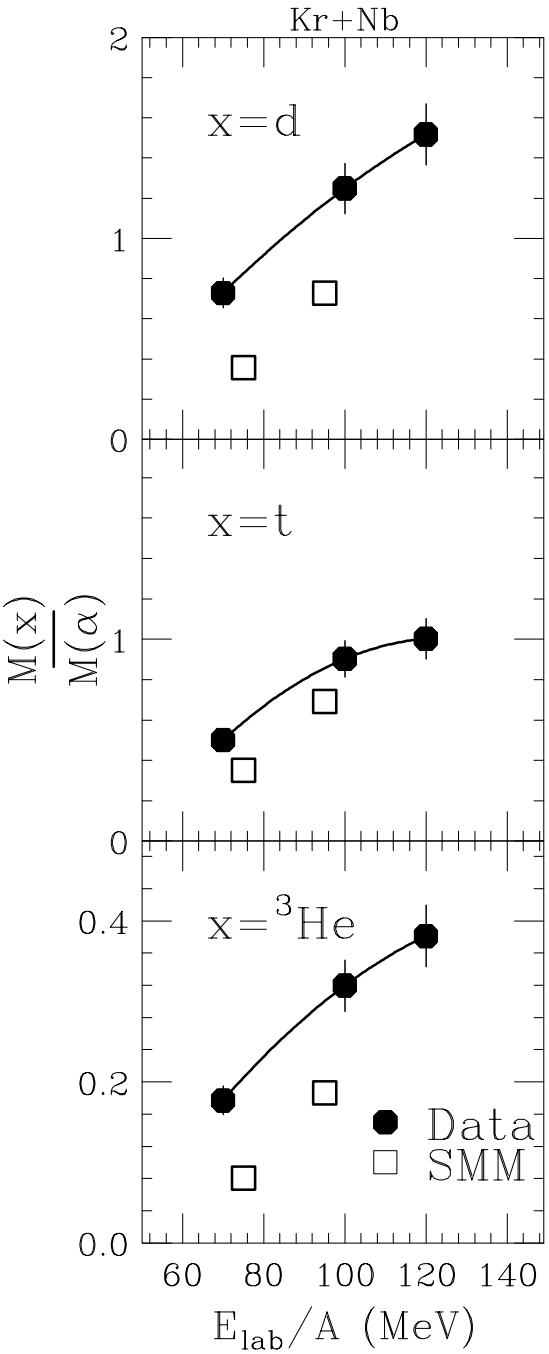

Figure 4.27: Ratio of Light Charged Particle Multiplicity to 4He. .

We now consider how well such differential multiplicities can be self consistently described within a statistical model assuming a single freezeout picture. For this illustration, we consider the Statistical Multifragmentation Model (SMM) which has been widely used to describe the emission of intermediate mass fragments (IMF's) at intermediate energies. In a typical SMM calculation, the emission of light particles and IMF's is calculated by assuming an equilibrated breakup configuration at density of about 1/3 to 1/6 saturation nuclear density [30, 113, 135, 3].

Some reductions in the size and excitation energy of the equilibrated system below the values characteristic of the total system in its center of mass are frequently assumed in such calculations to account for the mass and energy removed by non-equilibrium emission prior to breakup [30, 97, 113, 135, 3, 50]. Following refs. [135, 3], we adjust the excitation energy of the source by a multiplicative factor F_E to reproduce the previously measured IMF charge distribution and adjust the source nucleon number by a multiplicative factor F_A to reproduce the previously measured IMF multiplicity. We further assumed values for the radial flow energy given by 3.5MeV/A(Kr+Nb 75MeV/A) and 6.5MeV/A(Kr+Nb 95MeV/A) consistent with the systematics of [135].

Fig. 4.28 shows a comparison between the angle integrated experimental charge distribution for $3 \leq Z \leq 18$ measured by ref. [114] at 75 AMeV (solid points) and the charge distribution provided by the SMM calculation after correction for the acceptance of the experimental device (histogram). Fig. 4.29 shows the comparison at E/A=95 MeV. The corresponding values for F_E and F_A, given in the figure, were obtained by a least squares minimization procedure. Contours of constant χ^2 as functions of F_E and F_A are shown in Figures 4.30 and 4.31, where the upper panels are the actual χ^2 contours and the lower panels are parabolic fits to the contours that are used to determine the sensitivity of the fits to F_E and F_A and estimate the

uncertainties in those quantities. From these sensitivity analyses, we find that the source size is poorly determined with an uncertainty of the order of 20 percent for $F_A = .70(E/A = 75MeV)$ and $F_A = .64(E/A = 95MeV)$, but the excitation energy is more strongly constrained with an uncertainty of about 8 percent for $F_E = .47(E/A = 75MeV)$ $F_E = .64(E/A = 95MeV)$. Predictions for the statistical contribution to the light particle multiplicities are indicated by the open squares in Figure 4.26. Clearly, there is a problem with these predictions at E/A=100 MeV/A where the statistical predictions exceed the data for t, and ^4He. The origin for this discrepancy may lie in the fact that the parameters F_E and F_A which determine the excitation energy and size of the source are obtained by comparing the SMM to fragment multiplicities that are integrated over angle, while the experimental light particle differential multiplicities are determined at $\theta_{CM} \approx 90^o$. When the emmision pattern for light particles or IMF's are anisotropic in the CM frame, this comparison may display a nonnormalization problem.

Ref. [76] reports that IMF distributions in the CM frame of the Xe+Sn multi-fragmenting system are emitted isotropically and that the light particle yields are considerably more anisotropic[76]. Because the light particle multiplicities reflect more sensitively preequilibrium contributions at forward angles than do the fragments, the option of integrating the light particle yield over angle before comparison to SMM would not be very instructive. Instead, we focus on the comparison, shown in Figure 4.27, of measured and calculated values for the relative yields of the light particles. Clearly the measured data displayed as solid points has much higher d/^4He, t/^4He, and $^3He/^4He$ yield ratios then the SMM calculation(open squares) that are constrained to reproduce the IMF measurements.

From the point of view of statistical physics, this trend is consistent with the actual system being characterized by a larger value for the entropy per nucleon than

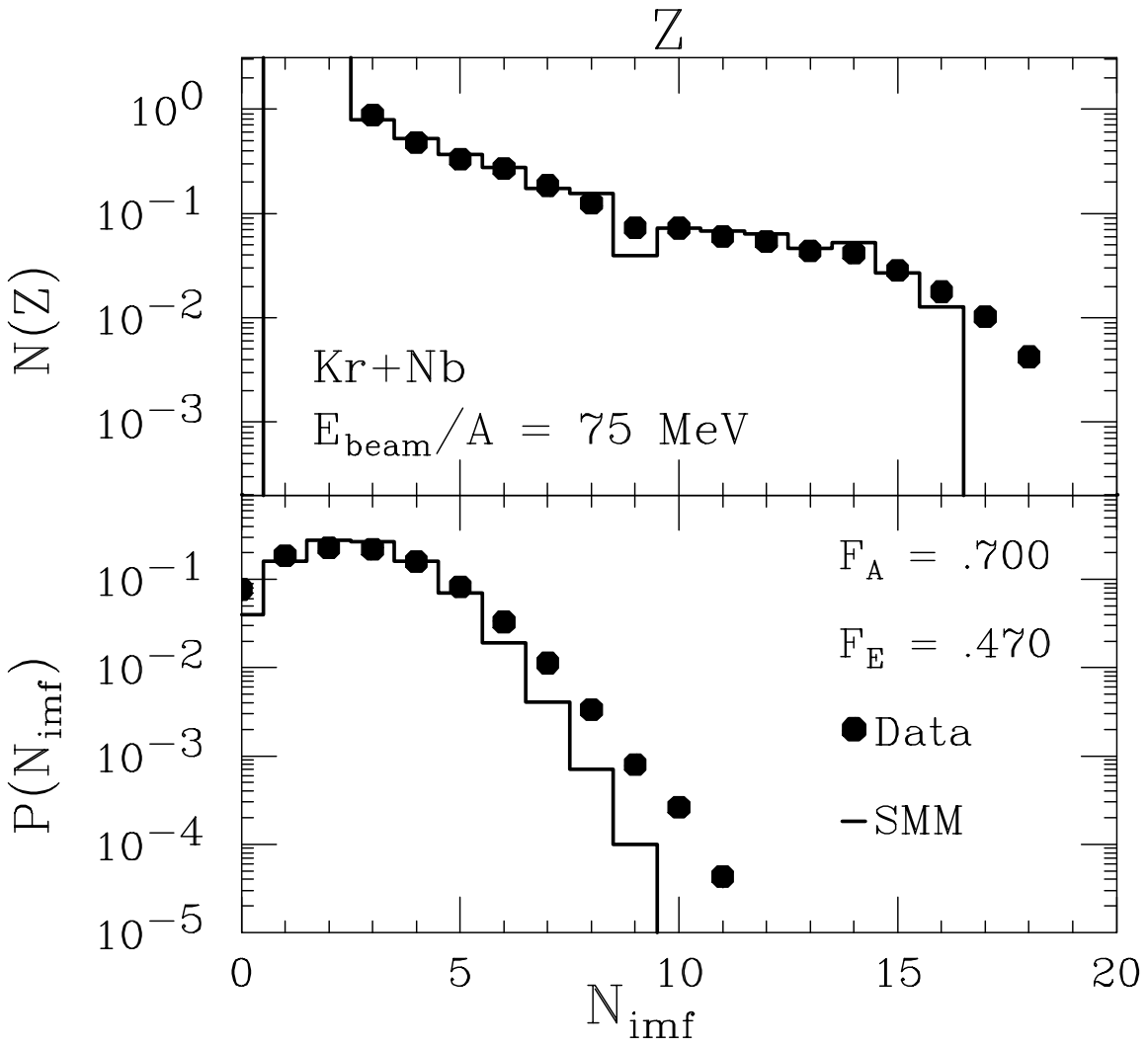

Figure 4.28: Best fit of Z distribution and IMF distribution for Kr+Nb 75 MeV/A. .

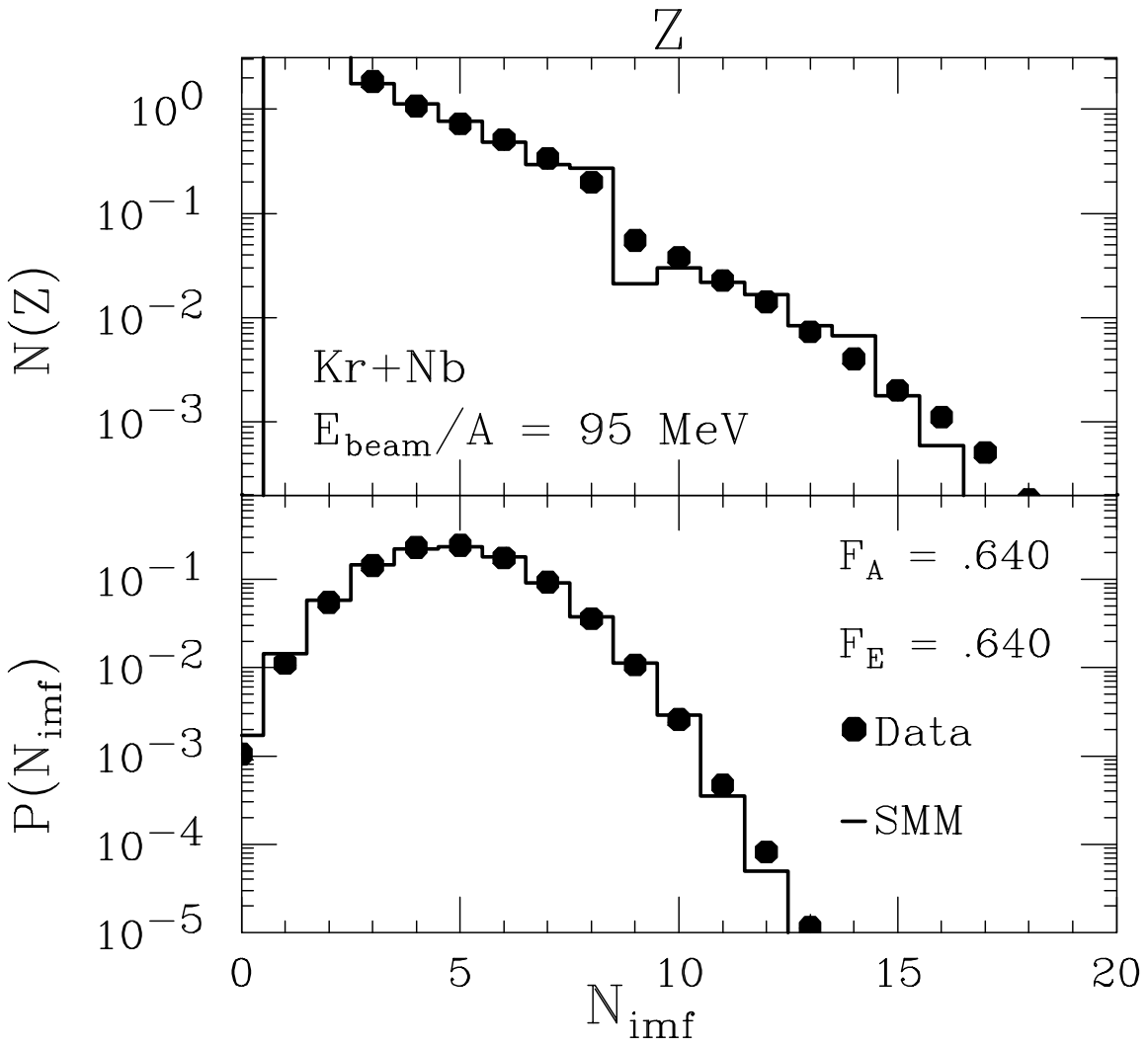

Figure 4.29: Best fit of Z distribution and IMF distribution for Kr+Nb 95MeV/A.

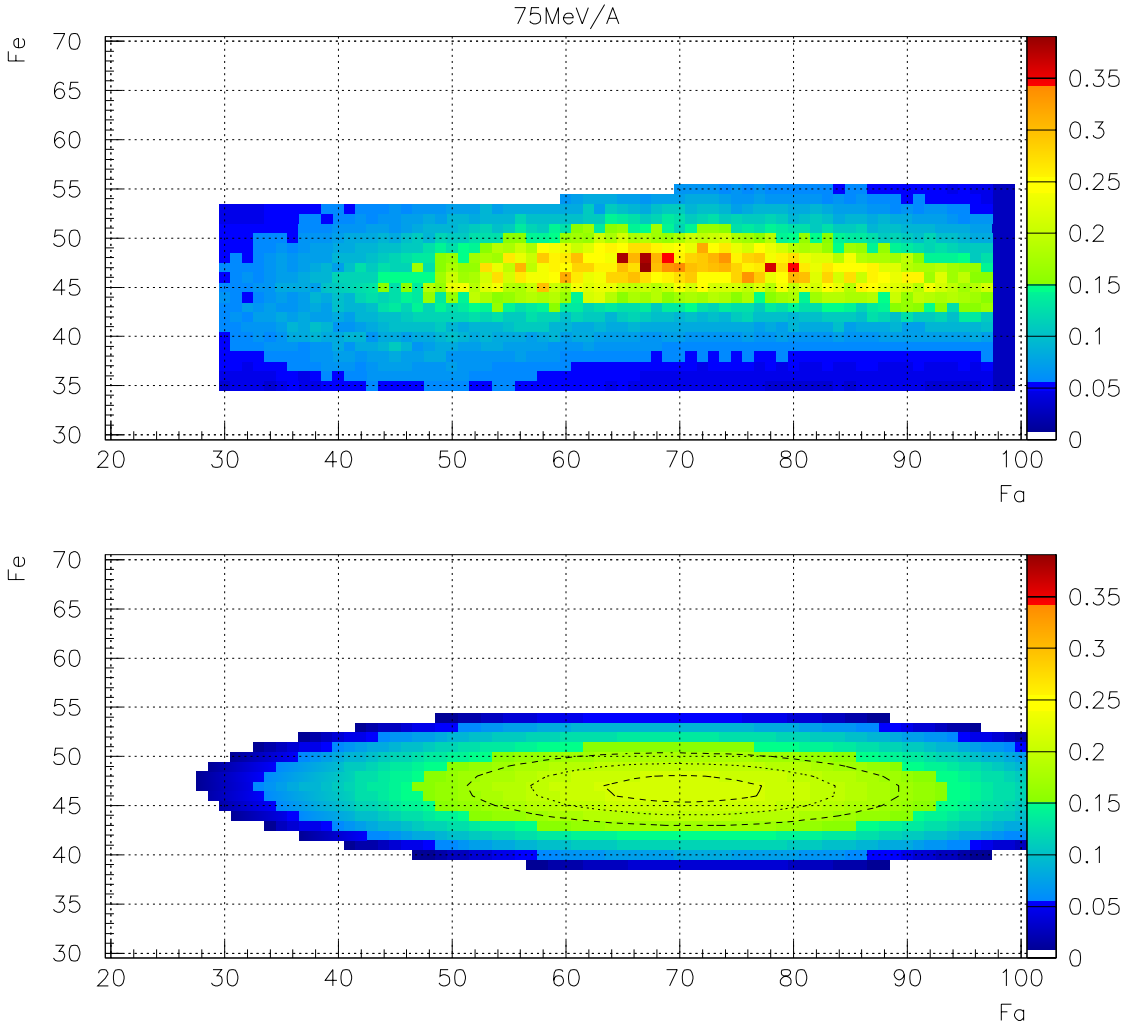

Figure 4.30: χ^{-2} vs Fe and Fa. for 75 MeV/A . The upper panel is the SMM result.The lower panel a parabolic fit, with the dashed curves standard deviations.

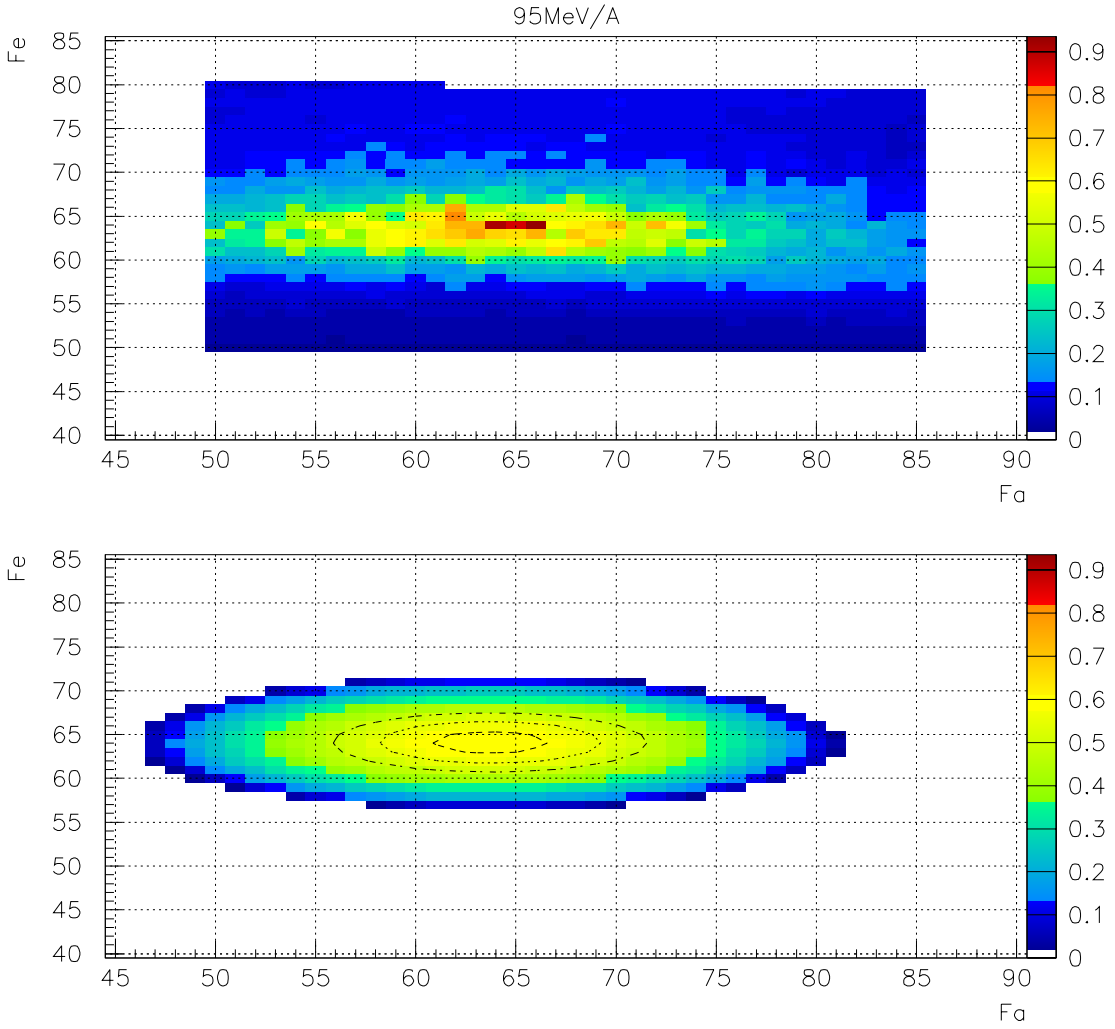

Figure 4.31: χ^{-2} vs Fe and Fa. for 95 MeV/A.The upper panel is the SMM result.The lower panel a parabolic fit, with the dashed curves standard deviations.

is that given by the calculations [30, 97, 11, 12]. Simply put, the average effective temperature of the system that emits the light particles appears to be higher than is the temperature of the system that emits the fragments.

Alternatively, one can propose that there are several sources for light particle emission. One source might be the statistical emission stage during which the fragments are emitted. If one assumes the α's are also emitted entirely during the statistical emission stage, then once fitted obtains a lower limit on the contributions from pre-equilibrium emission. In this limit the remainder of the deuteron, triton, and ^3He yields are emitted prior to the freezeout stage. This interpretation is also consistent with the fitted values for the source size obtained in figs 4.30 and 4.31 by comparing central collision data to the SMM calculation. This fitted value stipulate that size of the SMM system is about 65 percent of the size of the total system.

The Boltzmann Uehling Uhlenbeck model provides one way to directly to model the fraction of light particles that may be dynamically emitted before the system expands to low density. Such calculation was done by Hong Fei Xi using the numerical code and cluster production mechanics described in ref [108]. Using the approach described there ref. [108], the formation of clusters up to A=3 (d, ^{3}He, and ^{3}H) were calculated.

The upper four panels of Fig 4.32 shows the predicted differential multiplicity of protons, deuterons, tritons and ^3He's at $\theta_{cm} = 90^o$ as a function of time. The solid horizontal lines correspond to the experiment differential multiplicities for protons, deuterons, tritons and ^{3}He's at $\theta_{cm} = 90^o$; the horizontal dashed lines correspond to the experimental differential multiplicities minus those predicted by the SMM calculations of Fig. 4.26. The lower panel of fig 4.32 shows the evolution of the central density (density at the center of mass of the colliding system). The predicted multiplicity of light clusters increases very quickly with time. Thus many of the light

clusters are produced well before the system attains low density. Indeed, the predicted ^3He differential multiplicities approaches the experimental yield as early as 40 fm/c, at which time the system has a central density which is approximately equal to the saturation value. According to this transport model calculation, light clusters indeed are abundantly produced before the system multifragments at low density. This early dynamical emission of light clusters and expansion significantly cools the system.

It should be noted that if calculations are followed for much longer times, t>75fm/c, the predicted light cluster multiplicities greatly exceed the measured values. This may be attributed to the fact the present model neglects the competing ^4He and IMF emission channels which are not included in the model. As there is no time where the differential multiplicities by the transport model agree with the dotted lines, this simple hybrid calculation consisting of an early BUU emission stage coupled to a later SMM emission stage does not work that well. More work in this area is needed.

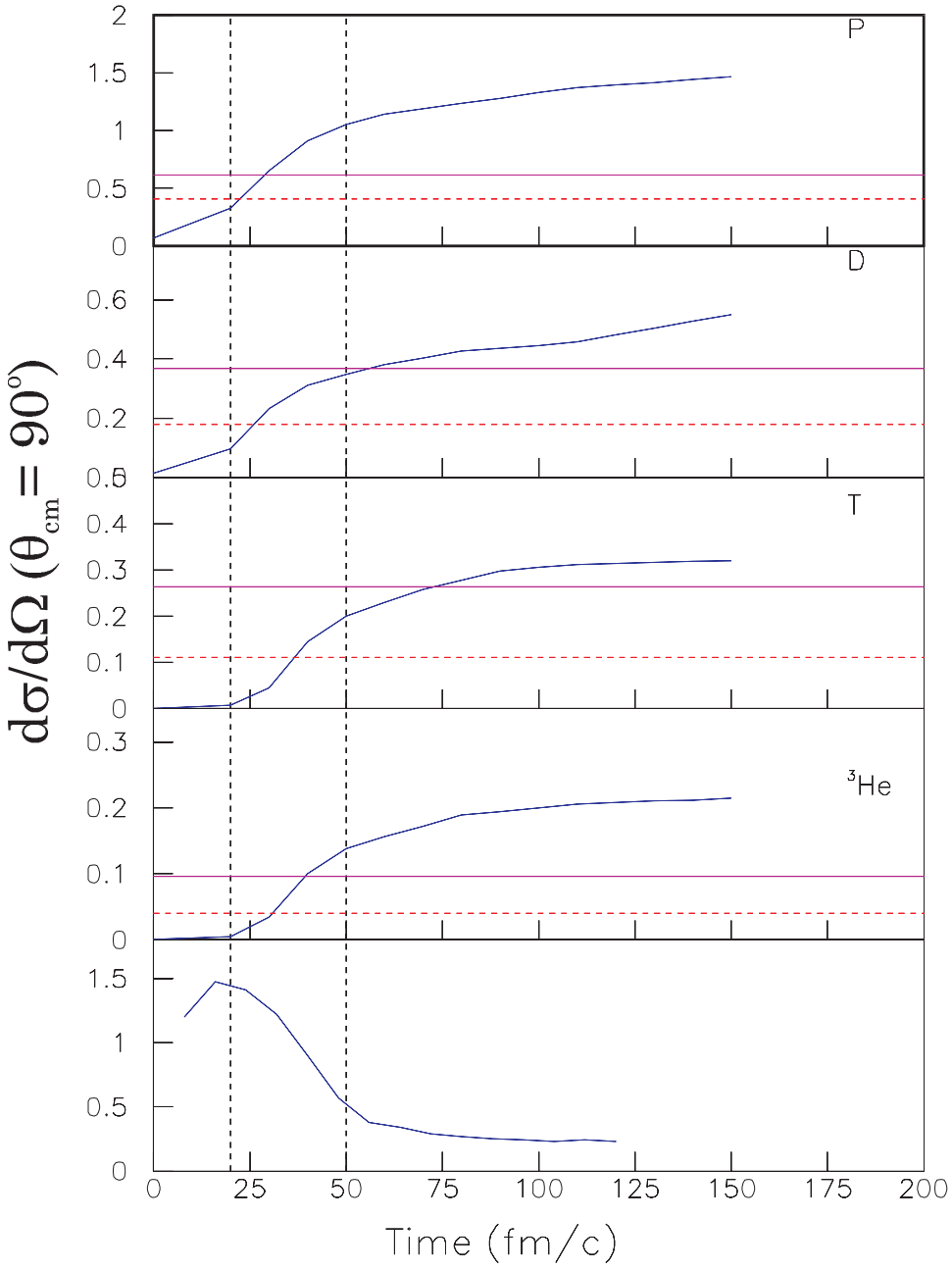

Figure 4.32: BUU calculations

4.3.3 Generalized Isoscaling of isotopic distributions

Dynamical processes appear to contribute to the emission of light particles. Presently, the description of such processes within the BUU model of ref. [110] encompasses only the emission of particles with $A \leq 3$. The formation of light clusters, within the BUU involves nucleation processes that, in the long time limit, could produce a form of equilibrium. In this context, it is relevant to compare the isotopic yield to statistical yields in order to assess how well statistical models can describe such fast emissions and cosequently whether local thermal equilibrium is a useful concept.

In this section, we compare the isotopic yields to a generalized isoscaling description. First we introduce the isoscaling observables and then generalize those observables to enable comparisons of two systems that are not at the same temperature. Finally, we compare this generalized isoscaling to the experimental data.

We begin by noting the experimental observation that isotope ratios from two statistical processes with same temperature exhibit isoscaling [142, 114], i.e. the isotope ratios depends exponentially on the neutron number, N, and proton number, Z, of the isotope (N, Z)

$$R_{21}(N,Z) = Y_2(N,Z)/Y_1(N,Z) = C\exp(\alpha N + \beta Z)\,, \tag{4.7}$$

where α and β be treated as empirical fitting parameters and C is the overall normalization factor. Eq. 4.7 can be derived from the simple Grand Canonical model expression for the primary fragment yield for the i^{th} fragment in its j^{th} state before secondary decay.

$$Y_{i,j}^{pri} = V\frac{A_i^{3/2}}{\lambda_T^3}(2J_{ij}+1)exp\frac{N_i\mu_n + Z_i\mu_p + B_{ij}}{T_i}\,, \tag{4.8}$$

where μ_p and μ_n are the proton and neutron chemical potentials. B_{ij} and J_{ij} are the binding energy and spin of the fragment in the j^{th} state, and V is the free (unoccupied) volume of the system. The insertion of the ground state yields predicted by Eq.

4.8 into Eq. 4.7 results in the cancellations of binding energy terms provided the temperatures of the two reactions are equal. Similarly, the insertion of the ground state yields predicted by Eq. 4.8 into Eq. 4.5 results in the cancellation of the chemical potential terms; the spin and mass number terms that contribute to the factor a in Eq. 4.5. What is measured in an experiment, however, are the secondary yields after sequential decay. Calculations of the yields of secondary fragments after sequential decay require an accurate accounting for feeding from the particle decay of highly excited heavier nuclei [140, 21, 84]. Such calculations are tenable if one can assume thermal population of the unbound levels. Unfortunately, this is subject to uncertainties regarding the levels that can be excited and the structure effects that govern their decay [140, 75, 21, 84, 131, 2].

To construct simple thermal expression, we adopt instead the thermal expressions in Eqs. 4.5 and 4.7 as rough empirical guides to the possible relationships between the temperature and the charge and mass distributions and explore the extent to which they can be used to describe experimental observations. A similar approach has been taken with Eq. 4.7 in refs. [142, 114] and justified therein by statistical model calculations [115], which suggest that secondary decay corrections cancel when the two systems are at the same temperature. Likewise, this approach has also been taken with the isotope thermometric expression in Eq. 4.5; discussions of the modifications of Eq. 4.5 can be found in refs. [113, 140].

We take this approach in order to see whether the isoscaling relationship can be extended to consider two systems at different temperatures. In general, the binding energy factors in Eq. 4.8 are not cancelled by the ratio in Eq. 4.7 if the two systems have different temperatures. However, one may try to extrapolate the isoscaling behavior to systems with different temperatures by multiplying $R_{21}(N, Z)$ by a binding

energy dependent term:

$$R_{21}(N,Z)\exp(k_{21}BE(N,Z)) = C'\exp(\alpha' N + \beta' Z)\,, \tag{4.9}$$

where $k_{21} = 1/T_1 - 1/T_2$ is a temperature dependent correction factor. Because the two systems are at different temperatures, the scaling relationship of Eq. 4.9 may be more sensitive than that of Eq. 4.7 to the temperature dependent secondary decay corrections of the isotopic yields. In the following, we will use measured isotope ratio temperatures in Eq. 4.5 to test whether empirical isotope temperatures and the generalized isoscaling relationship in Eq. 4.9 can describe the evolution of the isotope distributions with excitation energy. We note that it might be possible to invert Eq. 4.9 and obtain a temperature for one system if the temperature of the other is known.

To examine whether a generalized isoscaling can be applied to these reactions, we construct the isotope ratios, $R_{21}(N,Z)$ from measurements on the same system at two different incident energies. The top panels of Fig. 4.33 show the isotope ratios measured in Kr+Nb collisions and the top panels in Fig. 4.34 show the isotope ratios measured in Ar+Sc collisions for Z=1, (open circles), Z=2 (closed circles), Z=3 (open squares), and Z=4 (closed squares) isotopes and different combinations of incident energies. The different incident energies involved in each ratio are labeled in each panel; the notation "70/35" in the upper left panel in Fig. 4.33 denotes the ratio of isotopic yields measured at E/A=70 MeV in Kr+Nb collisions to the corresponding yields measured at E/A=35 MeV. For simplicity, we adopt the convention that isotope yields from the higher energy collision are placed in the numerator.

Clearly, the uncorrected isotopic ratios in the upper panels of these figures don't show the systematic trend predicted by Eq. 4.7. Instead, the ratios fluctuate from isotope to isotope by a factor of two. To determine whether these fluctuations are consistent with the binding energy term that results from a difference between the temperatures T_1 and T_2 for the two reactions measured at incident energies of E_1 and

E_2, we compensated approximately for the temperature difference using Eq. 4.8. For k_{12}, we used the average value $\langle k_{app} \rangle$ where:

$$\langle k_{21,app} \rangle = \langle \frac{1}{T_{2,APP}} - \frac{1}{T_{1,APP}} \rangle \,, \tag{4.10}$$

where $T_{1,APP}$ and $T_{2,APP}$ are the isotopic temperature for a specific isotopic thermometer at the average is over all of the isotopic thermometers in plotted in Figs. 4.22,4.24 . These corresponding mean values given in Table 4.4 and used as labels for the lower panels of Fig. 4.33 where the adjusted isotope ratios,
$R_{21}(N,Z)\exp(\langle k_{21,app} \rangle BE(N,Z))$ are shown as the open and closed points. The degree to which this procedure removes the fluctuations in isotopic ratios in Fig. 4.33 is remarkable.

Alternatively, one can extract the k values by fitting the R_{21} data in the top panels of Fig. 4.33 with Eq. 4.8. These best fit values, given in the column in Table 4.4 labeled $k_{21,fit}$, are statistically consistent with the mean values of $\langle k_{21,app} \rangle$. The values for α' and β' that describe the dependence in Eqs. 4.7 and 4.8 upon neutron and proton number are also given in the table.

When one performs the same procedure for Ar+Sc collisions, mean values of are obtained for the pairs of incident energies involved in the left and right panels of Fig. 4.34. The consistency between $\langle k_{21,app} \rangle$ and the corresponding best fit values for k_{21} is not as good as that obtained for the Kr+Nb system, see Table 4.4 .

If the values for $\langle k_{21,app} \rangle$ are used to adjust the isotope ratios as shown in the lower panels of Fig. 4.34, the adjusted ratios do not follow parallel lines on a semi-log plot. The same results are obtained if the best fit values for k_{21} are used. Thus, the generalized isoscaling relationship is not as well satisfied by the Ar+Sc data as for the Kr+Nb data.

Dynamical stochastic mean field calculations suggest that the yields of excited

Isotope ratio	a	B(MeV)	ln(k/B)(MeV^{-1})
$^{6,7}Li^{3,4}He$	2.18	13.32	-0.0051
$^{2,3}H^{3,4}He$	1.59	14.29	0.0097
$^{1,2}H^{3,4}He$	5.60	18.4	0.0496
$^{7,8}Li^{3,4}He$	1.98	18.54	0.0265
$^{9,10}Be^{3,4}He$	0.38	13.76	-0.084

Table 4.3: Parameters for emission temperatures.

System	E_2/E_1(MeV)	$< k_{app} >$	k_{fit}	α	β
Kr+Nb	70/35	-.047±0.005	-.040±0.005	0.3489	0.4034
Kr+Nb	100/70	-.025±0.005	-.024±0.004	0.0885	0.2073
Kr+Nb	120/70	-.035±0.005	-.028±0.003	0.1561	0.2340
Ar+Sc	100/50	-.039±0.005	-.028±0.004	0.2962	0.1461
Ar+Sc	150/100	-.028±0.005	-.025±0.003	0.2303	-0.051

Table 4.4: General scaling parameters. k_{app} are the averaged data of figures 4.22 and 4.24 α and β are the weighted average from both k's

fragments produced by dynamical models are not as consistent with isoscaling relations as are the final yields after secondary decay [18]. Thus, the consistency of the Kr+Nb data with the generalized scaling relationships could be due to a higher degree of equilibration in the heavier system or to a greater abundance of heavier fragments that sequentially decay to the observed ones. In any case it is clear that measurements of other systems would be useful to better establish the validity of generalized isoscaling more.

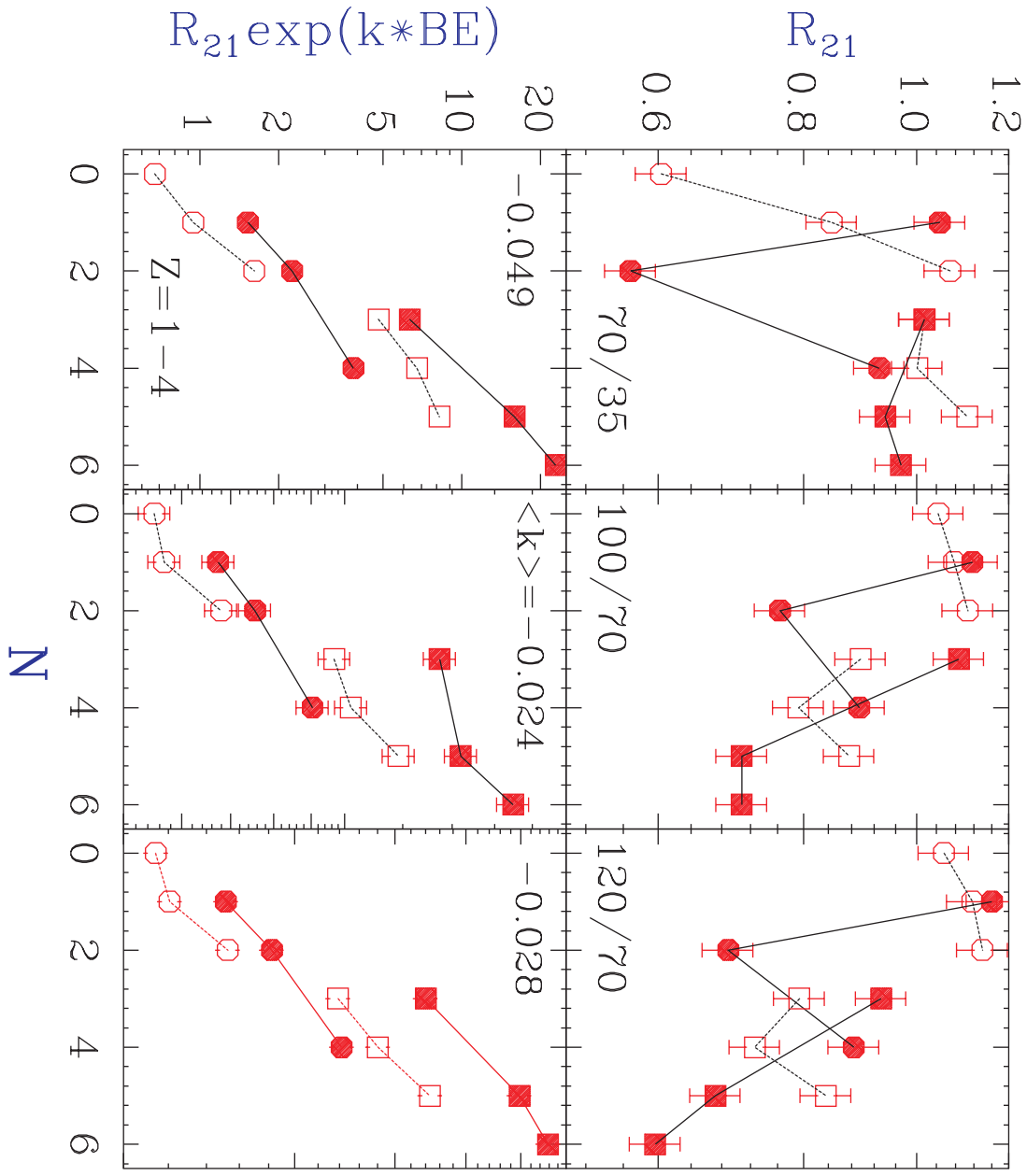

Figure 4.33: Isoscaling comparison of Kr+Nb for different beam energy ratios, using the Fourier perturbed source model and yield extracted from 5A(MeV) to ∞ . Upper and lower panels show uncorrected and corrected temperature factor respectively

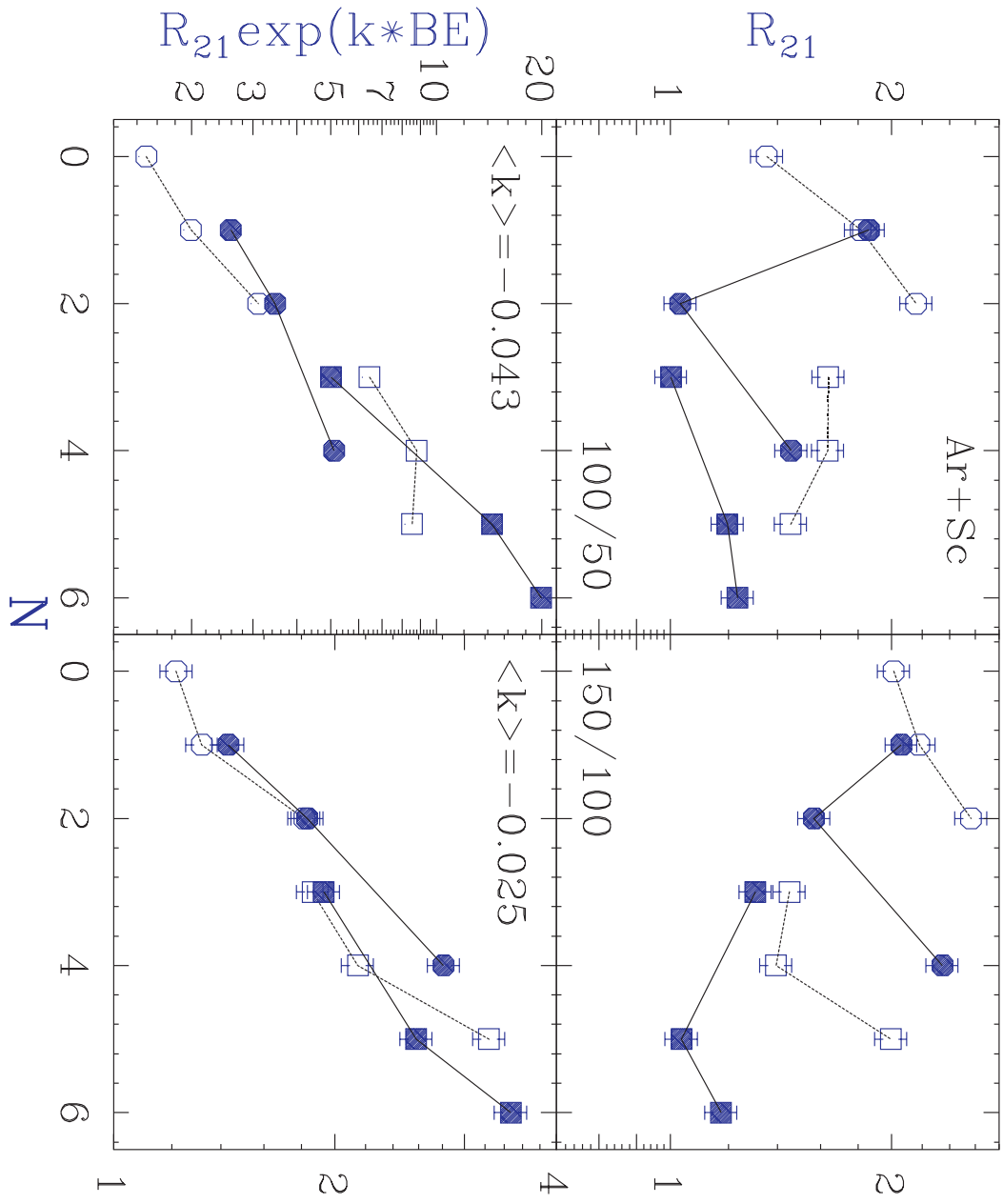

Figure 4.34: Isoscaling comparison of Ar+Sc for different beam energy ratios, using the Fourier perturbed source model and yield extracted from 5A(MeV) to ∞ . Upper and lower panels show uncorrected and corrected temperature factor respectively

Chapter 5

Two particle correlations and excited state populations

In this chapter we present experimental results for the two particle correlations and an investigation of time dependence of the temperature extracted from excited state populations is described. Fits to the data are performed using either S-matrix or Breit-Wigner forms and different forms for the background functions are also tried. From these fits the best values for the temperatures and their correlations are obtained. The Albergo thermometer is presented here as a consistency check. This analysis also gives the similar conclusion. Comparison of different colliding systems are performed to explore the dependence on system size and on the beam energy .

5.1 Pair counting Combinatorics

5.1.1 The Theoretical evaluation

During the breakup of a nuclear system, some of the particles may be directly emitted from the composite system formed by the projectile and target. The emission of

other particles may follow a more complicated history during which they may be part of an excited particle unbound nucleus are emitted earlier in the collision and then decay. The excitation spectra of such unbound nuclei will reflect the random "thermal" excitation of the surrounding nuclear medium. As discussed in Chapter 1, measurements of the relative probabilities that a nucleus, such as ^4He,^5Li, etc. is in its ground and excited states provides information about the temperature of that medium.

If the unbound nucleus in question decays to two daughter nuclei labelled i and j in their ground states that move apart with a relative energy E_{rel}, we can obtain the differential multiplicity for their excited parent nucleus from a measurement of the total coincidence yield, $Y_{coin}(E_{rel})$ as a function of the relative energy of the daughter nuclei. The coincidence yield has two contributions

$Y_{coin}(E_{rel}) = Y_{res}(E_{rel}) + Y_{back}(E_{rel})$

The first term $Y_{res}(E_{rel})$ corresponds to the decay of the unbound resonances of the emitted nucleus and the second term $Y_{back}(E_{rel})$ corresponds to the yield that does not originate directly from the binary decay of an emitted unbound parent nucleus.

Discussion of the data in terms of yields is awkward because yields are not normalized quantities and they depend on the efficiency of the detection apparatus. This criticism does not apply to the differential multiplicity. We generally apply gates on the impact parameter in this dissertation using the charged particle multiplicity in the 4π detector and sometimes on the energy of the measured particles as well. Taking the case where an impact parameter gate has been applied, we can define differential multiplicities for single and two particle emission. For single particle emission of particle type i at energy E_i and angles Ω_i, one can define the single particle differential multiplicity by $\frac{d^2M(E_i,\Omega_i)_i}{dE_i d\Omega}$:

$$\frac{d^2M(E_i,\Omega_i)_i}{dE_i d\Omega_i} = \frac{Y(E_i,\Omega_i)_i}{\Delta E_i \Delta\Omega_i N_{events}}, \tag{5.1}$$

where $Y(E_i, \Omega_i)_i$ is the number of particles measured in energy and angle intervals ΔE_i and $\Delta\Omega_i$ and N_{events} is the total number of events in the selected impact parameter interval. As defined by Eq. 5.1, the single particle differential multiplicity is the number of particles of type i emitted with energy E_i and angles Ω_i per collision per unit solid angle per unit energy. Similarly, one can define the two particle differential multiplicity for the coincident emission of particles i and j by

$$\frac{d^4M(E_i,\Omega_i,E_j,\Omega_j)_{ij}}{dE_i d\Omega_i dE_j d\Omega_j} = \frac{Y(E_i,\Omega_i,E_j,\Omega_j)_{ij}}{\Delta E_i \Delta\Omega_i \Delta E_j \Delta\Omega_j N_{events}}, \tag{5.2}$$

where the definitions of the terms for the j^{th} particle are analogous to these for the i^{th} particle.

Returning to the decomposition of the coincidence yields with resonant and background contributions, we have a corresponding relationship for the multiplicity. Thus,

$$\frac{d^4M(E_i,\Omega_i,E_j,\Omega_j)_{ij}}{dE_i d\Omega_i dE_j d\Omega_j} \mid_{coin} = \frac{d^4M(E_i,\Omega_i,E_j,\Omega_j)_{ij}}{dE_i d\Omega_i dE_j d\Omega_j} \mid_{res} + \frac{d^4M(E_i,\Omega_i,E_j,\Omega_j)_{ij}}{dE_i d\Omega_i dE_j d\Omega_j} \mid_{back} . \tag{5.3}$$

The decomposition of $\frac{d^4M(E_i,\Omega_i,E_j,\Omega_j)_{ij}}{dE_i d\Omega_i dE_j d\Omega_j} \mid_{coin}$ into resonant and background differential multiplicities, implied by Eq. 5.3, requires one to assume functional forms for each of the two terms.

Let's discuss the background yield first. Explicitly, the background yield corresponds to all processes that generate particle i and particle j in coincidence with the exception of those that directly result from the production and subsequent decay of an unbound parent nucleus with $Z_{par} = Z_i + Z_j$ and $A_{par} = A_i + A_j$. The momenta of the two particles in such processes are more weakly dependent on the relative energy than are the resonant yield described by $Y_{res}(E_{rel})$ because the two particles must be emitted sufficiently far apart in space and time so that the nuclear final state interaction between the two particles can be neglected. In this case, the Coulomb

force is the only mutual interaction of importance and the background coincidence differential multiplicity can be expressed as [56]:

$$\frac{d^4M(E_i,\Omega_i,E_j,\Omega_j)_{ij}}{dE_i d\Omega_i dE_j d\Omega_j} \mid_{back} = [1 + R_{Coul}(E_{rel})] \cdot \frac{dM^2(E_i,\Omega_i)_i}{dE_i d\Omega_i} \cdot \frac{dM^2(E_j,\Omega_j)_j}{dE_j d\Omega_j} \quad (5.4)$$

Here, $1 + R_{Coul}(E_{rel})$ describes how the background correlation function is modified by the Coulomb final state interaction between the two fragments. As will be seen below, this modification occurs primarily at small relative energies; $R_{Coul}(E_{rel})$ generally vanishes at high relative energies. Functional forms for the Coulomb correlation are discussed later in section 5.1.3 of this dissertation. The determination of the exact parameter values of the Coulomb correlation functions are discussed there as well. In some cases there can also be an additional correlation function term from collective motion that influences the background correlation function. This turns out to be of negligible importance for the cases discussed in this dissertation. The single differential multiplicities in Eq. 5.4 can be obtained by fitting the measured differential multiplicities for particles i and j at the same impact parameter gate; however it is easier to obtain the background yield by the mixed event method described in Section 5.1.2.

Now, let's discuss the resonant contribution. The resonant decay occurs in two stages. The first stage results in the emission of the parent unbound nucleus with $Z_{par} = Z_i + Z_j$ and $A_{par} = A_i + A_j$. It is described by a differential multiplicity $\frac{d^2M(E_{par},\Omega_{par})}{dE_{par}d\Omega_{par}}$ which must be approximately determined by fitting the experimental data for ground state nuclei with $Z = Z_{par}$ and $A = A_{par}$ or if such data are not available by fitting the singles data of a neighboring isotope obtained at the same impact parameter as discussed in section 4.1.2. The second stage is the decay of this unbound nucleus and is denoted by $\frac{dn(E_k)}{4\pi dE_k}$. It too, is fitted and constrained along with the Coulomb correlation function by the measured coincident yield. The fitting parameters and detailed procedures are discussed in section 5.2. The resonant

contribution to the coincidence multiplicity is:

$$\frac{d^4M(E_i,\Omega_i,E_j,\Omega_j)_{ij}}{dE_i d\Omega_i dE_j d\Omega_j}\mid_{res} =$$

$$\frac{d^2M(E_{par},\Omega_{par})}{dE_{par}d\Omega_{par}}\cdot\frac{dn(E_{rel})}{4\pi dE_{rel}}\cdot J(E_{par},\Omega_{par},E_{par},\Omega_{par};E_i,\Omega_i,E_j,\Omega_j) \tag{5.5}$$

where, $J(E_{par},\Omega_{par},E_{rel},\Omega_{rel};E_i,\Omega_i,E_j,\Omega_j)$ is the Jacobian for transformation from the relative and total to the individual coordinates for the two decay products. Here, it is assumed that the decay of parent nucleus is isotropic in its rest frame. A discussion of the influence of decay anisotropies may be found in ref. [84].

The fits to obtain the parameters of the Coulomb correlation and of the excited state populations that govern the coincidence differential multiplicity are integrated over the parent energies and angles, leaving only the dependence on excitation energy. This integration includes only the energies and angles where the detection system, i.e. the Catania hodoscope, can detect and resolve the particles of interest. In practice, this is implicitly done with the data, where we start by making a change of variables from E_i and E_j to the total energy $E_{tot} = E_i + E_j$ and the relative energy E_{rel} defined by:

$$E_{rel} \approx \frac{1}{2}\frac{q^2}{m_A} + \frac{1}{2}\frac{q^2}{m_B}\,, \tag{5.6}$$

where

$$q^2 = \frac{\left(\mathcal{E}_A\mathcal{E}_B/c^2 - \vec{p}_A\cdot\vec{p}_B\right)^2 - m_A^2m_B^2c^4}{m_A^2c^2 + m_B^2c^2 + 2\mathcal{E}_A\mathcal{E}_B/c^2 - 2\vec{p}_A\cdot\vec{p}_B}\,, \tag{5.7}$$

and $\mathcal{E}_A$,$\mathcal{E}_B$ are the total energies, and $\vec{p}_A$,$\vec{p}_B$ are the momenta measured in the lab frame. Then, we sum over total energy keeping E_{rel} fixed to obtain

$$Y_{coinc}^{total}(E_{rel}) = \sum_{1,2} Y_{1,2}^{total}(E_1,E_2)\mid_{E_{rel,fixed}}\,, \tag{5.8}$$

The end result is a one dimensional spectrum of counts as a function of E_{rel}, $Y_{coin}(E_{rel})$, which contains both the resonant $Y_{res}(E_{rel})$ and the background $Y_{back}(E_{rel})$ contributions discussed previously. When one fits the coincidence data one has to correct

for the detection efficiency. Let us first consider how one does an efficiency correction to the theory in order to obtain an efficiency corrected theoretical expression for $Y_{res}(E_{rel})$.

5.1.2 Efficiency Calculation

The efficiency function $\epsilon(E_k, E_{meas})$ corrects the theoretic decay spectrum for detector efficiency in order to allow comparisons to the measured one. It basically states how many of the decays that occur at relative E_k are observed experimentally at measured relative energy E_{meas}. It is calculated via a computer simulation [79] that assumes for simplicity an isotropic decay in the rest frame of the unstable parent nucleus. This simulation peformed a Monte Carlo integration over the entire detector geometry, which takes into account the position of each detector relative to the target and the beam axis, the solid angle of each detector, the energy resolution of each detector, the beam spot size, and the various energy losses in the target and the brass sheet in front of the Catania telescopes . The simulation assumes the unstable parent nucleus to be emitted according to the fitted single particle spectrum $d^2M/dEd\Omega$ for the parent nucleus in the ground state. This provides the weighted energy and the angular distribution for the unstable parent nuclei before it decays. In the end, one expresses efficiency function as a summation over the decay spectrum $\frac{dn(E_{rel})}{dE_{rel}}$ which provides the resonance contribution of the coincidence yield, $Y_{res}(E_{meas})$ in bin of relative energy E_{meas} that are of the same size as used in the data analysis.

$$Y^{meas}_{reson}(E_{meas}) = \sum_k \Delta E \epsilon(E_k, E_{meas}) \mid \frac{dn(E_k)}{dE} \mid_{chan} , \tag{5.9}$$

Here the summation is over bins in E_k, the actual excitation energy in the rest frame of the excited particle unbound nucleus. Those bins are typically chosen to be much finer than the step size over which $\frac{dn(E_{rel})}{dE_{rel}}$ varies significantly.

The efficiency function $\epsilon(E_k, E_{meas})$ is computed following [79] and stored as a matrix. It contains both the information about the probability that both decay products will be detected in the hodoscope and about the resolution with which their excitation energy can be reconstructed. By summing the efficiency function over E_{meas} for fixed E_k

$$\epsilon(E_{rel}) = \sum_l \epsilon(E_{rel}, E_{meas,l}) \Delta E_{meas} \,, \tag{5.10}$$

one obtains the total detected yield one would expect if the decay spectrum were $\frac{dn(E_k)}{4\pi dE_k} \approx \delta(E_k - E_{rel})$. An example of this efficiency measure is shown in the upper panel of Fig. 5.1. The normalization is such that it gives the number of exited nuclei you would reconstruct if there were as many excited nuclei produced as there were ground state nuclei making up the spectrum $\frac{d^2M(E_{par},\Omega_{par})}{dE_{par}d\Omega_{par}}$ and if all these excited nuclei had an excitation energy of E_{rel}.

The resolution information is reflected in the degree to which the efficiency matrix is non-diagonal and can be quantified by

$$\sigma(E_{rel}) = \left[\frac{\sum_l (E_{meas,l} - E_{rel})^2 \epsilon(E_{rel}, E_{meas,l}) \Delta E_{meas}}{\sum_l \epsilon(E_{rel}, E_{meas,l}) \Delta E_{meas}} \right]^{1/4} \,, \tag{5.11}$$

An example of the resolution is shown in the lower panel of Fig. 5.1. Now, let's turn to the calculation of the background function. In the early analyses of decay spectra, simulations were performed to calculate the non-resonant background via a Monte Carlo integral that is essentially the same as the one use to obtained the decay efficiency [83]. Soon afterward, however, it was realized that the technique of mixed singles could be used to provide the non-resonant background more easily. The expression for the unnormalized mixed single background is:

$$Y_{mix}(E_{rel}) = const \cdot \Sigma Y(E_i, \Omega_i)_i \cdot Y(E_j, \Omega_j)_j = const' \cdot \Sigma \frac{dM^2(E_i, \Omega_i)_i}{dE_i d\Omega_i} \cdot \frac{dM^2(E_j, \Omega_j)_j}{dE_j d\Omega_j}\,, \tag{5.12}$$

where the summation runs over the angle and energies for particles i and j that can be detected in the hodoscope subjected to the constraint that the computed relative energy is E_{rel}. In practice, each particle in the mixed event pair come from a different event making that pairing statistically independent.

Because of the fact that $Y(E_i, \Omega_i)_i \propto \frac{d^2M(E_i,\Omega_i)_i}{dE_i d\Omega_i}$, it follows that the mixed event yield $Y_{mix}(E_{rel})$ is proportional to $Y_{back}(E_{rel})/[1 + R_{Coul}]$. Thus, if there were no resonant coincident yield at specific relative energies, dividing $Y_{coin}(E_{rel})$ by $Y_{mix}(E_{rel})$ would yield $1 + R_{Coul}$ to within a multiplicative constant. Thus if there are a sufficient range of relative energies where $Y_{res}(E_{rel})$ vanishes, one can easily determine the correct parameters for $1 + R_{Coul}$.

In practice, the easiest way to clearly see the background is to construct the total correlation function defined by

$$\frac{d^4M(E_i, \Omega_i, E_j, \Omega_j)_{ij}}{dE_i d\Omega_i dE_j d\Omega_j} \mid_{coin} = [1 + R_{tot}(E_{rel})] \cdot \frac{d^2M(E_i, \Omega_i)_i}{dE_i d\Omega_i} \cdot \frac{d^2M(E_j, \Omega_j)_j}{dE_j d\Omega_j}, \tag{5.13}$$

or, if we sum over the center of mass coordinates and the decay angles for the unbound fragment and use Eq. 5.12 we can obtain

$$Y_{coin}(E_{rel}) = [1 + R_{tot}(E_{rel})] \cdot Y_{mix}(E_{rel})/C_{norm}\,. \tag{5.14}$$

Here, C_{norm} may be determined by the requirement that R_{tot} vanishes at large E_{rel} where final Coulomb state interactions do not strongly influence the coincident yield.

The correlation function R_{tot} has been the focus of intense investigations [10] because of its sensitivity to the size of the source from which the particles are emitted and its lifetime. Here, however, we do not focus upon this sensitivity, but rather on

the use of correlation functions to define the non-resonant background so that we can remove it. Because the non-resonant coincidence yield is related to the mixed event background via the correlation function, the influences of the geometrical efficiency and of the energy thresholds, etc., are the same for the two quantities. This really simplifies the understanding of the background.

In the detailed data analysis, we determine R_{tot} from the equation:

$$1 + R\left(E_i\right) = C_{norm}\frac{Y^{total}_{coinc}(E_i)}{Y_{mixed}(E_i)} = C_{norm}\frac{\sum Y^{total}_{1,2}(E_1,E_2)}{\sum Y_1(E_1)Y_2(E_2)} =$$

$$C_{norm}\cdot\frac{\sum\limits_{k,k}\left[\Theta\left(E^{k,k}_{rel,m,n}-E_i+\Delta E/2\right)-\Theta\left(E^{k,k}_{rel,m,n}-E_i-\Delta E/2\right)\right]}{\sum\limits_{k,l}^{k<l}\left[\Theta\left(E^{k,l}_{rel,m,n}-E_i+\Delta E/2\right)-\Theta\left(E^{k,l}_{rel,m,n}-E_i-\Delta E/2\right)\right]}, \quad (5.15)$$

Where i is the bin number. ΔE is the energy bin width. k, l are event numbers. $E^{k,l}_{rel,m,n}$ is the relative energy between particles m and n in the parent frame. Θ is the unit step function. The numerator or denominator terms have the value of zero or one depending on whether the value of energy $E^{k,l}_{rel,m,n}$ falls within the i^{th} bin .

The coincident pairs Y_{coin} are the numerator, and summed within an event. Here, only combinations not permutations of coincident pairs detected are counted to prevent double counting . If there is some interaction(at least Coulomb repulsion) between the pairs in an event we would expect to see some correlation.

The denominator Y_{mixed} is constructed by an "event mixing" method. The pair counting comes from different events. This makes the particles statistically independent because one event is physically independent of another. Another result of this statistical independence is that the probability of this mixed yield is also proportional to product of the single yields which is indicated in the second form of equation 5.15. The inequality in event mixing above the summation ensures we don't double count pairs. The case of counting in the same detector for different events is also excluded from the counting.

In practice four consecutive events are combined with the k^{th} event in the event mixing algorithm for every event k in the numerator. Both the yields of coincident pairs and event mixed pairs are saved as functions of the relative energy E_i as histograms files and are then divided during analysis. The correlation function is normalized by the constant C_{norm} so as to obtain a value of unity , typically in the range of E_{rel}=5.5-8 MeV or a momentum range of 150-200 MeV/c. The data normalization is computed including the statistical error using:

$$C_{norm}^{-1} = \sum_i \frac{Y_{coinc}^{total}(E_i)}{Y_{mixed}(E_i)} \frac{1}{\sigma_i^2} / \sum_i \frac{1}{\sigma_i^2} \,, \tag{5.16}$$

where

$$\sigma_i^2 = \left[\frac{Y_{coinc}^{total}(E_i)}{Y_{mixed}(E_i)} \sqrt{\frac{1}{Y_{coinc}^{total}(E_i)} + \frac{1}{Y_{mixed}(E_i)}} \right]^2 \,, \tag{5.17}$$

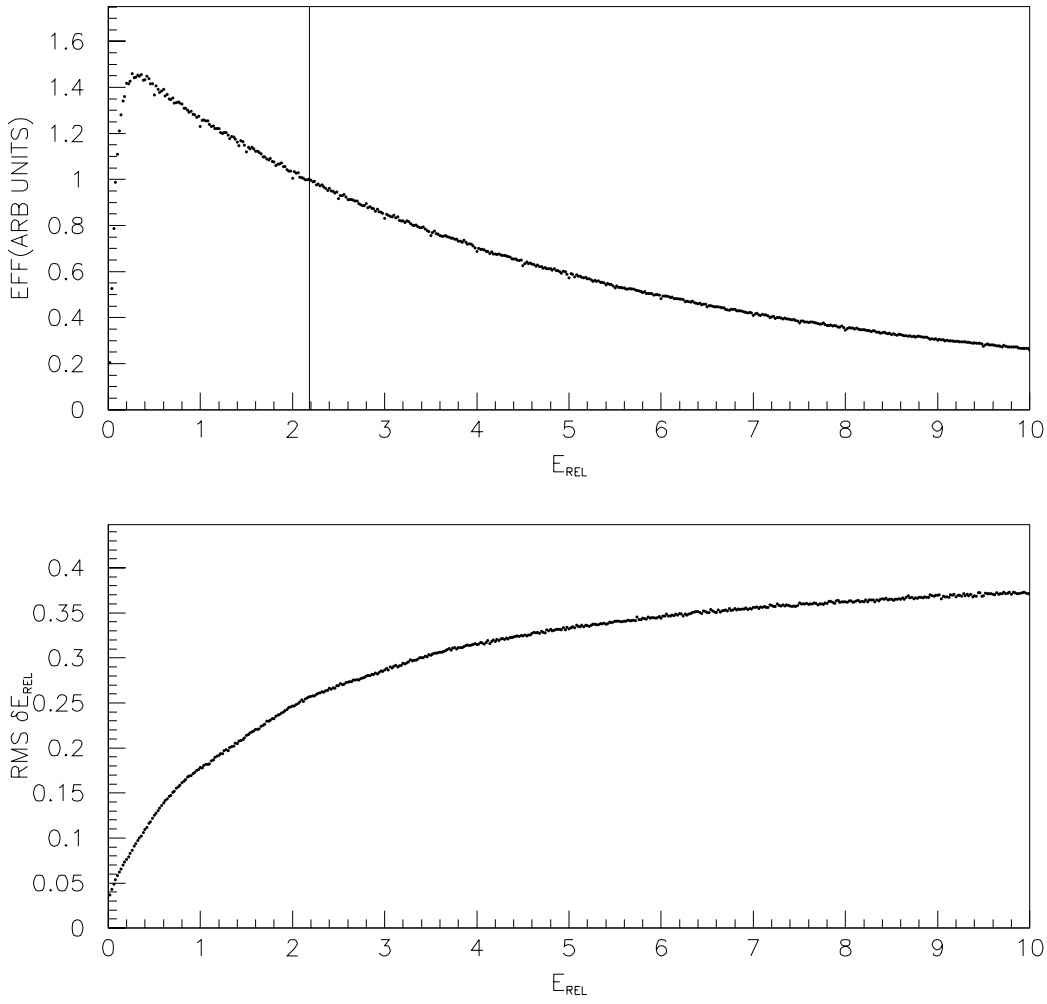

Figure 5.1: Detector efficiency and resolution of d-α for Kr+Nb 120MeV/A. The efficieny is normalized at 2.186 MeV the main peak location.

5.1.3 Efficiency Folding and Line shaping(fitting)

The correlation function in the equation 5.15 has resonant and nonresonant components.

$$1 + R_{tot}(E_{rel}) = C_{norm} \frac{Y_{res}(E_{rel}) + Y_{back}(E_{rel})}{Y_{mixed}(E_{rel})} , \tag{5.18}$$

Following the arguments in the previous section

$$1 + R_{coul}(E_{rel}) = C_{norm} \frac{Y_{back}(E_{rel})}{Y_{mixed}(E_{rel})} , \tag{5.19}$$

One simple form of the Coulomb correlation function is an exponential form[99] :

$$1 + R_{coul}(E_{rel}) = C_{norm} \frac{Y_{back}}{Y_{mixed}} = 1 - e^{-(\frac{E_{rel}}{\Delta_b})^{0.9}} , \tag{5.20}$$

We recall C_{norm} is determined by eq. 5.16. The values for Δ_b will be determined for a fit to the correlation function data and Y_{mixed} is measured. Thus, one can invert eq 5.20 to obtain $Y_{back}(E_{rel})$ Equation 5.18 is rewritten:

$$Y_{res}(E_{meas}) = Y_{coin}^{total}(E_{meas}) - Y_{back}(E_{meas}) =$$

$$[1 + R(E_{meas}) - R_{coul}(E_{meas})]\, Y_{mixed}(E_{meas}) C_{norm}^{-1} , \tag{5.21}$$

This expression must equal the theoretical expression in which the efficiency is folded with the decay yield:

$$Y_{res}^{theory}(E_{meas}) = \sum_k \Delta E \epsilon(E_k, E_{meas}) \mid \frac{dn(E_k)}{dE} \mid_{chan} , \tag{5.22}$$

From the expression $(dn(E_{meas})/dE)_{chan}$.

For many decay spectra, the theoretical decay yield calculated as the sum of Breit-Wigner resonant line shapes. The original Breit-Wigner function was developed during an experiment with neutron scattering and later generalized in R-matrix theory.[17, 63] Taking the Breit-Wigner form for the phase shifts, the decay yield can

be expressed as the sum of the contributions from the various levels that decay to the specific decay channel given in table 5.1

$$\left(\frac{dn(E)}{dE}\right)_{chan} = \sum_{\lambda} \left(\frac{dn_{\lambda}(E)}{dE}\right)_{chan} , \tag{5.23}$$

where

$$\left(\frac{dn_{\lambda}(E)}{dE}\right)_{chan} = a_{\lambda} e^{-\frac{E}{T}} \frac{2J_{\lambda}+1}{\pi} \frac{\Gamma_{\lambda}/2}{(E_{res}-E)^2 + \frac{1}{4}\Gamma_{\lambda}^2} \frac{\Gamma_{chan,\lambda}}{\Gamma_{\lambda}} , \tag{5.24}$$

and $\frac{\Gamma_{chan,\lambda}}{\Gamma_{\lambda}}$ is the partial width divided by the total width of the channel, a ratio sometimes called the branching ratio. J_{λ} is the spin of the state. E_{res} is the resonance energy of the state. The resonance energy is the difference between the pair binding energies and the parent binding energy in the resonance. In principal, the normalization constants a_{λ} should be unity if there are no secondary decays. In practice, however, there are secondary decay contributions and better fits are sometimes obtained by letting a_{λ} vary. Examples of fits are given in the figures 5.2-5.11 for states measured in central collision with a reduced impact parameter $b/b_{max} \leq 0.45$ using all 96 detectors on the hodoscope[83]. These fits were fitted with the Boltzmann factor constant over the states and the parameters a_{λ} to vary. The data are the solid points. The best fit theoretical correlation and background are the solid curves. When the peaks near threshold are broad or the resolution is poor, it is difficult to constrain the shape of the Coulomb correlation strongly. Then one must let the shape of the Coulomb correlation vary to assess the uncertainties in the yield of the state due to uncertainties in the background subtraction. The dashed and dotted lines in the figures show the range of possible backgrounds and fits that are consistant with the data. More details of the fitting procedure are given in the next section. These extremes are made by varying the background parameter Δ_b.

Parent	J^π	Energy	E_{rel}	decay channel	Γ_c/Γ	Γ
^{4}He	0^+	0	-	stable	-	-
^{4}He*	0^+	20.1	0.5	p + t	1.00	0.27
^{4}He*	0^-	21.1	1.28	p + t	.76	0.84
^{4}He*	2^-	22.1	1.5	p + t	.76	0.84
^{4}He*	1^-	24.25	3.5	p + t	.51	3.08
^{5}Li	$3/2^-$	0.0	1.637	p + ^{4}He	1.00	0.055
^{5}Li*	$3/2^+$	16.66	0.45	d + ^{3}He	0.86	0.3
^{8}Be	2^+	3.04	2.94	^{4}He + ^{4}He	1.00	1.5
^{8}Be*	1^+	17.64	0.4	p + ^{7}Li	1.00	0.0107
^{8}Be*	1^+	18.15	1.9	p + ^{7}Li	0.96	0.0138

Table 5.1: Excited nuclei studied for standard analysis.[20, 34, 134]

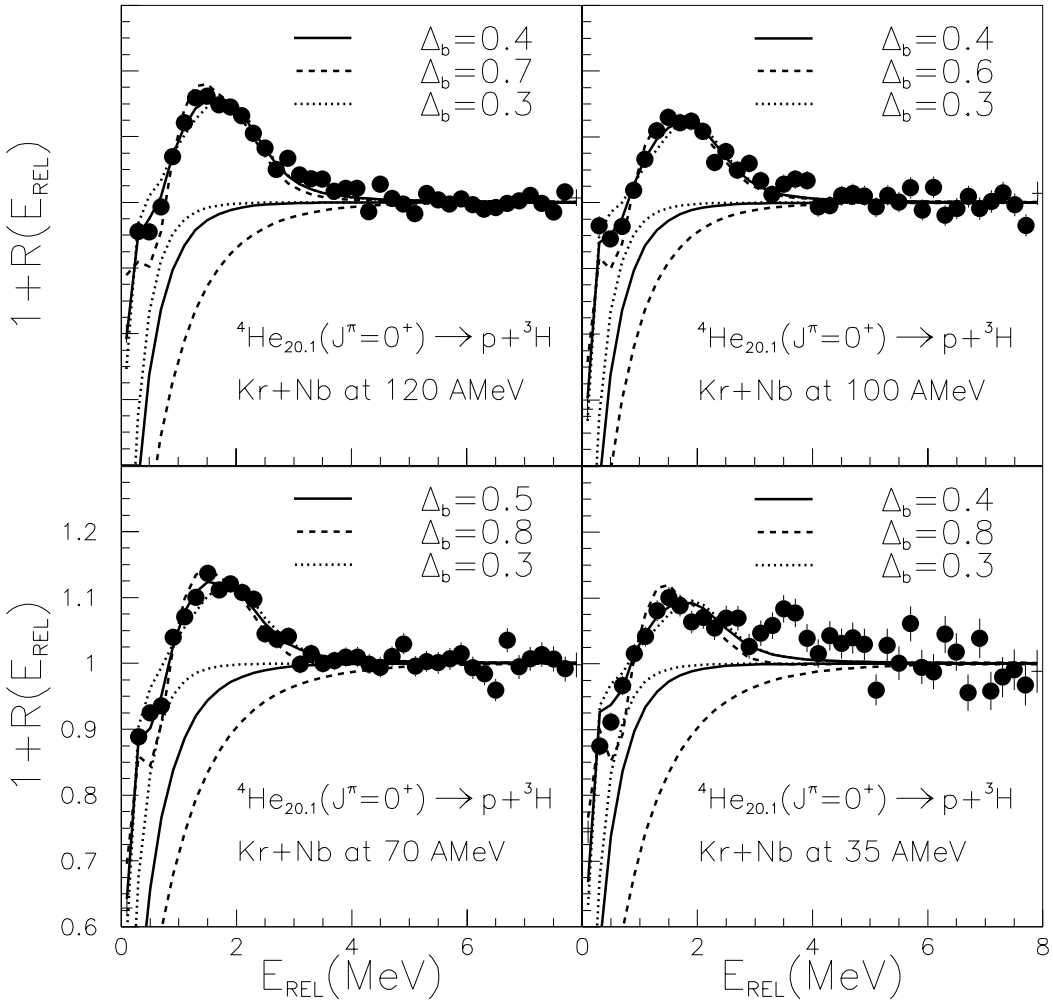

Figure 5.2: The p-t Correlation for Kr+Nb for 120,100,70,35 MeV/A respectively . The extremes of the background parameter are indicated in dashed and dotted curves. The narrow width method(Lorentzian) was used in fitting.

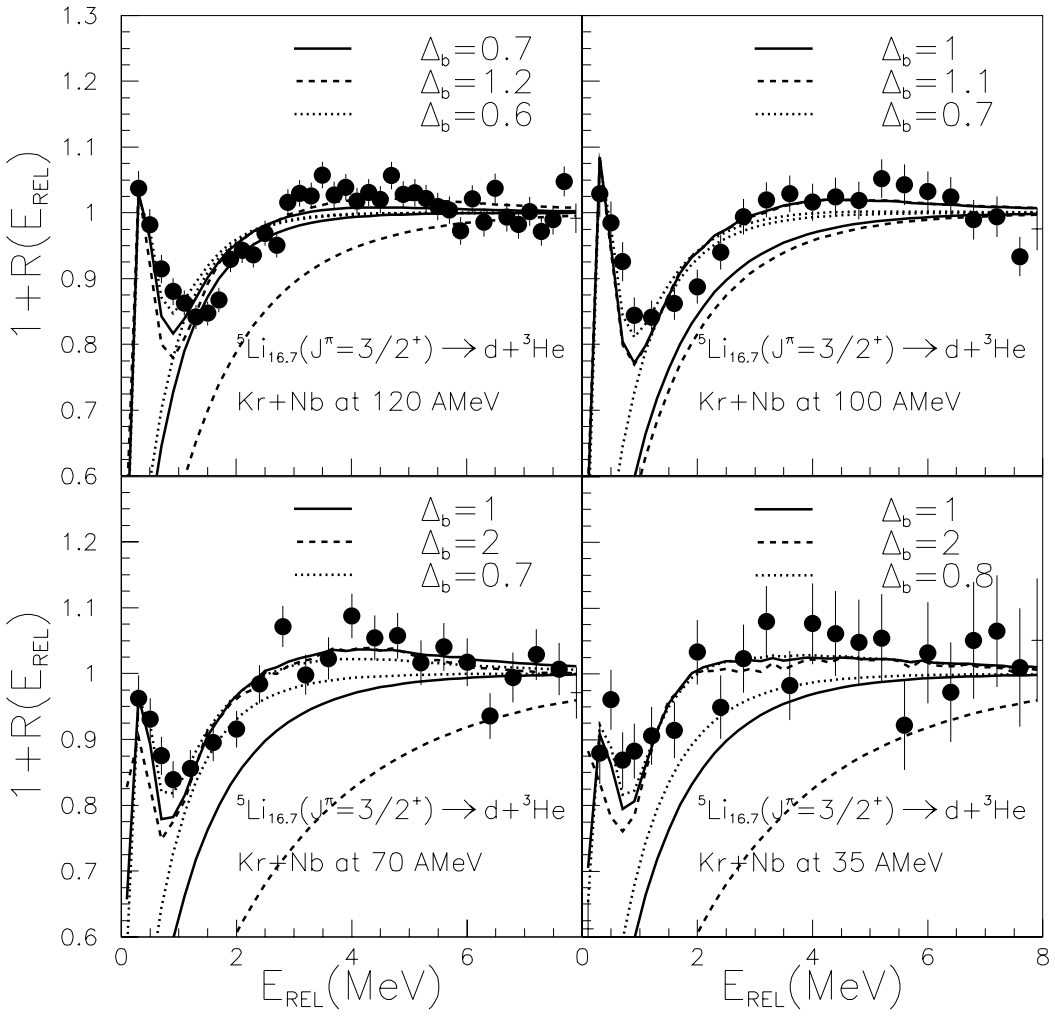

Figure 5.3: The d-^3He Correlation for Kr+Nb for 120,100,70,35 MeV/A respectively . The extremes of the background parameter are indicated.

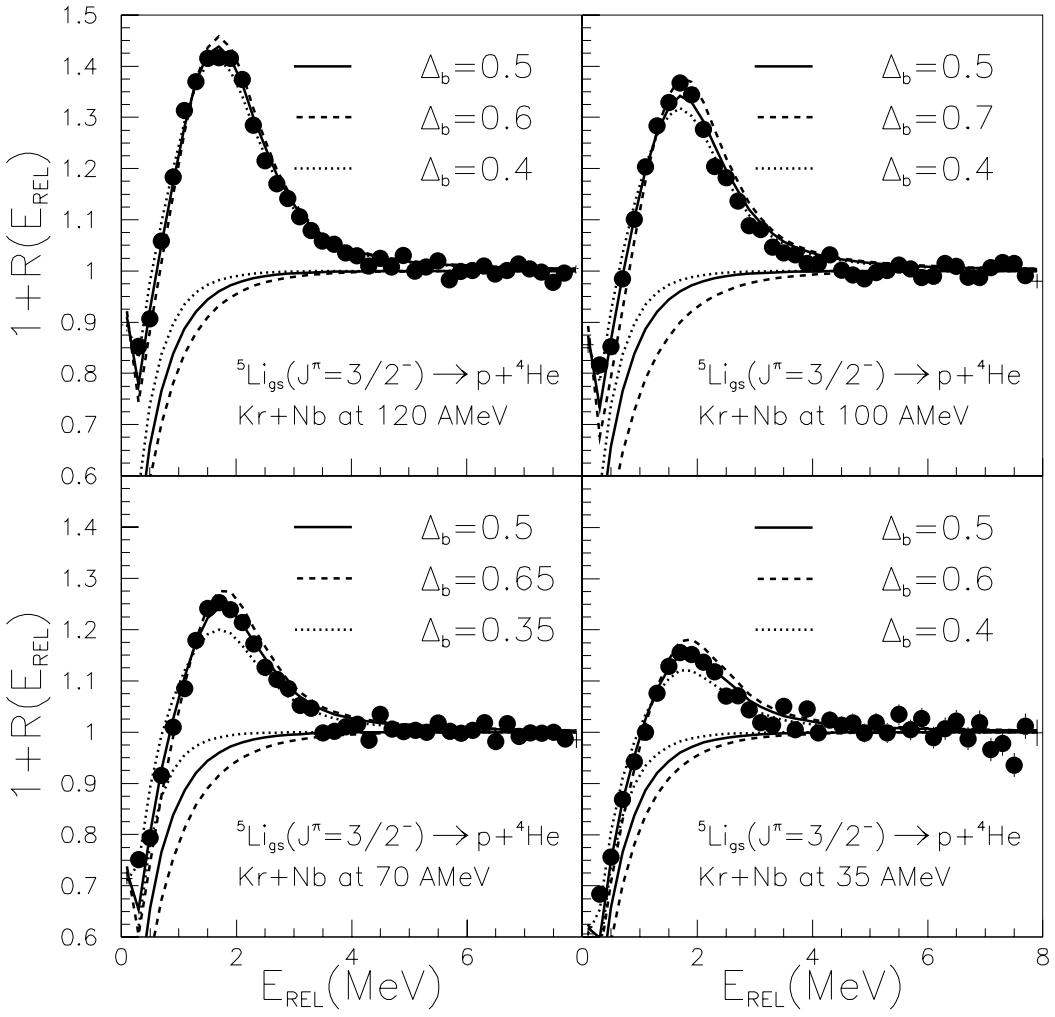

Figure 5.4: The p-^4He Correlation for Kr+Nb for 120,100,70,35 MeV/A respectively . The extremes of the background parameter are indicated.

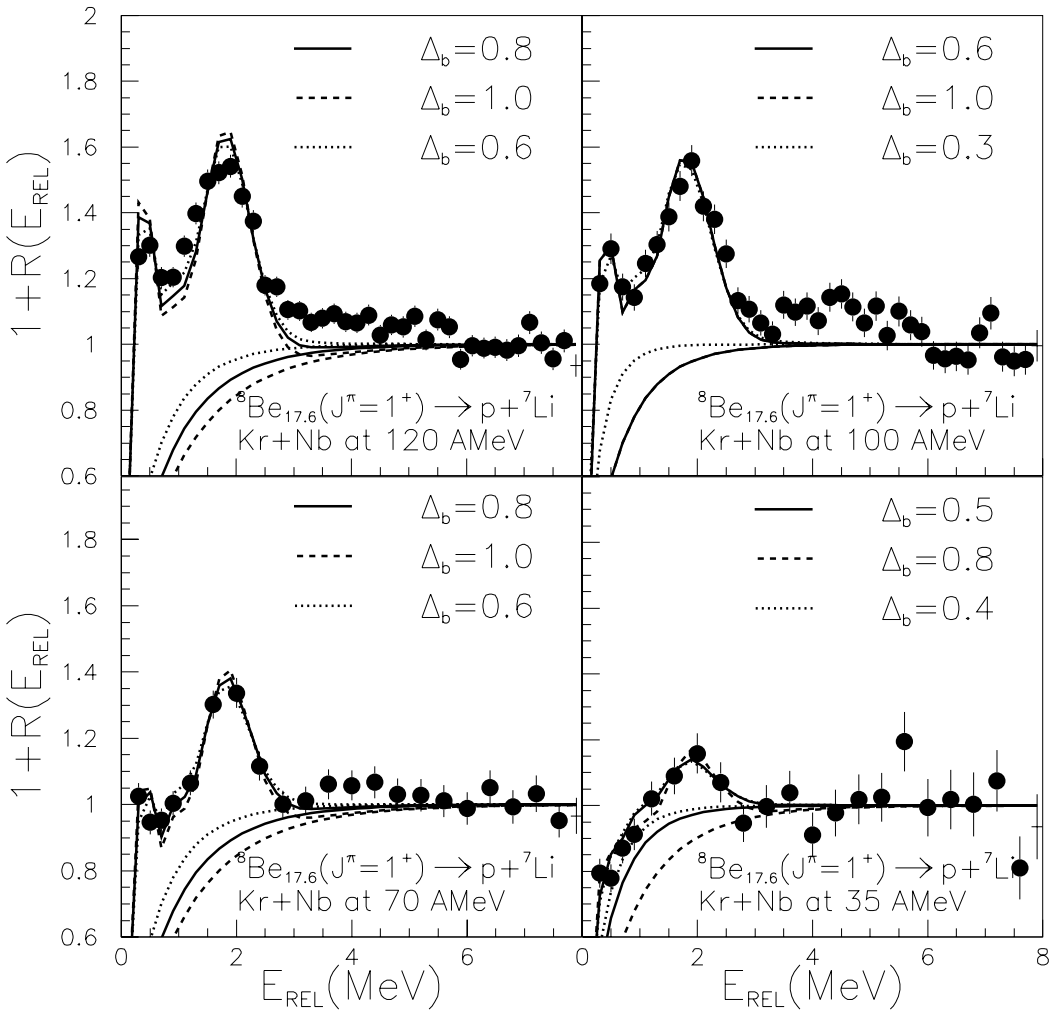

Figure 5.5: The p-^7Li Correlation for Kr+Nb for 120,100,70,35 MeV/A respectively . The extremes of the background parameter are indicated.

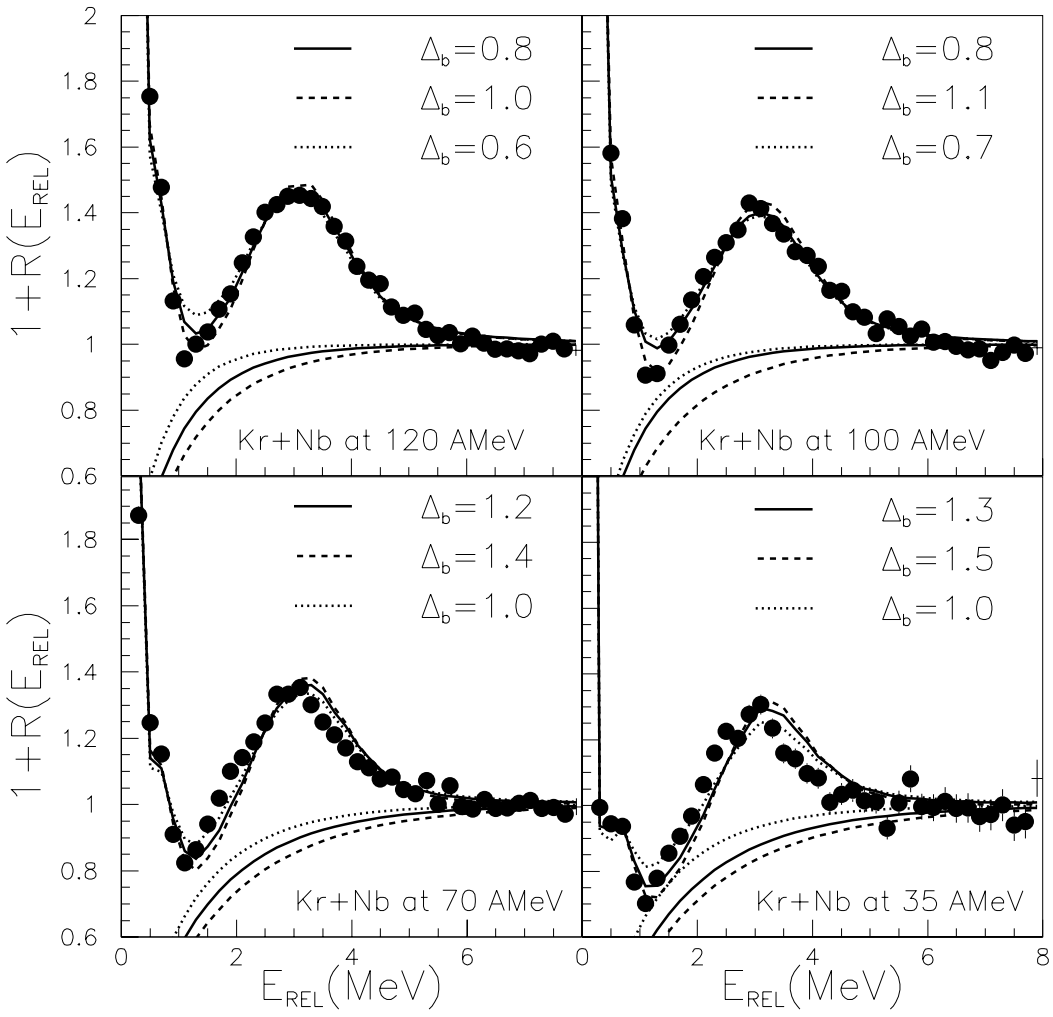

Figure 5.6: The ^4He-^4He Correlation for Kr+Nb for 120,100,70,35 MeV/A respectively . The extremes of the background parameter are indicated.

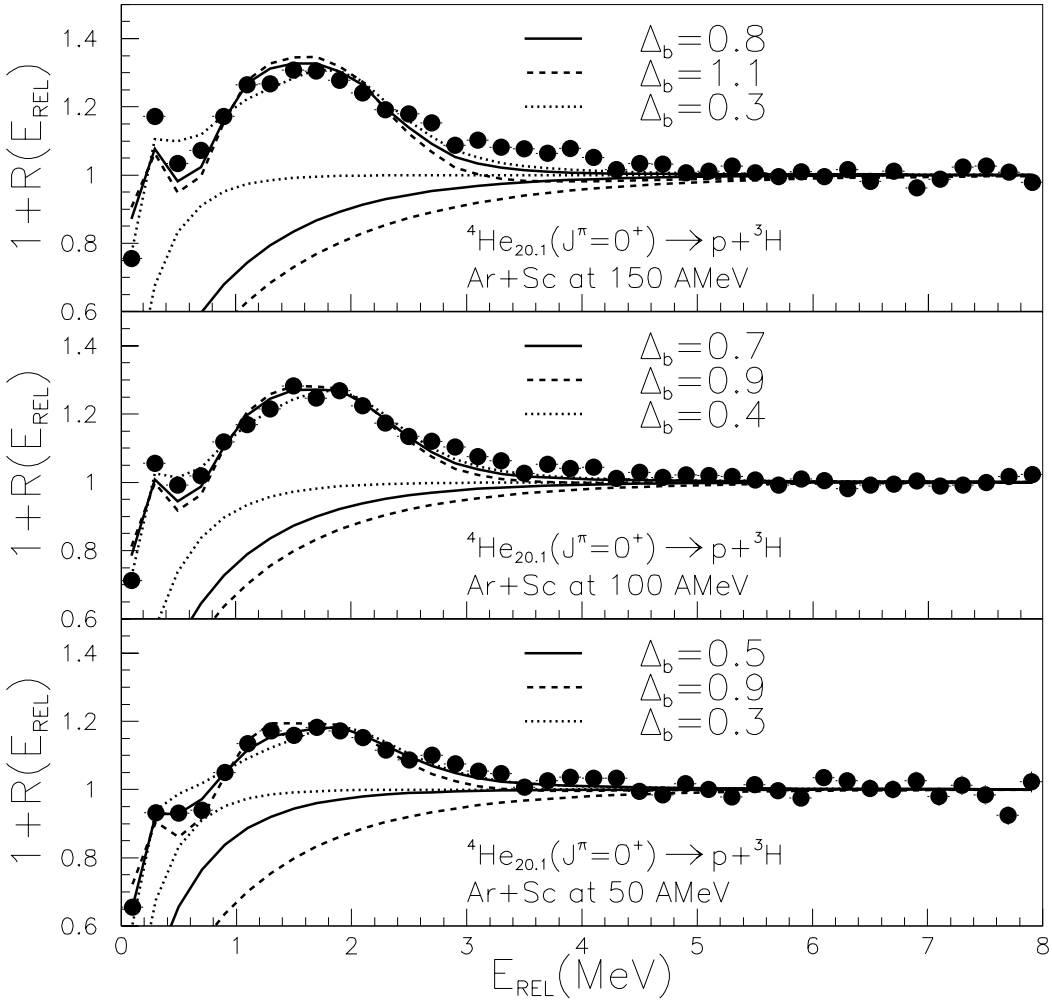

Figure 5.7: The p-t Correlation for Ar+Sc for 150,100,50 MeV/A respectively . The extremes of the background parameter are indicated.

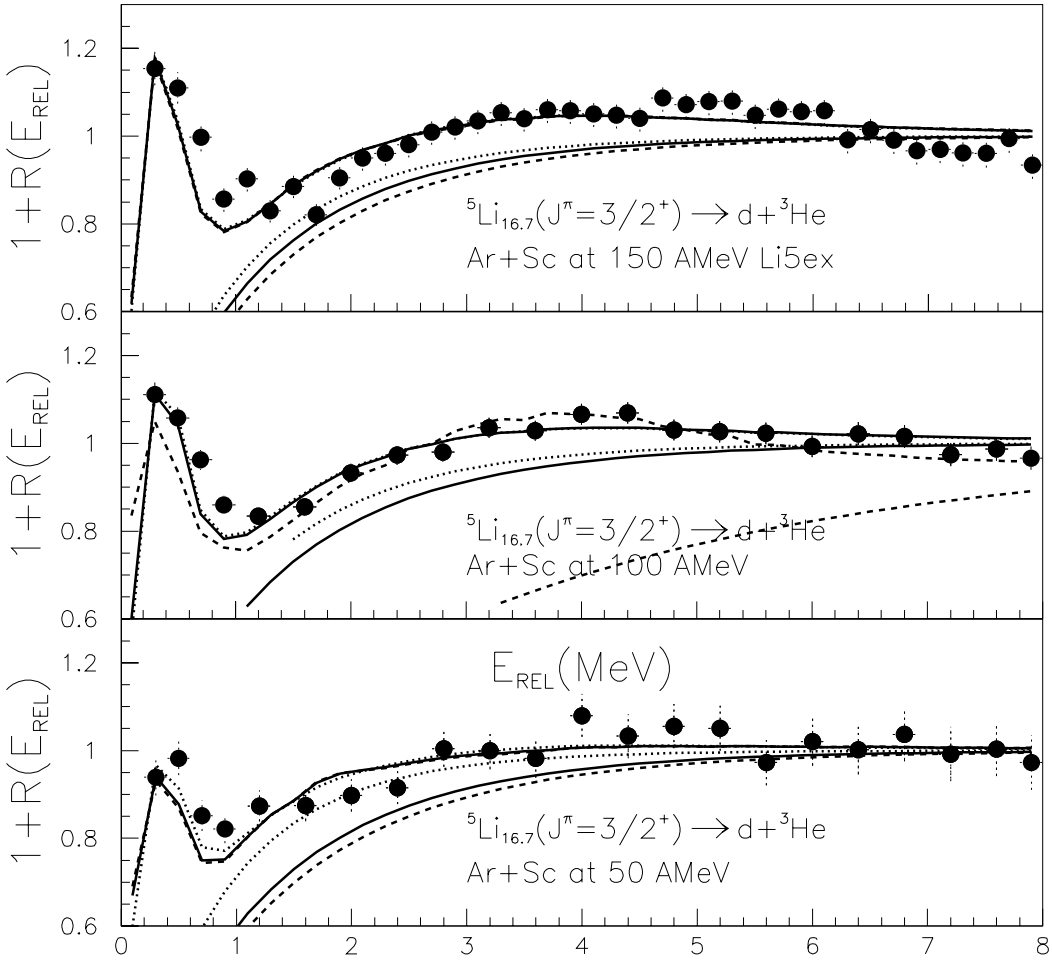

Figure 5.8: The d-^3He Correlation for Ar+Sc for 150,100,50 MeV/A respectively . The extremes of the background parameter are indicated.

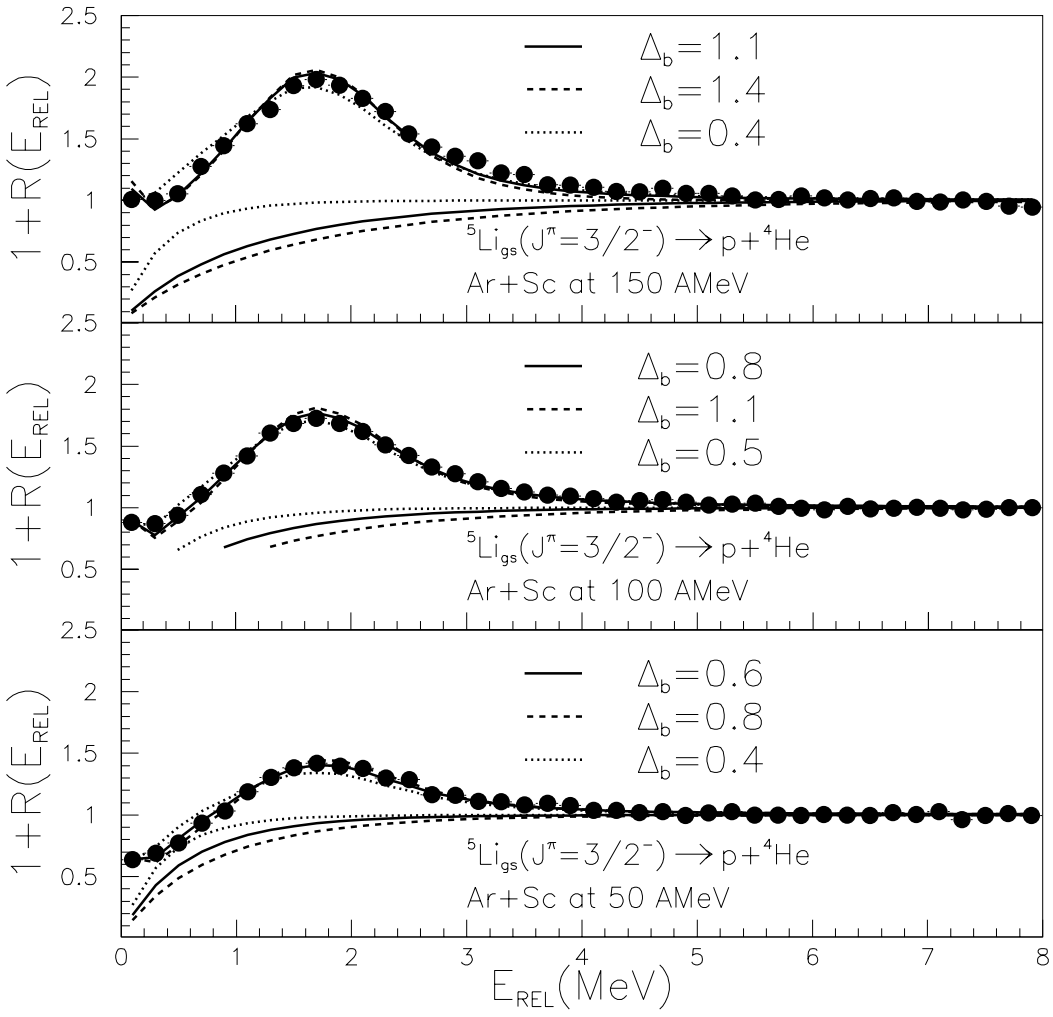

Figure 5.9: The p-α Correlation for Ar+Sc for 150,100,50 MeV/A respectively . The extremes of the background parameter are indicated.

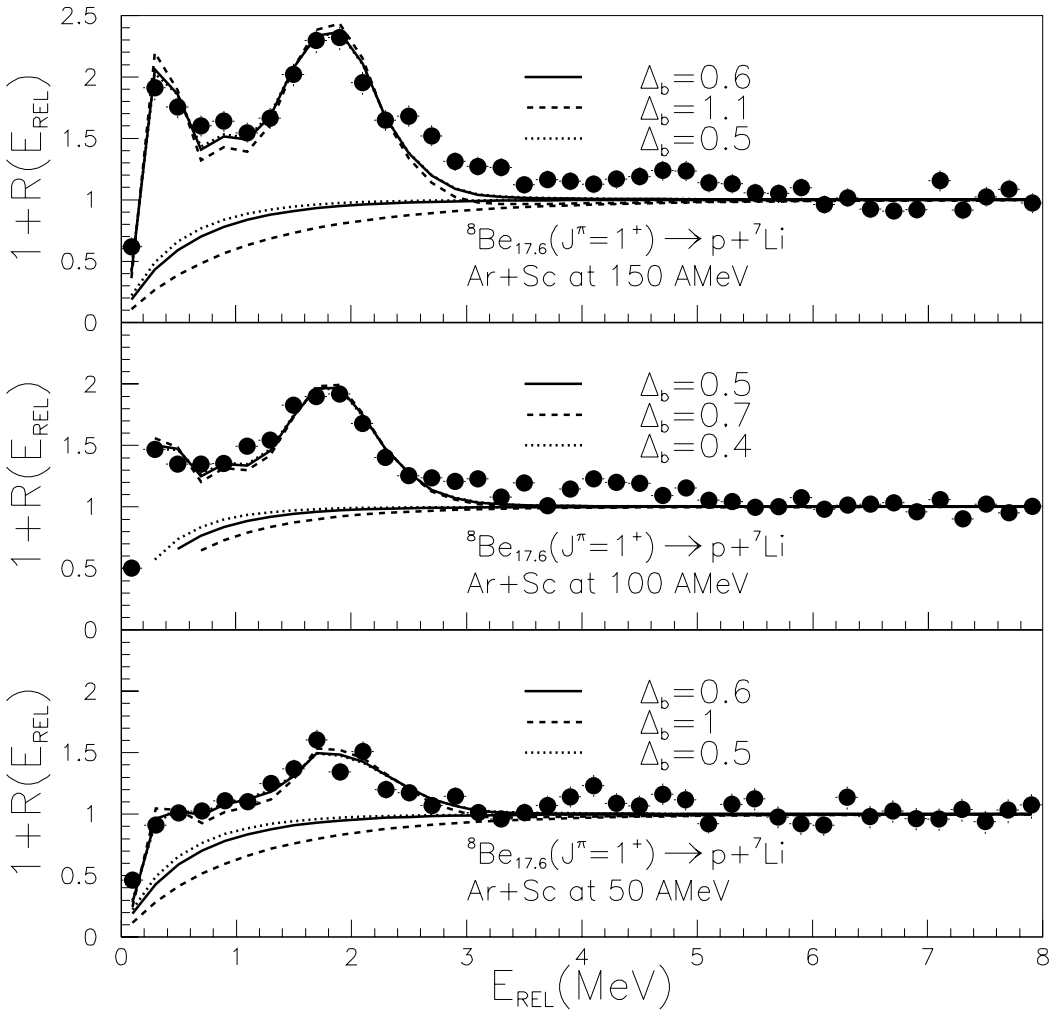

Figure 5.10: The p-^7Li Correlation for Ar+Sc for 150,100,50 MeV/A respectively . The extremes of the background parameter are indicated.

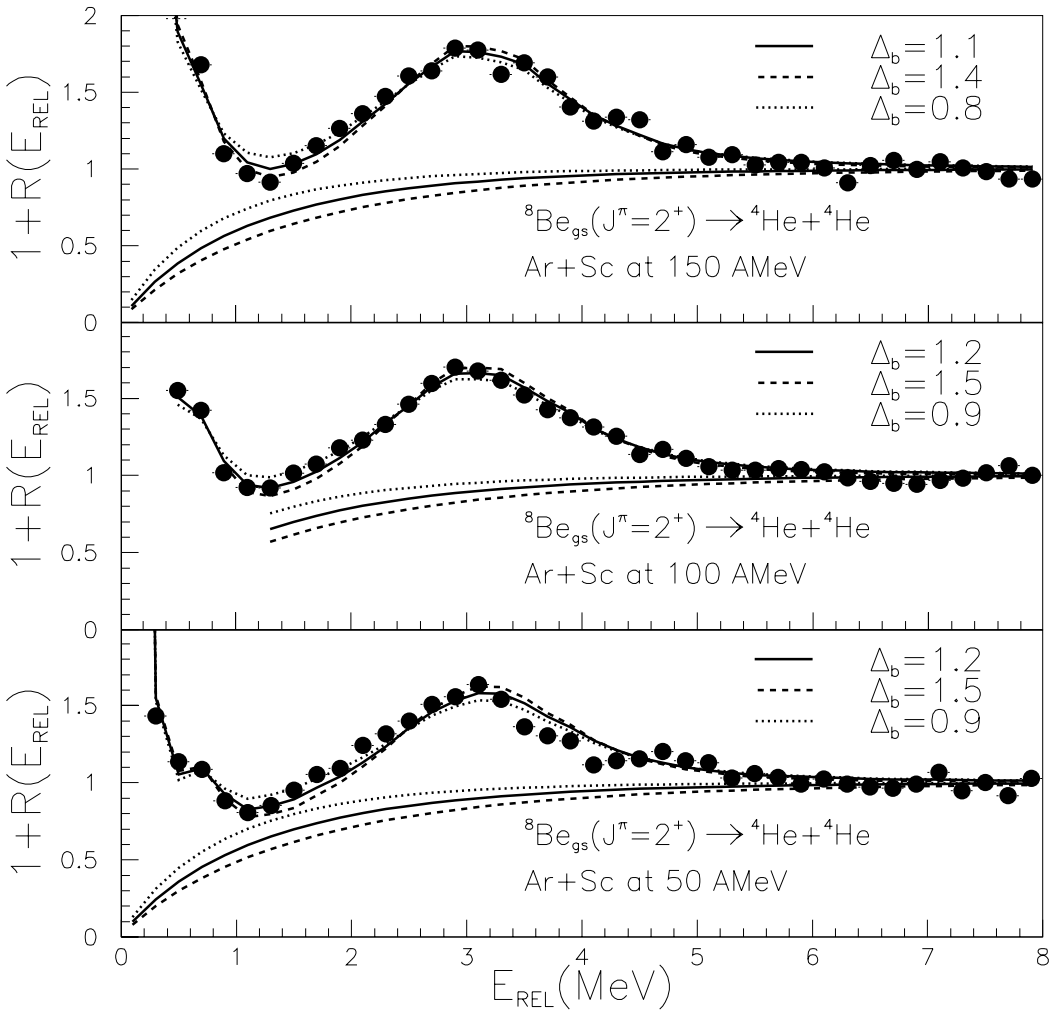

Figure 5.11: The α-α Correlation for Ar+Sc for 150,100,50 MeV/A respectively . The extremes of the background parameter are indicated.

5.2 Techniques of temperature extraction from correlation analysis.

Fundamentally, fitting the decay spectra in Figs. 5.2-5.11 is a relatively straightforward exercise, given

1) a well characterized background correlation function $[1 + R_{tot}(E_{rel})]$,

2) no significant secondary decay corrections to the excited state yields and

3) well known resonance line shapes that can be given by accurate phase shifts:

$$\mid \frac{dn_\lambda(E)}{dE} \mid_{chan} = e^{-\frac{E}{T}} \frac{2J_\lambda + 1}{\pi} \frac{d\delta_{i,res}}{dE} \frac{\Gamma_{chan,\lambda}}{\Gamma} , \tag{5.25}$$

Problems arise, however, when these conditions are not met, which often occurs when secondary decay corrections are not negligible. The simplest way to address this is to include a multiplicative constant a_λ to the right hand side of eq 5.25.

$$\mid \frac{dn_\lambda(E)}{dE} \mid_{chan} = a_\lambda e^{-\frac{E}{T}} \frac{2J_\lambda + 1}{\pi} \frac{d\delta_{i,res}}{dE} \frac{\Gamma_{chan,\lambda}}{\Gamma} , \tag{5.26}$$

It is an approximate correction to the original expression because it assumes that sequential feeding will populate the resonance lineshape in accordance to the original Boltzmann factor. With this modification, however, the expression is adequate to describe the experimental data and we will therefore do this even though it adds to the complexity of the description. This added complexity requires a more involved exploration of the uncertainties in the temperatures that are extracted. We discuss this strategy here.

The simplest procedure is to use Eq. 5.25 and fit for temperature T. In this case, the fit may be somewhat poorer in quality than desired, but the procedure is clear. A second procedure is to choose a reasonable value for T and then fit the spectra to obtain values for a_λ. The complexity of this second procedure depends upon whether the total widths Γ_λ are negligible compared to T or not. When the widths are negligible, it doesn't make any difference to the fit or to the final population probabilities

what you assume for T. For such narrow states, the excitation probability P_λ to be in an m-substate of the level λ is given by

$$P_\lambda \approx a_\lambda \cdot e^{-E_\lambda/T}. \tag{5.27}$$

When Γ_λ cannot be neglected, however, the population probability is given by a more complicated expression involving an integral over the experimental line shape:

$$P_\lambda = \frac{1}{2J_\lambda + 1} \int dE_{rel} [\sum_{chan} \{\frac{dn_\lambda}{dE_{rel}}\}_{chan}]. \tag{5.28}$$

For broad states, this integral can yield a population probability that is somewhat different than the value of the Boltzmann factor at energy E_λ. However, the impact of this difference on the temperature extracted from the excited state population will be small if the excitation energy is much larger than the temperature. This turns out to be the case for the inclusive spectra in Figs. 5.2-5.11.

Now we turn to the specific cases. The first case to discuss is that for ^4He. The efficiency function was calculated using the differential multiplicity of stable ^4He. The fits in Figs. 5.2 and 5.8 are obtained assuming the Breit-Wigner resonance parameters in Table 5.1. Because the first excited state at $E^* = 20.1MeV$ is rather narrow, these spectra were initially fitted in the narrow level limit by ignoring the Boltzmann factor $e^{-E^*/T}$ in Eq. 5.14 and determining from the fit the parameters a_λ for each of the state in Table 5.1. As we will see below during the discussion of the ^5Li and ^8Be spectra, this assumption introduce possible errors in the extracted temperatures for these spectra that are less than 100 KeV, which is negligible compared to the uncertainty from background subtraction. Ignoring the Boltzmann factor, provided the yield in the 20.21 MeV 0^+ excited state. Neglecting, for simplicity, the influence of feeding from heavier unbound nuclei, the excited state temperatures for this case which has a stable ground state are calculated from the expression:

$$\frac{Y_\lambda(2J_{stable}+1)}{Y_{stable}(2J_\lambda+1)} = a_\lambda^{fitted} * \frac{(2J_{stable}+1)}{(2J_\lambda+1)} = e^{-E_\lambda/T}\,, \tag{5.29}$$

which yields temperatures of 4.15, 4.3 ,4.25, and 4.35 at E/A = 35, 70, 100, and 120 MeV for central Kr+Nb collisions and 5.0, 5.6, and 5.55 at E/A = 50, 100, and 150 MeV for central Ar+Sc collisions. These results are listed in Table 5.2. From the other three excited states in ^4He, only the 2^- state at $E^* = 21.84MeV$, which is mainly responsible for the broad peak at $E_{rel} \approx 1.5MeV$, can be determined with sufficient accuracy to determine a temperature. Corresponding analyses of this peak are also given in Table 5.2. In both analyses, the major contribution to the uncertainty comes from the uncertainty in background subtraction.

The second case to discuss is that for ^5Li. Because ^5Li is not stable, the efficiency function was calculated using the differential multiplicity of stable ^6Li. This introduces some uncertainty into the analyses, but previous explorations of this uncertainty [90] have found that the uncertainty is to be small for analyses that do not have energy gates on the emitted species. The fits in Figs. 5.3-5.4 and 5.8-5.9 are obtained assuming the Breit-Wigner resonance parameters in Table 5.1. The spectra for the $p-\alpha$ correlation function are dominated by the $J^\pi = 3/2^-$ ground state and the spectra for the $d-^3He$ correlation function are dominated by the $J^\pi = 3/2^+$ excited state at $E^* = 16.7MeV$. These spectra were fitted in the narrow level limit by ignoring the Boltzmann factor $e^{-E^*/T}$ in Eq. 5.23 and determining from the fit the parameters a_λ for each state in Table 5.1. This provided the yields for both state. Neglecting, for simplicity, the influence of feeding from heavier unbound nuclei, the excited state temperatures for this case are calculated from the expression:

$$\frac{Y_1(2J_2+1)}{Y_2(2J_1+1)} = \frac{a_1^{fitted}(2J_2+1)}{a_2^{fitted}(2J_1+1)} = e^{-(E_1-E_2)/T}\,, \tag{5.30}$$

which yields temperatures of 4.4, 4.55,4.7, and 4.54 at E/A = 35, 70, 100, and

System	State(s) J^{π}	Temperature
Kr+Nb035AMeV	^{4}He* 0^{+}	4.15
Kr+Nb035AMeV	^{4}He* 2^{-}	4.35
Kr+Nb070AMeV	^{4}He* 0^{+}	4.3
Kr+Nb070AMeV	^{4}He* 2^{-}	4.86
Kr+Nb100AMeV	^{4}He* 0^{+}	4.25
Kr+Nb100AMeV	^{4}He* 2^{-}	4.603
Kr+Nb120AMeV	^{4}He* 0^{+}	4.35
Kr+Nb120AMeV	^{4}He* 2^{-}	4.726
Kr+Nb035AMeV	^{5}Li $3/2^{-}$ + ^{5}Li $3/2^{+}$	4.4
Kr+Nb070AMeV	^{5}Li $3/2^{-}$ + ^{5}Li $3/2^{+}$	4.55
Kr+Nb100AMeV	^{5}Li $3/2^{-}$ + ^{5}Li $3/2^{+}$	4.7
Kr+Nb120AMeV	^{5}Li $3/2^{-}$ + ^{5}Li $3/2^{+}$	4.55
Kr+Nb035AMeV	^{8}Be 2^{+} + ^{8}Be 1^{+}	3.71
Kr+Nb070AMeV	^{8}Be 2^{+} + ^{8}Be 1^{+}	4.23
Kr+Nb100AMeV	^{8}Be 2^{+} + ^{8}Be 1^{+}	4.48
Kr+Nb120AMeV	^{8}Be 2^{+} + ^{8}Be 1^{+}	4.5
Ar+Sc050AMeV	^{4}He* 0^{+}	5.0
Ar+Sc050AMeV	^{4}He* 2^{-}	4.8009
Ar+Sc100AMeV	^{4}He* 0^{+}	5.6
Ar+Sc100AMeV	^{4}He* 2^{-}	5.2404
Ar+Sc150AMeV	^{4}He* 0^{+}	5.55
Ar+Sc150AMeV	^{4}He* 2^{-}	5.2948
Ar+Sc050AMeV	^{5}Li $3/2^{-}$ + ^{5}Li $3/2^{+}$	4.4
Ar+Sc100AMeV	^{5}Li $3/2^{-}$ + ^{5}Li $3/2^{+}$	4.5
Ar+Sc150AMeV	^{5}Li $3/2^{-}$ + ^{5}Li $3/2^{+}$	4.46
Ar+Sc050AMeV	^{8}Be 2^{+} + ^{8}Be 1^{+}	4.3
Ar+Sc100AMeV	^{8}Be 2^{+} + ^{8}Be 1^{+}	4.62
Ar+Sc150AMeV	^{8}Be 2^{+} + ^{8}Be 1^{+}	5.0

Table 5.2: Excited state temperatures using exponential background ,and assuming narrow peaks.

120 MeV for central Kr+Nb collisions and 4.4, 4.5, and 4.46 at E/A = 50, 100, and 150 MeV for central Ar+Sc collisions. These results are listed in Table 5.2. In these analyses, the major contribution to the uncertainty comes from the uncertainty in background subtraction.

The last case to discuss is that for ^8Be. Because ^8Be is not stable, the efficiency function was calculated using the differential multiplicity of stable ^9Be. This introduces some uncertainty into the analyses, but previous explorations of this uncertainty [90] have found that the uncertainty appears to be small for analyses that do not have energy gates on the emitted species. The fits in Figs. 5.5-5.6 and 5.10-5.11 are obtained assuming the Breit-Wigner resonance parameters in Table 5.1. The spectra for the $\alpha - \alpha$ correlation function are dominated by the $J^\pi = 2^+$ ground state and the spectra for the $p - ^7 Li$ correlation function are dominated by the $J^\pi = 1^+$ excited state at $E^* = 17.6 MeV$. These spectra were fitted in the narrow level limit by ignoring the Boltzmann factor $e^{-E^*/T}$ in Eq. 5.23 and determining from the fit the parameters a_λ for each of the state in Table 5.1. This provided the yields for both state. Neglecting, for simplicity, the influence of feeding from heavier unbound nuclei, the excited state temperatures for this case are calculated from the expression:

$$\frac{Y_1(2J_2+1)}{Y_2(2J_1+1)} = \frac{a_1^{fitted}(2J_2+1)}{a_2^{fitted}(2J_1+1)} = e^{-(E_1-E_2)/T}\,, \tag{5.31}$$

which yields temperatures of 3.71, 4.23,4.48, and 4.5 at E/A = 35, 70, 100, and 120 MeV for central Kr+Nb collisions and 4.3, 4.62, and 5.0 at E/A = 50, 100, and 150 MeV for central Ar+Sc collisions. These results are listed in Table 5.2. In these analyses, the major contribution to the uncertainty comes from the uncertainty in background subtraction.

These fits described above were obtained by setting $T = \infty$ in Eq. 5.23, which introduces small distortions to the resonance line shapes. In order to assess the

influence of these distortions on the temperature values we refitted the ^5Li and ^8Be decay spectra by setting the a_λ for the two states to be equal and adjusting the temperature to find the best fit. This was done only for the data at E/A=100 MeV. The resulting temperatures for the ^5Li thermometer were 4.5 and 5.1 MeV for the new fits to the Ar+Sc collisions and Kr+Nb collisions, respectively, instead of the previous values of 4.59 and 5.14 MeV. Similarly,the resulting temperatures for the ^8Be thermometer were 4.7 and 4.1 MeV for the new fits to the Ar+Sc collisions and Kr+Nb collisions, respectively, instead of the previous values of 4.6 and 4.0 MeV. These changes are less than the uncertainty due to the background subtraction.

5.3 Dependence of the temperature on incident energy and system size

When the Caloric curve result was first published by the Aladin collaboration, questions raised about the increase in the isotope temperature at small Z_{bound} that was attibuted to the system leaving the mixed phase region and becoming a nucleonic gas. One of the main questions could be understood by considering the reaction within the context of the participant spectator model. This model, central to the physical picture proposed by the Aladin group, suggested that the nuclear fragments whose charge summed to Z_{bound} were the bound remnants of the projectile spectator. The decrease in Z_{bound} reflects to a large extent the decrease in the size of the hot projectile spectator that avoids that target as the impact parameter is decreased. Natowitz et al. [80] noted that calculations of the maximum or limiting temperatures of projectile-like residues predicted an increase of the limiting temperature as the system size is decreased. Could this be the origin of the increase at small Z_{bound}?

The present study was motivated to explore this by measuring the caloric curve

as a function of incident energy for central collisions for a variety of physical systems. Each system had a fixed total mass and the measurement of the excited state and isotope temperatures as a function of incident energy could be regarded as effectively a measurement of the caloric curve for a system of fixed size as a function of excitation energy or temperature. However, we need to be able to calculate the relationship between excitation energy and beam energy in order to convert the resulting data into a caloric curve.

Figs. 5.13 and 5.14 show the incident energy dependence of the excited state temperatures for central Ar+Sc and Kr+Nb collisions. Fig. 5.15 shows the corresponding data for Au+Au collisions measured by ref. [100]. In all three figures, the isotope temperatures for the HeLi thermometer are shown and in Figs. 5.13 and 5.14, the isotope temperatures for the CLi thermometer are shown as well. In order to relate the trends from one reaction to another, a dotted line is drawn through the average trends for the Ar+Sc excited state temperatures and a dashed line is drawn through the corresponding trends for the HeLi thermometer. These same trendlines are also shown on the other two figures that follow as well.

In all cases, the trends for the excited state thermometers are similar. A gradual increase in average trends in the temperature values is observed, ranging from values of about 3.7-4.4 MeV at E/A=35 MeV to 4.25-5.6 MeV at E/A=100 MeV to 4.6-5.6 MeV at the E/A=150 MeV. Somewhat higher values would result if an attempt were made to correct the observed values for secondary decay in order to obtain the corresponding temperatures of the primary fragments. Such corrections were made by Huang et al. [51, 50], but can only be accurately done if the system is assumed to be in equilibrium.

Values observed for the CLi isotopic thermometer are similar to those obtained from the excited state thermometers. The values for the temperature extracted from

the HeLi thermometer starts out equal to the other thermometers at E/A = 35 MeV, but the HeLi values increase more rapidly with incident energy. This increase is dependent on the mass of the system; which can be readily seen by comparing the extracted values to the dashed line, which is the same in all figures. The energy dependence for the Ar+Sc system coincides with the line, but energy dependence Kr+Nb system is significantly lower than the line and this is even more so for the Au+Au system.

We note that E/A=100 MeV is an energy which is measured for all three systems. It is the natural energy at which the temperature values for the three systems can be compared. This comparison is shown in Fig. 5.12. One can see that the excited states thermometers give temperatures that decrease only slightly with mass or are constant. The temperatures values for the HeLi thermometer, however, decrease strongly in magnitude with increasing system size. This trend is consistent with some of the increase in temperature observed in the original Aladin caloric curve due to a system size effect.

Here, however, we have the benefit of the reasoning laid out in Section 4.3.2. There it was noted that the ^3He abundance is in great excess of the thermal predictions for the temperatures that describe the fragment multiplicities. We recall the discussion in Section 4.3.2 where it was noted that transport theory predicts abundant emission of ^3He prior to the breakup stage where the fragments are emitted. We also note from section 4.3.3 that generalized isoscaling applied to these light particles. Thus, one could argue that the high HeLi temperatures represent the early dynamical stage, when the system is as high density and high "temperature" and the other thermometers are measuring the temperatures at a later stage after the systems has cooled by expansion and radiative emission.

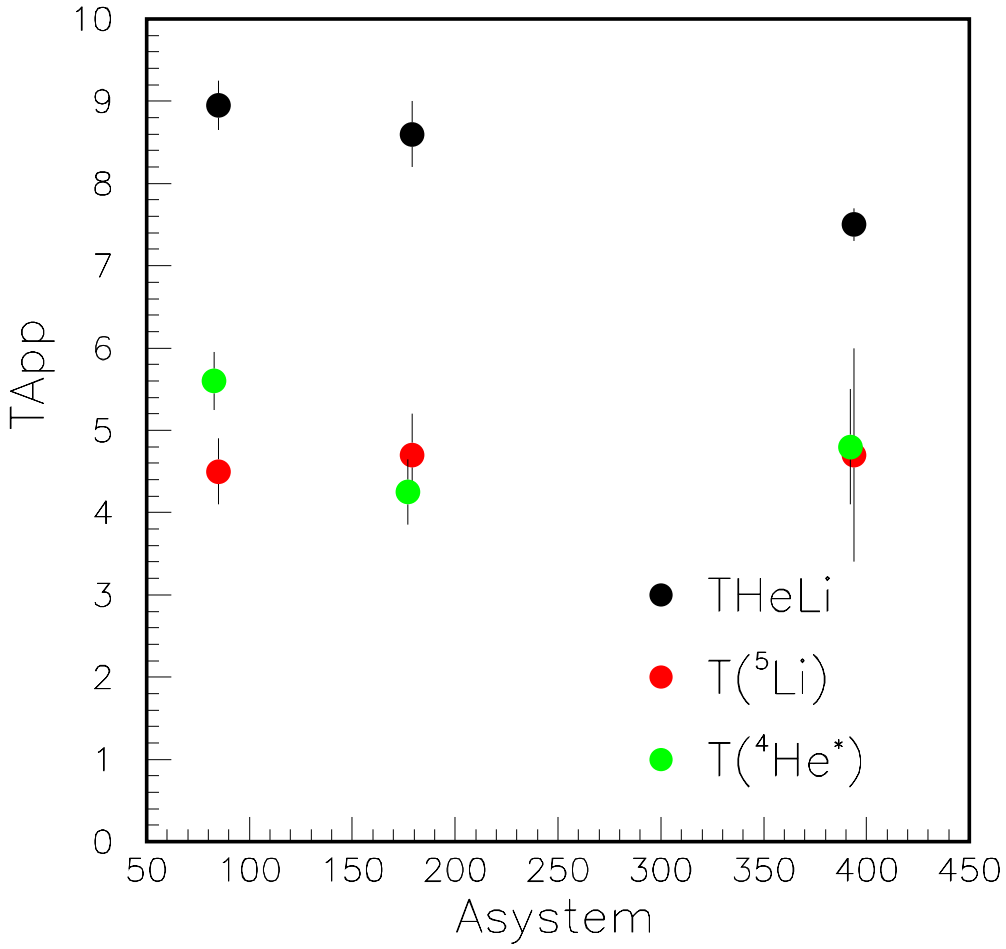

Figure 5.12: Temperature dependence on system size for a common beam energy of 100 MeV/A.

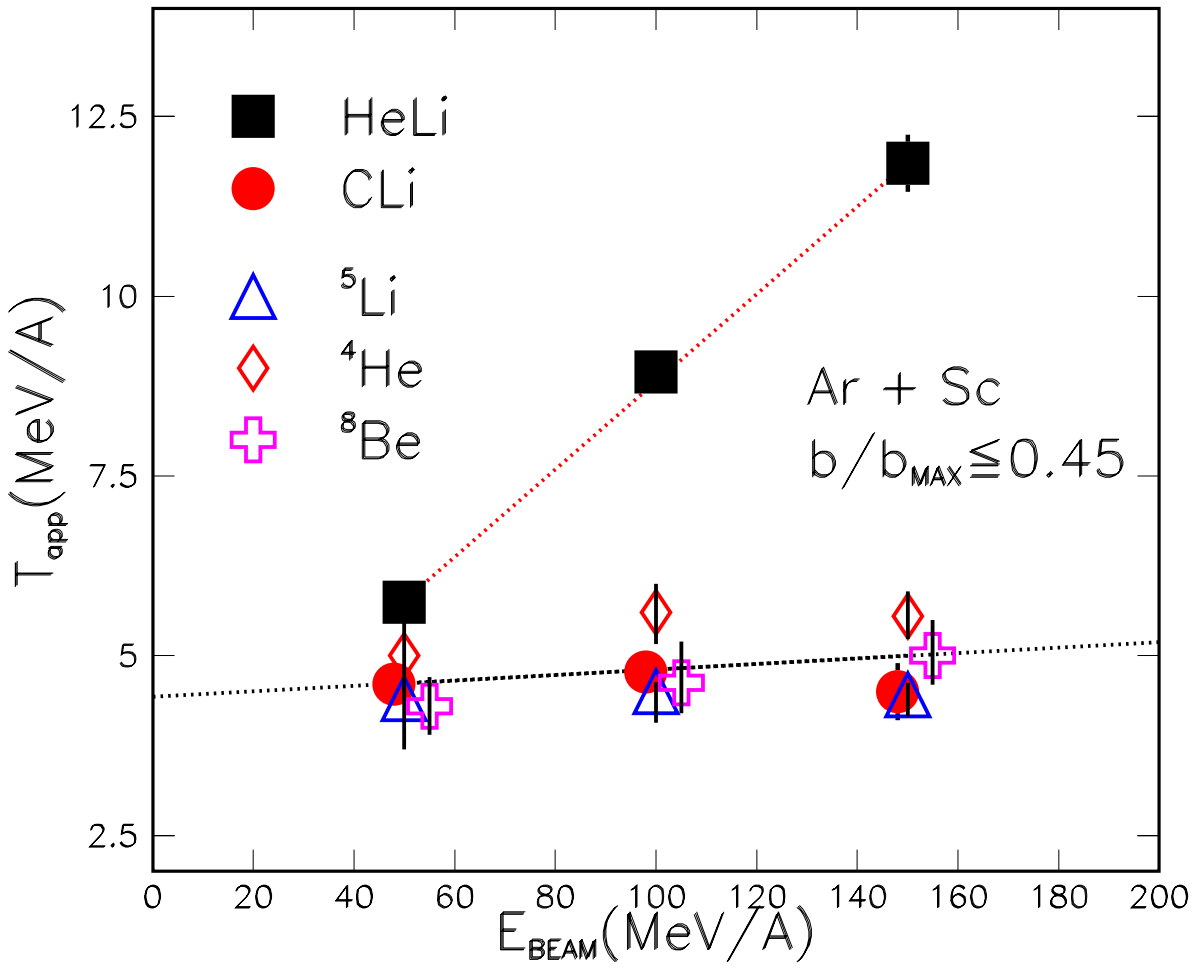

Figure 5.13: Temperature dependence on system Ar+Sc, $A_{sys} = 81$.

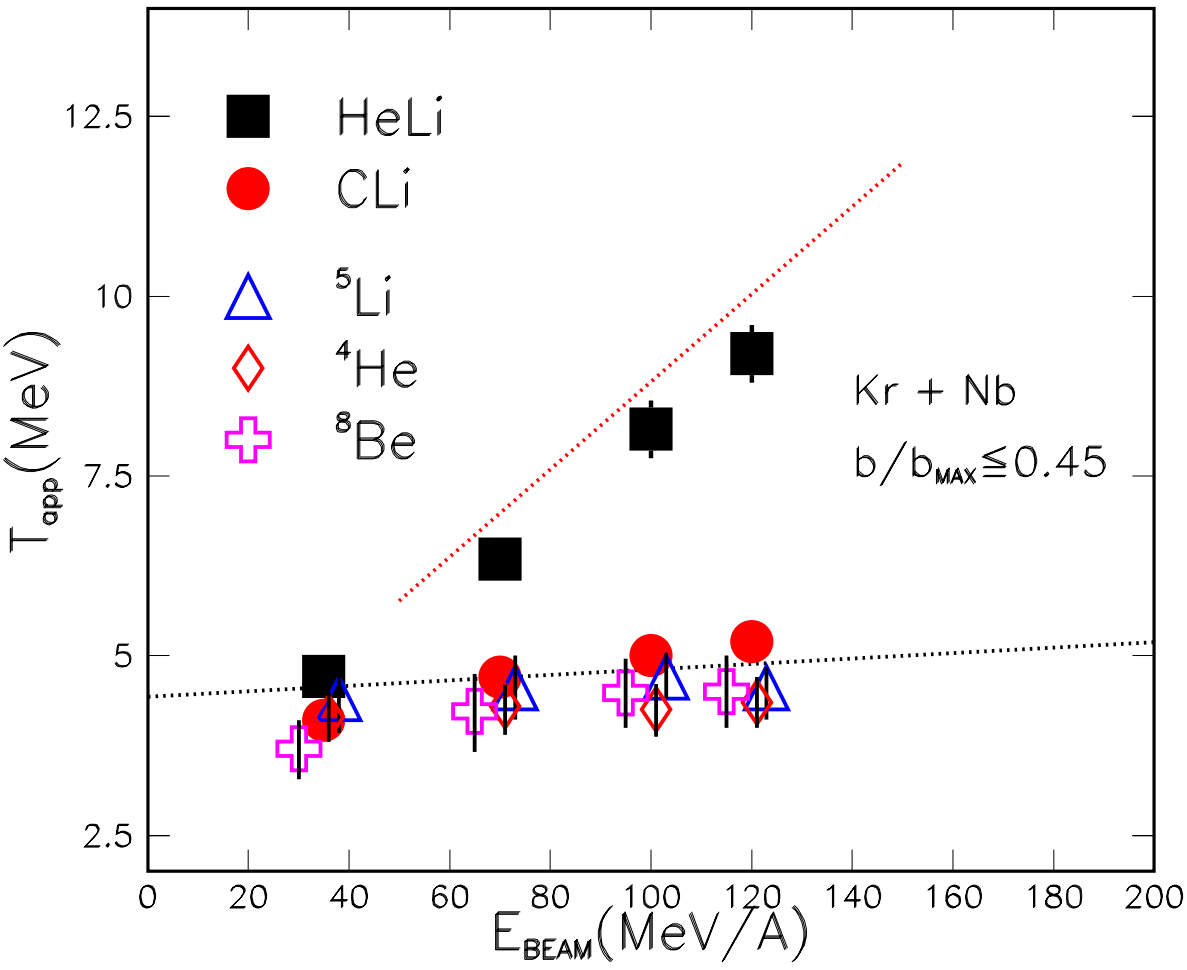

Figure 5.14: Temperature dependence on system Kr+Nb, $A_{sys} = 179$.

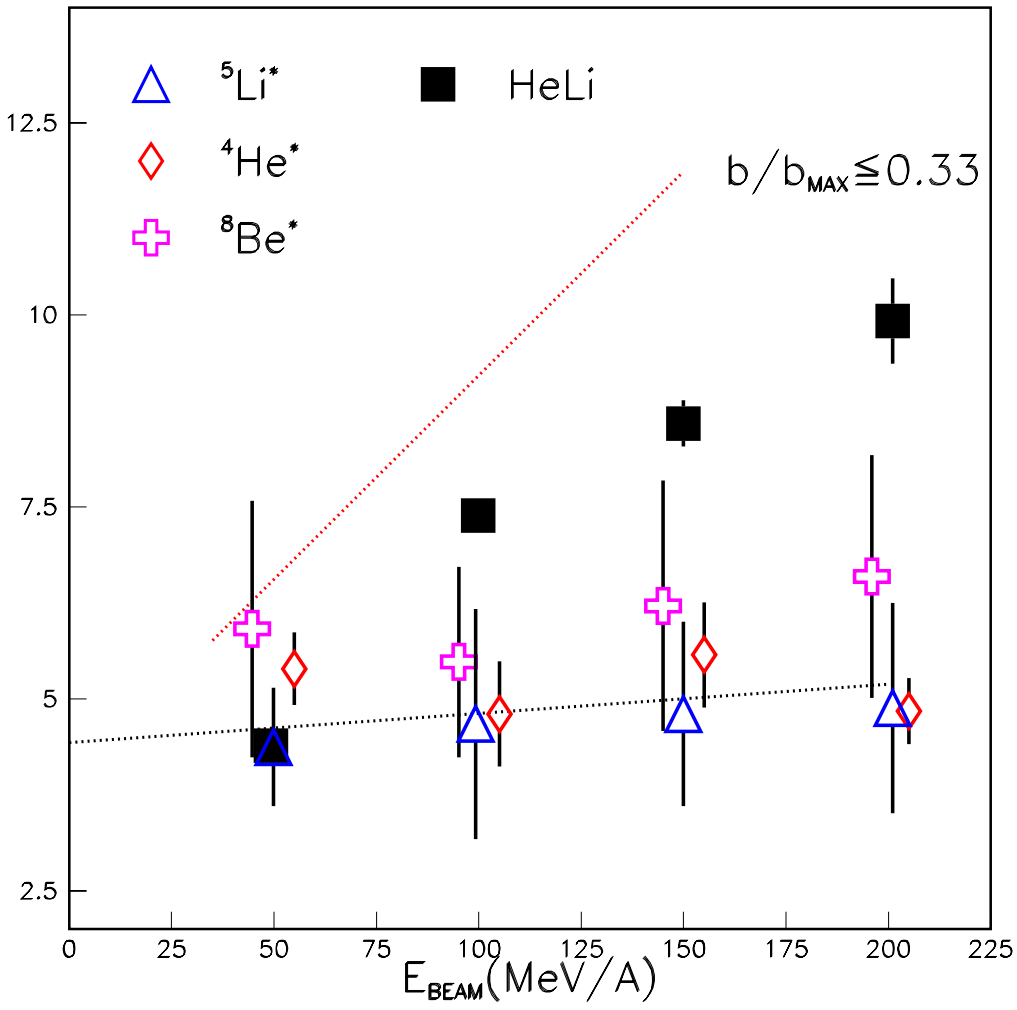

Figure 5.15: Temperature dependence on system Au+Au $A_{sys} = 358$. Data from Serfling *et. al.* [100]

5.4 Evidence for cooling from excited state population measurements: Breit-Wigner analysis

The difference between the trends shown by the excited state thermometers, the CLi isotope thermometer and the trend shown by the HeLi thermometer is potentially rather disturbing. On the one hand, we have a large number of thermometers that give similar results. We can also partly discount the HeLi temperature because of the theoretical arguments presented in Section 4.3.2 which state that there is a large contribution to the ^3He from preequilibrium emission with a potentially large dynamical component. On the other hand, however, the HeLi thermometer combined with the generalized isoscaling results suggest that the early high density stage was considerably more excited than the later breakup stage. This is bolstered by the large excitation energies per nucleon or temperatures one would compute if the early stage could be approximated by a thermalized source. Why is there no indication of this cooling in the excited state population data?

Cooling can be most easily examined by looking for a dependence of the excited state temperature on the energy of the detected species. This follows from several considerations. First, the temperature of the system will decrease monotonically with time reflecting cooling by expansion and by radiation. Second, more energetic particles tend to be emitted earlier in the collisions. The simplest reason for this, of course, is that the more energetic particles move away more quickly. If collective motion is important, dynamical BUU calculations predict that the more energetic particles will tend to be on the outside of the system and be emitted earlier. If radiative emission is important, the initial temperature will be higher; the spectrum for emission decrease as exp(-E/T); again the most energetic particles correlate with the highest temperatures.

To address this question, we undertook to analyze the ^4He thermometer data subject to gates on the energy of the ^4He in the center of mass. To select excited ^4He nuclei from the participant source, we selected events with $\hat{b} \leq 0.45$ and ^4He nuclei emitted at angles of $70^o \leq \theta_{CM} \leq 110^o$. Figure 5.16 shows the p-t correlation functions for Ar+Sc (left side) and Kr+Nb (right side) collisions at E/A=100 MeV. The figure is arranged into four rows corresponding from top to bottom to gates on the ^4He kinetic energy of $E_{CM} \leq 30MeV$, $30MeV < E_{CM} \leq 50MeV$, $50MeV < E_{CM} \leq 70MeV$, and $70MeV < E_{CM}$. The solid lines correspond to the exponential background fit shown also in Figure 5.16.

The correlation functions show a broad structure at $E_{rel} \leq 4MeV$ which corresponds to excitation of four excited states in ^4He. For ease of reference, detailed structural information for these states is recapitulated in Table 5.4 and the summary in Table 5.7. The magnitudes of these correlation functions increase significantly as the center of mass energy of the ^4He increases. This increase indicates that the spatial region from which the p and t are emitted is larger or longer-lived or both for the less energetic particles in the center of mass. If a significant fraction of the protons or tritons were originating from long lived secondary decay of nuclei other than ^4He, this could be a reason for the decrease.

The extraction of temperature information from these data requires an accurate estimation of the background. The exponential backgrounds shown in Fig. 5.16 represent a reasonable choice for that background, but it is interesting to consider whether one can use data from neighboring nuclei without strong resonances at low energy in order to place constraints on the form of the background correlation and its energy dependence. Thus, correlation functions between the various hydrogen and helium isotopes were analyzed, but many of them have resonances complicating the analysis. Perhaps, the best case is the p-d correlation function, which has been

analyzed with the same energy and impact parameter gates as for the p-t correlation function.

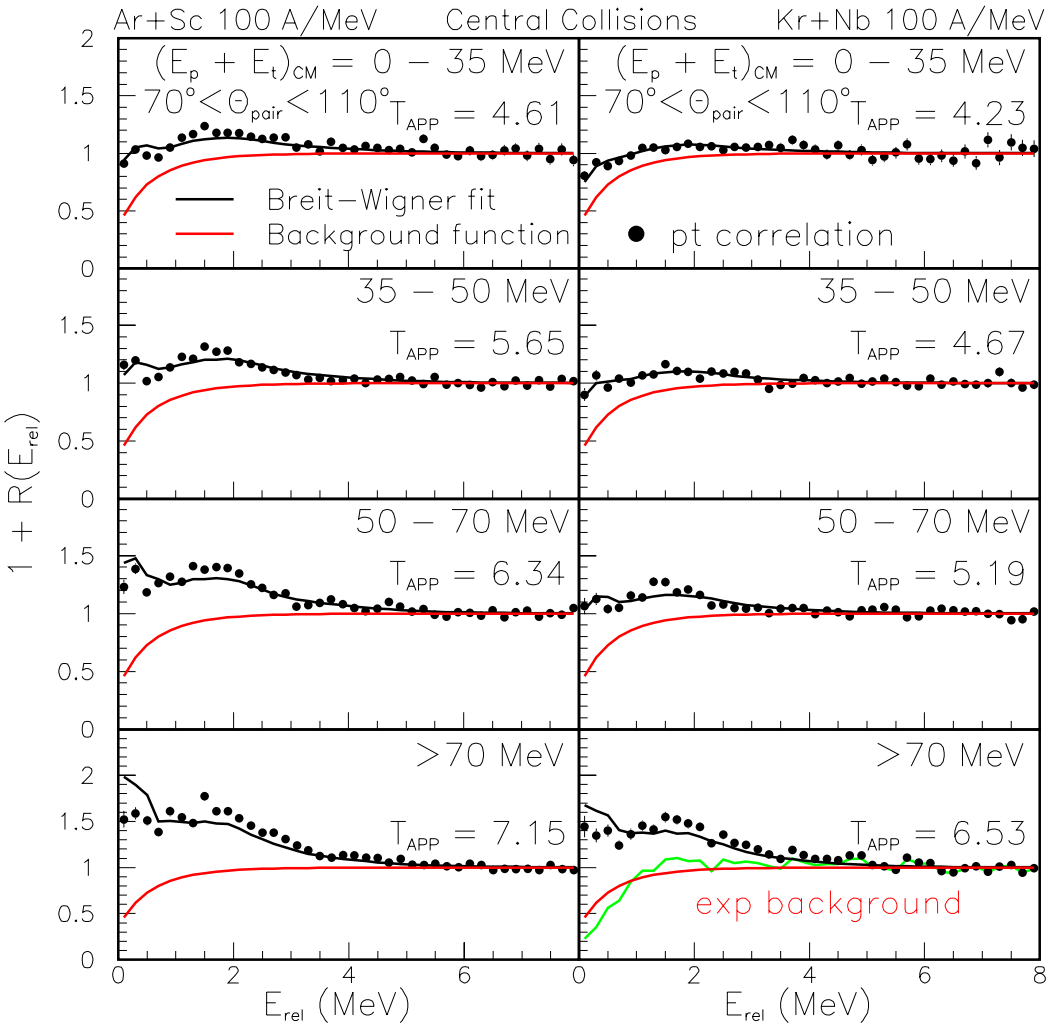

Figure 5.16: Single parameter Breit-Wigner fit of pt correlation on an exponential background. The data was obtained using a cut between 70 and 110 degrees in CMS and four energy cuts are indicated.

Figure 5.17 shows the gated p-d correlation functions. They are nearly flat except for a minimum at low relative energy that has about the same width for all energy gates. The red solid line in the figure is the function

$$BG_{pd}(E) = 1 - \frac{2}{3} e^{-(\frac{E}{\Delta_b})^d} , \tag{5.32}$$

which lies closer to the data than does the exponential background discussed previously, which is shown here by the dashed line. We designate this as the fitted p-d background. These two functional forms, fitted p-d background and exponential background, were used in the analysis. Surprisingly, the experimental p-d correlation function exceeds unity at some relative energies in the two highest energy gates. This effect cannot be attributed to Coulomb interactions. It could be the result of some repulsive strong interaction effect or due to the influence of collective motion; it is not clear that the p-t background correlation function should exceed unity.

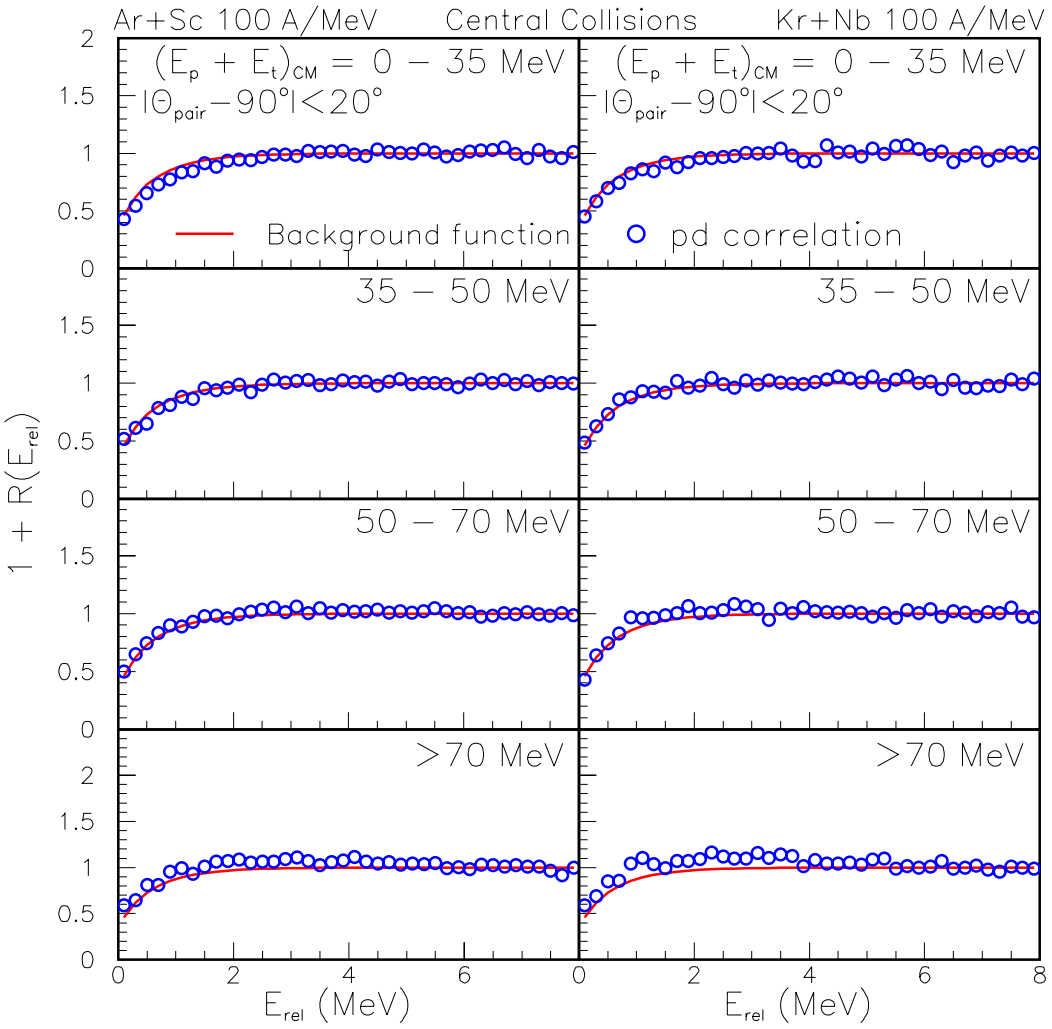

Figure 5.17: p-d background versus relative energy used for pt correlation for both Breit-Wigner and S-matrix analysis. The data was obtained using a cut between 70 and 110 degrees in CMS.

Fits assuming the exponential background and a single fixed temperature for all four states are shown in Figure 5.16. Fits assuming the fitted p-d background and a single fixed temperature for all four states are shown in Figure 5.18. The excited state temperatures extracted from the fits are shown in the panels of the figure also in Table 5.4 and the summary table 5.7 . In both cases, the extracted temperatures increase with center of mass energy, confirming the expectation that the excited state thermometers will show evidence for the earlier stages of the reaction being hotter.

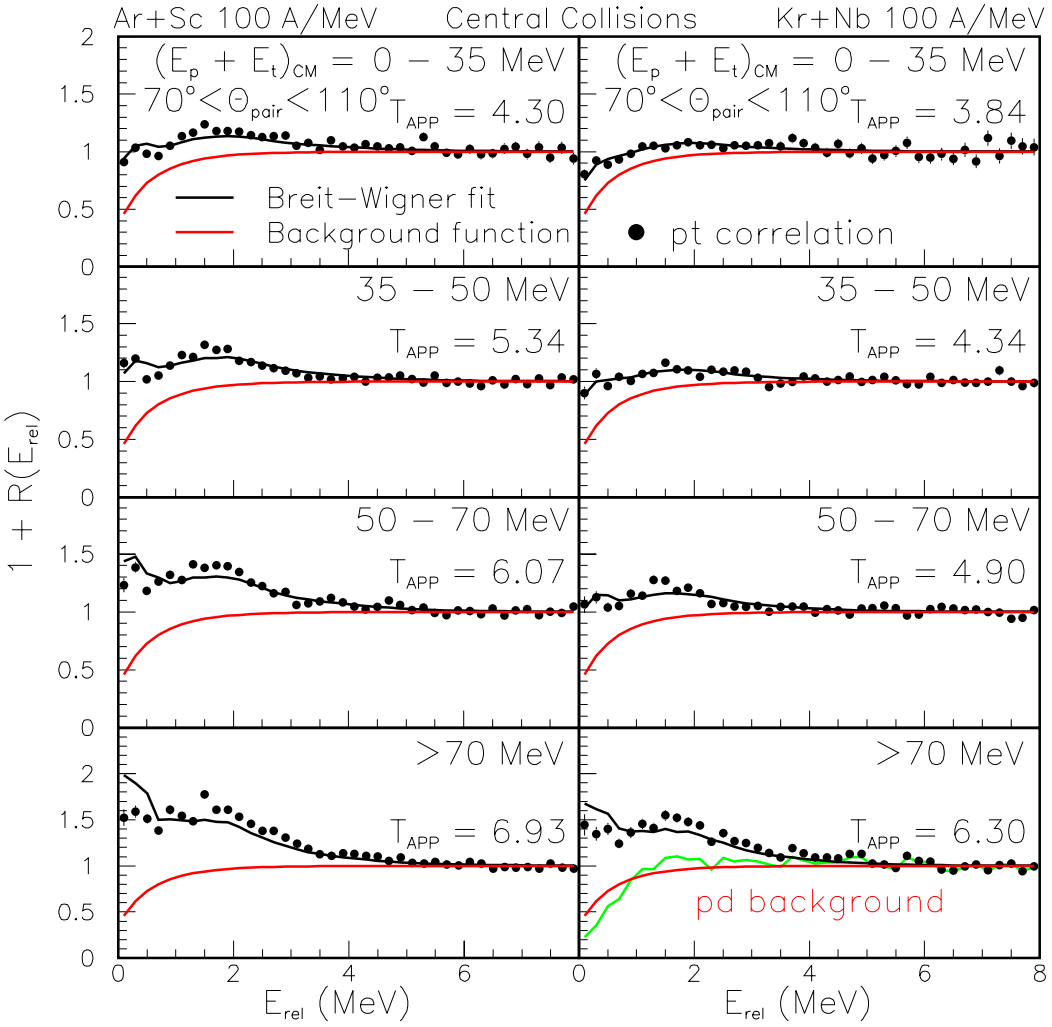

Figure 5.18: Single parameter Breit-Wigner fit of pt correlation on a pd background. The data was obtained using a cut between 70 and 110 degrees in CMS.

In general, the quality of the fits are reasonably good for the lower three energy gates, but the calculation overpredicts the yield at $E_{rel} < 0.35MeV$. We have explored three possible explanations for this:

1) the possibility that the background has the wrong shape,

2) The possibility that the states are not populated statistically, and

3) the possibility that the line shapes for the excited states are not correct.

Concerning the possibility that the background has the wrong shape, it is clear that one can construct a background that will make the fit go through the points. This can be done by taking the difference between the black solid line and the data and subtracting this difference from the background curve. Keeping the resonance contribution the same, the sum of resonances and background will equal the data. The background necessary to do this is illustrated by the solid green line in the lower right panel of Fig. 5.18. Note, that the green background lies below the fitted p-d background at $E_{rel} < 1MeV$, which is opposite to the trend of the actual p-d correlation (see Fig. 5.18).

Turning to the possibility that the states are not populated statistically, we have refitted the correlation function, allowing the low spin 0^+ and 0^- states to have a different population probability and temperature from the higher spin 2^- and 1^- states. These fits are shown in Figs. 5.19 and 5.20. Clearly, this improves the fit, but at the cost of having a higher temperatures for the higher spin states than for the lower spin states, for the highest E_{rel} gate. (The differences in the lower energy gates are smaller than the error bars of those fits.)

A tendency for high spin state to be overpopulated with respect to the low spin states was observed in case of ^{10}B fragments emitted in inclusive $^{14}N + Ag$ and peripheral $^{36}Ar + Au$ collisions at E/A=35 MeV [83, 130]. This was interpreted as an indication that equilibrium was not achieved in those reactions. It could also be the

case here that the most energetic particles are emitted before the system thermalizes.

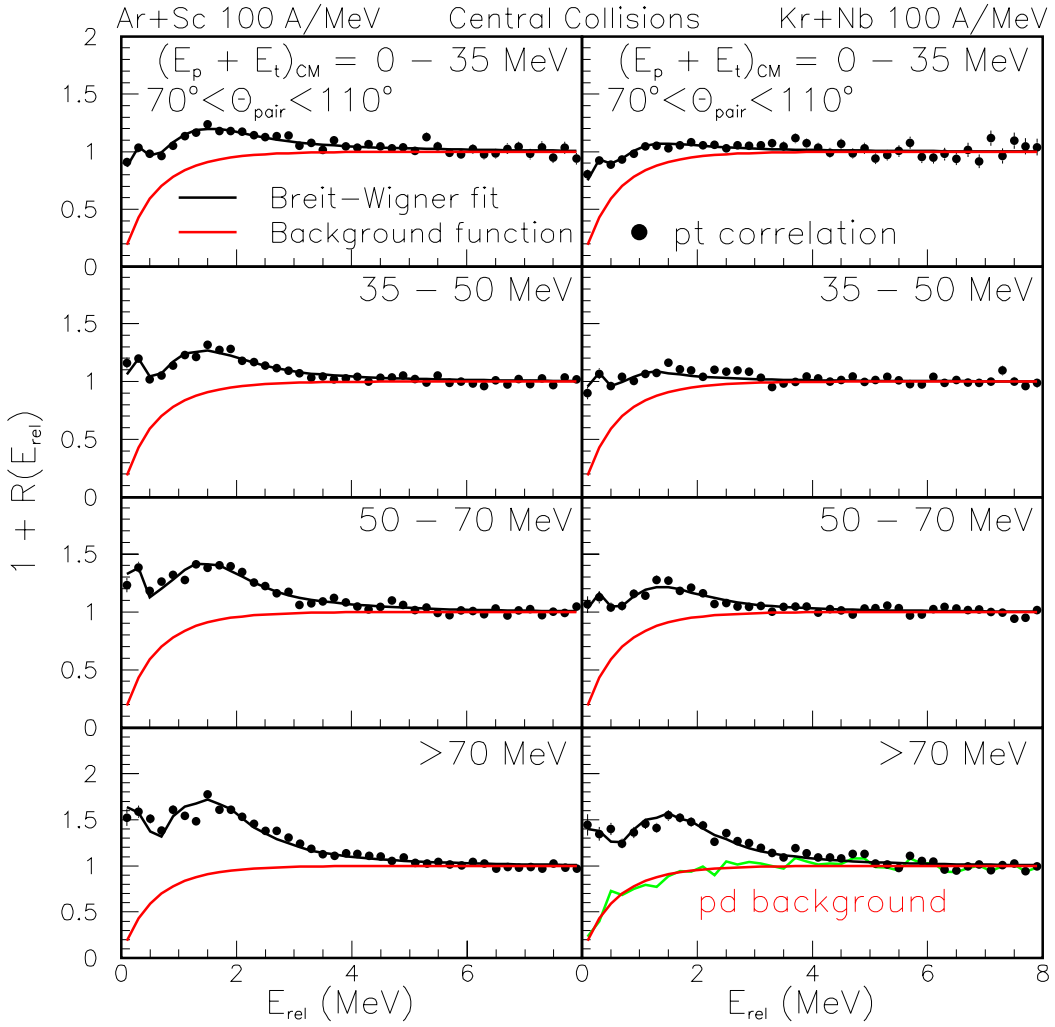

Figure 5.19: Two parameter Breit-Wigner fit of pt correlation on a pd background. The data was obtained using a cut between 70 and 110 degrees in CMS.

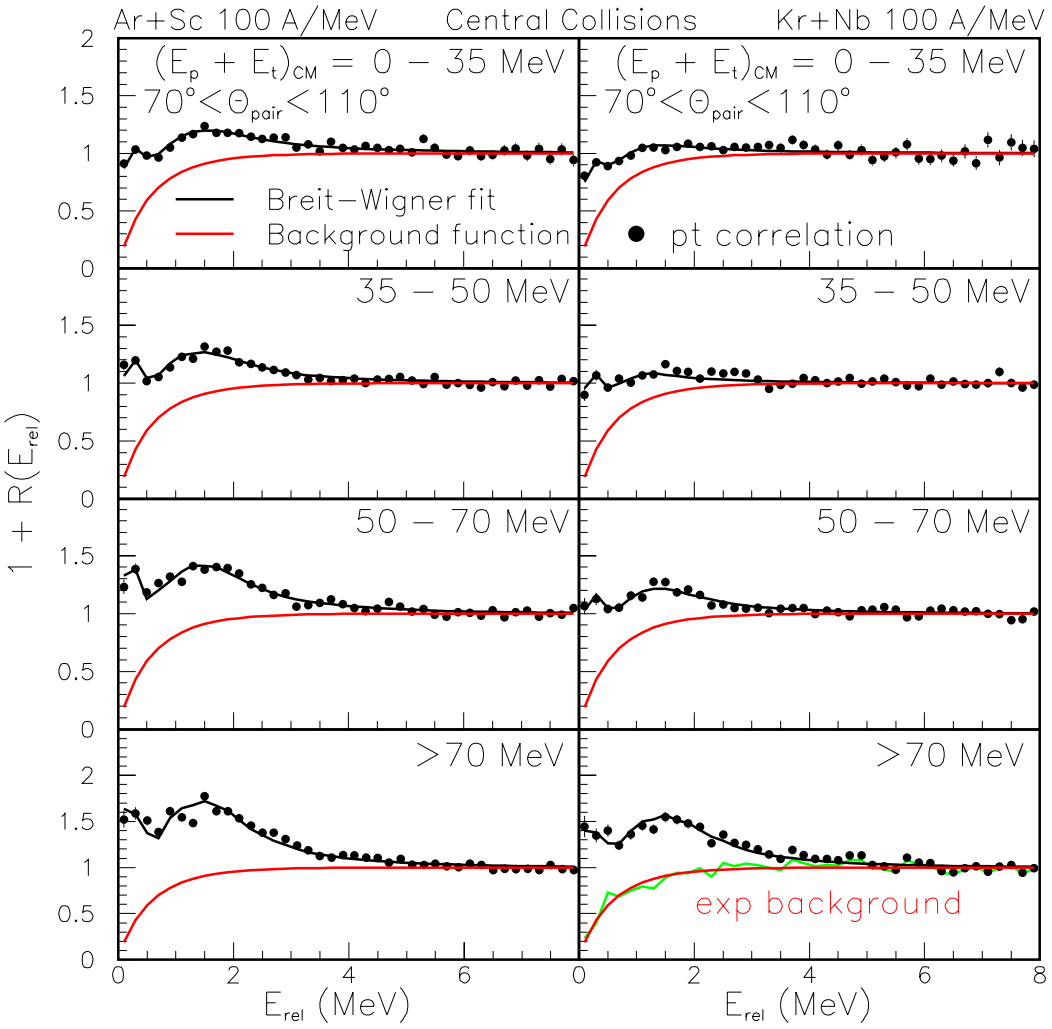

Figure 5.20: Two parameter Breit-Wigner fit of pt correlation on an exponential background. The data was obtained using a cut between 70 and 110 degrees in CMS and four energy cuts are indicated.

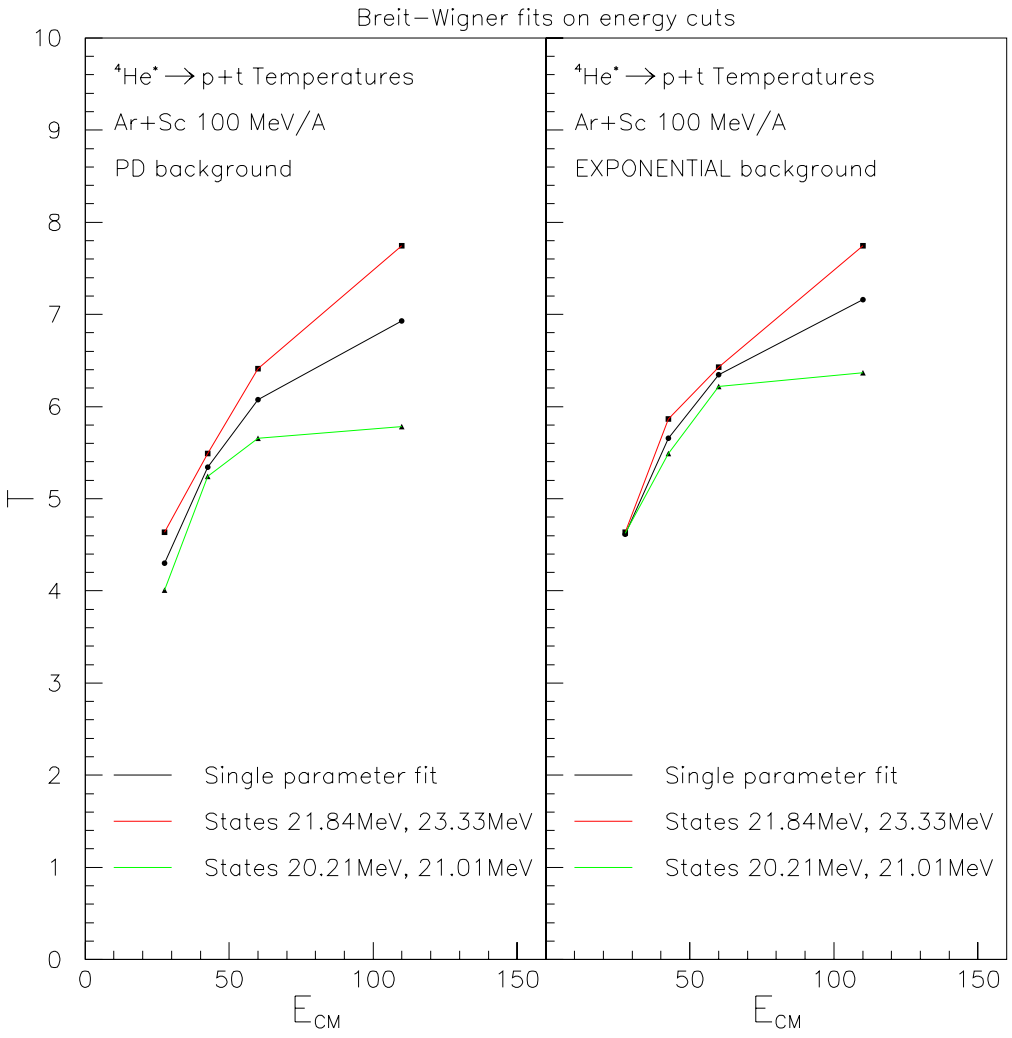

Figure 5.21: Single parameter Breit-Wigner fit of pt correlation for Ar+Sc 100 MeV/A. The upper and lower temperature bounds are the temperatures determined by two parameter fit. The two paramater fit gives a measure of systematic error with the previous panels.

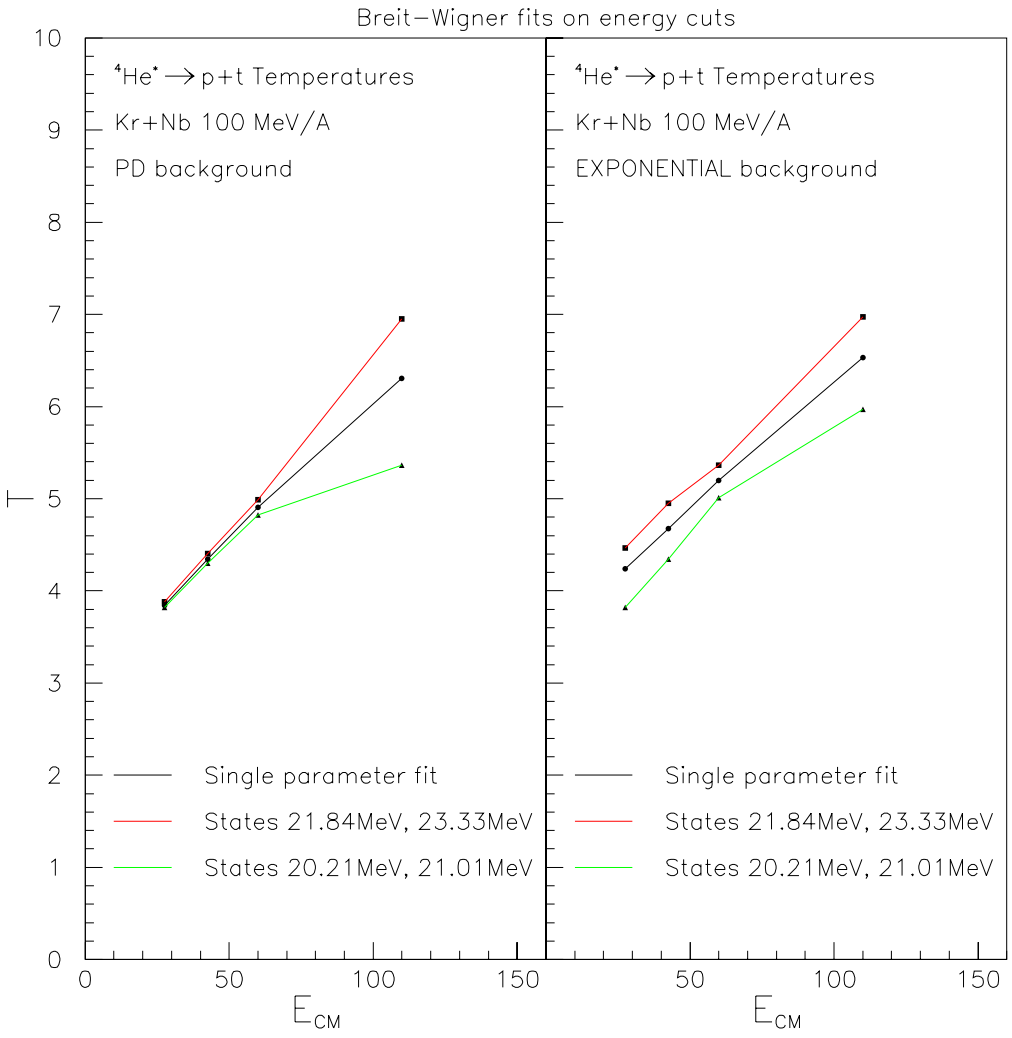

Figure 5.22: Single parameter Breit-Wigner fit of pt correlation for Kr+Nb 100 MeV/A. The upper and lower temperature bounds are the temperatures determined by two parameter fit. The two paramater fit gives a measure of systematic error with the previous panels.

J^{π}	E(MeV)	$Width\Gamma$(MeV)	Branching ratio(%)
0^+	20.21	0.50	100.
0^-	21.01	0.64	76.
2^-	21.84	1.26	63.
1^-	24.25	3.08	51.

Table 5.3: α^* $\rightarrow$p+t spectroscopic information for Breit-Wigner energy cuts analysis.[105]

System:background	CUT(MeV)	T(MeV)	$T_{0^+0^-}$(MeV)	$T_{2^-1^-}$(MeV)
Kr+Nb100MeV:exp	<35	4.23831	3.82095	4.46786
Kr+Nb100MeV:exp	35-50	4.67654	4.34264	4.94783
Kr+Nb100MeV:exp	50-70	5.19825	5.01043	5.36519
Kr+Nb100MeV:exp	70-∞	6.53381	5.97037	6.97204
Ar+Sc100MeV:exp	<35	4.61394	4.62481	4.63481
Ar+Sc100MeV:exp	35-50	5.65735	5.49040	5.86603
Ar+Sc100MeV:exp	50-70	6.34599	6.22078	6.42946
Ar+Sc100MeV:exp	70-∞	7.15985	6.36686	7.74416
Kr+Nb100MeV:PD	<35	3.84182	3.82095	3.88356
Kr+Nb100MeV:PD	35-50	4.34265	4.30092	4.40526
Kr+Nb100MeV:PD	50-70	4.90609	4.82262	4.98957
Kr+Nb100MeV:PD	70-∞	6.30426	5.36519	6.95117
Ar+Sc100MeV:PD	<35	4.30000	4.00876	4.63481
Ar+Sc100MeV:PD	35-50	5.34432	5.23998	5.49040
Ar+Sc100MeV:PD	50-70	6.07471	5.65735	6.40800
Ar+Sc100MeV:PD	70-∞	6.93030	5.78255	7.74416

Table 5.4: Temperature fit information on energy cuts for Breit-Wigner analysis. The third column is the temperature from the single parameter fit. The fourth and fifth columns are upper and lower bounds from the two parameter fits.

5.5 Evidence for cooling from excited state population: S-matrix analysis

Since the Breit-Wigner analyses yielded poor fits to the decay spectra for the highest E_{CM} gate with $E_{CM} > 70MeV$, it is natural to inquire whether this is because the resonance line shapes of the Breit-Wigner discussed earlier are inaccurate. For this reason, we contacted Gerry Hale, whose group had performed detailed measurements of the p+t reaction. Unfortunately, that data has never been published in a form that is directly usable for our purposes, but we were able to obtain advice from him as a private communication.

Dr. Hale proposed that we use an "S-matrix" form for the decay spectrum and provided us with a parameterized line shape. As a detailed justification of this form in terms of measured phase shifts was not provided, we take this as an empirical resonance line shape for the relevant states in ^4He. This "S-matrix" expresses the line shape in the following form:

$$dN_c^{J^\pi}/dE = e^{-E/T}\frac{1}{\pi}P_c(E)|\sum_\mu C_\mu \frac{g_{\mu c}}{E_\mu - E}\ |^2 =$$

$$e^{-E/T}\frac{1}{\pi}P_c(E)\sum_\mu C_\mu \bar{C}_\mu \frac{g_{\mu c}\bar{g}_{\mu c}}{(E_\mu - E)(\bar{E}_\mu - E)}\ , \tag{5.33}$$

where the separation on the last step is valid , because spins and parities of the states we are investigating are different. Otherwise we would have cross terms. Here $P_c(E)$ is the penetrability given by

$$P_c(E) = \frac{\rho}{F_l(\eta,\rho)^2 + G_l(\eta,\rho)^2}\ , \tag{5.34}$$

Where F_l and G_l are solutions to the Coulomb wave equation,and we also have

$\rho = kr$, and

$\eta = 0.158 \cdot Z_1 Z_2 \sqrt{A_1 A_2/(A_1 + A_2)/E}$, is the Somerfeld parameter.

k is the wave number and r is the channel radius. For $\alpha^* \rightarrow p + t$ the channel radius is 4.93fm [45].

Table 5.5 shows the other spectroscopic information for $\alpha \rightarrow p + t$ in this S-matrix analysis. Using the expression for the decay spectrum figures 5.24 and 5.26 show the temperature trend for energy cuts 0-35, 35-50, 50-70, >70 MeV for systems Ar+Sc 100 Mev/A and Kr+Nb at 100 Mev/A for the p-d and the exponential background, respectively . Figures 5.25 and 5.23 show the corresponding examples of two parameter fitting where as before the $0^+, 0^-$ state has one parameter and the $2^-, 1^-$ states have the other. We again see that there is a problem fitting the correlation function for the highest energy gates. The temperatures from these fits are also given in Table 5.6 and the summary table 5.7. Thus, this S-matrix approach suffers the same problem that it fails to fit the relative energy spectrum at $E_{rel} < 0.5MeV$ for the gate with $E_{CM} > 70MeV$ when all states are assumed to be populated in a manner that is consistent with a single temperatures. When the high spin states and low spin states are fitted separately, the fit is best when the high spin state are populated at a higher temperature than are the low spin states.

Putting this together, we have used the various fits to estimate the systematic error in the extracted temperatures. The cross-shaded area in Fig. 5.22 shows the range of temperatures extracted from the Breit-Wigner fits as a function of the center of mass energy. The cross-shaded area in Fig. 5.28 shows the range of temperatures extracted from the S-Matix fits as a function of the center of mass energy. Both figures show a clear trend of increasing temperature with E_{CM}. Since the Breit-Wigner resonance line shapes are the published values and the S-Matrix parameterization is not published, we take the previous Fig. 5.22 as the most reliable demonstration that cooling influences the excited state thermometer values.

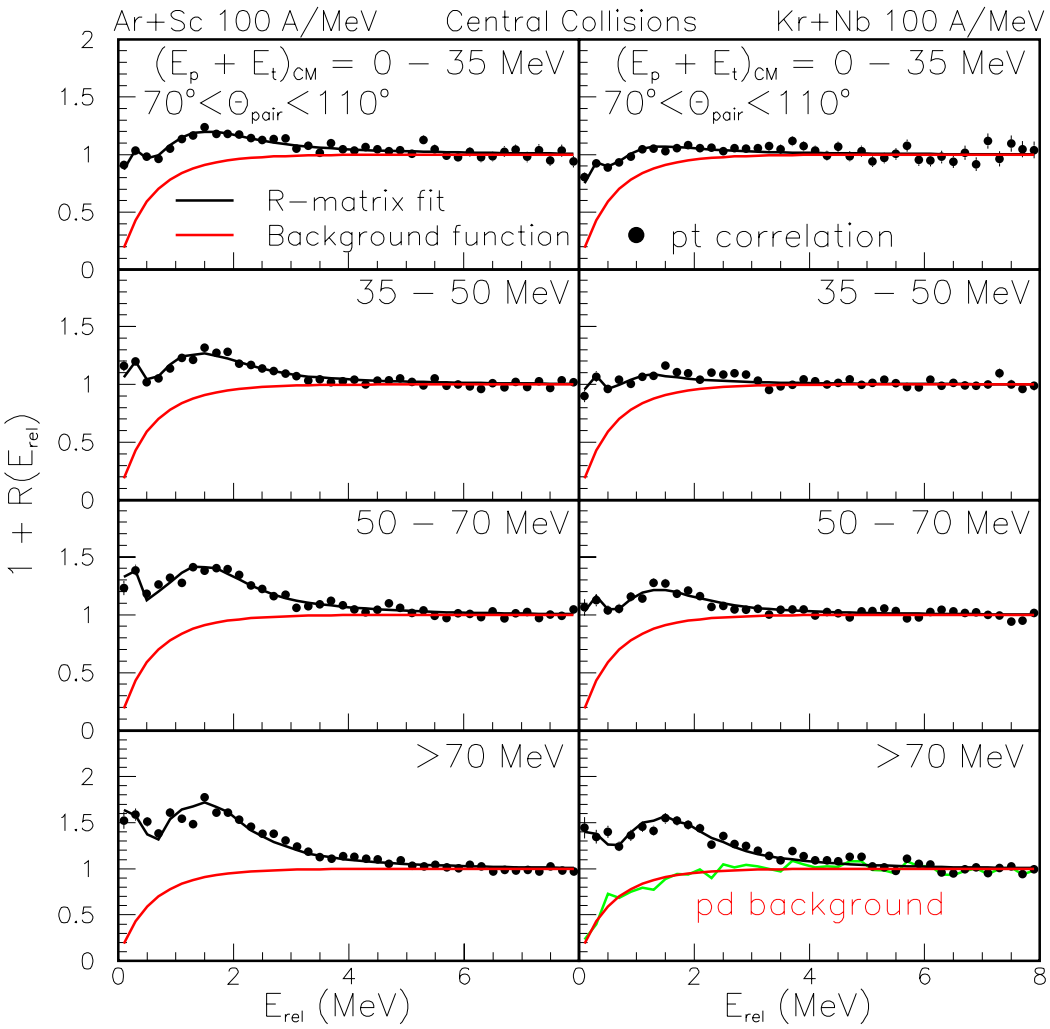

Figure 5.23: Two parameter S-matrix fit of pt correlation versus relative energy(MeV). This panel is intended to demonstrate how well the fits are for a two parameter fit to get error limits on extracted temperatures for the single parameter fit. The data was obtained using a cut between 70 and 110 degrees in CMS and relative energy cuts indicated. The apparent temperatures indicated here is the average temperatures of the minimum χ^2 of the fit.

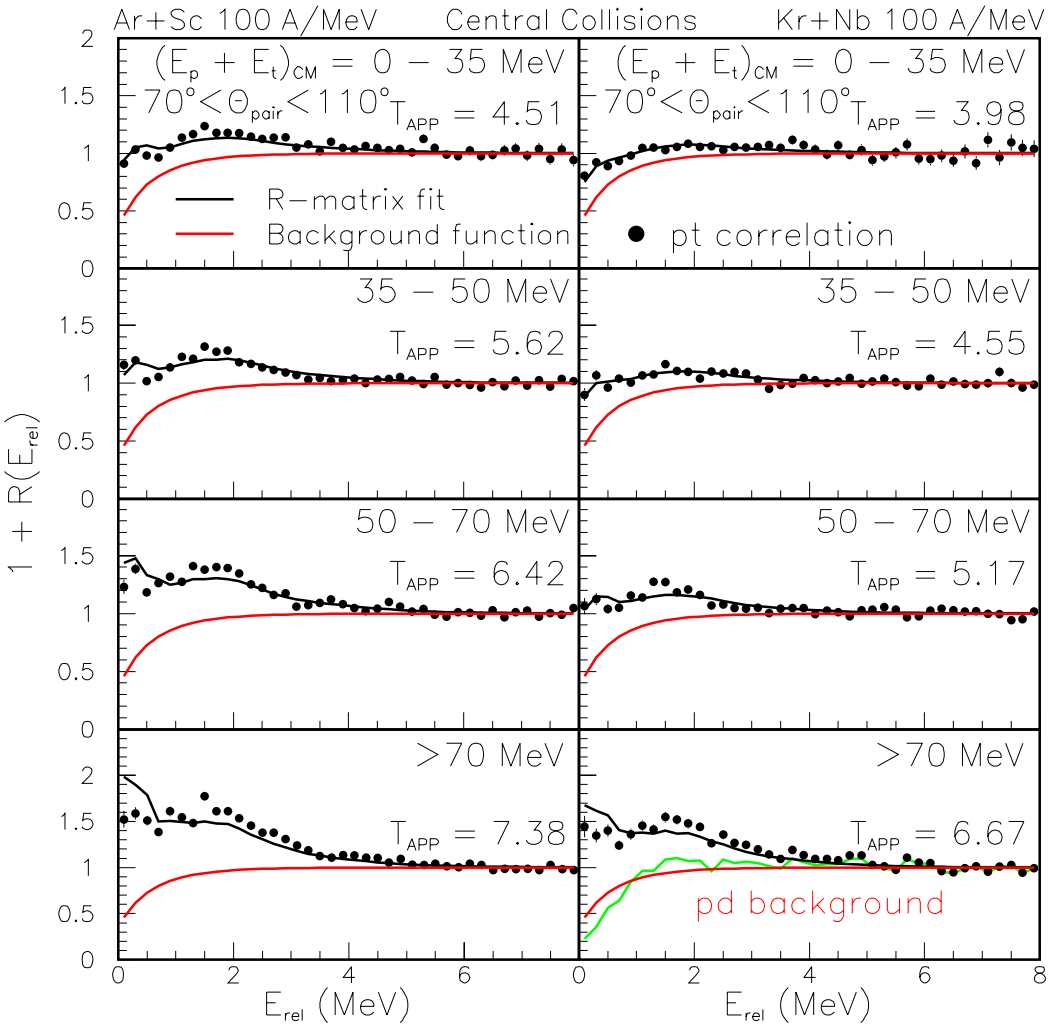

Figure 5.24: Single parameter S-matrix fit of pt correlation versus relative energy(MeV) on a pd background. The data was obtained using a cut between 70 and 110 degrees in CMS and relative energy cuts indicated.

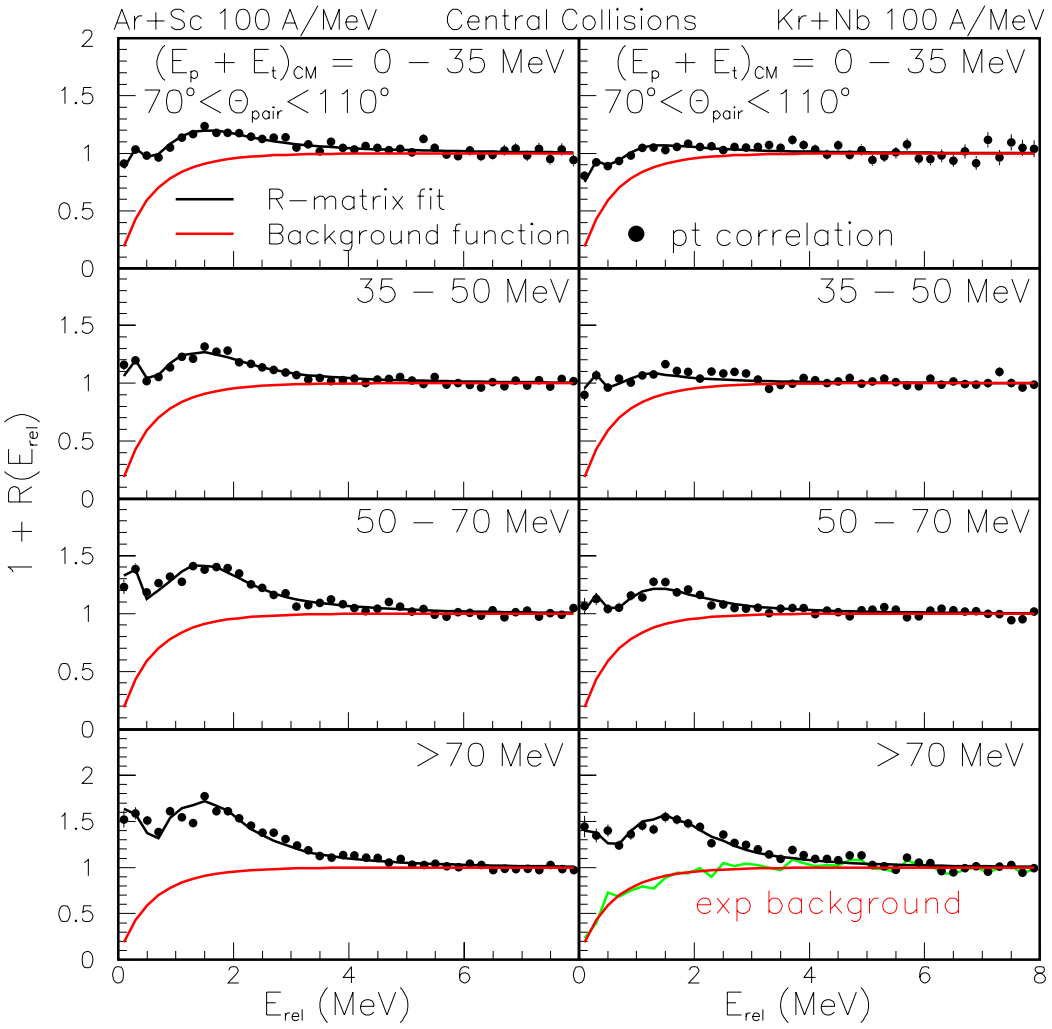

Figure 5.25: Two parameter S-matrix fit of pt correlation versus relative energy(MeV)on an exponential background. The data was obtained using a cut between 70 and 110 degrees in CMS and relative energy cuts indicated.

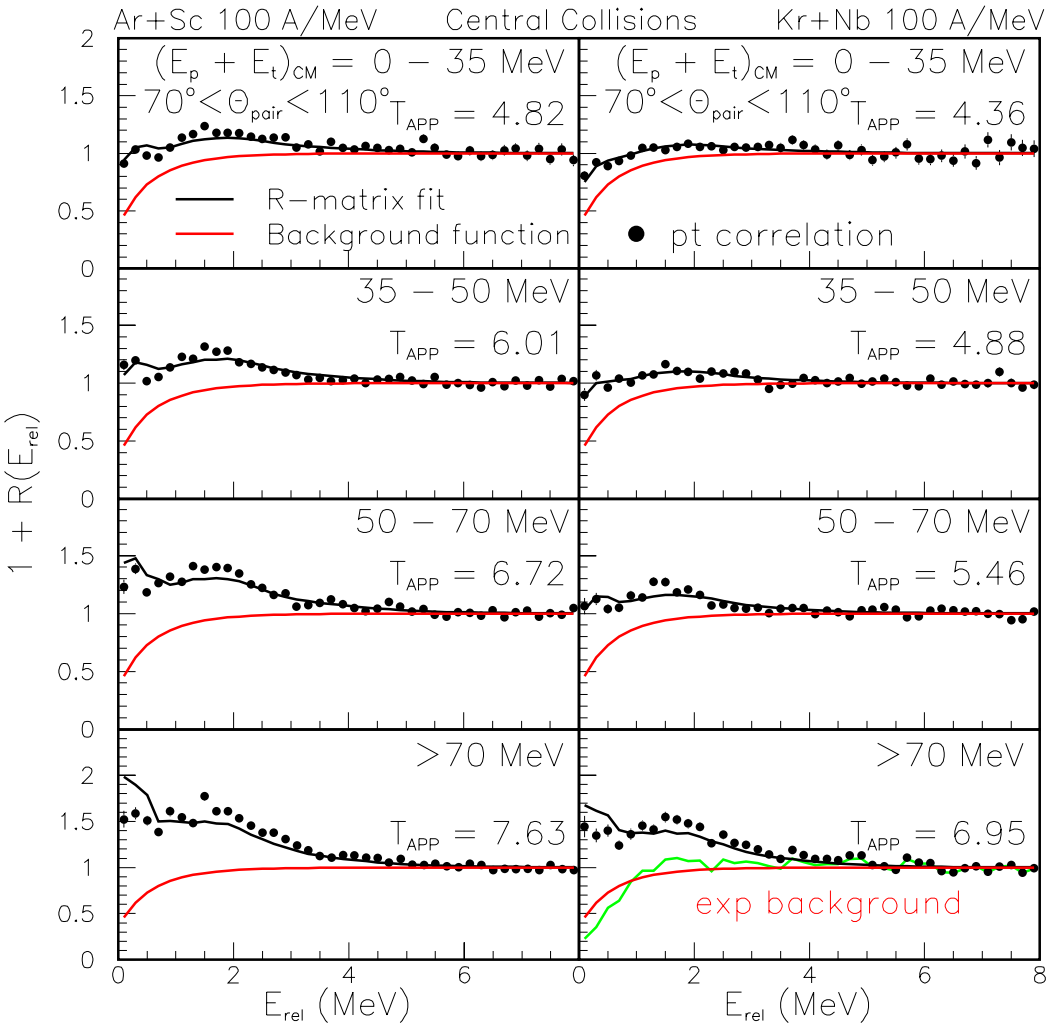

Figure 5.26: Single parameter S-matrix fit of pt correlation versus relative energy(MeV)on an exponential background. The data was obtained using a cut between 70 and 110 degrees in CMS and relative energy cuts indicated.

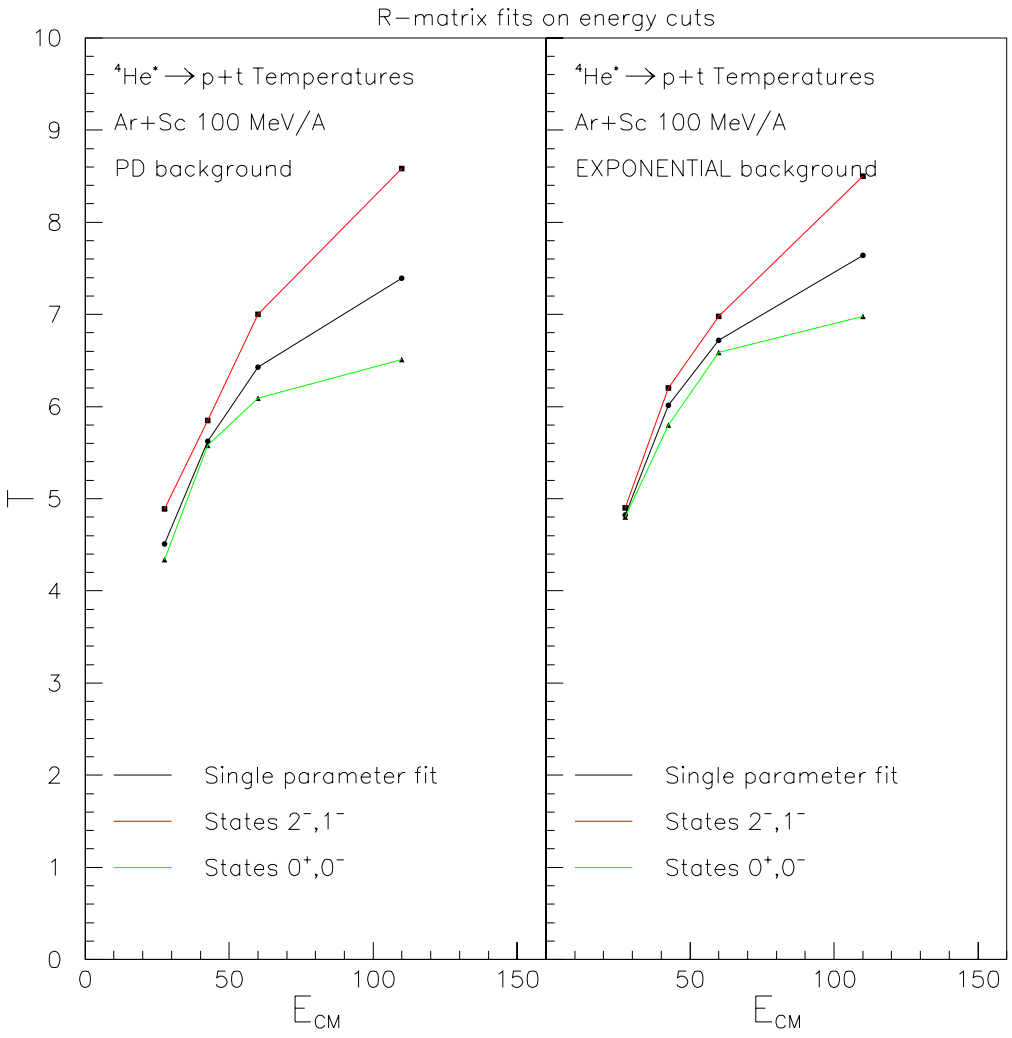

Figure 5.27: Single parameter S-matrix fit of pt correlation for Ar+Sc 100 MeV/A. The upper and lower temperature bounds are the temperatures determined by two parameter fit. The two paramater fit gives a measure of systematic error with the previous panels.

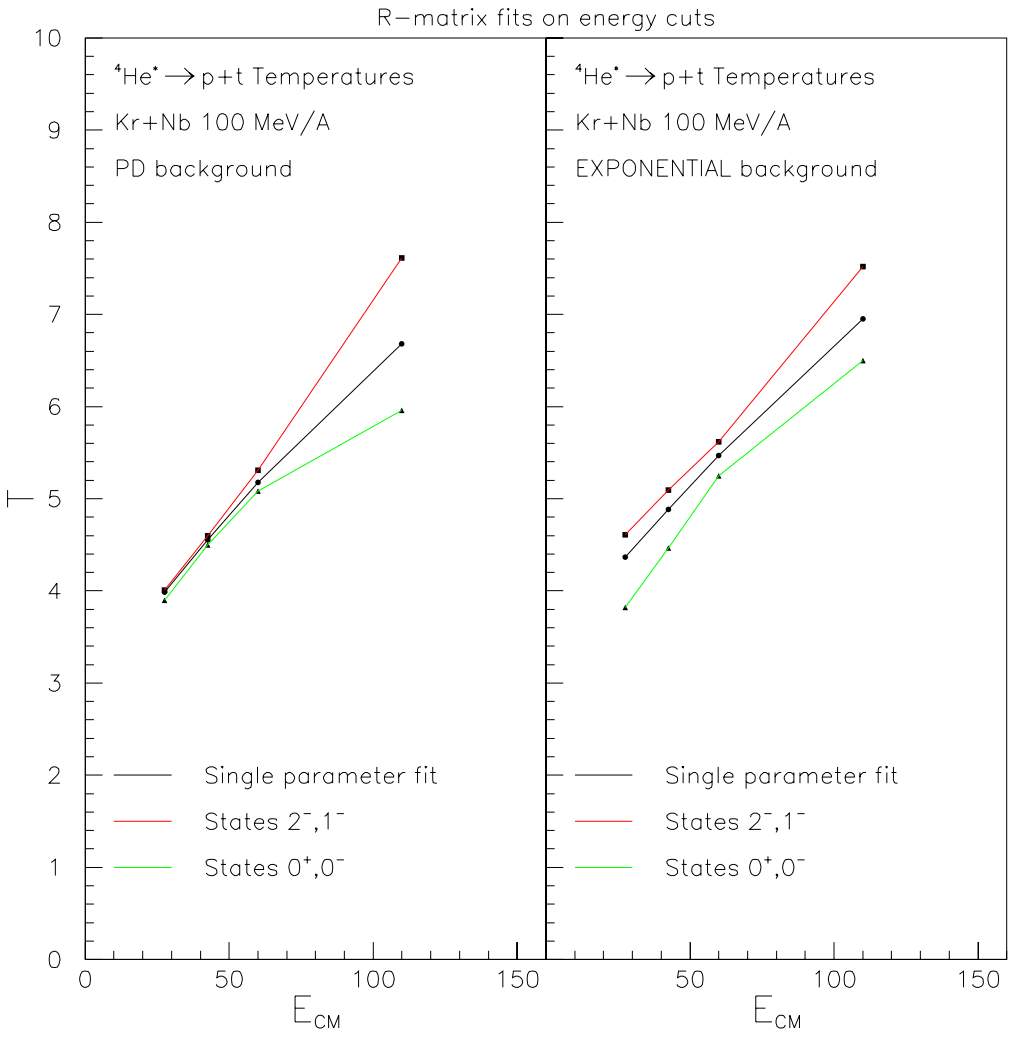

Figure 5.28: Single parameter S-matrix fit of pt correlation for Kr+Nb 100 MeV/A. The upper and lower temperature bounds are the temperatures determined by two parameter fit. The two paramater fit gives a measure of systematic error with the previous panels.

J^π	C^2_μ	E_μ(MeV)	$g^2_{\mu p}$
0^+	1	0.11386-i0.19627	0.78301
0^-	1	1.0309-i0.30109	0.56843
2^-	5	1.5841-i0.73189	0.62836
1^-	3	2.8043-i2.33620	1.0221

Table 5.5: α^* $\rightarrow$p+t spectroscopic information for S-matrix analysis.[45]

System:background	CUT(MeV)	T(MeV)	$T_{0^+0^-}$(MeV)	$T_{2^-1^-}$(MeV)
Kr+Nb100MeV:exp	00-35	4.36352	3.82	4.61
Kr+Nb100MeV:exp	35-50	4.88523	4.46786	5.09391
Kr+Nb100MeV:exp	50-70	5.46953	5.25	5.62
Kr+Nb100MeV:exp	70-∞	6.95117	6.50	7.52
Ar+Sc100MeV:exp	00-35	4.82262	4.8	4.9
Ar+Sc100MeV:exp	35-50	6.01210	5.8	6.2
Ar+Sc100MeV:exp	50-70	6.72162	6.59	6.98
Ar+Sc100MeV:exp	70-∞	7.63982	6.98	8.5
Kr+Nb100MeV:PD	00-35	3.98790	3.90	4.01
Kr+Nb100MeV:PD	35-50	4.55134	4.50	4.60
Kr+Nb100MeV:PD	50-70	5.17738	5.08	5.31
Kr+Nb100MeV:PD	70-∞	6.67988	5.96	7.61
Ar+Sc100MeV:PD	00-35	4.50960	4.34	4.89
Ar+Sc100MeV:PD	35-50	5.62250	5.58	5.85
Ar+Sc100MeV:PD	50-70	6.42946	6.09	7.00
Ar+Sc100MeV:PD	70-∞	7.38940	6.51	8.58

Table 5.6: Temperature fit information on energy cuts for S-matrix analysis. The third column is the temperature from the single parameter fit. The fourth and fifth columns are upper and lower bounds from the two parameter fits.

5.6 Summarized results of Breit-Wigner and S-matrix analysis

We summarize here the previous tables into a single table 5.7 . The extremes in temperature are indicated by the shaded areas in figures 5.29 and 5.30. Each figure picks the highest and lowest temperatures of both backgrounds and both line shapes. We expect that a better choice of background and line shape would fall in these shaded reqions. The same trend in a higher temperature at an earlier time is still indicated.

System:background	CUT(MeV)	T(MeV)	$T_{0^+0^-}$(MeV)	$T_{2^-1^-}$(MeV)	T(MeV)	$T_{0^+0^-}$(MeV)	$T_{2^-1^-}$(MeV)
–	–	Breit−Wigner	Breit−Wigner	Breit−Wigner	S−matrix	S−matrix	S−matrix
Kr+Nb100MeV:exp	<35	4.23831	3.82095	4.46786	4.36352	3.82	4.61
Kr+Nb100MeV:exp	35-50	4.67654	4.34264	4.94783	4.88523	4.46786	5.09391
Kr+Nb100MeV:exp	50-70	5.19825	5.01043	5.36519	5.46953	5.25	5.62
Kr+Nb100MeV:exp	70-∞	6.53381	5.97037	6.97204	6.95117	6.50	7.52
Ar+Sc100MeV:exp	<35	4.61394	4.62481	4.63481	4.82262	4.8	4.9
Ar+Sc100MeV:exp	35-50	5.65735	5.49040	5.86603	6.01210	5.8	6.2
Ar+Sc100MeV:exp	50-70	6.34599	6.22078	6.42946	6.72162	6.59	6.98
Ar+Sc100MeV:exp	70-∞	7.15985	6.36686	7.74416	7.63982	6.98	8.5
Kr+Nb100MeV:PD	<35	3.84182	3.82095	3.88356	3.98790	3.90	4.01
Kr+Nb100MeV:PD	35-50	4.34265	4.30092	4.40526	4.55134	4.50	4.60
Kr+Nb100MeV:PD	50-70	4.90609	4.82262	4.98957	5.17738	5.08	5.31
Kr+Nb100MeV:PD	70-∞	6.30426	5.36519	6.95117	6.67988	5.96	7.61
Ar+Sc100MeV:PD	<35	4.30000	4.00876	4.63481	4.50960	4.34	4.89
Ar+Sc100MeV:PD	35-50	5.34432	5.23998	5.49040	5.62250	5.58	5.85
Ar+Sc100MeV:PD	50-70	6.07471	5.65735	6.40800	6.42946	6.09	7.00
Ar+Sc100MeV:PD	70-∞	6.93030	5.78255	7.74416	7.38940	6.51	8.58

Table 5.7: Combined table for Breit-Wigner and S-matrix analysis . The third column is the temperature from the single parameter Breit-Wigner fit. The fourth and fifth columns are upper and lower bounds from the two parameter Breit-Wigner fits. The sixth, seventh and eightth columns corresond to the third,fourth and fifth except that S-matrix analysis is used.

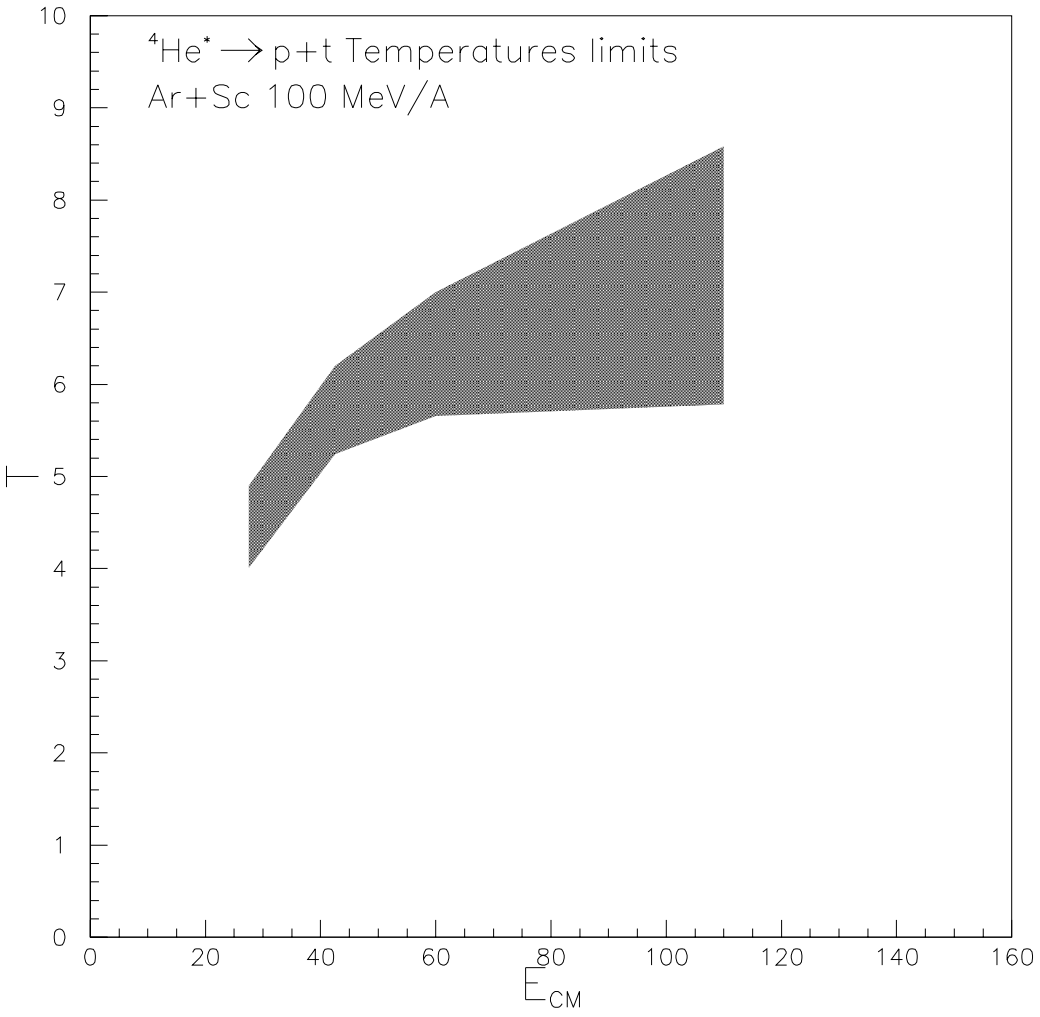

Figure 5.29: Combined temperature limits of Ar100 energy cut analysis .

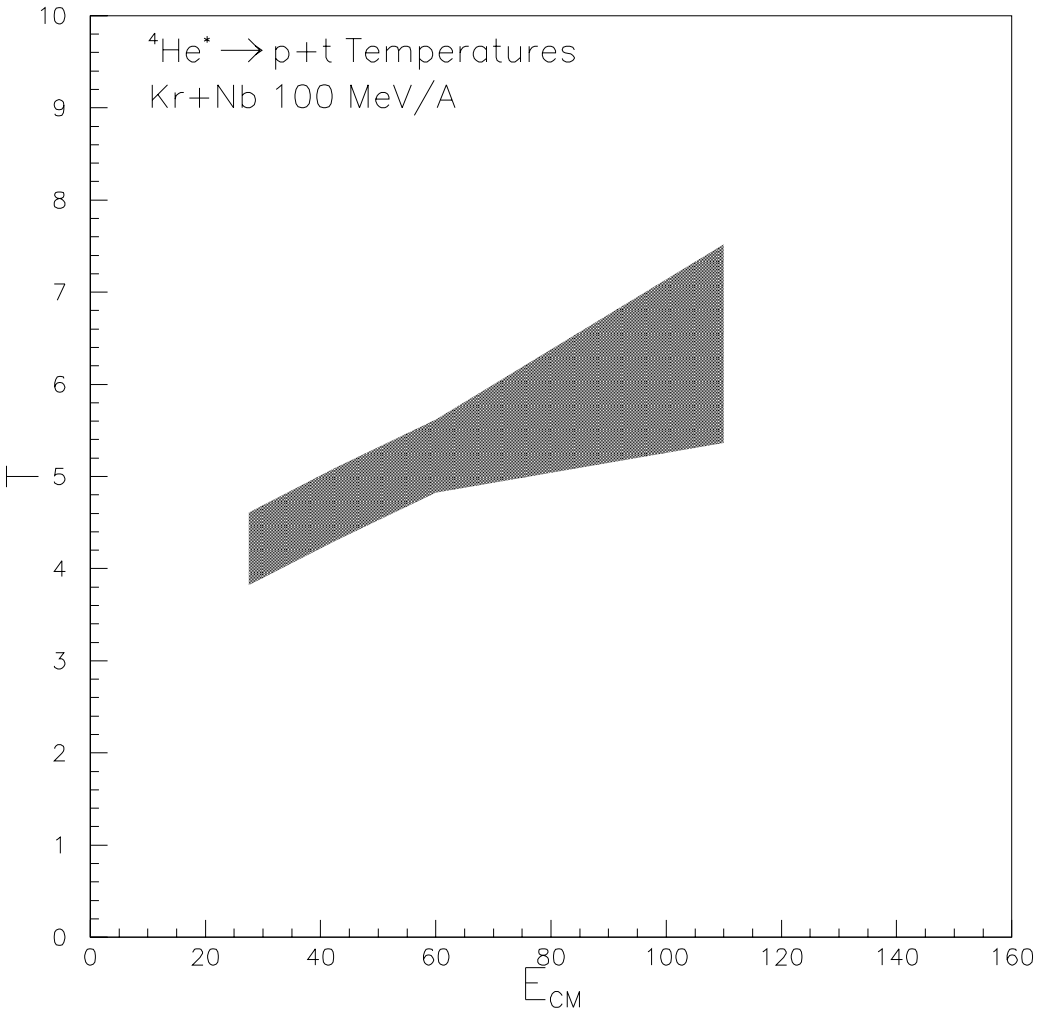

Figure 5.30: Combined temperature limits of Kr100 energy cut analysis .

5.7 Evidence of cooling using the Albergo Thermometer

It is interesting to ask whether comparable evidence for cooling in these reactions can be provided by isotope thermometer measurements. Evidence for cooling has been observed in Xe+ Cu reactions at E/A=30 MeV [137] where an isotopic thermometer contructed from $[Y(^3He)/Y(^4He)]/[Y(^2H)/Y(^3H)]$ was analyzed as a function of the energy of the outgoing particle species. Investigation of cooling is potentially more ambiguous with isotopic thermometers than with excited state thermometers because four different fragments enter into the isotopic ratio. Nevertheless, we analyze the isotope ratio with gates on the velocity or equivalently energy/nucleon in the center of mass system in order to see whether cooling effects can be observed.

To calculate the gated double isotope ratios, we integrated the yields of fragments emitted in central collisions at $70^o \leq \theta_{CM} \leq 110^o$ in 4 MeV/nucleon bins.

$$Y_n = \int_{4A(n-1)}^{4An} \frac{dY}{dE} dE \,, \tag{5.35}$$

and then constructed double isotopic ratios $[Y(^3He)/Y(^4He)]/[Y(^2H)/Y(^3H)]$ and $[Y(^3He)/Y(^4He)]/[Y(^6Li)/Y(^7Li)]$. The isotopic temperatures calculated from these ratios are plotted in Fig. 5.31 for Kr+Nb collisions and in Fig. 5.32. for Ar+Sc collisions. There is a clear increase the resulting isotopic temperatures with the energy/nucleon in the center of mass. For Kr+Nb collisions, the lowest temperature of $T_{ISO} \approx 4 - 5MeV$ occurs for Kr+Nb collisions at energies that are about 50% above the Coulomb barrier. This is comparable to the temperatures extracted from the excited state populations. The maximum values of $T_{ISO} \approx 10 - 12MeV$ occur at an energy/nucleon of about 20-25 MeV in the center of mass. Such high temperatures are hard to reconcile to a thermal interpretation. For Ar+Sc collisions at E/A= 50

MeV, the temperatures are similar, but there is an increasing discrepancy between the temperature calculated from the $[Y(^3He)/Y(^4He)]/[Y(^2H)/Y(^3H)]$ ratio and the $[Y(^3He)/Y(^4He)]/[Y(^6Li)/Y(^7Li)]$ ratio at the higher incident energies of E/A=100 and 150 MeV.

In all of the panels, the values for the isotope temperatures calcuated by integrating over the entire energy spectrum is shown by the solid horizontal lines. Clearly, these integral isotopic temperatures shown here and also earlier in 5.12-5.15 reflect the averaging over faster and earlier emissions characterized by higher isotopic temperatures and slower and later emissions characterized by lower isotopic temperatures.

It has been noted [61] that phase space consideration favors the emission of more weakly bound ^3He at earlier stages of the breakup when the temperature is higher and that the emission of more strongly ^4He may be rather delayed until the system expands to subnuclear density. Thus the differences between the values extracted from these isotopic temperatures and the ^4He excited state temperatures discussed earlier may be a reflection of the fact that these emission sample somewhat different times.

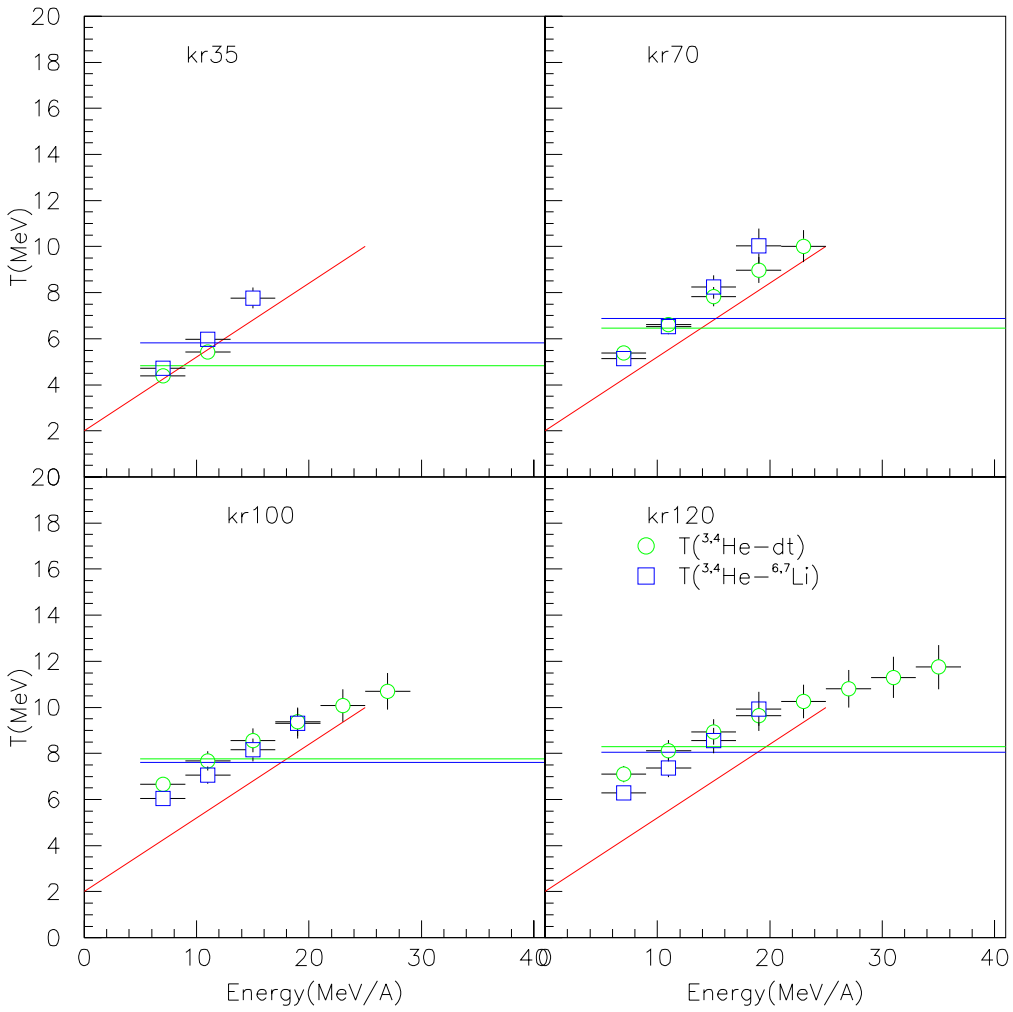

Figure 5.31: Albergo temperatures on energy cuts for Kr+Nb systems. This shows a trend in increasing temperature with higher energy cuts. The circles are the ^{3,4}He-dt thermometer and the squares are the ^{3,4}He-^{6,7}Li thermometer. The horizontal lines represent the temperatures from the yields of all the data added together without an energy gate. The red line is a guide to indicate the increasing trend with respect to beam energy. The uncertainties are the sum of the statistical uncertainty and a 5% PID uncertainty per isotope in quadrature.

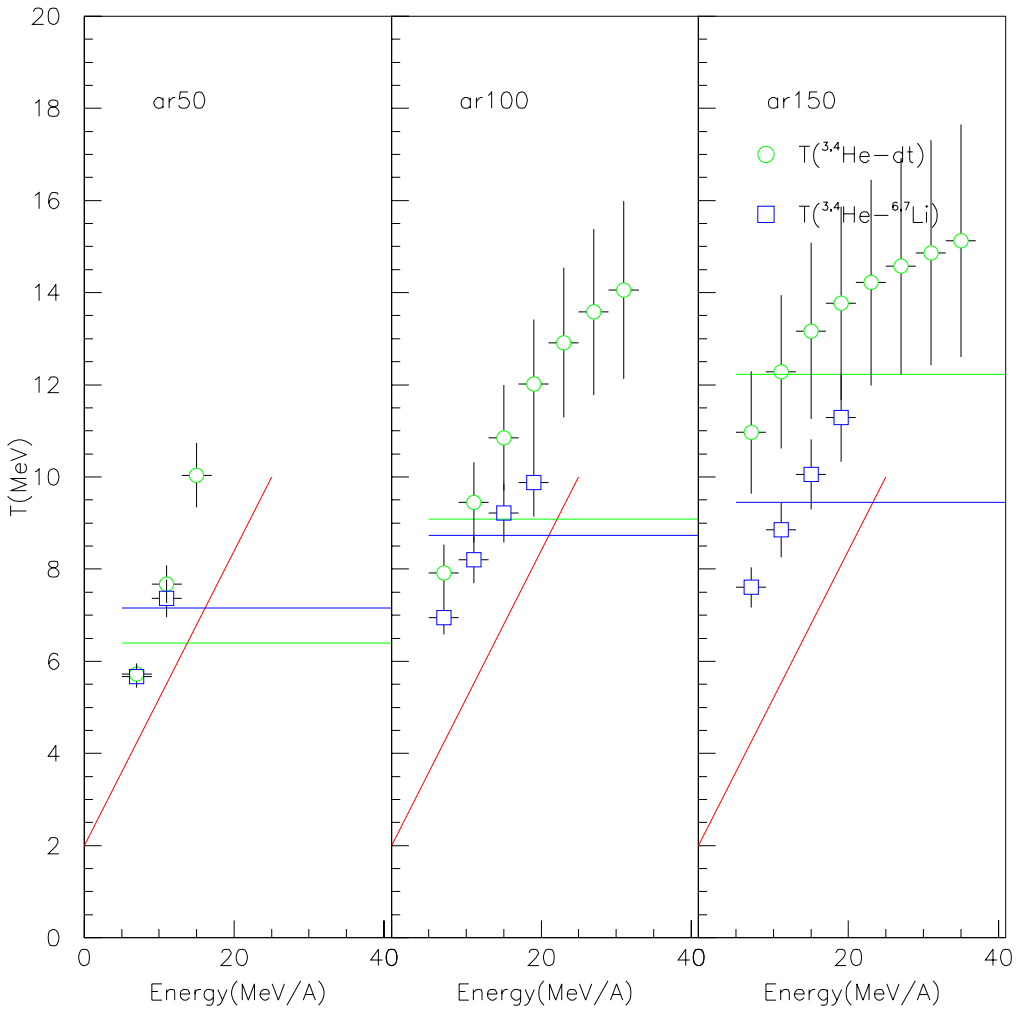

Figure 5.32: Albergo temperatures on energy cuts for Ar+Sc systems. This shows a trend in increasing temperature with higher energy cuts. The circles are the ^{3,4}He-dt thermometer and the squares are the ^{3,4}He-^{6,7}Li thermometer. The horizontal lines represent the temperatures from the yields of all the data added together without an energy gate. The red line is a guide to indicate the increasing trend with respect to beam energy. The uncertainties are the sum of the statistical uncertainty and a 5% PID uncertainty per isotope in quadrature.

5.8 Sequential decay

In this thesis, we have not explored the effects of secondary decay on temperatures extracted from the excited state populations and isotopic ratios. Clearly, our observations of significant yields of nuclei in their excited states implies the existence of secondary decay contributions. Correction for secondary decay, however, is difficult because one cannot assume an equilibrium distribution of hot unstable fragments before decay; instead we have limited our corrections to the empirical approach discussed in Section 4.3.3.

Because this thesis concentrates largely on the ^4He excited state thermometer and the comparison of this to the temperatures extracted from the $^3He/^4He$ isotope ratio, the studies of ref. [136] are especially significant. These studies point out that both the ^4He excited state thermometer and thermometers based on the $^3He/^4He$ isotope ratio have very similar secondary decay corrections, because both are primarily influenced by secondary decay to comparably well-bound ^4He in its ground state. Thus, the differences between the temperatures derived from the two thermometers are unlikely the result of the secondary decay. They are more likely a result of non-equilibrium contributions to the ^3He yields as discussed in section 4.3.2 or some other effect.

Chapter 6

Summary

Whether equilibrium can be assumed in modeling the multi-fragment decays of highly excited nuclear systems is an important question. If one can assume equilibrium, then a large number of equilibrium analyses of multi-fragmentation can be attempted. Such analyses are mainly aimed at determining thermal properties of nuclear matter. These include some recent and somewhat more speculative topics, such as determining the caloric curve for nuclear matter [91, 80], whether it displays a region of "negative heat capacit" [22, 29, 30] and extracting critical exponents for the nuclear liquid-gas phase transition [78, 31, 32]

Unfortunately for such studies, there are not many cases where the validity of thermal equilibrium has been tested. One test, performed for central Au+Au collisions at E/A=35 MeV [50], found excited state and isotopic temperatures in agreement with equilibrium statistical model calculations. In addition a systematic analyses of isotopic temperatures [81] found consistent equilibrium interpretation of isotopic temperatures could be proposed. These analyses also indicated a systematic decrease with system size for the temperature in the "plateau regio", where the isotopic temperature varies gradually with deduced excitation energy.

For other systems, the data indicated substantial disagreement with equilibrium

predictions [100]. In the work of Serfling et al. [100], isotopic temperatures extracted from the Helium Lithium isotopic thermometer increased with incident energy. The temperatures extracted from excited state thermometers did not indicate either a problem with thermal equilibrium or a problem with either the HeLi isotopic thermometer or the ^{4}He,^{5}Li and ^{8}Be excited state thermometers or both. In this dissertation, we reexamined this issue by studying the incident energy dependence of the same thermometers, plus the CLi isotopic thermometer for central Kr+Nb and Ar+Sc collisions.

The trends observed for the Kr+Nb and Ar+Sc systems are in many ways similar to those observed by Serfling. In particular, the HeLi temperatures increase strongly with incident energy, while those for ^{4}He,^{5}Li and ^{8}Be excited state thermometers increase only slightly. Interestingly, the CLi thermometer yields values that are similar to those observed for the ^{4}He,^{5}Li and ^{8}Be excited state thermometers.

Calculations were performed with the Statistical Multi-fragmentation model to see whether the observed ^{3}He yields, which govern the temperatures for the HeLi thermometer, are consistent with an equilibrium statistical model calculation that reproduces the fragment charge distribution and fragment multiplicities previously observed for the Kr+Nb system. In fact, the statistical calculations that reproduced the fragment yields, grossly underpredicted the yields for deuterons, tritons and ^{3}He's. This supports the interpretation that early preequilbrium emission of ^{3}He is responsible for a major fraction of the observed yield, an interpretation that is also supported by calculations for light cluster production within an extended BUU model. The possibility that secondary decay may be partly responsible for the differences between the HeLi thermometer and the ^{4}He,^{5}Li and ^{8}Be excited state thermometers cannot be entirely ruled out, but the predicted similarity between the effect of secondary on the HeLi thermometer and on that on the ^{4}He excited state thermometer argues

against this possibility.

We also examined whether the light cluster yields are inconsistent with local thermal equilibrium by comparing their isotopic distributions to an extended isoscaling formalism. Interestingly, we find that thermometers based on the $^3He - ^4He$ binding energy difference and the isotopic distributions can be analyzed in a consistent approach. This suggests that both are roughly consistent with the assumption of local thermal equilibrium during the early emission stage before the system expands and multi-fragmentation occurs.

Despite the existance of a possible explanation for the difference between HeLi temperatures and the ^4He,^5Li and ^8Be excited state temperatures in terms of early pre-equilibrium the ^3He emission, the observation of such low values for the ^4He,^5Li and ^8Be excited state temperatures is difficult to explain in light of the large available excitation energies of these collisions to explore this issue, the ^4He excited state thermometer was analyzed as a function of the kinetic energy of the ^4He in the center of mass system.

Analyses were performed for ground and excited ^4He particles emitted to $70^o \leq \theta_{cm} \leq 100^o$ and for four gates on E_{cm}. These analyses revealed that ^4He temperatures increase with the ^4He kinetic energy in the center of mass. Such behavior is consistent with cooling of the system as it expands and radiates particles. Similar trends were observed for the HeLi and HeH isotopic temperatures. In all cases, we found evidence for cooling phenomena that more strongly influence the HeLi temperature values than the ^4He temperature values. Thus, there is little support for the validity of overall or global thermal equilibrium at E/A=100 MeV from either thermometer. At other incident energies, the HeLi isotopic thermometer reveals significant cooling effects, which are admittedly stronger at higher incident energies than at lower incident energies.

Looking beyond this dissertation, we hope more measurements will be performed that explore the degree to which equilibrium is achieved in multifragmentation processes. Evidence is emerging from analyses of central Sn+Sn [106] that similar cooling effects occur at E/A=50 MeV, in the spectra of heavy carbon fragments. Such observations suggest that fragments with different kinetic energies are emitted at different times from a system that is cooling with time. Thus, it may be more appropriate to consider interpreting the emission in terms of a rate equation that assumes emission from the surface of the expanding system, such as assumed in the EES model. The widespread interpretation of such data in terms of equilibrium approaches cannot be continued in its present form. Model approaches are required that take this time dependence into account.

Appendix A

Derivation of the Relativistic Boltzmann Distribution

A.1 Expression for Volume Emission

We start with the integral of ref [42] pp358

$$\int_0^\infty e^{-\beta\cosh x}\sinh^{2\nu}x dx = \frac{1}{\sqrt{\pi}}(\frac{2}{\beta})^\nu\Gamma\left(\nu+\frac{1}{2}\right)K_\nu(\beta)\ , \tag{A.1}$$

This distribution is obtained by evaluating and normalizing the integral [62]:

$$\int_0^\infty e^{\frac{-\sqrt{m^2c^4+p^2c^2}}{T}}p^2dp \tag{A.2}$$

If we substitute p=mc$\cdot\sinh x$ into equation A.2 we obtain an equation that is a derivative of A.1 with respect to β. Setting $\nu = 1$:

$$\int_0^\infty e^{-\beta\cosh x}\sinh^2 x\cosh x dx = -\frac{d}{d\beta}\frac{K_1(\beta)}{\beta} = \frac{2K_1(\beta)}{\beta^2}+\frac{K_0(\beta)}{\beta}\,, \tag{A.3}$$

here the relation $K_1'(z) = -K_1(z)/z - K_0(z)$ was used.

Now equation A.2 after normalization becomes the probability distribution in terms of momentum:

$$P_V(p)\,dp = \frac{e^{\frac{-\sqrt{m^2c^4+p^2c^2}}{T}} p^2 dp}{\left[2\left(\frac{T}{mc^2}\right)^2 K_1\left(\frac{mc^2}{T}\right) + \left(\frac{T}{mc^2}\right) K_0\left(\frac{mc^2}{T}\right)\right] m^3c^3}, \tag{A.4}$$

This can be expressed in other kinematic variables using conservation of probability: $P(p)dp = P(E)dE = P(v)dv$

Perhaps the most useful expression is in terms of the kinetic energy, because it is measured in the lab:

$$P_V(E)\,dE = \frac{e^{-\frac{mc^2+E}{T}} \sqrt{(mc^2+E)^2 - m^2c^4}\,(mc^2+E)\,dE}{\left[2\left(\frac{T}{mc^2}\right)^2 K_1\left(\frac{mc^2}{T}\right) + \left(\frac{T}{mc^2}\right) K_0\left(\frac{mc^2}{T}\right)\right] m^3c^6}, \tag{A.5}$$

An asymptotic expansion is used on the MacDonald functions $K_0(z)$ and $K_1(z)$ in the fitting procedure. For large (mc^2/T) which is the nonrelativistic case it can be shown eq. A.5 reduces to the classical Maxwell-Boltzmann distribution. Note in the fitting coulomb energy is subtracted from the total energy term so that the kinetic energy at breakup appears in the 3 source fitting function.

The expression can be simplified slightly by the identity $K_2(z) = 2K_1(z)/z + K_0(z)$.

LIST OF REFERENCES

[1] M. Abramowitz and I. Stegun , *Handbook of Mathematical Functions* (Dover, 1970).

[2] F. Ajzenberg-Selove , Nuc. Phys. A 392, 1(1983); A 413, 1(1984); A 433, 1(1985); A 449, 1(1985); A460, 1(1986)

[3] S. Albergo *et al.*, Nuovo Cimento **89**, 1 (1985).

[4] C.A. Balanis , *Antenna Theory* (Second Edition, Wiley&Sons 1996).

[5] Bao-An Li , *Phys. Rev. Lett.* **85**, 4221 (2000).

[6] Bao-An Li, A.R. De Angelis, and D.H.E. Gross, Phys Lett. B 303 , 225 (1993)

[7] Bao-An Li , C.M. Ko, Zhongshou Ren, *Phys. Rev. Lett.* **85**, 4221 (1997).

[8] G. Baym and C. Pethick , *Landau-Fermi Liquid Theory* (Wiley, New York, 1991).

[9] G. Bertsch and S. Das Gupta, Phys. Rev. 160, 189 (1988).

[10] D.H.Boal , C.K. Gelbke and B.K. Jennings, Rev. of Mod. Phys. 62 (1990) 553

[11] J. Bondorf *et al.*, Nuc. Phys. A 443, 321(1985).

[12] J. Bondorf *et al.*, Nuc. Phys. A 444, 460(1985).

[13] J. Bondorf *et al.*, Nuc. Phys. A 448, 753(1986).

[14] J. Bondorf *et al.*, Phys. Rep. 257, 133(1995).

[15] A. S. Botvina *et al.*, Nuc. Phys. A 475, 663(1987).

[16] J.D. Bowman,W.J. Swiatecki, and C.-F. Tsang, LBL Report No. LBL-2908 (1973) (unpublished)

[17] W.E. Burcham , *Nuclear Physics* (McGraw-Hill, 1963).

[18] C. Cavata *et al.*, *Phys. Rev.* **C42**, 1760 (1990).; Y.D. Kim, et. al., ibid 45, 338(1992)

[19] C.B. Chitwood, et. al. Phys Lett. B 172 , 27 (1986)

[20] Ziping Chen, Ph.D. Thesis , (Michigan State University 1988).

[21] Z. Chen and C. K. Gelbke *Phys. Rev.* **C38**, 2630 (1988).

[22] Ph. Chomaz,V. Duflot, and F. Gulminelli , *Phys. Rev. Lett.* **85**, 3587 (2000).

[23] M. Colonna ,M. Di Toro, G. Fabbri, and S. Maccarone, *Phys. Rev.* **C57**, 1410 (1988).

[24] C. Csoto and G. M. Hale *Phys. Rev.* **C55**, 2366 (1997).

[25] M.W. Curtin, H. Toki, D.K. Scott, Phys Lett. B123 , 289 (1983)

[26] P. Danielewicz Nuc. Phys A314, 465(1979)

[27] P. Danielewicz *et al.*, *Phys. Rev.* **C38**, 120 (1988).

[28] M. D'Agostino, et. al. Nuc. Phys A650, 329(1989)

[29] M. D'Agostino, et. al. Phys Lett. B 371 , 175 (1996)

[30] M. D'Agostino, et. al. Phys Lett. B 473 , 219 (2000)

[31] J.B. Elliot *et al.*, *Phys. Rev. Lett.* **88**, 042701 (2002).

[32] J.B. Elliot *et al.*, *Phys. Rev.* **C67**, 024609 (2003).

[33] S. Fiarman and W. E. Meyerhof Nuc. Phys A206, 1(1973)

[34] Richard B. Firestone,*Table of Isotopes* (Eighth Edition, Vols. 1&2, Wiley&Sons 1996).

[35] W. A. Friedman and W.G. Lynch, *Phys. Rev.* **C28**, 16 (1983).

[36] W. A. Friedman and W.G. Lynch, *Phys. Rev.* **C28**, 950 (1983).

[37] W. A. Friedman *et al.*, *Phys. Rev.* **C42**, 667 (1990).

[38] A. P. French, *Special Relativity* (Norton & Company1968).

[39] W.G. Gong, Ph.D. Thesis , (Michigan State University 1991).

[40] J. Gosset et. al. *Phys. Rev.* **C16**, 629 (1977).

[41] J. Gosset , J.I. Kapusta and G.D. Westfall *Phys. Rev.* **C18**, 844 (1978).

[42] I.S. Gradshteyn and I.M. Ryzhik , Table of Integrals,Series, and products, Academic Press(1980)

[43] D. H. E. Gross, Phys. Rep. 279, 119(1997)

[44] Francesca Gulminelli and Dominique Durand Nuc. Phys A 615, 117(1997)

[45] Gerry Hale, Los Alamos National Laboratory , Private communication (2002)

[46] J. A. Hauger *et al.*, *Phys. Rev.* **C57**, 764 (1998).

[47] H. Ho and P.L. Gonthier, Nuclear Instruments and Methods 190, 75-80 (1981)

[48] H.M. Hofmann and G.M. Hale Nuc. Phys A 613, 69(1997)

[49] Min-Jui Huang Ph.D. Thesis , Michigan State University, (1997)

[50] M.J. Huang *et al.*, *Phys. Rev. Lett.* **78**, 1648 (1997).

[51] M.J. Huang *et al.*, *Phys. Rev. Lett.* **77**, 3739 (1996).

[52] W.C. Hsi *et al.*, *Phys. Rev. Lett.* **73**, 3367 (1994).

[53] Wen-Chien Hsi Ph.D. Thesis , Michigan State University, (1995)

[54] Wen-Chien Hsi originally named REGR5_ORG_TOP.FOR upgraded to SPECTRUM_FIT.FOR

[55] Earl H. Kennard, Kinetic Theory of gases, McGraw-Hill, (1938)

[56] Y.D. Kim, et. al. Phys Rev. C 67, 14(1991)

[57] Y.D. Kim, et. al. Phys Rev. C 45, 387(1992)

[58] A. Kolomiets, et. al. Phys Rev. C 54, R472(1996)

[59] S.E. Koonin, Phys. Lett 70B, 43(1977)

[60] Theodore Korneff, Introduction to Electronics, Academic Press, 1966

[61] G.J. Kunde, et. al. Phys Rev. Lett. 77 , 2897 (1996)

[62] L.D. Landau and E.M. Lifshitz ,Statistical Physics 3rd , Academic Press, Butterworth-Heinemann 1980

[63] A.M.Lane and R.G. Thomas , Rev. of Mod. Phys. 30 (1958) 257

[64] S. Levit and P. Bonche, Nucl. Phys. A437, 426 (1985)

[65] Michael Annan Lisa, *Ph.D. Thesis* (Michigan State University, 1993).

[66] Tong Qing Li Ph.D. Thesis , Michigan State University, (1993)

[67] J.A. Lopez and P.J. Siemems, Nucl. Phys. A431, 728 (1984)

[68] W.G. Lynch, et. al. Phys Lett. 168B , 274 (1982)

[69] W.G. Lynch, et. al. Phys Rev. Lett. 51 , 1850 (1983)

[70] W.G. Lynch, et. al. Phys Rev. Lett. 52 , 2302 (1984)

[71] W.G. Lynch, "Fragmentation and Multifragmentation in Nuclear Collisions" (1997) preprint

[72] J.D. Jackson, Classical Electrodynamics ,2nd Ed., Wiley & Sons, (1975)

[73] B.V.Jacak, Ph.D. Thesis , Michigan State University, (1984)

[74] B.V.Jacak, et. al., Phys Rev. C 35, 1751 (1987)

[75] A.Kolomiets, et. al., Phys Rev. C 54, R472 (1996)

[76] N.Marie, et. al., Phys Let. B 391, 15-21 (1997)

[77] Walter E. Meyerhof, Elements of Nuclear Physics, McGraw-Hill, 1967

[78] L.G. Moretto et. al. Phys. Rev. Lett. 76, 2822 (1996)

[79] Murakami et. al. Nuclear Instruments and Methods in Physics Research. A275, 123-132 (1989)

[80] J.B. Natowitz et. al. Phys. Rev. C 52, 2322 (1995)

[81] J.B. Natowitz et. al. Phys. Rev. C 65, 034618 (2002)

[82] Nayak et. al. Phys. Rev. Lett. 62, 1021 (1989)

[83] Tapan Kumar Nayak Ph.D. Thesis , Michigan State University, (1990)

[84] Nayak et. al. Phys. Rev. C 45, 132 (1992)

[85] A. Ono et. al. , Prog. Theor. Phys. 87, 1185 (1992)

[86] R. K. Pathria , *Statistical Mechanics* , (1977)

[87] G.F. Peaslee et. al. Phys. Rev. C 49, 2271 (1994)

[88] L. Phair et. al. Nucl. Phys. A548, 489 (1992)

[89] L. Phair Ph.D. Thesis , Michigan State University, (1993)

[90] J. Pochodzalla et. al. Phys. Rev. C 35, 1695 (1987)

[91] J. Pochodzalla et. al. Phys. Rev. Lett 75, 1040 (1995)

[92] Scott Pratt and M.B. Tsang Phys. Rev. C 36, 2390 (1987)

[93] Scott Pratt, Private Communication , (2000)

[94] W. Lynch,David Poe,Al McCartney,N. Anantaraman, Private Communication , (1999)

[95] J. Randrup and S.E. Koonin Nuc. Phys. A356, 223 (1981)

[96] A. Ruangma et. al. nucl-ex/0110004

[97] W. Reisdorf et. al. Nuc. Phys. A612, 493 (1997)

[98] A. Schuttauf et. al. Nuc. Phys. A607, 457 (1996)

[99] C. Schwarz et. al. Phys. Rev. C 48(2), 676 (1993)

[100] V. Serfling et. al. Phys. Rev. Lett. 80, 3928 (1998)

[101] R. Shomin, M.B. Tsang et. al. Phys. Rev. C 66, 044618-1 (2002)

[102] R. Shomin et. al. *Temperature evolution of a hot system.* Submitted for publication

[103] Nathan Stone Ph.D., Thesis, Michigan State University, (1996)

[104] W. P. Tan Ph.D., Thesis, Michigan State University, (2002)

[105] D.R. Tilley et. al. Nucl. Phys. A541, 1 (1992)

[106] Tianxiao Liu -private communication (2003)

[107] M.B. Tsang et. al. Phys. Rev. C 40, 1685 (1989)

[108] M.B. Tsang et. al., Phys Let. B 297, 243 (1992)

[109] M.B. Tsang et. al. Phys. Rev. Lett. 71, 1502 (1993)

[110] M.B. Tsang et. al. Phys. Rev. C 47, 2717 (1994)

[111] M.B. Tsang et. al. *Nuclear temperature thermometers from isotope yield ratios* July 96 preprint msucl-1035 same as [113]

[112] M.B. Tsang et. al. Phys. Rev. C 51, 1057 (1996)

[113] M.B. Tsang et. al. Phys. Rev. Lett. 78, 3839 (1997)

[114] M.B. Tsang et. al. Phys. Rev. Lett. 86, 5023 (2001)

[115] M.B. Tsang et. al. Phys. Rev. C 64, 054615 (2001)

[116] M.B. Tsang et. al. Phys. Rev. C 64, 041603 (2001)

[117] M.B. Tsang, R. Shomin et. al. Phys. Rev. C 66, 044618-1 (2002)

[118] A.M. Vander Molen et. al., Users Guide to the MSU 4π Array 3'rd ed. (1996)

[119] A.M. Vander Molen Private Communication, (2002)

[120] V. Weisskopf, Phys. Rev. 52, 295 (1937)

[121] Carl Werntz et. al. Nucl. Phys. A121, 38 (1968)

[122] G.D. Westfall et. al. Phys. Rev. Lett. 37, 1202 (1976)

[123] G.D. Westfall , J. Gosset, et. al. Westfall firestreak paper *Phys. Rev.* **C18**, 8 (4).4 1978

[124] G.D. Westfall et. al. Phys. Rev. C 17, 1368 (1978)

[125] C. Williams et. al. Phys. Rev. C 55, R2132 (1997)

[126] A. H. Wilson F.R.S., Thermodynamics and Statistical Mechanics, Cambridge,(1966)

[127] William Wilson Ph.D., Thesis, Michigan State University, (1991)

[128] Samuel Wong, Introductory Nuclear Physics, Prentice Hall,(1990)

[129] Zajc W. A. et. al. Phys. Rev. C 29, 2173 (1984)

[130] Fan Zu Ph.D., Thesis, Michigan State University, (1992)

[131] Fan Zu et. al. Phys. Lett. B 282, 299 (1992)

[132] Fan Zu et. al. Phys. Rev. C 52, 784 (1995)

[133] Xi H. et. al. "Secondary decays and the He-Li isotope thermometer" (1996) preprint msucl-1040 or Phys. Rev. C 54, R2163 (1996)

[134] Xi H. et. al. Phys. Rev. C 58, 2636 (1998)

[135] Xi H. et. al. Phys. Rev. B 431, 8 (1998)

[136] Xi H. et. al. Nucl. Phys. A630, 160c (1998)

[137] Xi H. et. al. Phys. Rev. C 57, 462 (1998)

[138] Xi H.F. unpublished -private communication (1998)

[139] Xi H. et. al. Phys. Rev. C 59, 1 (1999)

[140] Xi H. et. al. Phys. Rev. C 59, 1567 (1999)

[141] Xu H.S. "Neutron Enrichment of Nuclear gas phase in heavy ion collisions" preprint

[142] Xu H.S. et. al. Phys. Rev. Lett. 86, 716 (2000)